Population Synthesis of Evolved Massive Binary Stars in the Magellanic Clouds

Dissertation
zur
Erlangung des Doktorgrades (Dr. rer. nat.)
der
Mathematisch-Naturwissenschaftlichen Fakultät
der
Rheinischen Friedrich-Wilhelms-Universität Bonn

von
Christoph Schürmann
aus
Attendorn

Bonn, Juli 2024

Angefertigt mit Genehmigung der Mathematisch-Naturwissenschaftlichen Fakultät der Rheinischen Friedrich-Wilhelms-Universität Bonn

Gutachter/Betreuer:	Prof. Dr. Norbert Langer
Gutachter:	Prof. Dr. Thomas Reiprich

Tag der Promotion:	21. Januar 2025
Erscheinungsjahr:	2025

Abstract

Massive stars are crucial building blocks of the Universe. They produce heavy elements, drive the evolution of galaxies, and are the origin of spectacular events such as supernovae and gravitational-wave coalescences. While the evolution of massive single stars alone is complicated, observations have shown that most of them are part of close binary systems, in which the two stars sooner or later interact by mass transfer between them, leading to an even more complex evolution that is only partially understood.

Among the many phases of binary evolution, we study binaries in which one component has become a stellar remnant, as this is the first long-lived phase after the well-understood phase with two stars. To study these, we focus not on individual systems, but on their entire population. We use two methods that assume two different physical conditions for stable mass transfer. The first method, based on detailed binary models in which the stellar structure equations derived from first principles are solved, uses an energy criterion, and the second method, rapid population synthesis, which models the stars and their evolution in a simplified way, uses a thermodynamic criterion. To use the second method, we need to make some preparations and derive new and more flexible descriptions of binary physics. These are rotation, mass transfer on the nuclear timescale, and accretion.

Rotation is a ubiquitous phenomenon in stellar evolution. To predict the spin of stellar remnants, we need to know how the angular momentum is distributed inside a star. We compare the outcome of different model assumptions with the star LB-1, which has recently lost its envelope, providing a direct view into the stellar interior, and find a strong preference for magnetic angular momentum transport.

Massive binary stars prefer close orbits, which makes the interaction phase more complex. This is a challenge for the rapid method, so we use dense grids of detailed models to derive recipes for the outcome of their interaction. We find that for fixed initial masses for close systems there is a correlation between the final mass and the orbital periods, and an anti-correlation between the duration of the mass transfer and the orbital period.

Finally, we need to understand the conditions under which binary interactions are stable and lead to the systems of interest. It has long been known that accreting stars can expand, and so we derive conditions for the intensity of the expansion. Assuming that this effect can lead to a massive loss of angular momentum from the binary, we derive which orbital configurations can stably interact and lead to a close binary containing a black hole or neutron star.

Using the above results, we derive synthetic populations of massive stars with remnant companions. Both methods are in good agreement with observations and predict a large number of yet unobserved massive stars with black hole companions, which can be identified either as binaries with large radial-velocity variations or as emission-line stars. We also predict that there are significant and testable differences between the two models.

Contents

CHAPTER 1

Introduction

"Wissen ist Nacht!"

— Walter Moers, *Die 13½ Leben des Käpt'n Blaubär*

Humans across all times and cultures are connected by a common marvel for the lights above them. The study of these lights is known as *astronomy*, which is derived from the ancient Greek words ἄστρον (star) and νόμος (law). Despite its name, astronomy studies not only the stars but all phenomena above the Earth's atmosphere. These include planets, nebulae, galaxies, and the Universe itself, but in the end all these objects are visible only because of the stars, which are by far the most dominant source of light. Even the "new" astronomies, such as radio-, X-ray-, neutrino-, and gravitational-wave astronomy, are, with a few exceptions, ultimately powered by the stars.

It is said that astronomy is the oldest of all sciences and, according to some, even the foundation of civilisation. This is not surprising as the stars are part of our natural environment. Astronomy has always been crucial in anchoring human existence in space and time, most prominently as a tool for navigation and in calendars. The Nebra Sky Disc, the oldest known depiction of the sky, was probably made for this purpose. It dates from around 1600 BCE, the same period as the Middle Kingdom in ancient Egypt, where the stars had been studied for more than a millennium for religious reasons, but also to predict the annual flooding of the Nile. In ancient Mesopotamia, astronomy had similar applications, as well as in classical antiquity, as, for instance, a bright full moon allowed night-time festivities. Today, with illuminated cities and bright screens everywhere, the lights of the sky are less present in our daily lives, but the fascination with them persists, as illustrated by the continued publication and financial success of books and movies such as *Dune* (1965) or *Interstellar* (2014).

Naturally, humans wondered about the nature of the lights above them and wanted to understand what stars are made of and why they shine. The first reference to the nature of the star can be found in the texts of the ancient Greek philosophers. Anaximander speculated that the Sun was a fire seen through a hole in the sky and according to Anaxagoras the Sun and the stars were flaming pieces of metal and stone. Both philosophers associated the stars with similar natural phenomena observed on Earth, but for Plato and Aristotle the stars and the Sun were made out of celestial pure materials (αἰθήρ, the infamous aether), untainted by the cacophony of the sub-lunar sphere. As many of their positions, it prevailed for a long time…

1.1 Observations of stars

The Aristotelian view persisted in Europe throughout the Middle Ages until the beginning of the Scientific Revolution. While it was challenged by the works of Galilei, Descartes, and Newton, it required the development of new observational techniques that transformed the old positional astronomy (e.g. Argelander's *Bonner Durchmusterung*) into modern astrophysics in order to understand the nature of the stars. These techniques were spectroscopy and photometry, which led to the Hertzsprung-Russell diagram.

1.1.1 Stellar spectroscopy

The first significant experiments in spectroscopy were carried out by Fraunhofer (1817, 1821), who discovered dark lines in the spectrum of the Sun and measured their wavelengths (Fig. 1.1, top). He was also able to identify similar lines in the spectra of stars, which he found to vary from one star to another (Fraunhofer, 1823). Over the next years it became clear that these dark lines are caused by the presence of chemical elements in the solar atmosphere, such as sodium (Kirchhoff, 1859) and hydrogen (Plücker, from Bonn, 1859, Longair, 2006). Kirchhoff (1859) also developed the theoretical basis for the formation of these lines. Finally, Kirchhoff (and Bunsen 1861, 1862, 1863) discovered that the solar spectrum contains lines of at least 40 chemical elements, showing that the Sun is made up of the same substances as found on Earth, thus falsifying the Aristotelian view.

Bessel (1838) determined the first trigonometric parallax of a star (61 Cygni) and thus provided the first interstellar distance measurement, which made it clear that the stars are as bright as the Sun and that both belong to the same class of objects. So it was not surprising that Huggins and Miller (1864), who took spectra of stars, found again the same chemical elements as on Earth. In the following decades, several attempts were made to classify the vast variety of stellar spectra. The first large and systematic scheme was put forward by Pickering (and Fleming, 1890b), with spectral classes from A to N. It was soon superseded by Maury and Pickering (1897), who proposed a two-dimensional classification distinguishing between stars with broad and sharp spectral lines. Finally, Cannon and Pickering (1901) introduced the Harvard classification scheme, which is still in use today, and rearranged the alphabetical spectral classes into the sequence OBAFGKM, each divided into subclasses 0 to 9. This sequence is shown in Fig. 1.1 (bottom). O-type stars show weak hydrogen and helium lines. While the latter fade as one advances in the spectral sequence, the hydrogen lines become more prominent until spectral class A is reached. From there on they become weaker. G-, K- and M-type stars show many increasingly strong metal lines, including molecular bands in M-type stars. The number of analysed stars had grown so large that Pickering (1912) was able to carry out the first population study of stellar spectra.

A physical understanding of the phenomenological OBAFGKM sequence was provided by Saha (1921), who deduced from ionisation processes that it is a temperature sequence from hot O-type stars (40 000 K) to cool M-type stars (3000 K). Based on this, Payne (1925) was able to make precise abundance measurements of the stellar atmospheres and found that they consist of 74% hydrogen and 24% helium by mass fraction. The remaining elements (2%) are called metals and their abundance, the metalicity, is different for different galaxies and different populations within them. It turns out that metallicity has a notable effect on stellar structure and evolution.

Among the thousands of stars classified by the end of the 19^{th} century, some showed peculiar spectra. The first to be discovered were the Be stars. Secchi (1866) reported that he had observed the star γ Cas to exhibit the Hα line not as the usual narrow absorption line, but as a broad and bright emission line (hence the latter "e"). Later, more stars of this type were discovered, almost all of them belonging to spectral class B and many

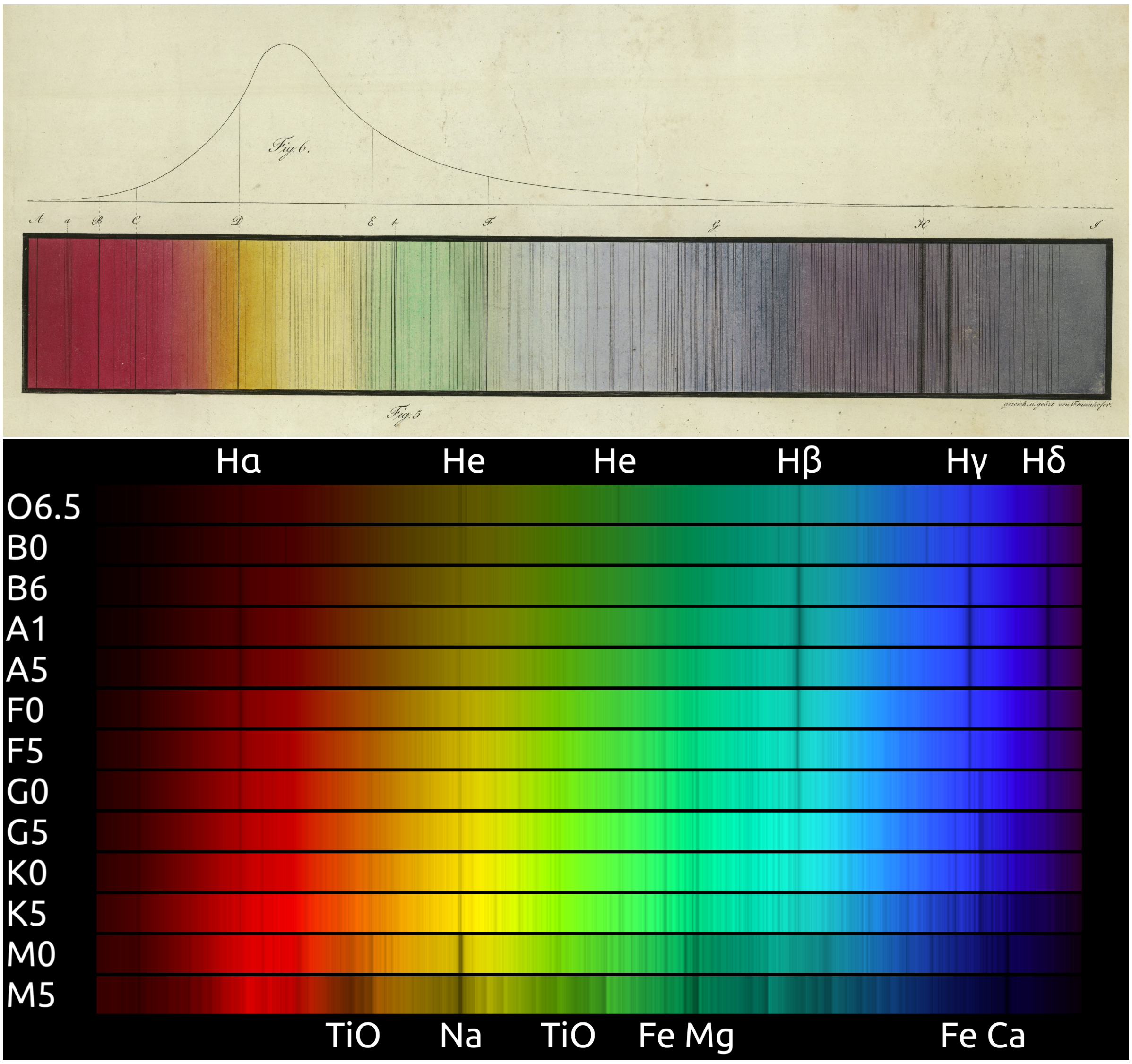

Figure 1.1: Top: The Solar spectrum recorded by Fraunhofer (1817) with dark lines within it. The curve on top shows the perceived brightness as function of wavelength. Bottom: Stellar spectra taken from Jacoby et al. (1984) and arranged following the Harvard classification scheme (Cannon and Pickering, 1901) with selected spectral lines marked. (Deutsches Museum, Archiv, BN 43952, CC BY-SA 4.0; NOIRLab/NSF/AURA, modified)

of them showing absorption lines much broader than in a normal stellar spectrum. Struve (1931) explained the Be phenomenon in terms of stellar rotation, to which we will return in Ch. 1.3.4. Wolf and Rayet (1867) found that the spectra of three stars in the constellation Cygnus show broad emission lines and bands on top of the continuum radiation, which are not associated with hydrogen but (depending on the star) with either helium and nitrogen or carbon. Beals (1929) explained the broad lines by the Doppler effect due to a stellar wind, by which the star constantly ejects material into space in a spherically symmetric flow. The origin of Wolf-Rayet stars is discussed in Ch. 1.3.2 and 1.4.5. Finally, Pickering (and Maury, 1890a) identified stars with periodically varying and split spectral lines, called spectroscopic binaries, to which we will return in Ch. 1.4.1.

1.1.2 The Hertzsprung–Russell diagram

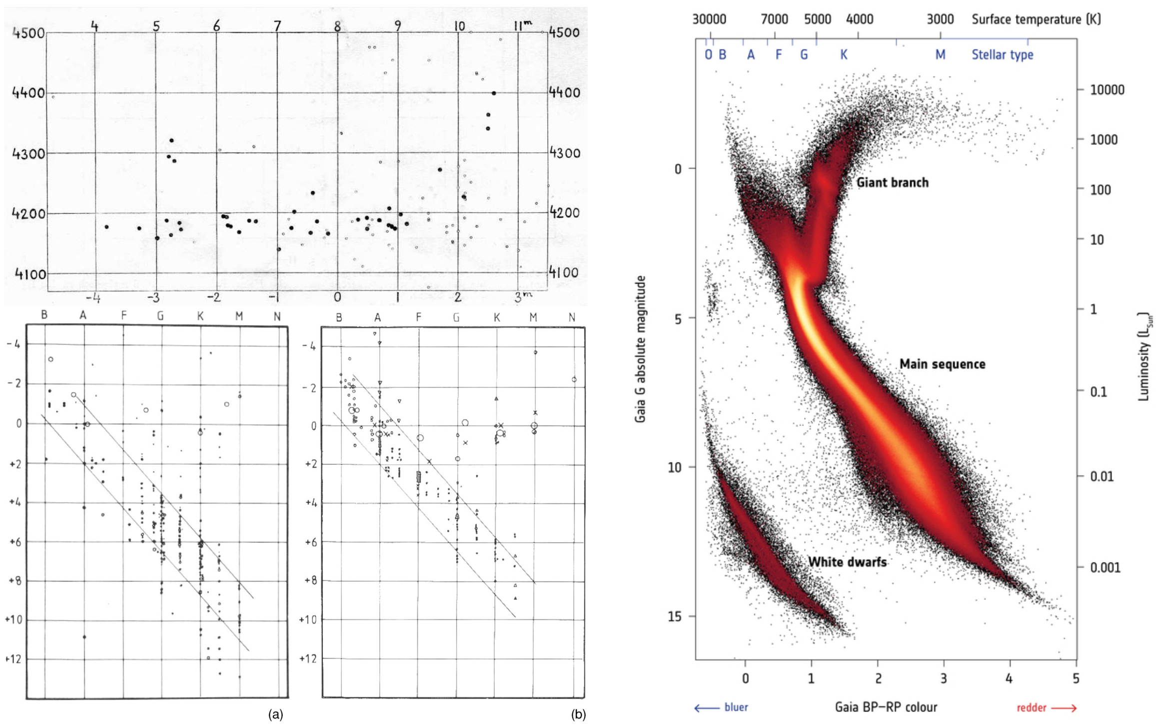

Figure 1.2: The earliest (left) and one of the latest (right) Hertzsprung-Russell diagrams. Top left: The diagram of Hertzsprung (1911) contains stars in the Hyades cluster (filled circles) and nearby stars (empty circles). The horizontal axis shows the magnitude (left bright, right faint) and the vertical axis shows the effective wavelength in Ångström (top red, bottom blue). Bottom left: Absolute magnitude–spectral class diagrams from Russell (1914a,b,c,d,e) for nearby field stars (left) and four star clusters (right, clusters indicated by symbol). Right: HRD containing more than four million stars based on the second data release from ESA's Gaia satellite. The colour corresponds to the number of stars per pixel. (Longair, 2006; Gingerich, 2013, ESA/Gaia/DPAC, CC BY-SA 3.0 IGO)

The apparent magnitude is the traditional measure of the perceived brightness of a star, dating back to Ptolemy or perhaps even to Hipparchus. It is a logarithmic measure of the electromagnetic flux in a given wavelength band. Distance measurements by parallax (Bessel, 1838) made it possible to determine the absolute magnitudes of stars, which measure the flux at a fixed distance.

It has also long been known that stars have different colours, which can be quantified by the difference between the magnitudes in the red and the blue band (Schwarzschild, 1900), or by the effective wavelength at which the spectrum appears brightest. Based on this, Hertzsprung (1911) produced a magnitude–effective wavelength diagram (Fig. 1.2, top left) of the stars in the Pleiades and Hyades star clusters. (In a star cluster, all stars are close enough that their spread in distance to Earth can be neglected, making distance determination less problematic). In parallel to that, Russell (1914a,b,c,d,e), after measuring a large number of parallaxes, presented a spectral class–absolute magnitude diagram (Fig. 1.2, bottom left) which shows the same morphology as the diagram of Hertzsprung (1911). This is not unexpected, since not only the spectral class is a measure of temperature (see Ch. 1.1.1), but also the effective wavelength. This is because a star can be modelled as a black body whose emission peaks at a wavelength given by Wien's displacement law. Today, such diagrams are called Hertzsprung-Russell diagrams (HRD).

Among theorists, it is common to use the effective temperature T_{eff} and the total luminosity L (emitted electromagnetic energy per unit time) of a star as the axes of an HRD. From the Stefan-Boltzmann law follows that

$$\frac{L}{4\pi R^2} = \sigma_{\text{SB}} T_{\text{eff}}^4 \tag{1.1}$$

and so it is possible to draw lines of constant stellar radius R in the HRD. Since it is tradition to place low temperatures to the right, stars in the upper right are the largest and those in the lower left are the smallest.

The dominant feature of the HRD is a *main sequence* of stars from bright and blue to red and dim. These stars turn out to be in the long-lasting process of converting hydrogen to helium in their centres. Furthermore, there is a group of red and bright stars at the top right of the diagram, called red giants, which are in the helium-burning stage. The dichotomy that red stars can be either faint or bright was already implicitly noted by Maury and Pickering (1897), since the spectral lines of red giants are weak while those of red dwarfs are strong. This is because red giants have a much lower surface gravity due to their large radii, and so their spectral lines are less affected by pressure broadening. In the lower left of the HRD, the white dwarfs can be found, which are the remnants of low-mass stars.

The development of the HRD led to speculation about the origin of these patterns, in particular whether they reflect the evolution of stars. According to Lockyer (e.g. 1887, 1915), initially also supported by Russell, stars would begin their lives as gaseous red giants and evolve along the red giant branch to condensate into hot and liquid O-type main-sequence stars. From there they would cool and contract along the main sequence to end up as M-type dwarfs. A relic of this falsified hypothesis is that to this day hot stars are called *early* and cool stars *late*.

1.2 Principles of stellar physics

The results of stellar spectroscopy suggested that the Sun and the stars obey the same laws of nature as those established on Earth, in particular the laws of thermodynamics. Thus, by the middle of the 19$^{\text{th}}$ century, several models were proposed for the source of the Sun's energy. Thomson (1854) reviewed them and argued that it was not possible for the Sun to be a hot gradually cooling body, because then it would have changed its temperature significantly over the course of human history. Chemical reactions, i.e. the Sun being a great fire, are also not a satisfactory source of energy, since the Sun would have burned through its entire mass in about 10,000 years. Finally, a constant influx of meteorites whose kinetic energy was converted into heat was considered. This idea was favoured by Thomson as it could provide enough energy, but the necessary influx of meteorites would disturb the orbits of the inner planets.

Helmholtz (1854) proposed that the Sun would gain its thermal energy by contraction from an initial cool and rarefied state to its present configuration. Thomson (1862), assuming the Sun to be a liquid sphere, used this to derive the age of the Sun. For any star its gravitational energy can be estimated to be of order $GM^2/2R$, where M is the total mass, R is the radius, and G is the gravitational constant. Dividing this by the luminosity gives what is now known as the thermal or Kelvin-Helmholtz timescale

$$\tau_{\mathrm{KH}} = \frac{GM^2}{2RL} \approx 16\,\mathrm{Ma} \left(\frac{M}{M_\odot}\right)^2 \left(\frac{R}{R_\odot}\right)^{-1} \left(\frac{L}{L_\odot}\right)^{-1}, \tag{1.2}$$

where $M_\odot \approx 2.0 \cdot 10^{30}$ kg, $R_\odot \approx 7.0 \cdot 10^8$ m, and $L_\odot \approx 3.8 \cdot 10^{26}$ W are the solar mass, radius and luminosity. While this timescale is relevant to stellar astrophysics (see Ch. 5), it turns out that it is not the appropriate timescale to estimate the lifetime of a star. Rutherford (1907) determined the lower limit for the age of the Earth, and thus also of the Sun, by radiometric dating to be more than 30 times larger than the Kelvin-Helmholtz timescale. Today, the age of the Sun and the Earth is estimated to be about $4.6 \cdot 10^9$ years.

1.2.1 The mechanical structure

Based on the idea that a star is a spherically symmetric ball of fluid, Lane (1870), Ritter (1883a,b,c, 1898) and Emden (1907) developed the first mathematical model of stellar structure. Defining the mass coordinate $m \in [0, M]$ as the mass enclosed in a sphere of radius $r \in [0, R]$, one can write

$$\frac{\partial m}{\partial r} = 4\pi r^2 \rho, \tag{1.3}$$

where ρ is the density. This equation is equivalent to the conservation of mass and the continuity equation. In stellar modelling, the mass coordinate m is preferred to r as an independent variable, since the stellar radius can vary by several orders of magnitude during stellar evolution, while the stellar mass can be treated as a constant for most episodes.

Secondly, Lane, Ritter and Emden assumed that the star is in hydrostatic equilibrium, i.e. the self-gravity of the fluid is balanced by the internal pressure gradient. This can be expressed as

$$\frac{\partial p}{\partial r} = -\frac{Gm\rho}{r^2}, \tag{1.4}$$

where p is the pressure. When this equation is derived from the Navier-Stokes equation, assuming radial symmetry and negligible viscosity, an additional acceleration term $\rho\ddot{r}$ remains on the left hand side. This term is associated to the dynamical timescale, which can be estimated as

$$\tau_{\mathrm{dyn}} = \sqrt{\frac{R^3}{GM}} \approx 30\,\mathrm{min} \left(\frac{R}{R_\odot}\right)^{3/2} \left(\frac{M}{M_\odot}\right)^{-1/2}. \tag{1.5}$$

This means that when a star is perturbed, it returns to hydrostatic equilibrium very quickly, and that for the secular processes we are interested in, the assumption of hydrostatic equilibrium is well fulfilled.

When Lane, Ritter and Emden published their works, it was not yet clear what the nature of the stellar material was, so they worked with general equations of state in the form of polytropic relations $p \sim \rho^\gamma$, which turn out to be applicable to fully convective and degenerate stars, but also with the ideal gas law

$$p = \frac{\rho}{\mu} k_{\mathrm{B}} T, \tag{1.6}$$

where μ is the mean particle mass of the gas, T is the temperature, and k_{B} is Boltzmann's constant. Today, we know that the pressure of the (ionised) ideal gas is the dominant contribution to the equation of state for large parts of stellar evolution.

The virial theorem of Clausius (1870, from Bonn), from which follows that

$$E_{\mathrm{tot}} = E_{\mathrm{th}} + E_{\mathrm{gr}} = -E_{\mathrm{th}} = \frac{1}{2}E_{\mathrm{gr}} < 0, \tag{1.7}$$

where E_{tot}, E_{th}, and E_{gr} are the total, thermal, and gravitational energy of the star, provide important insights into stellar evolution. To withstand its gravitational pull, a star must be hot (Eq. 1.4 and 1.6), but because of its high temperature it constantly loses energy at its surface (Eq. 1.1), leading to a permanent state of contraction which heats the star further (Eq. 1.7). This contraction, which takes place on the Kelvin-Helmholtz timescale, can only be delayed if there is a source of energy to compensate for the loss of energy at the surface. Nuclear fusion of hydrogen is an example of this, causing a delay that lasts for about 90% of the star's life.

1.2.2 The thermal structure

The need for an additional energy source led Eddington (1916) to introduce a generic energy production rate per unit mass ε which, when integrated over the whole stellar volume, would give the luminosity L. Using the local luminosity l, which is the energy passing per unit time through a shell at radius r, one can write $\partial l = 4\pi r^2 \rho\varepsilon\, \partial r$. In modern treatments of stellar structure, this equation is extended to include terms for energy release from internal energy and from volume work, and becomes

$$\frac{\partial l}{\partial r} = 4\pi r^2 \rho \left(\varepsilon - c_p \frac{\mathrm{d}T}{\mathrm{d}t} + \frac{p}{\rho^2}\frac{\mathrm{d}\rho}{\mathrm{d}t} \right) = 4\pi r^2 \rho \left(\varepsilon - T\frac{\mathrm{d}s}{\mathrm{d}t} \right), \tag{1.8}$$

where c_p is the specific heat capacity at constant pressure. The two time-dependent terms can be rewritten using the second law of thermodynamics and the specific entropy s. It turns out that this derivative is related to the Kelvin-Helmholtz timescale. This term becomes important in episodes when nuclear energy production ceases and the star continues to contract. When the processes on the Kelvin-Helmholtz timescale can be neglected, one speaks of thermal equilibrium.

It turns out that the nuclear energy production is extremely concentrated towards the centre of the star, and so this energy must be transported to the surface. Convection was initially the favoured transport mechanism, but Schwarzschild (1906), based on works from Sampson (1895) and Schuster (1902, 1905), developed a prescription for radiative energy transport by photon diffusion and showed that the onset of convection requires the temperature gradient in the star to exceed the adiabatic temperature gradient. Radiative energy transport has been applied to stars by Eddington (1916). It requires an optically thick medium in which the photons are constantly absorbed and re-emitted, thereby thermalising them. This creates a temperature gradient

$$\frac{\partial T}{\partial r} = -\frac{3\kappa\rho}{16\sigma_{\mathrm{SB}} T^3}\frac{l}{4\pi r^2}, \tag{1.9}$$

where κ is the opacity (photon interaction cross-section per mean particle mass) of the material. At high temperatures and low densities the most important contribution is Thomson (electron) scattering, but in general it is a complex function of temperature, density and chemical composition.

On the other hand, the adiabatic temperature gradient realised in convective regions is

$$\frac{\partial T}{\partial r} = -\frac{2\mu}{5k_{\mathrm{B}}}\frac{Gm}{r^2} \tag{1.10}$$

in the case of an ideal gas. According to Schwarzschild's convection criterion, the energy transport process which leads to the smaller temperature gradient (in magnitude) is realised, which is equivalent to the condition that the gradient of the specific entropy, or in meteorological terms the gradient of the potential temperature, must be non-negative. Ledoux (1947) generalised Schwarzschild's criterion to include the effects of chemical gradients. Convection also homogenises the chemical structure of a star within the convective regions.

Eddington (1917, 1924) used the above equations with radiative energy transport to derive a mass-luminosity relation for red giant stars, as he attested them a gaseous nature due to their low mean densities, but found that it applied much better to main-sequence stars ($L \sim M^{3.5}$, Halm, 1911; Hertzsprung, 1919), leading to the conclusion that these stars are not slowly contracting liquid spheres as he believed, but gaseous objects. This was also in contrast to the Russell-Lockyer picture, which argued for a constant stellar mass along the main sequence.

Eddington also found a maximum luminosity for stars where the transfer of momentum from photons to matter becomes stronger than the force of gravity. Using Eq. 1.4, 1.9, and the equation of state for radiation, $p = \frac{4\sigma}{3c}T^4$, one finds

$$L_{\rm Edd} = \frac{4\pi cGM}{\kappa}. \tag{1.11}$$

When the luminosity approaches the Eddington luminosity $L_{\rm Edd}$, matter at the stellar surface can easily become unbound. This may be related to the mass loss of Wolf-Rayet stars (see Ch. 1.1.1, and 1.3.2).

1.2.3 The chemical structure

While Rutherford (1907) speculated that radioactive decay was the energy source in the stars, Eddington (1920) proposed nuclear fusion reactions, since it was already known that the mass of a helium nucleus is slightly smaller than the mass of four protons, and Einstein had provided the relation between mass and energy. Today, the precise nuclear reaction chains are known. In lighter main-sequence stars (such as the Sun) the pp-chain dominates, while in heavier main-sequence stars hydrogen is converted to helium by the CNO-cycle (Weizsäcker, 1937, 1938; Bethe, 1939), in which gradual proton capture reactions of carbon and nitrogen isotopes and subsequent β^+-decay produce an oxygen isotope which regenerates the initial carbon isotope by α-emission.

The timescale of hydrogen burning can be derived by assuming that a fraction $f_{\rm fuel}$ of the star's mass is available as nuclear fuel, and that the fraction $f_{\rm equiv}$ of this mass is converted to energy. Dividing this energy by the luminosity gives the nuclear timescale

$$\tau_{\rm nuc} = f_{\rm equiv} f_{\rm fuel} \frac{Mc^2}{L} \approx 10\,{\rm Ga} \left(\frac{M}{M_\odot}\right) \left(\frac{L}{L_\odot}\right)^{-1} \sim 10\,{\rm Ga} \left(\frac{M}{M_\odot}\right)^{-2.5}, \tag{1.12}$$

using $f_{\rm fuel} = 0.1, f_{\rm equiv} = 0.007$ and the main sequence mass-luminosity relation. Therefore, the lifetime of more massive stars is shorter.

When the central hydrogen reservoir is depleted, the star contracts again and heats up further until the central temperature is high enough to ignite helium burning, which lasts for about 10% of a star's life. This cycle of contractional heating and nuclear burning of increasingly heavy elements continues until nuclear fusion becomes endothermic or the contraction is halted by degeneracy.

Since nuclear reactions change the composition of the stellar material, one can find equations for the chemical evolution of the stellar interior. Together with a term for the diffusion of elements within the star, they read

$$\frac{\partial X_i}{\partial t} = \frac{\mu_i}{\rho} \left(\sum_j r_{i,j} - \sum_j r_{j,i}\right) + \frac{\partial}{\partial m} \left((4\pi r^2 \rho)^2 D \frac{\partial X_i}{\partial m}\right), \tag{1.13}$$

where X_i is the mass fraction of a given element i, μ_i is its atomic mass, $r_{i,j}$ are the conversion rates from element j to element i, which can be related to the energy production rate $\varepsilon = \sum_{ij} r_{i,j} \rho^{-1} (\mu_i - \mu_j) c^2$, and D is the diffusion coefficient (Heger et al., 2000; Kippenhahn et al., 2013).

1.2.4 Solving the equations of stellar structure and evolution

Eq. 1.3, 1.4, 1.8, 1.9, 1.10, and 1.13 are the equations of stellar structure and evolution and must be solved to model the interior of a star. Due to their complex structure and the fact that the material functions pressure, entropy, opacity, and energy production rates are complicated functions of temperature, density and chemical composition, accurate stellar models must be computed numerically. Nevertheless, many analytical solutions have been derived, based for example on simplifications of the material functions. An example of this is the polytropic models of Emden (1907). An important contribution was made by Hoyle and Lyttleton (1942), who derived power-law relations between key stellar parameters, called homology relations, by assuming that different stellar models with similar assumptions have similar solutions. Schwarzschild (1946), Oke and Schwarzschild (1952), Sandage and Schwarzschild (1952), Schwarzschild et al. (1953) and Hoyle and Schwarzschild (1955) computed stellar models stellar models by manual numerical integration of the stellar structure equations[1].

The expansion of science after the Second World War, which provided the physical knowledge for sufficient material functions, and the advent of electronic computers made it possible to solve the stellar structure equations numerically on a large scale. Leading figures in this matter were Henyey et al. (1955, 1959a,b) and Kippenhahn et al. (1958). In recent decades, powerful detailed stellar evolution codes have been developed, such as the one of Eggleton (1971, 1972), Eggleton et al. (1973) and Eggleton (1973), BEC (Heger et al., 2000; Yoon et al., 2006; Brott et al., 2011), the Brussels codes STAREVOL and BINSTAR (Siess et al., 2000; Palacios et al., 2006; Siess, 2006; Siess and Arnould, 2008; Davis et al., 2013; Deschamps et al., 2013; Siess et al., 2013), and MESA (Paxton et al., 2011, 2013, 2015, 2018, 2019), which we will also use in this thesis.

1.3 Single star evolution

Since we are able to solve the stellar structure equations, in this section we present key results from single star evolution that are relevant to the description of binary stars. For illustration, we have calculated four stellar models with MESA (Paxton et al., 2011, 2013, 2015, 2018, 2019) and the same physical assumptions as in Ch. 5, which are shown in Figs. 1.3, 1.4, and 1.5. More detailed descriptions can be found in Kippenhahn et al. (2013).

1.3.1 Central hydrogen burning

The calculation starts with a chemically homogeneous model in thermal equilibrium. In its centre, hydrogen is converted to helium by the CNO-cycle (Fig. 1.3, red shading in lower left). Since the burning rate of the CNO-cycle is extremely temperature sensitive, the burning is strongly concentrated towards the centre, and the local luminosity is high enough to form a convective core, which is a typical feature of massive stellar models. For the $10 M_\odot$-model, the initial mass of the convective core is $4.5 M_\odot$ (Fig. 1.3). Convective regions are well mixed and so the whole convective core remains chemically homogeneous, but becomes increasingly helium-enriched during central hydrogen burning. At the same time, the chemical composition

[1] Schwarzschild (1958) wrote "For many problems in the theory of the stellar interior the speed of numerical integrations by hand is entirely sufficient."

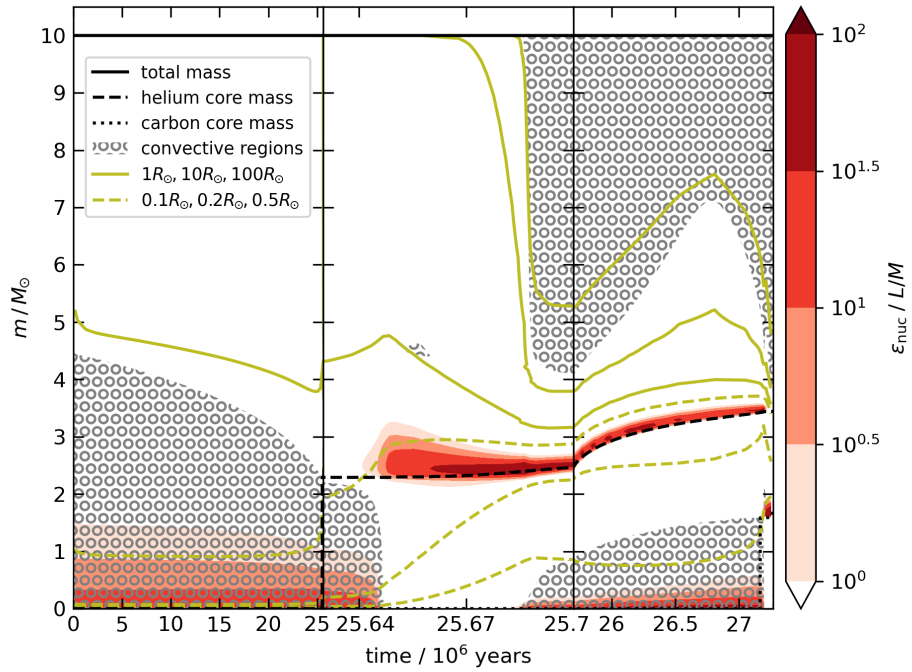

Figure 1.3: Kippenhahn diagram of the $10M_\odot$-model showing the total mass, the mass of the helium core (all layers with a helium mass-fraction of at least 0.99) and the mass of the carbon core. Red shading indicates where nuclear burning occurs, which is given in units of the model's luminosity-to-mass ratio. Convective regions are marked with grey circles and lines of constant radius are shown in yellow.

of the envelope remains unchanged (Fig. 1.4, blue lines). Over the course of the central hydrogen burning, the mass of the convective core shrinks to $2.3M_\odot$ (grey regions in Fig. 1.3), as hydrogen is converted to helium, which has a larger mean particle mass and a lower opacity, and thus radiative energy transport becomes more efficient. The combination of the shrinking convective core and the gradual conversion of hydrogen to helium within it leads to the formation of a transition layer between core and envelope with a chemical gradient (Fig. 1.4, dotted lines).

At the beginning of the model's evolution, its luminosity is about $5 \cdot 10^3 L_\odot$ and its radius is about $3R_\odot$ (Fig. 1.5). During central hydrogen burning, both values increase, which can be explained by the fusion of hydrogen to helium. The resulting decrease in the mean particle mass reduces the ability of the core to withstand the pressure of the envelope (Eq. 1.6). If a temperature increase alone had to compensate for the pressure loss, the luminosity would increase by an extreme amount ($\varepsilon \sim T^{18}$), but the outward energy transport rate cannot be arbitrarily high (Eq. 1.8 and 1.10), so the central temperature increases only marginally, leading to the observed increase in luminosity. Rather, the pressure exerted by the envelope must be reduced, which can be archived by expansion of the envelope (Eq. 1.4). This is also required by the virial theorem, since an energy overproduction would lead to expansion and cooling, keeping the luminosity at bay. The excess luminosity provides the energy to expand the envelope. At the end of central hydrogen burning, the model has a luminosity of about $2 \cdot 10^4 L_\odot$ and its radius is about $10R_\odot$.

Of its total lifetime of $27.3 \cdot 10^6$ years, the model spends $25.6 \cdot 10^6$ years in central hydrogen burning (Fig. 1.3). This is also indicated by the red colour between central hydrogen ignition and depletion in Fig. 1.5.

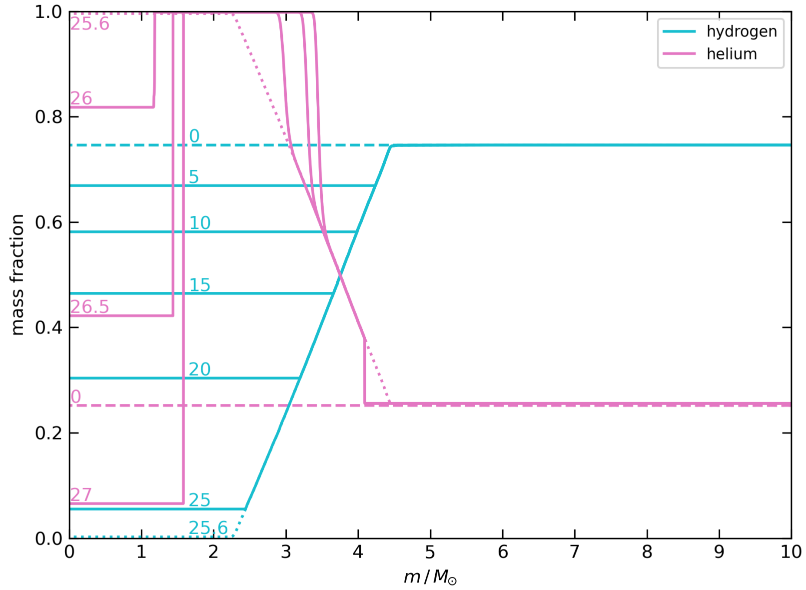

Figure 1.4: Mass fractions of hydrogen (blue) during central hydrogen burning and helium (pink) during central helium burning throughout the $10M_\odot$-model for selected times. The initial profiles are shown as dashed lines and those at central hydrogen depletion as dotted lines. The numbers indicate the respective age in 10^6 years.

It is typical for all stellar models to spend about 90% of their lifetime in this phase. Considering models with different initial masses, it can be seen that the hydrogen burning time decreases with mass (as predicted by Eq. 1.12) and that the luminosity of the models increases with mass. In Fig. 1.5, the core hydrogen burning regions form a diagonal from high luminosities and temperatures to low values. Using the luminosity of the models as a measure of the magnitude of a star, and relating the effective temperature to the spectral class, one can compare Fig. 1.5 with Fig. 1.2 and find that main-sequence stars can be understood by hydrogen burning models, as both regions occupy a diagonal from top left to bottom right. Thus, central hydrogen ignition and depletion are commonly referred to as zero-age main-sequence (ZAMS) and terminal-age main-sequence (TAMS).

1.3.2 After central hydrogen depletion

When the central hydrogen reservoir is depleted, there is no energy source to compensate for the loss of energy at the stellar surface. So the model contracts under its own gravity, leading to the small hook in the track near the position of central hydrogen depletion (Fig. 1.5). The contraction ends when the material above the helium core (Fig. 1.3, black dashed line) is dense and hot enough to ignite hydrogen shell burning around the core (the red region in Fig. 1.3 starting at an age of $25.64 \cdot 10^6$ years). However, the shell source does not prevent the core from contracting further. This can be seen from the lines of constant radius in Fig. 1.3, which have a positive slope below the burning shell. The shell contracts only marginally with the core (Fig. 1.3, upper yellow dashed line), because this already heats the shell enough to increase nuclear energy production. The additional luminosity is absorbed in the envelope by expansion (falling yellow lines). Expansion at nearly constant luminosity reduces the surface temperature according to the Stefan-Boltzmann law (Eq. 1.1). Therefore, the opacity in the envelope increases as ions recombine, leading to the formation of

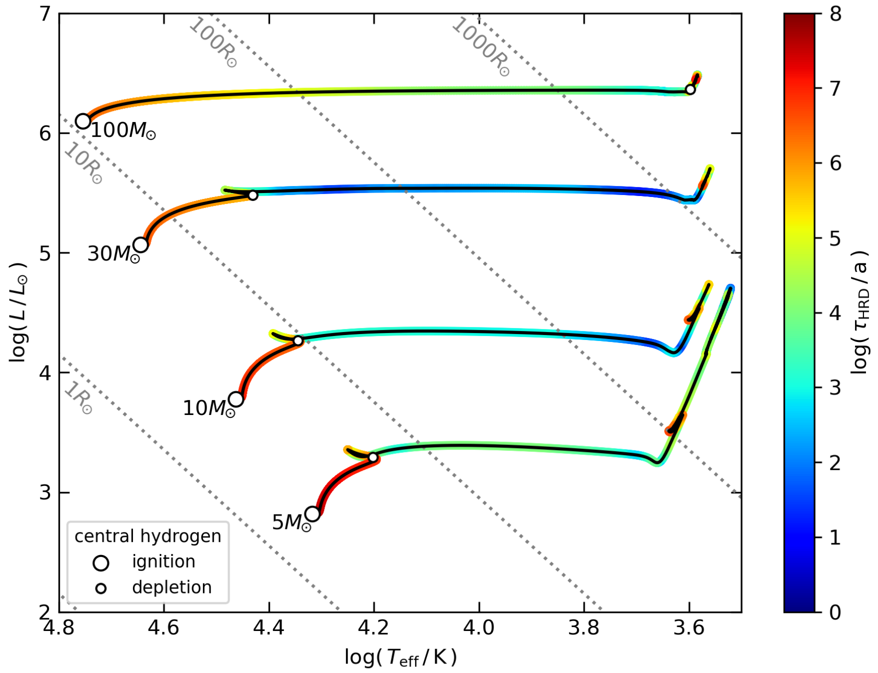

Figure 1.5: HRD showing the evolutionary tracks from hydrogen ignition to carbon depletion of four stellar models with different initial masses ($5M_\odot$, $10M_\odot$, $30M_\odot$, and $100M_\odot$). We have marked the position of the beginning and end of central hydrogen burning. Each track is coloured by the timescale τ_{HRD} defined as $\tau_{\mathrm{HRD}}^{-2} = \dot{T}_{\mathrm{eff}}^2/T_{\mathrm{eff}}^2 + \dot{L}^2/L^2$, where red means that the star is evolving slowly through the diagram while blue means fast evolution. Lines of constant radius are shown in grey. The horizontal axis is inverted by tradition to match Fig. 1.2.

a deep convective envelope (Fig. 1.3, grey region top right). A fully convective model has a strict temperature-luminosity relation, roughly $L \sim T_{\mathrm{eff}}^{10}$ (Hayashi and Hoshi, 1961), which the considered $10M_\odot$-model mast also obey, so its luminosity increases. The contraction of the helium core and the subsequent expansion of the envelope takes place on the thermal timescale, about 30,000 years (Fig. 1.3), but this rapid process makes up the largest section of the track in Fig. 1.5. So the time a star spends between the main sequence and the red-giant branch, the Hertzsprung gap, is very short.

As the helium core contracts, it heats up until the conditions for helium burning are reached. The contraction stops and the model settles into a phase of core helium burning, which lasts for about 10% of the model's lifetime. This can be seen in Fig. 1.5 by the reddish colour near $\log T_{\mathrm{eff}}/\mathrm{K} = 3.6$ and explains the second most prominent feature in Fig. 1.2, the red-giant branch. The hydrogen burning shell above the helium core slowly increases the mass of the helium core (Fig. 1.3, dashed line, and Fig. 1.4, pink lines around $m = 3M_\odot$). The helium core, like the hydrogen burning core, is convective and depletes its helium reservoir after about $1.5 \cdot 10^6$ years (Fig. 1.4, pink lines at $m = 0M_\odot$). Then a helium burning shell ignites and the core contracts again until central carbon burning begins, if possible. This cycle of stable core burning and contraction repeats until all possible nuclear burning stages have been reached, depending on the initial mass.

Due to their high luminosity, very massive stars can evolve close to their Eddington limit (see Ch. 1.2.2), which is lower for cooler stars, since the opacity increases with decreasing temperature. As stars evolve towards lower effective temperatures, the material at the stellar surface is only weakly bound and can be easily removed. The resulting mass loss, the stellar wind, is visible in stellar spectra and can explain nebulae around certain stars. If the stellar wind is strong enough, it can remove the entire envelope of a stellar model, exposing the helium-enriched layers of the former convective core (Fig. 1.4) or even the helium or carbon core. This process is a possible explanation for the formation of Wolf-Rayet stars (Ch. 1.1.1). Note that stellar wind is also important in massive main-sequence stars (Langer, 2012).

1.3.3 End of stellar lives and stellar remnants

Models with an initial mass below about $8M_\odot$ are not heavy enough to ignite central carbon burning. Rather, the central density becomes so high that the equation of state of an ideal gas no longer applies and the electrons become quantum mechanically degenerate. This means that the electron density is so high that the Pauli exclusion principle comes into play (Pauli, 1925), which allows only a limited number of particles per phase space volume $\Delta x \Delta p \sim \hbar$ (Fowler, 1926). At the same time, a strong mass loss develops, removing the entire envelope and exposing the degenerate carbon-oxygen core. It is very hot, but small and therefore faint, which places the objects, called white dwarf, in the lower left of the HRD (Fig. 1.2 and 1.5). For a short time it illuminates the shredded envelope around it to become a planetary nebula (Gurzadyan, 1997).

To ignite carbon and subsequent burning processes, the central temperature must be so high that neutrinos are produced which can carry such a significant amount of energy out of the core that this neutrino cooling determines and accelerates the final evolution of the core to a timescale of about 1000 years (Kippenhahn et al., 2013). The envelope of the model cannot react as fast and basically decouples from the central processes. So the outer appearance remains unchanged at the end of massive stellar life. If a model has an initial mass between about 8 and $12M_\odot$, it is heavy enough to ignite central carbon burning, but no further processes (Kippenhahn et al., 2013). The remaining ONeMg-core degenerates and forms a white dwarf within the model. It grows in mass due to the ongoing shell burning at its top. To obey the Pauli exclusion principle, the electrons must occupy increasingly higher momentum states and become relativistic (Anderson, 1929). At the ultra-relativistic limit, the density of states is so high that the amount of energy needed to push the electrons into a higher state is so small that the degenerate electrons cannot provide enough pressure to withstand gravity, and the white dwarf collapses. This gives a maximum mass for white dwarfs, called the Chandrasekhar mass, which is about $1.4M_\odot$ (Chandrasekhar, 1931). As also nuclei are present, it becomes favourable for the electrons to undergo electron capture reactions (inverse β-decay) to form neutron-rich nuclei during the collapse. This reduces the electron pressure in the core, accelerating the collapse, which can lead to a supernova explosion called an electron-capture supernova (Heger et al., 2003). It is possible that this scenario is only relevant for binary stars, and that single stars in this mass range shed their envelope in a similar way to lower mass stars, leaving behind a white dwarf (Podsiadlowski et al., 2004).

Models with masses above about $12M_\odot$ can ignite nuclear burning up to the formation of iron. From there, further nuclear burning stages are not possible because iron is the element with the highest nuclear binding energy per nucleon. Iron burning would capture energy rather than release it, and so the core becomes inert. At this stage, the stellar model has an onion-like structure, with different chemical layers separated by burning shells. As the degenerate iron core grows in mass through shell burning, it contracts and heats further until it reaches temperatures of about 10^{11} K, where the thermal photons are energetic enough to break up the iron nuclei into protons and neutrons. This reaction is endothermic and removes so much energy from the gas that it cannot withstand the external pressure, leading to the collapse of the core, called an iron-core collapse supernova (see e.g. Maeder, 2009; Langer, 2012; Kippenhahn et al., 2013; Tauris and van den Heuvel, 2023).

In both types of collapse, taking place in about 10 ms, the electrons are captured by the protons to form neutrons, creating a neutron-rich core. This and various other processes produce a large number of neutrinos, which carry away most of the released gravitational energy ($\sim 10^{53}$ erg). Although the interaction cross-section of the neutrinos is extremely small, their number is so large, and the material is so dense, that they are able to eject the outer core and envelope, which is observable as a supernova explosion (see e.g. Shapiro and Teukolsky, 1983; Langer, 2012; Kippenhahn et al., 2013; Tauris and van den Heuvel, 2023).

The neutron star is the main product of the supernova explosion (Baade and Zwicky, 1934). It is a macroscopic object ($R \approx 12$ km) with nuclear density ($M \approx 1.3 M_{\odot}$, Özel and Freire, 2016) composed almost entirely of neutrons. Their degeneracy pressure balances gravity, similar to the electron degeneracy pressure in white dwarfs (Shapiro and Teukolsky, 1983). Neutron stars were first observed in the radio regime as pulsars (Hewish et al., 1968). In addition to their short pulsation period (1 ms to 10 s Lorimer and Kramer, 2004), they show high proper motion around 265 km/s (Hobbs et al., 2005), which is thought to be caused by a kick the neutron star receives at birth, caused by an asymmetric supernova explosion due to anisotropic mass ejection, neutrino emission, or fallback on the neutron star (Janka et al., 2022).

Not all massive stars end their lives as supernovae and neutron stars. It is possible that the neutron star exceeds its upper mass limit, the Tolman–Oppenheimer–Volkoff limit, analogue to the Chandrasekhar mass (Oppenheimer and Volkoff, 1939; Tolman, 1939). It is between 2 and $3 M_{\odot}$, but the exact value is unknown, as is the mass-radius relation of neutron stars, due to the uncertain equation of state at nuclear densities (Özel and Freire, 2016). Above the Tolman–Oppenheimer–Volkoff limit the core collapses into a black hole (Landau, 1932; Oppenheimer and Snyder, 1939). In contrast to white dwarfs and neutron stars, this final stage of stellar life is not a material object, but a configuration of space-time from which nothing can escape. The state inside is therefore unobservable and only events in its vicinity can be studied, such as the infall of matter. For this reason, almost all known stellar-mass black holes are part of a binary star (see Ch. 1.4.1). A black hole can be formed during a supernova by the fallback of material onto the young neutron star, or by the direct collapse of the progenitor star, which can happen if the neutrinos are unable to unbind the stellar envelope (Tauris and van den Heuvel, 2023). Simulations show that the relationship between the initial mass of the progenitor star and the nature of the remnant is stochastic in large mass regimes and also depends on metallicity. It may be related to the compactness of the pre-explosion core (O'Connor and Ott, 2011), which is a measure of its central entropy (Schneider et al., 2021, 2024). In the work presented here, we restrict ourselves to a simple helium core mass limit for the formation of a black hole, following Sukhbold et al. (2018).

1.3.4 Stellar rotation

Rotation is a ubiquitous phenomenon in stars, the best known being the rotation of the Sun, which has a period of about 25 days. It is often quantified by the equatorial rotation velocity v_{rot}, which is about 2 km/s for the Sun, but can be significantly larger for massive stars, which can rotate more than a hundred times faster (Langer, 2012). Observationally, stellar rotation is inferred from the Doppler broadening of spectral lines, and thus the true equatorial rotational velocity is only known by a factor of $\sin i$, where the inclination i is the angle between the spin axis of the star and the line of sight (see e.g. Unsöld and Baschek, 2002; Karttunen et al., 2017).

Rotation causes a star to be subject to the centrifugal force, which changes the stellar structure equations, in particular the right-hand side of Eq. 1.4 is extended by a centrifugal term $m\omega^2 s$, where ω is the angular velocity of the star and s is the distance to the spin axis (Maeder and Meynet, 2000; Maeder and Meynet, 2004). This causes the star to lose its spherical symmetry as the equipotential surfaces bulge away from the equator. Thus the star deforms with an equatorial radius R_{eq} larger than the nearly unchanged polar radius R_{p} (de Mink et al., 2013). There is a critical equipotential surface that the star cannot overfill. At its equator, gravity and centrifugal force cancel each other out, since the centrifugal force is directed outward and opposes the gravitational force, resulting in a force-free ring. At this surface is $R_{\mathrm{eq}} = \frac{3}{2} R_{\mathrm{p}}$ (Kippenhahn et al., 2013). If the star were larger than this surface, its outer layers would be unbound and ejected into space. This gives a critical rotational velocity and a critical angular velocity

$$v_{\mathrm{cr}} = \sqrt{\frac{2GM}{3R_{\mathrm{p}}}} \quad \text{and} \quad \omega_{\mathrm{cr}} = \frac{2v_{\mathrm{cr}}}{3R_{\mathrm{p}}}, \tag{1.14}$$

which limit the rotation of the star, see de Mink et al. (2013) or Rivinius et al. (2013).

In the presence of rotation, the stellar structure equations can be rewritten to resemble the non-rotation ones (Maeder, 2009). However, von Zeipel (1924) showed that surfaces of constant pressure no longer coincide with surfaces of constant temperature. This means that the model has become baroclinic, which induces large scale circulations in the model that can homogenise it if the rotation is close to critical. Rotation also induces hydrodynamical instabilities that can contribute to the mixing of chemical elements within the star (Heger and Langer, 2000; Heger et al., 2000). Stellar rotation does not have to be rigid body rotation, and the rotational velocity can be a function of radius. While stellar models show that rigidity is reasonable for hydrogen burning models, it breaks down for advanced evolutionary phases (Maeder and Meynet, 2000), as can be seen from asteroseismlogy (Aerts et al., 2010). The aforementioned mixing processes also transport angular momentum within the star, which feeds back into the rotational profile of the star (Heger et al., 2000). Of particular interest are magnetic phenomena such as the Spruit-Tayler dynamo (Spruit, 2002), where the differential rotation induces magnetic fields that counteract the differential rotation. The Spruit-Tayler dynamo can be much more effective than hydrodynamical processes in controlling stellar rotation (Maeder and Meynet, 2004; Heger et al., 2005; Suijs et al., 2008). We will study it in Ch. B.

As mentioned above, a near-critical rotating star can lose material at its equator. Rather than disappearing, this material can accumulate in the vicinity of the star to form a Keplerian decretion disk. These objects are optically thin and give rise to line emission (Rivinius et al., 2013). In combination with the rotationally broadened absorption lines, this model can explain the Be star phenomenon mentioned in Ch. 1.1.1 (Struve, 1931). The details of the conditions under which a rapidly rotating star becomes a Be star are still unclear (Rivinius et al., 2013). For example, Regulus (α Leo) is a fast rotator but not a Be star (Slettebak, 1954). It is also unclear how a star can archive critical rotation. Two models are discussed in the literature, namely single star evolution and binary evolution (Bodensteiner et al., 2020b). In the case of single star evolution, the star is born moderately fast rotating and evolves to criticality by decreasing its momentum of inertia and increasing its radius during hydrogen burning evolution (Ekström et al., 2008; Hastings et al., 2020). The binary channel is discussed in Ch. 1.4.5.

1.4 Binary stars

Stars can have masses from 0.1 to more than $100 M_{\odot}$ (Kippenhahn et al., 2013). Massive stars, i.e. stars with masses above about $10 M_{\odot}$, are the most interesting. They are the origin of spectacular events such as supernovae (Burrows et al., 1995; Langer, 2012; Burrows and Vartanyan, 2021; Aguilera-Dena et al., 2023), breed heavy elements (Burbidge et al., 1957; de Mink et al., 2009b; Pignatari et al., 2010; Thielemann et al., 2011), and shape the evolution of galaxies (Mac Low and Klessen, 2004; Hopkins et al., 2014; Crowther et al., 2016). Recent observations have shown that most massive stars are part of a binary system (Sana et al., 2012; Moe and Di Stefano, 2017), in which the stellar evolution can change drastically (Podsiadlowski, 1992;

de Mink et al., 2013; Kruckow et al., 2018; Wang et al., 2020). This section outlines the basics of massive binary evolution.

1.4.1 History and observation

Binary stars are known since 1617, when Castelli, a student of Galilei, discovered that the star Mizar (ζ UMa) appeared as two sources of light rather than one when viewed through a telescope (Tauris and van den Heuvel, 2023). In the centuries that followed, more and more binary stars were discovered. While it may be a coincidence that two stars appear to be so close together and may have a large line-of-sight distance, Michell (1767) showed that these objects are more abundant than expected from a random distribution in the sky. This was not only the first population analysis of binary stars, but also showed that they are a physical phenomenon. Herschel (1803) was the first to observe the orbital motion of a binary star. He noticed that the fainter star of α Gem, Castor B, had moved relative to Castor A over the course of a century. This discovery showed that binary stars are not only gravitationally bound, but also that Kepler's laws of planetary motion could be applied to them. Kepler's third law is

$$\frac{GM}{4\pi^2} = \frac{a^3}{P^2}, \tag{1.15}$$

where M is the total mass of the binary system, a is the semi-major axis of the orbital eclipse, and P is the orbital period of the binary. In general, the orbit is elliptical (Kepler's first law), but for many applications it is reasonable to assume a circular orbit.

In addition to visual binaries such as Mizar and Castor, where both stars can be resolved, astronomers distinguish three other classes of binaries. These are astrometric binaries, where the binary nature is revealed by the orbital motion of a bright star around an unseen component, eclipsing binaries, and spectroscopic binaries. The first astrometric binary was discovered by Bessel (1844b), who noticed that Sirius (α CMa) does not move in a straight line across the sky, but shows a periodic motion superimposed on its proper mation, and suggested an invisible companion, which was found by Clark (1862). It turned out to be a white dwarf. Eclipsing binaries are characterised by a periodic dimming of a star when one component occults the other. Ancient Arab astronomers may have observed this phenomenon in the star Algol (β Per), which may explain its name, since الغول (al-ġūl) means demon, but the dimming of Algol was first documented by Montanari (1671). Vogel (1890) found spectroscopic evidence for the binary nature of this star, after this explanation for the dimming had been suggested a century earlier.

With the advent of stellar spectroscopy, the first spectroscopic binary was discovered. It was again Pickering (and Maury 1890a) who noticed that the spectral lines of Mizar A (which was already known to be a component of a binary star) are split into two components, and that both move periodically around the centre of the spectral line with a phase difference of π, meaning that when one component is maximally blue-shifted, the other is maximally red-shifted (by about 220 ppm). This behaviour is explained by the orbital motion of the two stars around their common centre of mass, which changes the observed wavelength of the spectral lines through the Doppler effect. The Doppler shift $\Delta\lambda = \lambda' - \lambda$, where λ' is the observed wavelength of a spectral line and λ is the wavelength in the rest-frame, is related to the radial velocity v_r of the star by

$$\frac{\Delta\lambda}{\lambda} = \frac{v_r}{c} \tag{1.16}$$

if $v_r \ll c$. When one star moves towards the observer, the other one recedes, and the spectral lines of the advancing star appear blue-shifted, while those of the receding one are red-shifted. This is illustrated in

Fig. 1.6, where we show the radial-velocity variations of the binary star Menkalinan (β Aur). Kepler's third law (Eq. 1.15) and the conservation of barycentre can be used to derive the mass ratio of the binary and, if the inclination angle of the orbit is known, the stellar masses. This technique is of major importance in modern astrophysics, as it is the most reliable way to measure the masses of stars. It is not uncommon for only the spectral lines of one star to be detectable and those of the other to be hidden, if it is much fainter, or if it is not a star but a black hole, as in the case of VFTS 243 (Shenar et al., 2022).

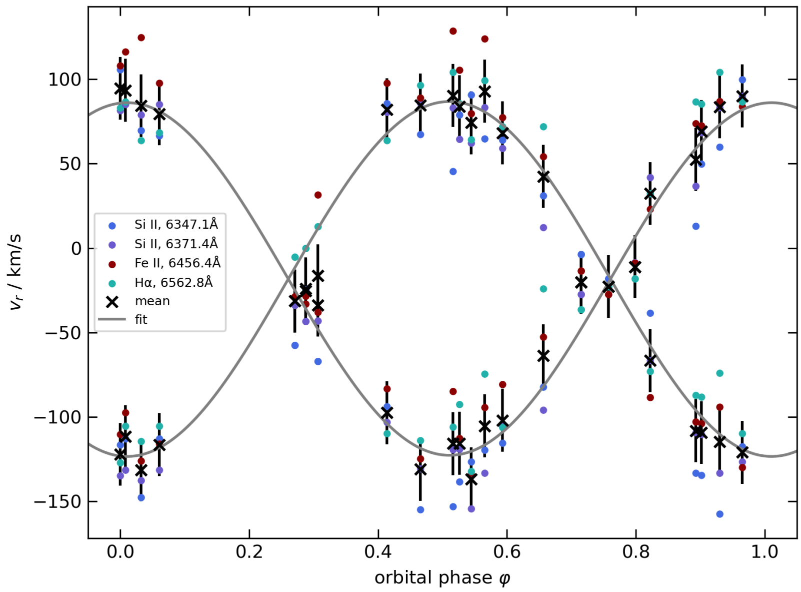

Figure 1.6: Radial velocity of the star Menkalinan (β Aur) as a function of orbital phase $\phi = t \bmod P$, monitored over the year 2021 by the students and tutors of the laboratory course *Spektroskopie von Sternen* at the University of Bonn. The orbital motion of the Earth has been subtracted so that the depicted radial-velocity variation is in the Sun's rest-frame. The coloured dots are the measurements of individual spectral lines. Their typical uncertainty is 30 km/s. The black symbols show the mean and standard deviation for each observation. The grey lines mark the best-fit model ($e = 0$, $P = 3.96$ d), which finds velocity semi-amplitudes of 105 ± 5 and 104 ± 5 km/s and thus a mass ratio of 1.01 ± 0.07 and a total mass of $M \sin^3 i = 3.8 \pm 0.4 M_\odot$. The barycentre of the system has a radial velocity of 18 ± 3 km/s towards the Sun.

Today the number of known binary stars is immense, thanks to large-scale observations such as TESS (Transiting Exoplanet Survey Satellite, Prša et al., 2022), which was designed for exoplanet transients, but eclipsing binaries are a welcome by-product, Gaia (Gaia Collaboration et al., 2023), which provides astrometry, photometry and radial-velocity spectroscopy, or VFTS (VLT-FLAMES Tarantula Survey, Evans et al., 2011) and TMBM (Tarantula Massive Binary Monitoring, Almeida et al., 2017), a multi-epoch optical spectroscopy programme aimed at the massive stars in the 30 Doradus region of the Large Magellanic Cloud.

While most known binaries consist of two main-sequence stars, there is a notable number of peculiar systems. Algol, whose two stars are on the main sequence, is a particularly interesting case, since the lighter component of the binary seems to be more evolved than the heavier one, in contrast to what one would expect from Eq. 1.12. The binary star φ Per is not only a Be star, but the other component is a subdwarf. This means that it lies to the left of the main sequence, so the star is hot, bright and small. It also has a helium-enriched surface (Poeckert, 1981; Gies et al., 1998). Similar binaries also exist at very high masses, consisting of an

O star and a Wolf-Rayet star (e.g. Shenar et al., 2016, 2018). Finally, there are binaries harbouring a stellar remnant, such as Sirius or VFTS 243, but the full picture was not revealed until it became possible to observe the stars in X-rays. All of these seemingly peculiar systems can be explained by binary interaction (Tauris and van den Heuvel, 2023).

The age of X-ray astronomy began with the advent of the space age. Previously, such observations were not possible because X-rays are (fortunately) blocked by the Earth's atmosphere. Soon X-ray point sources were discovered (the first was Sco X-1 Giacconi et al., 1962), which are explained by accreting neutron stars or black holes, into whose gravitational potential material falls, releasing energy at a rate

$$L_{\mathrm{acc}} \sim \frac{GM\dot{M}}{R}, \tag{1.17}$$

where $\dot{M}$ is the mass accretion rate and M and R are the mass and radius of the accretor. The high X-ray luminosities (10^{37} erg/s) cannot be produced by an accreting star or white dwarf, because the necessary mass accretion rate $\dot{M}$ would be so high that the X-rays would be absorbed by the in-falling material.

The discovery of Cen X-3 (Giacconi et al., 1971) provided evidence for this model, since this source displays X-ray pulsations similar to those of a radio pulsar (4.84 s). Its pulses are also subject to a periodic Doppler shift, as in a spectroscopic binary, and the source exhibits a regular X-ray dimming, like an eclipsing binary, with the same period as the variations of the pulsation (Schreier et al., 1972). An O-type star at the corresponding position in visual light (Krzeminski, 1974), led to the conclusion that this object is a binary containing a normal star and an accreting neutron star. Around the same time Cyg X-1 was discovered and it was found that this source position coincides with another O star (Bolton, 1971; Webster and Murdin, 1972). The X-ray source shows neither pulsations nor eclipses, but the O star is a single-lined spectroscopic binary. This allows a mass estimate of the invisible object, and a mass of more than $5M_\odot$ (today's best measurement is $21.1 \pm 2.2M_\odot$, Miller-Jones et al., 2021) has been found, certainly above the upper limit of neutron star mass. Only a black hole can be both so massive and so faint in visible light.

Such systems, consisting of a massive star and an X-ray emitting stellar remnant, are called high-mass X-ray binaries and are divided into two main classes. These are supergiant X-ray binaries, as the two sources described above, where the stellar remnant accretes the wind of an O- or B-type star, and Be/X-ray binaries, where the stellar component is a Be star and the accretor (usually a neutron star) periodically crosses its disc in an inclined and eccentric orbit, during which the binary emits X-rays (Tauris and van den Heuvel, 2023).

Binaries are also observed in the radio regime. 25 pulsars with neutron star companions and 233 pulsars with white dwarf companions are known (Manchester et al., 2005). In 2015 the gravitational wave observation channel was opened (Abbott et al., 2016), and by now more than 80 black hole–black hole mergers, two neutron star–neutron star mergers, and four black hole–neutron star mergers have been observed (Abbott et al., 2023a). In summary, binary stars can contain two stars of various evolutionary status, two remnants, or one of each. This raises the questions: How are does binary evolution connect these objects?

1.4.2 The Roche potential

We begin the discussion of binary evolution with a binary system consisting of two stars at the beginning of their stellar lives. If one of the stars has a radius of the order of the semi-major axis of the system, the material at its surface is not only subject to the gravitational pull of the star, but is also influenced by the companion's gravity and the centrifugal force of the orbital motion. This can happen as a result of the evolutionary expansion of the stars, a decay of the orbit, or if the binary is born this way. We have seen that most of a star's mass is near its centre, so it is a valid assumption to treat the stars' potential as that of point masses. If one further assumes that the orbit is circular and that no other forces (magnetic, radiation pressure, …) are relevant, the common potential in the co-moving frame is given by the so-called Roche potential

$$\Phi_{\mathrm{R}} = -\frac{GM_1}{r_1} - \frac{GM_2}{r_2} - \frac{\Omega^2 s^2}{2}, \tag{1.18}$$

where $M_{1,2}$ are the masses of the two components, $r_{1,2}$ are the distances to the two point masses, s is the distance to the axis of rotation, and $\Omega = 2\pi/P$ is the angular velocity of the orbital motion.

Besides the locations of the centres of the two stars and the common centre of mass, the Roche potential is characterised by the five Lagrange points L_i where the gradient of the potential vanishes and a test particle at rest becomes force-free, as shown in Fig. 1.7. L_1, L_2, and L_3 are located on the line connecting the centres of the stars. The inner Lagrange point L_1 is located between the two stars and is the Lagrange point with the lowest potential. The two outer Lagrange points are behind the less (L_2) and the more massive star (L_3). Since Eq. 1.18 is a quintic equation, no algebraic solution can be found for the location of the Lagrange points, and one has to rely on approximations or numerical solutions.

As a star expands during its evolution, it will slightly deform its outer layers so that the stellar surface follows an equipotential surface of the Roche potential. For stellar evolution, this deformation can be neglected because, as mentioned above, most of the star's matter lies so deep in the potential that single-star models can be applied. However, in the Roche model, the volume available to the star (called the Roche lobe) is limited to the volume enclosed by the equipotential surface passing through L_1. The Roche volume cannot be expressed analytically, but Eggleton (1983) found an approximate formula for the radius of a sphere with the same volume, called the Roche radius. It is the largest radius the star can reach and is given as

$$R_{\mathrm{RL},i} = a \cdot \frac{0.49 q_i^{2/3}}{0.6 q_i^{2/3} + \ln\left(1 + q_i^{1/3}\right)}, \tag{1.19}$$

where $q_i = M_i/M_{3-i}$ with $i \in \{1, 2\}$ is the mass ratio of the star whose Roche radius is considered to that of its companion.

The Roche model assumes a circular orbit, but it can be extended to eccentric orbits if the periastron distance is used instead of the semi-major axis. However, this is rarely relevant as the two stars exert a tidal torque on each other, which can change not only their rotational properties, but also the semi-major axis, eccentricity and inclination of the system through the conservation of energy and angular momentum. Following Kopal (1959), Zahn (1977), and Hut (1981), one can find equilibrium values for these quantities, which are co-rotation, meaning that the angular frequencies of the orbit and of the rotation of the stars are equal (this is well known from the Earth-Moon system, where the Moon is in co-rotation and always shows the same side to Earth), a circular orbit, and alignment (the angular momentum vectors of the spins and the orbit are parallel). The evolution towards equilibrium is typically described by a characteristic timescale that depends on a large (6^{th} to 8^{th}, depending on the stellar structure) power of the ratio of the stellar radius to the semi-major axis. This means that tides are predominantly important in close binary systems.

1.4.3 Mass loss and orbital evolution

If a star fills its Roche lobe, the material at its surface can easily be pushed easily over L_1, causing the star to lose mass. This is called a Roche-lobe overflow (RLO), and depending on the evolutionary state of the mass-losing star, the donor star, one distinguishes between Case A (RLO during core hydrogen burning), Case B (RLO during hydrogen shell burning), and Case C (RLO during helium burning, Kippenhahn and

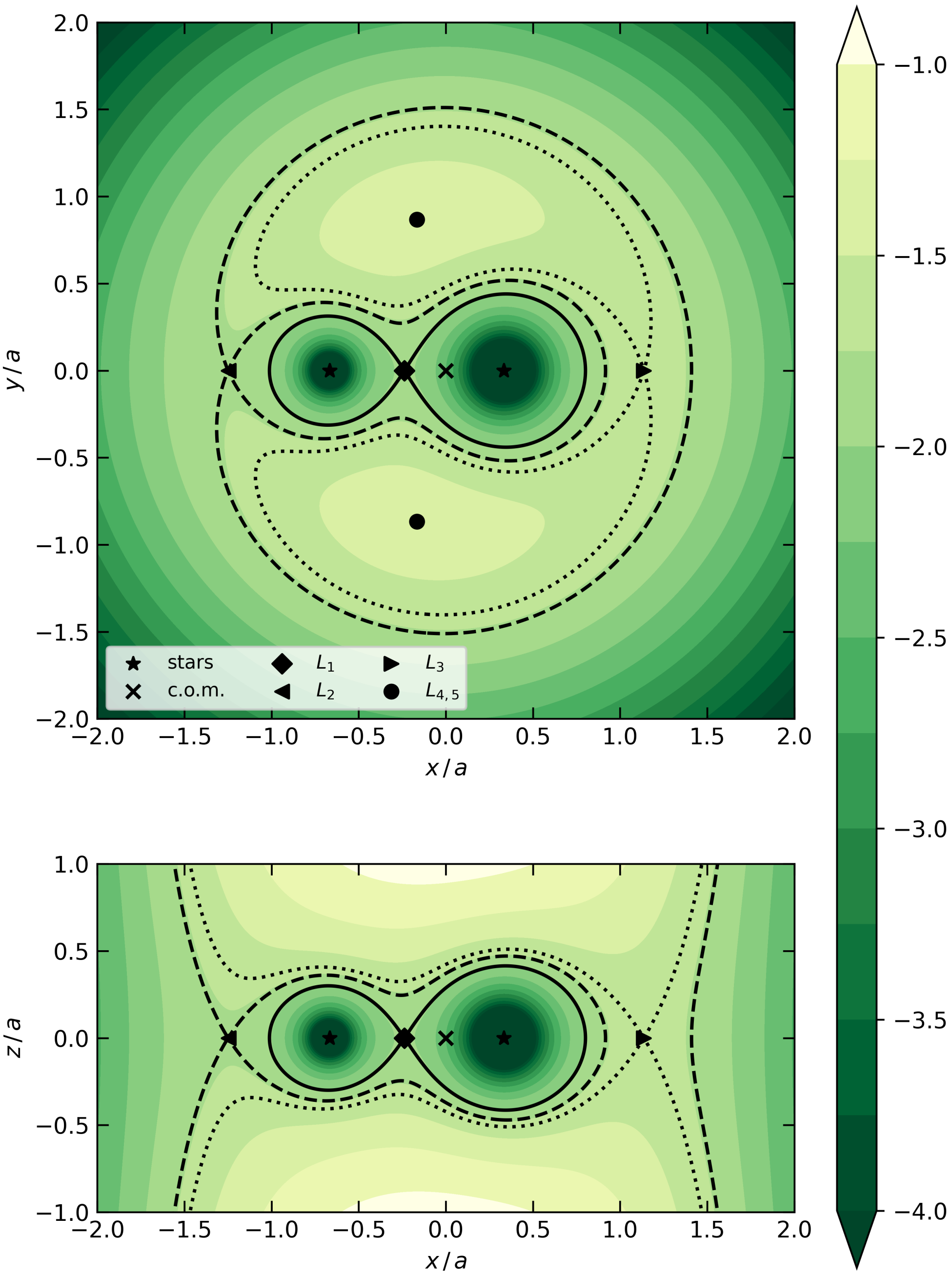

Figure 1.7: Map of the Roche potential for a mass ratio of 0.5 in units of GM/a, where M is the total mass and a is the semi-major axis. The two stars lie at $y = z = 0$ with the barycentre/centre of mass (c.o.m.) at the origin. The orbital angular momentum vector points in positive z-direction. The Lagrange points and their corresponding equipotential surfaces are marked. The top plot shows a slice through the xy-plane at $z = 0$ and the bottom plot through the xz-plane at $y = 0$.

Weigert, 1967). How the system evolves after Roche-lobe filling, depends on how the radius R of the star evolves relative to the Roche radius. According to Webbink (1985), this is often expressed in terms of the mass-radius exponents of the donor star (ζ_*) and the Roche lobe ($\zeta_{\rm RL}$), given as

$$\zeta_* = \frac{\partial \ln R}{\partial \ln M}, \quad \zeta_{\rm RL} = \frac{\partial \ln R_{\rm RL}}{\partial \ln M}, \tag{1.20}$$

where M is the mass of the donor.

For the mass-radius exponent of the star, a distinction is made between the dynamical or adiabatic response $\zeta_{\rm dyn}$, where the star remains in dynamical but not in thermal equilibrium, and the thermal or equilibrium response $\zeta_{\rm th}$, where the star remains in both dynamical and thermal equilibrium. If $\zeta_{\rm RL} > \zeta_{\rm dyn}$, the Roche radius shrinks faster than the stellar radius, leading to even more matter moving through L_1, so a runaway mass transfer on the dynamical timescale happens, which may lead to a common envelope evolution or to a merger of the two stars (see Ch. 1.4.6). If $\zeta_{\rm th} < \zeta_{\rm RL} < \zeta_{\rm dyn}$, a stable mass transfer on the thermal timescale occurs, since a faster mass transfer would lead to a reaction on the dynamical timescale, i.e. the donor would shrink, and a slower mass transfer would lead to an expansion of the donor in order to remain in thermal equilibrium. Finally, if $\zeta_{\rm RL} < \min(\zeta_{\rm dyn}, \zeta_{\rm th})$, the star can remain within its Roche lobe. If it continues to expand, e.g. by nuclear evolution, the star drives a stable mass transfer to its companion, which is then called the accretor or mass gainer (Webbink, 1985; Tauris and van den Heuvel, 2023). The mass-radius exponents $\zeta_{\rm dyn}$ and $\zeta_{\rm th}$ can be obtained numerically from the stellar structure equations. Very roughly, $\zeta_{\rm dyn} \sim 0$ for stars with convective envelopes, and $\sim 3 \ldots 10$ for stars with radiative envelopes (Ge et al., 2010, 2015, 2020), and $\zeta_{\rm th} \sim 1$.

The mass-radius exponent of the Roche lobe $\zeta_{\rm RL}$ can be calculated from Eq. 1.19 using Kepler's third law (Eq. 1.15). This requires information about the efficiency of the mass transfer, i.e. whether the mass lost from the donor star is deposited on the companion or if it is ejected from the system, and about the specific orbital angular momentum that the ejected material carries out of the system. Since this is a complex hydrodynamical problem, one relies on an effective description using a mass-transfer efficiency ε, which is often fixed, and a limited number of prescriptions for the specific angular momentum of the ejected material. Three cases that can be treated analytically are described by Soberman et al. (1997). These are wind mass loss from the donor, where the ejected material carries the same specific orbital angular momentum as the donor star, isotropic re-emission, where initially all the material is taken up by the mass gainer but a fraction is immediately ejected from the system with the specific orbital angular momentum of the accretor, and ejection from a circum-binary ring at fixed radius. Isotropic re-emission is the most commonly used model, which roughly gives $\zeta_{\rm RL} < 0$ if the donor is lighter than the accretor, and $\zeta_{\rm RL} > 0$ otherwise (Tauris and Savonije, 1999). As a rule of thumb, it can be said that in systems with donors with convective envelopes and in systems where the accretor is much lighter than the donor, the mass transfer becomes unstable.

The description outlined above can also be used to predict the evolution of the semi-major axis and the orbital period during the RLO. Assuming isotropic re-emission, it can be shown that the orbital period becomes a function of the mass ratio,

$$P = P_0 \left(\frac{q}{q_0}\right)^{-3} \left(\frac{1+q}{1+q_0}\right)^{-2} \left(\frac{1+\varepsilon q}{1+\varepsilon q_0}\right)^{5+3/\varepsilon}, \tag{1.21}$$

where q is the ratio of donor to accretor mass and a superscript 0 indicates the initial value (Soberman et al., 1997). This function has a minimum around $q \approx 1$, which means that the orbit shrinks if and as long as the donor is more massive than the accretor, and expands if the accretor is more massive than the donor. This comes into play in Case A evolution.

1.4.4 Evolution for Case A and Case B mass transfer

The stellar structure equations can be solved simultaneously for two stellar models, even with exchange of mass and angular momentum. This makes the detailed modelling of a binary star possible and was first done by Paczyński (1966) and Kippenhahn and Weigert (1967). In this section we present the typical results of these model calculations for Case A and B mass transfer of massive stars. We do not discuss Case C because the convective envelope often leads to unstable mass transfer (see however Ercolino et al., 2024). We start with Case B because it is easier to understand than Case A. More details can be found in e.g. Tauris and van den Heuvel (2023).

In a Case B RLO, the donor star has depleted its central hydrogen reservoir and thus has a helium core around which shell burning is taking place. As described in Ch. 1.3.2, these stars expand rapidly and initially have a radiative envelope which later becomes convective. Thus early Case B mass transfer will be stable and late Case B mass transfer will be unstable (Ch. 1.4.3). The stable expansion of the donor star pushes material steadily through L_1 until the core of the donor has contracted enough to ignite core helium burning (Fig. 1.8, □). Then the donor stops expanding and the mass transfer stops (◁). Since the evolution across the Hertzsprung gap happens on the thermal timescale of the donor, the Case B mass transfer also occurs on this timescale. The mass loss rate can be estimated from the ratio of the envelope mass of the donor to its thermal timescale. The mass gainer accretes material and grows in mass depending on the mass-transfer efficiency.

On the main sequence, massive stars have a radiative envelope, so Case A RLO is dynamically stable, but the high mass-radius exponent of the Roche-lobe makes it thermally unstable. Thus the thermal response to mass loss drives material through L_1 until the mass ratio reaches unity, where $\zeta_{\rm RL}$ becomes negative and the orbit begins to widen. After the donor has regained thermal equilibrium, the thermal timescale mass transfer (called fast Case A) ends (◇ in Fig. 1.8). The donor star has lost parts of its envelope and, being lighter, its convective core has become smaller (Fig. 1.8, bottom left). It remains Roche-lobe filling and drives a slow stable mass transfer due to its nuclear expansion (slow Case A), and thus the mass transfer rate is much lower. This phase is long-lived and is probably the current state of Algol (Pustylnik, 1998). Indeed, in our Case A donor, the donor is lighter than the accretor, but further evolved. At the end of central hydrogen burning (∘ in Fig. 1.8), the donor consists of a small helium core, a helium-enriched middle layer of the size of the convective core at the beginning of the RLO, and a hydrogen-rich envelope. Mass transfer halts briefly as the donor contracts, only to expand again as the helium core collapses beneath the shell source. Another phase of mass transfer starts, which is very similar to Case B mass transfer, since it is driven by the same expansion mechanisms and takes place on a thermal timescale, and is therefore called Case AB. The main difference to Case B is that (assuming identical initial conditions except for the initial separation) the final donor mass is smaller due to the reduction of the convective core. Details of this are treated in Ch. 4.

1.4.5 Products of mass transfer

At the end of Case AB or B mass transfer, the donor has lost so much mass that only its helium core and a thin hydrogen-rich envelope are left. It is common to treat the donor from this point on as a pure (naked) helium star, which can be modelled with the same stellar structure equations as a hydrogen-rich star, but the difference in chemical composition causes notable differences (Tauris and van den Heuvel, 2023). For the same mass, a helium star is much smaller than a hydrogen-rich star (less than $1R_\odot$ for $M < 10M_\odot$), but much

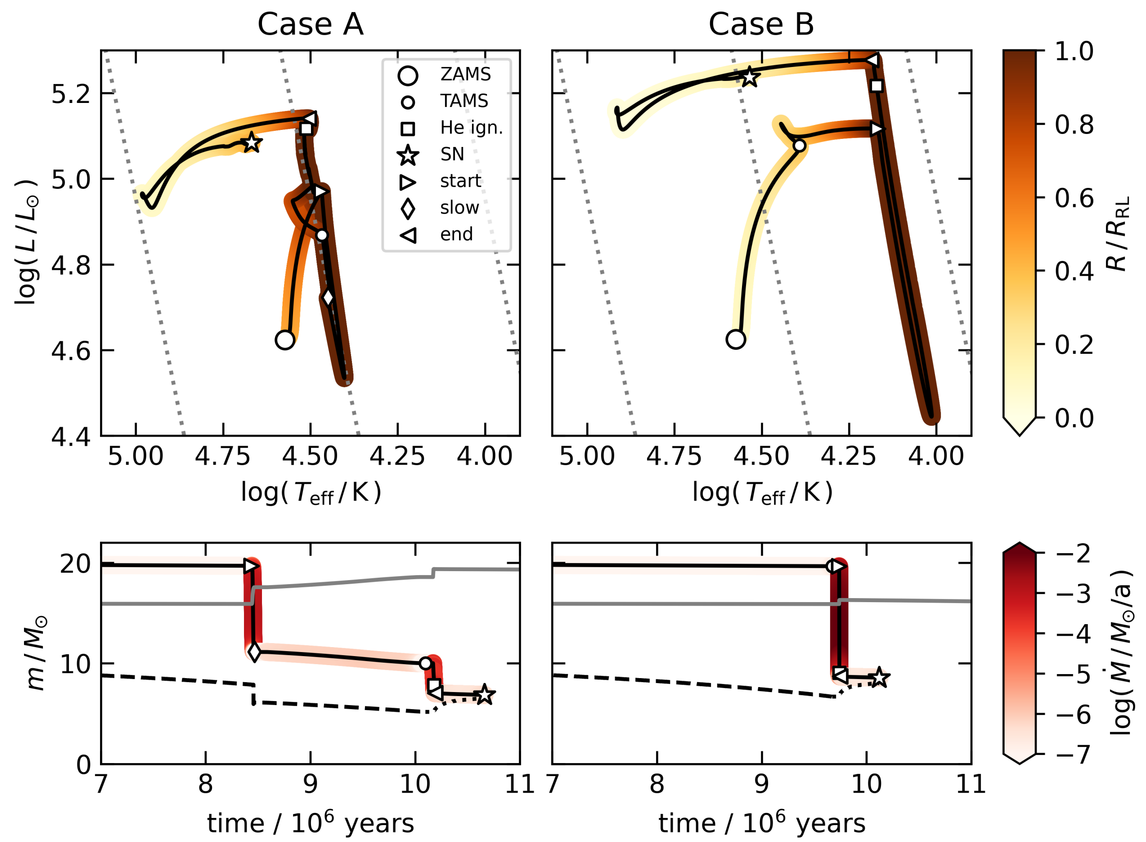

Figure 1.8: Stellar evolution for Case A (left) and B (right) RLO. The initial masses are $20M_\odot$ and $16M_\odot$ in both cases and the initial orbital periods are 3 d (left) and 30 d (right). The top panels show the evolution of the donor in the HRD with the Roche-lobe filling factor colour coded. Lines of constant radius ($1R_\odot$, $10R_\odot$, and $100R_\odot$) are shown in grey. The bottom panels show the evolution of the total donor mass (solid), the convective core mass (dashed), the helium core mass (dotted), and the accretor mass (grey), with the mass loss rate of the donor colour-coded. The evolution is not conservative. We have marked ZAMS, TAMS, helium ignition, end of stellar evolution (SN), start of RLO, switch from fast to slow Case A mass transfer, and end of RLO. The models are taken from Marchant Campos (2018) and Langer et al. (2020).

more luminous. However, it is dimmer than a hydrogen-rich Hertzsprung-gap star with the same core mass as the total mass of the helium star, since the latter lacks a hydrogen shell source (Kippenhahn et al., 2013). Helium stars can have a significant wind mass loss (Sander and Vink, 2020).

Three classes of objects are the observational counterparts of helium stars and all of them are rare. Low-mass helium stars have effective temperatures that make them appear as OB-type stars, but their high surface gravity broadens their spectral lines notably, so they are classified as subdwarfs (Götberg et al., 2018). The companion of φ Per fits into this picture (Poeckert, 1981; Gies et al., 1998). Subdwarfs are rare as they are often outshone by their companion (Wang et al., 2021). Heavy helium stars ($M \gtrsim 8M_\odot$) are luminous enough to launch a strong, optically thick wind and can be identified with Wolf-Rayet stars, in agreement with their surface chemical abundances (reduced or no hydrogen, enhanced helium and nitrogen, the dominant by-product of CNO-burning, see Crowther, 2007). Thus binary interaction can be seen as a possible formation channel for O-type star–Wolf-Rayet star binaries, (see however Shenar et al., 2020b). Intermediate mass helium stars are not luminous enough to launch a Wolf-Rayet wind and have such a high effective temperature that most of their energy output is in the extreme ultraviolet, with photon energies above the ionisation energy of hydrogen, and so most of their energy output is absorbed by the interstellar medium, making them barely observable (Götberg et al., 2018). For the third class, the model of a pure helium star breaks down, because after mass transfer the donor spends about 10% of its core helium burning time contracting towards the helium ZAMS (from $\triangleleft$ to the very left of the track in Fig. 1.8). During this episode it crosses the main sequence and thus appears to be a main-sequence star, but has a lower mass and a hydrogen-rich star of the same luminosity. Examples are the stars LB-1 (Shenar et al., 2020a) and HR 6819 (Bodensteiner et al., 2020a).

If the mass-transfer efficiency is non-zero, the companion star accretes a fraction ε of the mass lost from the donor, thereby increasing its mass. This expands the convective core of the accretor, incorporating unprocessed material into the convective core and increasing the central hydrogen abundance again. In this way, the mass gainer is set back in its evolution, a process called rejuvenation (Braun and Langer, 1995). The accretion process can also bring the mass gainer out of thermal equilibrium or close to the Eddington luminosity, as the accreted material carries entropy (Kippenhahn and Meyer-Hofmeister, 1977; Neo et al., 1977). We will discuss the consequences of this in Ch. 5. The incoming material also carries angular momentum onto the accretor, so its rotational properties change. Packet (1981) showed that only a small amount of matter is sufficient to spin up the accretor to critical rotation (Eq. 1.14), but it is an open question whether the mass gainer can continue to accrete even if it rotates critically (Popham and Narayan, 1991; Krtička et al., 2011). Nevertheless, the accretor has become a near-critically rotating star. Due to the processes discussed in Ch. 1.3.4, a decretion disc forms, and the mass gainer appears as a Be star. This is a natural explanation for systems containing a Be star and a subdwarf, such as φ Per and the other proposed formation channel for Be stars besides single-star evolution (Ch. 1.3.4). This is supported by the fact that no Be star with a main-sequence companion is known (Bodensteiner et al., 2020b) and many of them harbour products of mass transfer or stellar remnants (Tauris and van den Heuvel, 2006). The accretor can avoid becoming a Be star if tidal forces keep it in co-rotation with the orbit (typically Case A systems during slow mass transfer, de Mink et al., 2007; Sen et al., 2022) or if the wind mass loss is strong enough to remove enough angular momentum for the star to rotate sub-critically again (typically very massive systems, such as Wolf-Rayet stars with O-type companions, Vink, 2022; Hastings et al., 2023).

1.4.6 Supernovae and stellar remnants in binaries

As the helium star is the more evolved component of the binary, it will drive the subsequent evolution. During core helium burning it slightly increases its radius and luminosity, and after central helium depletion and the onset of helium shell burning it expands rapidly (Tauris and van den Heuvel, 2023). This can trigger another episode of mass transfer (Savonije and Takens, 1976; De Greve and De Loore, 1977), which we call Case ABC or BC, depending on whether Case A preceded it. However, the maximum radius for helium stars is a function of mass and has a maximum near $2.2M_\odot$ (Paczyński, 1971), and so helium stars more massive than about $3M_\odot$ (corresponding to an initial donor mass of about $10M_\odot$) do not initiate a Case (A)BC mass transfer (Tauris and van den Heuvel, 2023). This can be changed by the presence of a thin hydrogen-rich envelope, which can drastically increase the stellar radius (Laplace et al., 2020).

Regardless of the occurrence of Case (A)BC mass transfer, the final evolution is very rapid and the star either becomes a white dwarf ($M \lesssim 2.5M_\odot$) or explodes as a supernova due to electron capture ($2.6M_\odot \lesssim M \lesssim 2.7M_\odot$) or iron core collapse ($M \gtrsim 2.8M_\odot$, Tauris et al., 2015). In contrast to single-star evolution, an electron-capture supernova is possible because there is no hydrogen-rich envelope which can erode the helium core by deep convection (Podsiadlowski et al., 2004). Stars that become helium stars have a different relation between initial mass and remnant mass than single stars. This is because helium stars lose mass through stellar winds, rather than growing by shell burning like the helium cores of single stars (Podsiadlowski et al., 2004; Woosley, 2019). Since the envelope mass of helium stars is reduced, a weaker supernova kick is expected (Tauris and Bailes, 1996; Coleiro and Chaty, 2013; Tauris et al., 2017), which is further reduced after Case (A)BC mass transfer (Kruckow et al., 2018). Electron-capture supernovae are also predicted to have a reduced kick (Podsiadlowski et al., 2004; Dessart et al., 2006; Kitaura et al., 2006). It is unknown whether black holes receive a natal kick (Nelemans et al., 1999; Janka, 2013; Repetto and Nelemans, 2015; Mandel, 2016).

The sudden mass loss and the supernova kick massively change the kinematic properties of the binary. Flannery and van den Heuvel (1975) and Hills (1983) showed that the ratio of the post- to the pre-supernova semi-major axis of an initially circular orbit can be written as

$$\frac{a}{a_0} = \left(\frac{1 - \Delta M/M}{1 - 2\Delta M/M - (w/v)^2 - 2(w/v)\cos\theta} \right), \tag{1.22}$$

where $\Delta M/M$ is the relative mass change of the system, $v = \sqrt{GM/a}$ is the relative orbital velocity of the two stars, w is the kick velocity (see Ch. 1.3.3), and θ is the angle between the pre-supernova velocity of the exploding star and the kick velocity. If a/a_0 becomes negative, the two stars are no longer gravitationally bound, i.e. the binary breaks up. As a rule of thumb, the system will remain bound if both the relative mass change and the ratio of kick to orbital velocity are small. If the velocity ratio is large, or the relative mass change is large and the velocity ratio is small, the system will break up. For intermediate velocity ratios, the direction of the kick θ is crucial. The supernova changes not only the semi-major axis, but also the eccentricity (Tauris and van den Heuvel, 2006) and the peculiar velocity of the system (Tauris and Takens, 1998). This explains why the orbits of Be/X-ray binaries are often eccentric and is a possible cause of runaway stars, stars with spatial velocities $\gtrsim 30\,\mathrm{km/s}$ (Blaauw, 1961; Renzo et al., 2019).

If the system remains bound after the supernova, a new kind of binary system has formed, namely one containing a ”living” and a ”dead” star. Since the latter, in the considered mass regime either a neutron star or a black hole, is no longer evolving and the former has been rejuvenated, this kind of binary system is very long-lived and therefore relatively abundant (Tauris and van den Heuvel, 2023). These systems are very interesting in their own right, but they are also the observable link between well-understood binaries with two ”living” stars (Langer, 2012) and binary stellar remnants that may merge through gravitational-wave coalescence. Studying them can therefore shed light on the origin of such events.

Binaries with a star and a stellar remnant come in many flavours. If the star is a Be star and the remnant is a neutron star, the system can appear as a Be/X-ray binary, but if the star has a strong wind from which the remnant can accrete, it may be observed as a supergiant X-ray binary, such as Cyg X-1 or Cen X-3. Even if no X-rays are emitted, these systems can be observed, such as MWC 656, which contains a Be star and possibly a black hole (Casares et al., 2014; Janssens et al., 2023), J0045–7319, a B-type star with a radio pulsar (Bell et al., 1995; Kaspi et al., 1996; Manchester et al., 2005), or VFTS 243 (O-type star with black hole Shenar et al., 2022). These mixed systems are the subject of Ch. 2 and 6.

Although the mixed systems are long-lived, their time is finite. The possibilities for the further evolution are numerous (e.g. Han et al., 2020) and so we will discuss only a selection. If the star can fill its Roche lobe, it triggers yet another mass transfer, and if this is stable, the outcome might be a binary with a helium star and a stellar remnant in a wide orbit (Tauris et al., 2015; Tauris et al., 2017). If it is unstable, the system undergoes common envelope evolution, in which the stellar core and the remnant are embedded together in the envelope

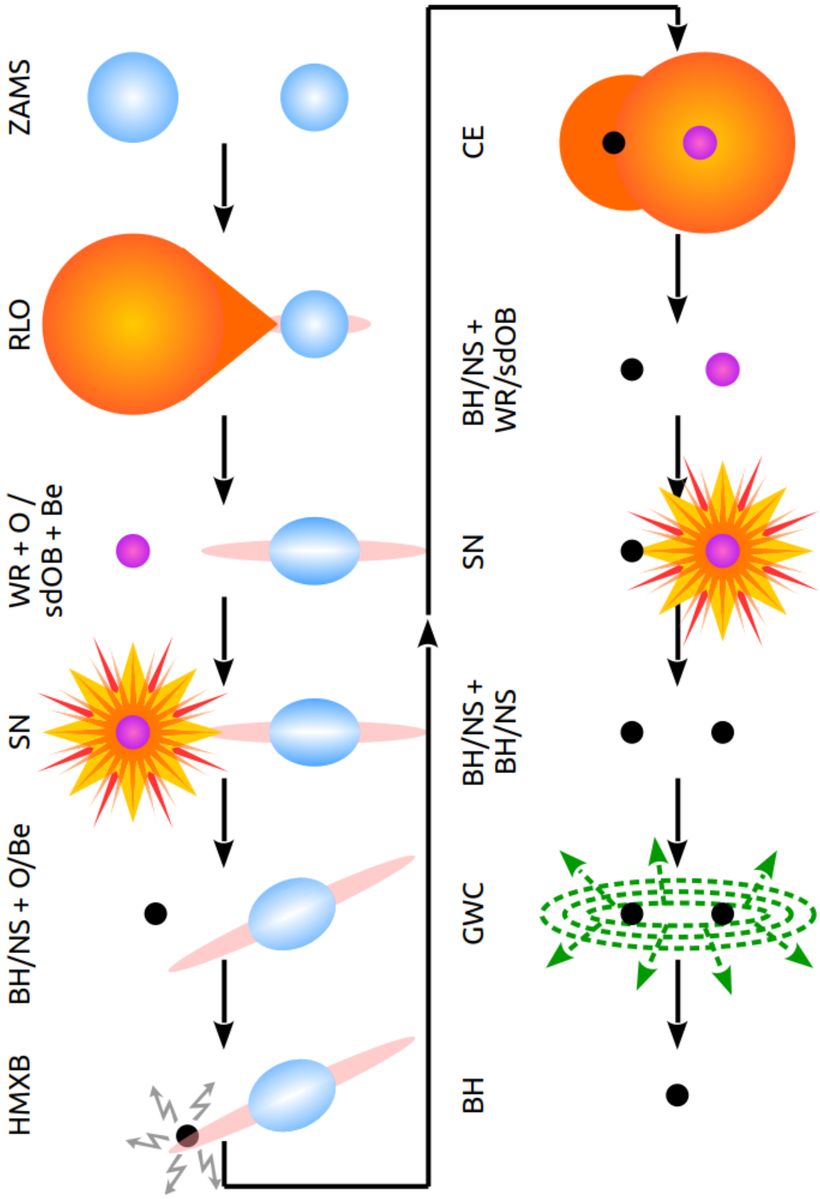

Figure 1.9: Schematic binary evolution from zero-age main-sequence (ZAMS) to gravitational wave coalescence (GWC). This is just one of many possible evolutionary paths for massive binary stars. There are several branches where the binary evolution can end by merger or break up. Abbreviations: RLO = Roche-lobe overflow, WR = Wolf-Rayet star, sdOB = OB-type subdwarf, SN = supernova, BH = black hole, NS = neutron star, HMXB = high-mass X-ray binary, CE = common envelope. Image inspired by Kruckow et al. (2018).

of the star (Ivanova et al., 2013). If the orbital energy of the remnant is large enough to unbind the envelope, the common envelope can be ejected and the orbit of the resulting helium star–stellar remnant binary will be much narrower (Webbink, 1984; de Kool, 1990; Kruckow et al., 2016). Cyg X-3, a high-mass X-ray binary with a Wolf-Rayet star, could be an example of this (van Kerkwijk et al., 1992; Belczynski et al., 2013). If the envelope ejection is not successful, the two objects may merge to form a Thorne-Żytkow object (Thorne and Żytkow, 1975, 1977). In either case, a second supernova will soon follow. If the system remains bound, a binary stellar remnant is left behind. Such objects are well observed as radio pulsars with white dwarf or neutron star companions (Lorimer and Kramer, 2004; Manchester et al., 2005). However, no pulsar with a black hole has yet been found. If the orbit of the binary remnant is close enough, it can decay by gravitational wave emission, making gravitational-wave coalescence events the final phase of binary evolution (Abbott et al., 2016; Kruckow et al., 2018). A graphical summary of this evolutionary path is shown in Fig. 1.9.

1.5 Population synthesis

We have seen that stars can exist in large parts of the HRD, but they are predominantly found in certain regions. We only know this because we observe a large number of stars. One star alone would not reveal this information because its evolution, even in the fastest sections such as the Hertzsprung gap, is far too slow to be observed. So we need to study a large number of stars, a stellar population, and compare them in a meaningful way with our stellar models to understand why, for example, certain parts of the HRD contain stars and others do not. On the other hand, many aspects of the physics of single and binary stars are uncertain. It is not possible to conduct laboratory experiments with stars, but we can do computer experiments and vary the assumed physics. Comparing a single star to a set of stellar models with different assumptions about the physics is not as fruitful as comparing a population of stars to a model grid. In recent years, campaigns such as Gaia (Gaia Collaboration et al., 2023) or the Zwicky Transient Facility (Bellm et al., 2019) have provided large observational databases. In order to compare stellar models with these data in a meaningful and statistical way, we need to construct synthetic populations from the models, a process called population synthesis.

The distribution of stellar parameters over a population is often given as a probability density function

$$f_x = \frac{\mathrm{d}N}{\mathrm{d}x}, \tag{1.23}$$

where N is the number of stars and x is the parameter of interest. An example might be the distribution of stellar masses f_M. Here one must distinguish between the observed current mass distribution of a stellar population and the initial mass distribution. This is because, as we have seen, the lives of massive stars are shorter, so their numbers are reduced when the population is old. This distinction is also generally true as stars evolve. So, with assumptions about stellar physics and the initial distributions, we can construct distributions of various stellar parameters and compare them with observations.

For recent overviews on population synthesis of binary stars see e.g. Eldridge (2017), Izzard and Halabi (2018), Han et al. (2020) or Tauris and van den Heuvel (2023, ch. 16).

1.5.1 Initial distributions

It turns out that most initial probability density functions show a power-law behaviour $f_x \sim x^\alpha$, where α is the power-law exponent. The exponent of the initial mass function has been studied extensively, for example, by Salpeter (1955), Scalo (1986), Kroupa et al. (1993), and Kroupa (2001) with the consensus that it is negative with values between −2 and −3, depending on the underlying population and mass regime. This means that massive stars are rarer than low-mass stars.

To model the evolution of binary star populations, the initial masses of both stars and an initial orbital period P must be set. The mass of the heavier component of the binary follows the initial mass function of single stars. For massive stars, the power-law exponent of the mass ratio probability density function has values between −2.8 (close to random pairing from the single-star initial mass function) and 0 (flat distribution, Öpik's law) and for the exponent of $f_{\log P}$ values between −0.55 (preference for close orbits) and 0 have been found, both depending on the population analysed (e.g. Sana et al., 2012, 2013; Kobulnicky et al., 2014; Dunstall et al., 2015). Moe and Di Stefano (2017) showed that the distributions of mass ratio and orbital period may not be independent but correlated. Since the Roche-lobe filling leads to a rapid circularisation of the orbit, we do not need to consider an initial eccentricity distribution.

We mentioned in Ch. 1.3.4 that stellar rotation can play a role in stellar evolution. So the initial rotational velocity needs to be addressed. For example, Dufton et al. (2013) found a bimodal initial rotational velocity distribution for single early B-type stars, with one peak around 50 km/s and the other around 300 km/s. For binaries, this distribution is more complicated because of synchronising tides. One approach (e.g. Langer et al., 2020) is to assume that binaries begin their lives in co-rotation (see however Lennon et al., 2024).

Other population parameters are the initial binary fraction, the initial metallicity, and the star formation rate. The initial binary fraction lies between 50% and 70% (Sana et al., 2012, 2013; Dunstall et al., 2015) and is probably mass dependent with a high value for more massive stars (Moe and Di Stefano, 2017). The population syntheses in Ch. 2 and 6 treat massive star populations in the Magellanic Clouds, which have well known metallicities of half (Large Magellanic Cloud) and a quarter (Small Magellanic Cloud) of the solar value (Korn et al., 2000; Trundle et al., 2007). Since we investigate massive stars, we do not need to consider a time-dependent star formation rate, since the timescale of massive stellar evolution is shorter than the timescale on which the star formation rate varies (Harris and Zaritsky, 2004; Rubele et al., 2015; Hagen et al., 2017; Rubele et al., 2018; Schootemeijer et al., 2021).

1.5.2 Rapid binary population synthesis

A naive approach to population synthesis would be to compute a model for each star in the population. However, this quickly becomes computationally very expensive. The Milky Way contains about 10^{11} stars and even a globular cluster has between 10^3 and 10^6 stars (Unsöld and Baschek, 2002). Even if we assume a computation time of one hour per model (which is conservative as it excludes the final collapse or thermal pulses), this becomes impossible to achieve on a personal computer. So, other approaches have to be taken.

Recent studies (e.g. Langer et al., 2020; Wang et al., 2020; Sen et al., 2022, 2023) attack the problem by calculating dense binary model grids. The models are then weighted by the initial distributions. Again, however, a large number of models must be computed. For a reasonable resolution of such a grid in mass, mass ratio, and orbital period, one needs about $20 \cdot 20 \cdot 100 = 40\,000$ models (Marchant Campos, 2018), which as a conservative estimate would take about four years on a personal computer. This approach makes it difficult to use different physical assumptions, as many quantities need to be fixed in advance and only some can be changed in post-processing.

The solution to the computing-time problem is to avoid solving the stellar structure equations, but to use pre-calculated single-star models. These can be provided as functions fitted to the evolution of certain parameters (e.g. Hurley et al., 2000, 2002) or as data tables which are interpolated to generate a stellar model (e.g. Kruckow et al., 2018). The evolution of binaries is then modelled by treating them as two single stars for as long as possible. If one component initiates a RLO, this process is treated semi-analytically. For example, for Case B mass transfer, it can be assumed that the mass transfer lasts for a thermal timescale (Eq. 1.2), the donor star loses its entire envelope and becomes a naked helium star with the mass of its former core, determined from the fits or tables. On the other hand, the evolution of the orbital period can be calculated directly, e.g. using Eq. 1.21. The resulting helium star is again modelled by fits or tables. Supernovae are also evaluated semi-analytically. The mass of the produced stellar remnant is estimated from the core mass of the progenitor using the fits or tables, but the changes in orbit can be calculated directly (Eq. 1.22). Also other shortcuts are taken based on the knowledge gained from detailed models, too.

This technique is called rapid population synthesis. Within this, two methods are used. Either the underlying stellar models are weighted by the initial distributions, as in the BPASS-code (Eldridge et al., 2008; Eldridge et al., 2017; Stanway and Eldridge, 2018; Byrne et al., 2022), or by using a Monte Carlo method, i.e. drawing a large number of binaries from the initial mass, mass ratio and orbital period distributions. These binaries are then rapidly evolved as described above, for which the ComBinE-code is an example (Kruckow et al., 2018), which we will use in Ch. 6. Other notable rapid population synthesis codes include `binary_c` (Izzard et al., 2004; Izzard et al., 2006, 2009; Schneider et al., 2015) and COMPAS (Stevenson et al., 2017; Riley et al., 2022). Rapid binary population synthesis makes it possible to predict the rates of very rare events, such as gravitational-wave coalescences, because these require a very large number of binaries to be modelled, since the probability that a binary will survive to this stage is very small. For example, Kruckow et al. (2018) evaluated 10^9 models per simulation.

1.6 This thesis

The overarching goal of this thesis is to understand the evolution of massive binary stars in the Magellanic Clouds using population synthesis. We chose the Magellanic Clouds as a target because these satellite galaxies of the Milky Way form a nearby low metallicity environment, which makes the study of massive stars interesting due to the lower stellar winds (Vink, 2022). Therefore, fast rotators are expected to be more abundant, as they do not lose as much angular momentum through wind (Langer, 2012). These conditions are similar to those at high redshifts, where most gravitational-wave signals originate (Abbott et al., 2023a).

The discovery of gravitational wave events has raised the question of how such close double black hole systems can form. One possibility is the formation through binaries as outlined in Ch. 1.4.6. It consists of several evolutionary steps and so has large uncertainties. Three phases of this evolution are long-lived and can be observed in abundance, namely binaries with two main-sequence stars, two stellar remnants, and systems with one of each. Main-sequence star–stellar remnant binaries are the last phase that can be reached without interruptions by detailed binary models. So we have used a dense grid of binary models to predict the properties of massive main-sequence stars with a black hole companion. We have assumed that during a mass-transfer event the accretor can only gain mass until it reaches critical rotation (Eq. 1.14). If the combined luminosity of the two stars does not provide enough power to remove the excess material from the system, the binary will merge into a single star. We find that massive main-sequence stars with black hole companions appear either as nitrogen-enriched single-lined spectroscopic binaries with large radial-velocity variations, or as rapid rotators with moderate radial-velocity variations. These results can be tested with observations. This work is published as a scientific article (Langer et al., 2020) and is the topic of Ch. 2.

However, by using a computationally expensive grid of detailed models, we have limited ourselves to certain assumptions about the binary physics. To be more flexible, we turned to ComBinE, a rapid binary population synthesis code where we can easily change the physical assumptions (Kruckow et al., 2018). To carry out such a study, we had to make some preparations, which are described in published or submitted scientific papers and are reproduced in Ch. 3, 4 and 5. In Ch. 3 we study the evolution of stellar rotation in binaries. For the reasons given in Ch. 1.5, it is convenient to use rapid binary population synthesis when targeting rare events and exotic systems. As such systems can host rapid rotators, such as pulsars or Kerr black holes, it is of interest to predict the rotation rates of the stellar remnants. It was therefore necessary to understand how the angular momentum of a star is distributed within it. The discovery of the binary star LB-1, which harbours a recently stripped star, gave us the opportunity to test predictions for the rotation velocity of such stars against observations. We studied two main cases: internal angular momentum transport by hydrodynamic effects and by magnetic effects, and found that only the latter can reproduce the observations. These models imply that stars can be modelled as near-rigid rotators during central hydrogen burning, but afterwards the stellar core and envelope rotate at separate rates. Prior to this decoupling, angular momentum is removed from the stellar core. This work is published as a scientific article (Schürmann et al., 2022).

We have seen in Ch. 1.5.1 that close binary systems are preferred to wider systems. This makes Case A mass transfer an important factor in binary evolution. However, this process is difficult to model in rapid binary population synthesis because the final donor mass and the duration of mass transfer cannot be estimated from single star models as easily as for Case B mass transfer. To accurately predict the outcome of Case A mass transfer, we have analysed two large grids of binary star models and derived prescriptions for the duration of mass transfer and the final donor mass in Ch. 4. We find that for fixed initial masses, the final donor mass becomes smaller as the initial orbital period becomes smaller, independent of the initial mass ratio. This is because in narrow systems the size of the convective core shrinks more during fast Case A mass transfer than in wide systems, and because in narrow systems the slow Case A mass transfer takes longer and so more mass is lost. Case A mass transfer lasts longer in close systems because the donor is less evolved. This work is submitted as a scientific article and is the topic of Ch. 4.

In order to predict the outcome of a RLO, it is necessary to know whether the mass transfer is stable or not. We presented the classical argument based on the mass-radius exponent in Ch. 1.4.3. In the stable case, the donor is stripped of its envelope and its companion accretes at least some of that material. However, it has long been known (Kippenhahn and Meyer-Hofmeister, 1977; Neo et al., 1977) that the accretion of matter can lead to the expansion of the accretor. Since the accretor, like the donor, is located in a volume-limited Roche lobe, such expansion can cause the accretor to fill its Roche lobe, and a contact system forms. It only needs a little more expansion and material can leave the system through the L_2-point. This has drastic consequences, as this material carries a large amount of angular momentum out of the system, and so the orbit decays and the system can merge into a single star. We have used this concept in Ch. 5 to determine what mass accretion rate leads to the expansion of the accretor. We find that there are three accretion regimes. If the accretion rate is below the thermal accretion rate, i.e. the ratio of the accretor's mass to its thermal timescale (Eq. 1.2), the accretor can remain in thermal equilibrium and does not expand. If the accretion rate is higher, it expands moderately as a function of the accretion rate. An even higher accretion rate, where the rate of energy release by accretion (Eq. 1.17) exceeds the Eddington luminosity (Eq. 1.11), leads to a rapid expansion of the accretor. From this we can derive which initial masses, mass ratios and orbital periods will lead to a L_2-overflow. The only free parameter left in this recipe is the mass-transfer efficiency. We use this result to determine the evolution of Wolf-Rayet star–O-type star binaries. This work is submitted as a scientific article and is the topic of Ch. 5.

In this final project, Ch. 6, we bring together the previous results and apply them to the Small Magellanic Cloud, where a large number of Be/X-ray binaries is observed. In the previous project, the mass-transfer efficiency was left as a free parameter for the boundary between stable mass transfer and mergers, and so we perform Monte Carlo based population syntheses with different constant mass-transfer efficiencies. Based on the number of Be/X-ray and Wolf-Rayet binaries, we can quantify the mass-transfer efficiency and find an anti-correlation between it and stellar mass. This allows us to construct an observationally gauged synthetic population from which we derive properties of the massive main-sequence stars with remnant companions in good agreement with observations. We predict a large number of about 150 O- and B-type stars with black hole companions, with two sub-populations, namely spectroscopic binaries with high orbital velocities and low rotational velocities, and early Be stars in wide orbits. In parallel, a study of the same type of objects has been carried out, but using detailed binary models as in Ch. 2, but for the metallicity of the Small Magellanic Cloud. The differences resulting from the different physical assumptions can be tested by observations.

CHAPTER 2

Properties of OB star–black hole systems derived from detailed binary evolution models

N. Langer[1,2], C. Schürmann[1,2], K. Stoll[1], P. Marchant[3,4], D.J. Lennon[5,6], L. Mahy[3], S.E. de Mink[7,8], M. Quast[1], W. Riedel[1], H. Sana[3], P. Schneider[1], A. Schootemeijer[1], C. Wang[1], L.A. Almeida[9,10], J.M. Bestenlehner[11], J. Bodensteiner[3], N. Castro[12], S. Clark[13], P.A. Crowther[11], P. Dufton[14], C.J. Evans[15], L. Fossati[16], G. Gräfener[1], L. Grassitelli[1], N. Grin[1], B. Hastings[1], A. Herrero[6,17], A. de Koter[8,3], A. Menon[8], L. Patrick[6,17], J. Puls[18], M. Renzo[19,8], A.A.C. Sander[20], F.R.N. Schneider[21,22], K. Sen[1,2], T. Shenar[3], S. Simón-Días[6,17], T.M. Tauris[23,24], F. Tramper[25], J.S. Vink[20], and X.-T. Xu[1]

[1] Argelander-Institut für Astronomie, Universität Bonn, Auf dem Hügel 71, 53121 Bonn, Germany
[2] Max-Planck-Institut für Radioastronomie, Auf dem Hügel 69, 53121 Bonn, Germany
[3] Institute of Astrophysics, KU Leuven, Celestijnenlaan 200D, 3001 Leuven, Belgium
[4] Center for Interdisciplinary Exploration and Research in Astrophysics (CIERA) and Department of Physics and Astronomy, Northwestern University, 2145 Sheridan Road, Evanston, IL 60208, USA
[5] Instituto de Astrofisica de Canarias, 38200 La Laguna, Tenerife, Spain
[6] Departamento de Astrofisica, Universidad de La Laguna, 38205 La Laguna, Tenerife, Spain
[7] Center for Astrophysics, Harvard-Smithsonian, 60 Garden Street, Cambridge, MA 02138, USA
[8] Anton Pannenkoek Institute for Astronomy, University of Amsterdam, 1090 GE Amsterdam, The Netherlands
[9] Departamento de Física, Universidade do Estado do Rio Grande do Norte, Mossoró, RN, Brazil
[10] Departamento de Física, Universidade Federal do Rio Grande do Norte, UFRN, CP 1641, Natal, RN 59072-970, Brazil
[11] Department of Physics and Astronomy, Hicks Building, Hounsfield Road, University of Sheffield, Sheffield S3 7RH, UK
[12] AIP Potsdam, An der Sternwarte 16, 14482 Potsdam, Germany
[13] School of Physical Sciences, The Open University, Walton Hall, Milton Keynes MK7 6AA, UK
[14] Astrophysics Research Centre, School of Mathematics and Physics, Queen's University Belfast, Belfast BT7 1NN, UK
[15] UK Astronomy Technology Centre, Royal Observatory Edinburgh, Blackford Hill, Edinburgh, EH9 3HJ, UK
[16] Space Research Institute, Austrian Academy of Sciences, Schmiedlstrasse 6, 8042 Graz, Austria
[17] Universidad de La Laguna, Dpto. Astrofisica, 38206 La Laguna, Tenerife, Spain
[18] LMU Munich, Universitätssternwarte, Scheinerstrasse 1, 81679 München, Germany
[19] Center for Computational Astrophysics, Flatiron Institute, New York, NY 10010, USA
[20] Armagh Observatory, College Hill, Armagh BT61 9DG, UK
[21] Zentrum für Astronomie der Universität Heidelberg, Astronomisches Rechen-Institut, Mönchhofstr. 12-14, 69120 Heidelberg, Germany
[22] Heidelberger Institut für Theoretische Studien, Schloss-Wolfsbrunnenweg 35, 69118 Heidelberg, Germany

[23] Aarhus Institute of Advanced Studies (AIAS), Aarhus University, Hoegh-Guldbergs Gade 6B, 8000 Aarhus C, Denmark
[24] Department of Physics and Astronomy, Aarhus University, Ny Munkegade 120, 8000 Aarhus C, Denmark
[25] IAASARS, National Observatory of Athens, Vas. Pavlou and I. Metaxa, Penteli 15236, Greece

Astronomy & Astrophysics **638** A39 (2020)
DOI 10.1051/0004-6361/201937375

Author contributions. NL gave the initial idea for this project, based on a suggestion from DL. PM computed the grid of binary models. KS conducted a pilot study. CS did the data analysis and interpreted the results together with NL. NL wrote the first draft, which was edited by CS. All authors reviewed the manuscript.

Summary

We have seen in Ch. 1.4 that the evolution of massive binary stars includes long-lived and well-observed phases such as double main-sequence stars or binary pulsars, but also short-lived and difficult to observe phases such as RLO. Since 2015, it is possible to observe another short-lived phase, namely the gravitational-wave coalescence of two black holes (Abbott et al., 2016). It is debated whether these systems originate from binary stars or through other channels, such as primordial formation or dynamical interactions. A first step in answering this question is to consider the long-lived intermediate phase with one star and one black hole, which can be modelled in detail without interruption starting from the double main-sequence stage. Predictions of their properties can be compared with local samples of massive stars, such as the population in 30 Doradus in the Large Magellanic Cloud, which is well observed by the VFTS (Evans et al., 2011; Almeida et al., 2017).

To this end, we have analysed a large grid of almost 50,000 detailed binary evolution models at the metallicity of the Large Magellanic Cloud, with initial primary masses between 10 and $40M_{\odot}$, computed by Marchant Campos (2018) with MESA (Paxton et al., 2011, 2013, 2015, 2018, 2019). This model grid makes certain assumptions about the physics of binary mass transfer. The accretor is assumed to gain mass and angular momentum until it reaches critical rotation. For Case B mass transfer, where tidal forces can be neglected, the mass-transfer efficiency is about 5%. For Case A, the efficiency is greater because the tides brake the accretor and remove angular momentum from it, allowing it to accrete more mass before reaching critical rotation. It is further assumed that if the non-accreted material cannot leave the system, the RLO will result in a merger. The condition for the ejection of this material is that the combined luminosity of both stars can provide enough power to unbind it. This leads to characteristic combinations of initial mass ratios and orbital periods for the systems that survive the RLO. From these we have identified the model systems that could evolve into a binary consisting of a black hole and a massive main-sequence star, namely systems with donor stars that have final helium core masses above $6.6M_{\odot}$. We assume that the mass of the black hole is the same as that of the progenitor's helium core, and that the black hole does not receive a birth kick. To derive the observable properties of such systems, as well as the peculiarities of the OB star, we weight each binary model in the grid according to the birth probability of such a system (see Ch. 1.5) and the remaining lifetime of the OB star.

We derive the distribution of OB star masses, black hole masses, mass ratios, orbital periods, orbital velocity semi-amplitudes, OB star rotation velocities, and surface abundances. Many features of these predictions can be verified by observations. We find a bimodal orbital period distribution stemming from our assumptions on the mass-transfer stability, with each maximum associated with either Case A or Case B. We expect the vast majority of OB star–black hole binaries to be X-ray quiet, because the orbital periods are predicted to be long enough for the black hole to accrete the OB-star wind in an advection-dominated flow rather than through

an accretion disc. Our models suggest that there is a subset of OB star–black hole binaries where orbital velocities of the OB stars are large enough ($> 50\,\mathrm{km/s}$) to identify them spectroscopically, and where the surface is nitrogen-enriched. A faint main-sequence companion can be excluded easily due to the predicted mass ratios. The other subset shows moderate radial-velocity variations ($> 10\,\mathrm{km/s}$), but the OB star is predicted to be a rapid rotator. Overall, we find that about 3% of the late O-type and early B-type stars in the Large Magellanic Cloud have a black hole companion, which translates to a total number of about 120. For the Milky Way this implies about 1000 OB star–black hole binaries. We compare our results with the observed OB star–Wolf-Rayet binaries in the Large Magellanic Cloud, which are expected to evolve into OB star–black hole binaries, and find good agreement between the mass and orbital period distributions. However, there is a mismatch at long orbital periods (about 100 d), where the observed number of Wolf-Rayet binaries is lower than expected. On the other hand, when our predictions are compared with the observed Be/X-ray orbital period distribution, there is good agreement at high orbital periods, supporting our results.

We predict a substantial, previously undetected population of OB star–black hole binaries, which could be uncovered through spectroscopic observations. Discovering these binaries would test assumptions and reduce uncertainties in our models, and enhance our understanding of the role of close binary evolution in gravitational wave events.

The publication (Langer et al., 2020) is reproduced in Appendix A.

CHAPTER 3

The spins of stripped B stars support magnetic internal angular momentum transport

C. Schürmann[1,2], N. Langer[2,1], X.-T. Xu[1,2], and C. Wang[2,3]

[1] Max-Planck-Institut für Radioastronomie, Auf dem Hügel 69, 53121 Bonn, Germany
[2] Argelander-Institut für Astronomie, Universität Bonn, Auf dem Hügel 71, 53121 Bonn, Germany
[3] Max-Planck-Institut für Astrophysik, Karl-Schwarzschild-Str. 1, 85748 Garching, Germany

Astronomy & Astrophysics **667** A122 (2022)
DOI 10.1051/0004-6361/202244153

Author contributions. CS analysed the stellar models, which were calculated by XTX based on models of CW, and wrote the first draft. NL helped to interpret the results and edited the draft. All authors reviewed the manuscript.

Summary

It is well known that stellar remnants can be fast rotators, most notably radio pulsars. The origin of their high spin must be addressed and can be understood as a consequence of stellar evolution, since stars can also be fast rotators. In order to accurately predict the spin of the remnant, we need to understand how the angular momentum is distributed within the progenitor star, which is both computationally and observationally challenging. The recently discovered Galactic B-type binary LB-1 (Liu et al., 2019) gave us the opportunity to test model predictions of stellar rotation. Initially thought to be a B-type star–black hole binary, it turned out to consist of a Be star and a recently stripped companion that has not yet reached the subdwarf state, but is in the process of contracting and masquerades as a main-sequence star. This is evident from the high luminosity-to-mass ratio and the low rotation velocity of 7 km/s (Shenar et al., 2020a; Lennon et al., 2021).

With this aim, we have analysed the large grid of of binary star models by (Wang et al., 2022) computed with MESA (Paxton et al., 2011, 2013, 2015, 2018, 2019) to identify possible initial masses and orbital periods for this system. Using the observed luminosity-to-mass ratio and surface abundances, we found initial masses of about $4M_\odot$ and $3.5M_\odot$ and an initial orbital period of about 16 d. This system has undergone a Case B mass transfer, where the accretor star has been spun up to become a Be star and the donor star has been stripped to reveal its core. Using these values, we calculated new stellar models to address the angular

momentum distribution within the donor. We assumed two different initial rotation rates (20% and 55% of the critical rotation, see Eq. 1.14) and two different angular momentum transport mechanisms. The first is based on hydrodynamic effects, such as shear-induced turbulence, in which rising and sinking mass elements carry angular momentum up or down. The second is the magnetic Spruit–Tayler dynamo (Spruit, 2002), where differential rotation generates magnetic fields in the stellar interior. Due to the high conductivity of the stellar plasma, magnetic torques act between the layers of the model. Theory predicts that the Spruit–Tayler dynamo becomes less efficient in layers with strong gradients in entropy or chemical composition.

We find that only models with magnetic angular momentum transport are able to reproduce the observed low rotation velocities, regardless of the initial rotation. In these, the rotation is close to that of a rigid body until central hydrogen depletion. The subsequent expansion causes the rotation rate of the envelope to decrease, as expected from the conservation of angular momentum, but the contraction of the core does not increase its rotation rate. On the contrary, we find that the rotation of the core decreases. This is due to the efficient transport of angular momentum by the Spruit–Tayler dynamo. However, as the model evolves towards core helium burning, a strong gradient in chemical composition develops between the core and the envelope, which reduces the efficiency of the magnetic angular momentum transport. As a result, the core spins up slightly as it continues to contract until helium ignition. The envlope slows down further as tidal torques brake it when filling the Roche lobe. At the end of mass transfer, the envelope contracts, causing it to spin up again, and is able to archive rotational velocities of about 10 km/s as it crosses the main-sequence and about 20 km/s by the time it reaches the subdwarf phase. The rotational decoupling of the core and the envelope is evident from the fact that the envelope, after its contraction, rotates at a higher frequency than the core and is not spun up by the rotation of the core.

Models with purely hydrodynamic angular momentum transport do not agree with the observations. In these models, a strong angular velocity gradient develops already during the main sequence, which is amplified enormously after the core contraction and the envelope expansion after central hydrogen exhaustion. Thus, almost no angular momentum is removed from the core during the expansion and RLO phases. After the mass transfer, the slowly rotating envelope is accelerated by its own contraction and the immense shear between core and envelope, which overcomes the weak hydrodynamic rotational coupling. Thus, by the time the model reaches the subdwarf phase, the surface rotation is about 100 km/h. Compared to a single-star model (with magnetic angular momentum transport), the angular momentum distribution within the model is similar, and even after RLO the differences are small. So it does not matter whether the angular momentum is drained from the core by the expansion of the envelope or by tidal forces. It is more important that it is removed to explain the observed rotation rates. This implies that the spin of white dwarfs is independent of mass stripping. Precise measurements of the rotation rates of subdwarfs should be able to further constrain the angular momentum transport.

The publication (Schürmann et al., 2022) is reproduced in Appendix B.

CHAPTER **4**

Analytic approximations for massive close post-mass transfer binary systems

C. Schürmann[1], N. Langer[1,2], J. A. Kramer[2], P. Marchant[3], C. Wang[4], and K. Sen[5]

[1] Argelander-Institut für Astronomie, Universität Bonn, Auf dem Hügel 71, 53121 Bonn, Germany
[2] Max-Planck-Institut für Radioastronomie, Auf dem Hügel 69, 53121 Bonn, Germany
[3] Instituut voor Sterrenkunde, KU Leuven, Celestijnenlaan 200D, 3001 Leuven, Belgium
[4] Max-Planck-Institut für Astrophysik, Karl-Schwarzschild-Str. 1, 85748 Garching, Germany
[5] Institute of Astronomy, Faculty of Physics, Astronomy and Informatics, Nicolaus Copernicus University, Grudziadzka 5, 87-100 Toruń, Poland

Accepted for publication in *Astronomy & Astrophysics*. (At the time of publication of this thesis, this chapter is published as Schürmann et al. (2024), *Astronomy & Astrophysics* **690** A282, DOI 10.1051/0004-6361/202450353.)

Author contributions. CS analysed the stellar models computed by PM and CW after a pilot study by JAK. NL and KS helped to interpret the results. CS wrote the first draft, which was edited by NL. All authors reviewed the manuscript.

Abstract

Massive binary evolution models are needed to predict massive star populations in star forming galaxies, the supernova diversity, and the number and properties of gravitational wave sources. Such models are often computed using so called rapid binary evolution codes, which approximate the evolution of the binary components based on detailed single star models. However, about one third of the interacting massive binary stars undergo mass transfer during core hydrogen burning (Case A mass transfer), whose outcome is difficult to derive from single star models. Here, we use a large grid of detailed binary evolution models for primaries in the initial mass range 10 to $40 M_\odot$ of LMC and SMC composition, to derive analytic fits for the key quantities needed in rapid binary evolution codes, i.e., the duration of core hydrogen burning, and the resulting donor star mass. Systems with shorter orbital periods produce up to 50% lighter stripped donors and have a up to 30% larger lifetime than wider systems. We find that both quantities depend strongly on the initial binary orbital period, but that the initial mass ratio and the mass transfer efficiency of the binary have little impact on the outcome. Our results are easily parameterisable and can be used to capture the effects of Case A mass transfer more accurately in rapid binary evolution codes.

Key words. binaries: general – binaries: close – stars: evolution – stars: massive

4.1 Introduction

Massive stars are key constituents of the Universe, as they produce heavy elements, drive the cosmic matter cycle in galaxies, and are the origin of supernovae, black holes, and other spectacular phenomena (e.g. Langer, 2012). It has become clear that most massive stars are born in binary or multiple systems (Vanbeveren et al., 1998; Sana et al., 2012; Moe and Di Stefano, 2017; Banyard et al., 2022). Since stars tend to increase their radius during their life, most binary stars are expected to interact sooner or later, drastically altering the course of their evolution (Podsiadlowski et al., 1992; de Mink et al., 2013).

Stellar evolution codes have been constructed, which are capable of predicting the progression of the properties of both stellar components and of the binary orbit in detail — even though using various physical approximations (Vanbeveren and De Loore, 1994; Nelson and Eggleton, 2001; Wellstein et al., 2001; Eldridge et al., 2008). This includes the mass transfer phases, as long as mass transfer does not become dynamically unstable. In particular the numerically robust MESA code, which can compute highly resolved models of both stars in a binary simultaneously, has been extended to include a large spectrum of binary physics (Paxton et al., 2011, 2013, 2015).

In order to derive population synthesis predictions, several of these codes have been used to produce large grids of massive binary evolution models (Vanbeveren et al., 1997; de Mink et al., 2007; Han et al., 2020; Langer et al., 2020; Wang et al., 2020; Fragos et al., 2023). In these efforts, like also in the BPASS code (Eldridge et al., 2008; Eldridge et al., 2017), synthetic populations are produced by interpolating in grids of detailed binary evolution models, and by applying weight factors which account for the birth probability and lifetime of individual binary models. The latter code has also been used to obtain the spectra of synthetic populations (Stanway and Eldridge, 2018; Byrne et al., 2022). Because their initial parameter space is so much larger than that of single star models, comprehensive grids sufficiently dense to produce well resolved population predictions need to include 10^4 to 10^5 individual detailed binary evolution models (e.g. Langer et al., 2020), constituting a considerable effort. While these efforts have been successful in providing new and important predictions (e.g. Wang et al., 2020; Sen et al., 2022), they are hampered by assumptions on weakly constrained essential physics parameters, for single star and binary evolution physics. It is currently still prohibitively time consuming to perform the required parameter studies with such large detailed binary model grids.

For this reason, so called rapid binary evolution codes have been developed. In most of these, a star is just resolved by two grid points, representing the stellar core and the envelope, and their properties as function of time are approximated from single star models, either analytically or interpolated from detailed single star models (e.g. Lipunov et al., 1996; Hurley et al., 2000, 2002; Izzard et al., 2006; Stevenson et al., 2017; Kruckow et al., 2018; Vigna-Gómez et al., 2018; Shao and Li, 2021; Riley et al., 2022; Romero-Shaw et al., 2023). While this can not describe the short term thermally unstable evolutionary phases of stars, including phases of mass transfer, it may capture the essential result of mass transfer well enough in most cases, i.e., when the mass donor is essentially stripped of its complete envelope.

However, mass transfer during core hydrogen burning (Case A mass transfer, e.g. Pols, 1994) is particularly unruly, since a clear division of the donor star into a core and an envelope is only possible after core hydrogen exhaustion. While Case A mass transfer occurs only in rather short period binaries, those are favoured by the initial orbital period distribution, such that it concerns about one third of all interacting massive binary stars (Sana et al., 2012, 2013; de Mink et al., 2014), or even the majority above about $40M_\odot$ (Sen et al., 2023). While many rapid codes treat Case A mass transfer as if core hydrogen burning was already over at the onset of mass transfer, we show below that this can lead to large errors in the predicted donor masses and ages after the mass transfer. In particular, the post-mass transfer donor properties in Case A binaries are known to strongly depend on the initial orbital period of the binary (cf., fig. 14 of Wellstein et al., 2001) and can not be easily derived from single star models. This has important implications for the final fate of the donor stars, as one can see in fig. B.1 of Langer et al. (2020), where Case A models produce neutron stars and Case B (mass transfer after central hydrogen exhaustion) models produce black holes. This directly effects the predicted number of black holes and neutron stars.

To remedy this problem, we make use of existing large binary evolution model grids computed with MESA, to derive analytic predictions for the key quantities of donor stars directly after Case A mass transfer, as function of the initial binary parameters. We briefly discuss the key physics and initial parameters of these grids in Sect. 4.2. In Sect. 4.3, we explore the dependencies of the donor properties on the initial binary parameters, and derive analytic fits to our main results. We discuss caveats and uncertainties in Sect. 4.4, before we give our conclusions in Sect. 4.5.

In this paper, we neither investigate the properties of the accretor, as they were covered by e.g. Renzo and Götberg (2021) and Renzo et al. (2023), nor contact binaries, as contact alters the course of evolution and they are expected to merge sooner or later (Menon et al., 2021).

4.2 Detailed binary model grids

We use the grids of detailed binary models calculated by Marchant Campos (2018), see also Langer et al. (2020) and Sen et al. (2022), with Large Magellanic Cloud (LMC) metallicity and by Wang et al. (2020) with Small Magellanic Cloud (SMC) metallicity, using MESA version 8845 (Paxton et al., 2011, 2013, 2015). The LMC grid contains models with initial primary (i.e. the initially heavier component of the binary) masses from $10M_\odot$ to $40M_\odot$ with initial orbital periods from $10^{0.15}\,\mathrm{d} = 1.4\,\mathrm{d}$ to $10^{3.5}\,\mathrm{d} = 3162\,\mathrm{d}$ and initial mass ratios (mass of the initially less massive star over the mass of the primary) from 0.25 to 0.975. The SMC grid contains initial primary masses from $5M_\odot$ to $100M_\odot$ with initial orbital periods from 1 d to $10^{3.5}\,\mathrm{d} = 3162\,\mathrm{d}$ and mass ratios from 0.3 to 0.95. We use all models of these grids which undergo Case A mass transfer with donor masses between $10M_\odot$ to $40M_\odot$, as the models outside of this range tend not to yield a stripped donor star, either due to physical (no stable mass transfer) or numerical reasons, see Marchant Campos (2018). An extension of the LMC grid by Pauli et al. (2022) will be used in Sect. 4.3.2 to test if our results are applicable outside the adopted mass range. The upper initial period limit for Case A is a function of donor mass as discussed in Sect. 4.3.2.

The initial chemical composition of the models is as in Brott et al. (2011), and custom-built OPAL opacities (Iglesias and Rogers, 1996) were used to match the initial abundances. The models were computed using the standard mixing-length theory with $\alpha_{\mathrm{ml}} = 1.5$, the Ledoux criterion for convection and step-overshooting with $\alpha_{\mathrm{ov}} = 0.335$ (Brott et al., 2011). We assume thermohaline mixing following Cantiello and Langer (2010) with $\alpha_{\mathrm{th}} = 1$ and apply semiconvection with $\alpha_{\mathrm{sc}} = 0.01$ for the LMC (Langer, 1991) and $\alpha_{\mathrm{sc}} = 1$ for the SMC (Langer et al., 1983). The effect of the difference in semiconvection is small during hydrogen burning in the considered donor models (Schootemeijer et al., 2019).

The initial spin of both stars is assumed to be synchronous with the orbit (Langer et al., 2020) and the tides are treated as in Detmers et al. (2008). Differential rotation, rotational mixing (with the ratio of the ratio of the turbulent viscosity to the diffusion coefficient $f_c = 1/30$, Chaboyer and Zahn, 1992) and angular momentum transport are modelled as in Heger et al. (2000, 2005) including the Taylor-Spruit dynamo (Spruit, 2002). During Roche-lobe overflow (RLO), the secondary star accretes matter either ballistically or from a Keplerian disk (Petrovic et al., 2005) based on the results from Lubow and Shu (1975) and Ulrich and Burger (1976). Rotationally enhanced mass loss (Langer, 1998) stops accretion when the accretor reaches critical rotation (Langer, 2012). The material that has not been accreted leaves the system with the specific orbital angular momentum of the accretor following Soberman et al. (1997). If the combined luminosity of both stars does not provide enough energy to unbind the excess material from the system, the calculations were stopped (see eq. 2 of Sen et al., 2022, in particular). Models in which overflow at the outer Lagrange point or reverse mass transfer occurs where terminated, too. The remaining models were calculated at least up to central helium depletion.

4.3 Results

Case A mass transfer is rather complex, in that it is composed of three distinct phases (Pols, 1994; Wellstein et al., 2001). It starts with a phase of rapid mass transfer (fast Case A), which proceeds on the Kelvin-Helmholtz timescale of the mass donor, during which the donor is stripped of a large fraction of its envelope mass. For shorter initial orbital periods, this rapid mass transfer happens earlier during the core hydrogen burning evolution of the donor. It is followed by a nuclear timescale mass transfer phase, driven by the slow expansion of the donor star (slow Case A), which ends due to its overall contraction of the donor near core hydrogen exhaustion. Immediately thereafter, another rapid mass transfer occurs, driven by the expansion of the remaining hydrogen-rich envelope due to the ignition of shell hydrogen burning.

This third mass transfer episode (often called Case AB), which concludes Case A mass transfer, strips the donor star so much that its envelope mass becomes very small, and it can be approximated for many purposes as a helium star (see however Laplace et al., 2020, 2021). This is analogous to the situation after Case B mass transfer, which occurs in binaries which have sufficiently large orbital periods that the donor star avoids mass transfer during core hydrogen burning. However, while in Case B systems the mass of the stripped helium star closely follows the helium core mass–initial mass relation of single stars, the helium stars emerging from Case A binaries do not obey this relation. Similarly, the age of a donor star at the end of the Case B mass transfer is very close to the core hydrogen burning life time of a single star of the same initial mass. However, since Case A donors undergo part of their core hydrogen burning with a significantly reduced mass, their ages at the end of Case A mass transfer are larger than those of corresponding single stars. Both effects are shown in detail in the following.

4.3.1 Analysis of the MESA models

For this analysis, we define the beginning of a Case A RLO as the moment where the donor fills more than 99.9% of its Roche lobe during central hydrogen burning. As the end of Case AB we use the time when the donor star becomes smaller than 99% of its Roche lobe after central helium ignition (central carbon abundance surpasses 0.1%). We found that these assumptions ensured the best tracking of the RLO in our models.

Fig. 4.1 shows the post-Case AB donor masses $M_{\rm AB}$ of all donors in the considered binary model grids, for LMC and SMC metallicities, as function of their initial mass $M_{\rm ini}$ and initial orbital period $P_{\rm ini}$. In this figure, we have depicted the median values of the post-Case AB masses across different mass ratios for binaries with the same initial donor mass and orbital period, to enhance the clarity. One can see from the top panels, where

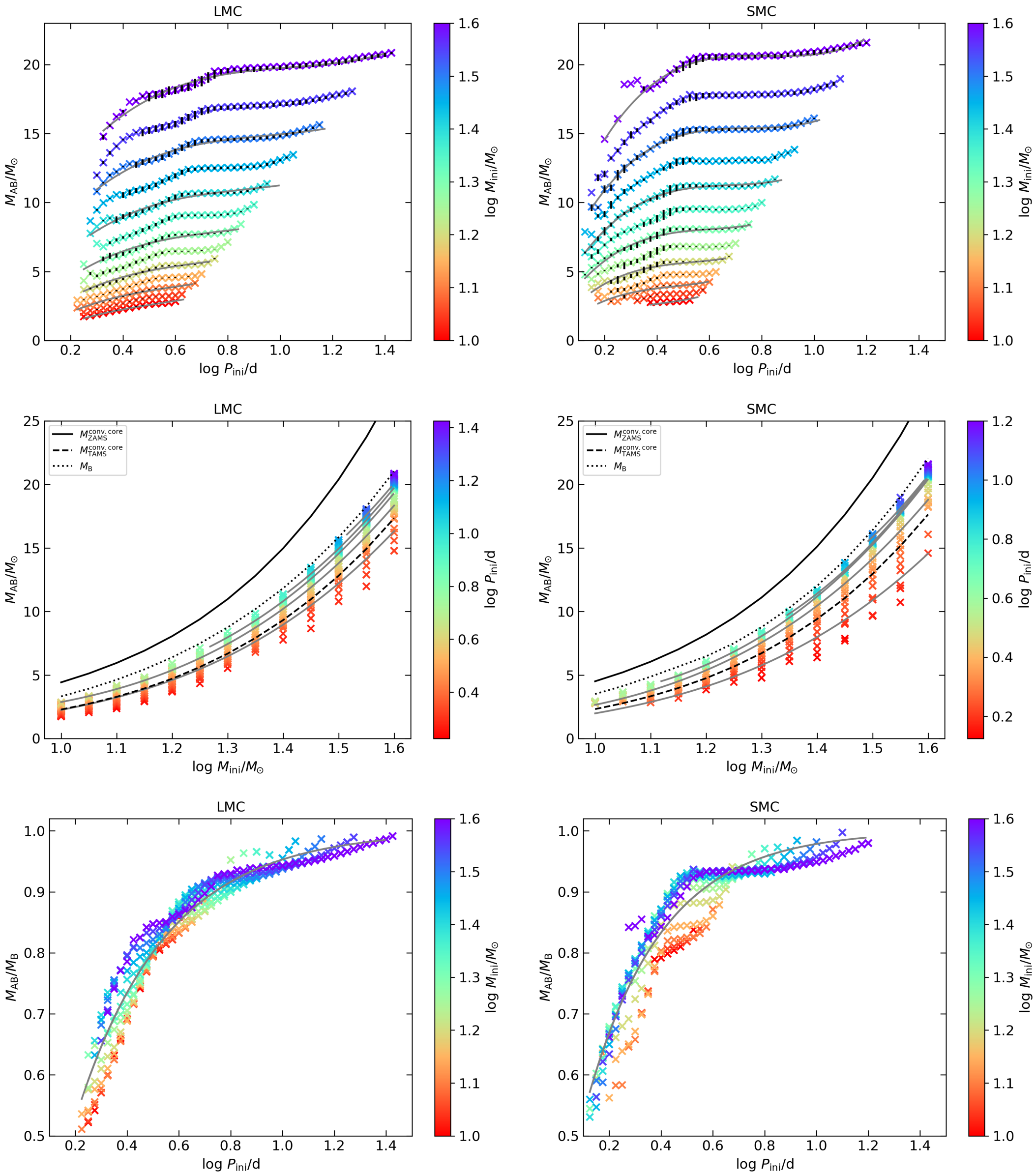

Figure 4.1: Donor mass immediately after Case AB mass transfer (M_{AB}) in units of the Solar mass (top and middle) and in units of the donor mass after Case B mass transfer (M_B, bottom), as function of the initial orbital period P_{ini}, with the initial donor mass M_{ini} colour coded (top and bottom). The middle panel shows M_{AB} as functions of the initial donor mass, where models with the same initial orbital period are indicated with the same colour. Each cross represents the median of M_{AB} across different initial mass ratios and in the top plots we indicted in black its interquartile range (distance from first to third quartile of the mass ratio distribution). In the middle plots the black lines show the mass of the convective cores of single stars at the beginning ($M_{ZAMS}^{conv.core}$) and the end ($M_{TAMS}^{conv.core}$) of core hydrogen burning, as well as the mass after Case B mass transfer, as function of the initial stellar mass. Grey lines indicate our best fit to the data. The panels on the left show LMC models, and on the right SMC show models.

we display the interquartile range (i.e. first to third quartile of the mass ratio distribution), that the scatter in post-Case AB donor masses (for a fixed initial donor mass and initial orbital period) from different initial mass ratios is very limited. Around an orbital period of roughly $10^{0.5}$ d ≈ 3 d the interquartile range is for both metallicities slightly larger than elsewhere. See Sect. 4.4.1 for a further discussion.

The top and middle panels of the figure show that, as expected, the post-Case AB donor masses depend strongly on the initial donor mass. However, on top of that, a clear dependence on the initial orbital period can also be seen. The latter effect is largest for the largest initial donor mass ($\sim 40M_{\odot}$), for which the LMC post-Case AB donor masses cover the range from $14.8M_{\odot}$ to $20.9M_{\odot}$. For $10M_{\odot}$ donors, the post-Case AB donor masses are found to range from $1.7M_{\odot}$ to $2.8M_{\odot}$, such that the relative variation is as large as it is for the $40M_{\odot}$ donors. For SMC metallicity we find slightly different masses. The post-Case AB masses of the $40M_{\odot}$ donors are $14.6M_{\odot}$ to $21.8M_{\odot}$, and for the $10M_{\odot}$ donors only $2.8M_{\odot}$ to $2.9M_{\odot}$, due to a smaller number of models surviving the RLO. For all models a small hydrogen-rich layer remains on the donor. In the middle panels, we also indicate the convective core mass at be beginning and the end of core hydrogen burning for single stars of the same initial mass. For a given initial donor mass, the largest post-Case AB mass is always clearly smaller than the initial convective core mass and the convective core mass at central hydrogen exhaustion is only loosely related to the smallest post-Case AB mass, since central hydrogen exhaustion in single star evolution and Case AB evolution have followed different evolutionary paths. The donor mass after Case B mass transfer with same initial donor mass is a much better indicator for the behaviour of the post-Case AB mass. It is either equal (upper end of the initial donor mass range) or slightly smaller (lower end) than the largest post-Case AB mass at same initial donor mass. For the SMC models this difference between post-Case B mass and largest post-Case AB mass is larger.

Inspired by that, in the bottom panels of Fig. 4.1, we have scaled the post-Case AB donor mass to the post-Case B mass of a model with same initial mass. Interestingly, this ratio shows a very high (but non-linear) correlation with the initial orbital period. This behaviour is more pronounce for the LMC models than for the SMC models. The larger scatter for the SMC models may arise from the post-Case B mass of the lighter models being heavier than the heaviest post-Case AB models of the same initial mass. This causes those models to deviate from the curve. Towards smaller initial orbital periods, the ratio of post-Case AB to post-Case B mass decreases and, as expected, the ratio converges towards unity for large orbital period. The main difference between the two metallicities is that Case A occurs at slightly lower initial orbital periods for the lower metallicity. This shift causes the post-Case AB mass to be higher for the lower metallicity at the same orbital periods. The underlying reason is that for the same initial orbital period the SMC donor fills its Roche lobe later into central hydrogen burning than a corresponding LMC donor, because SMC models are more compact. Thus the SMC donor resembles to a LMC donor at higher initial orbital period.

The period dependence of the post-Case AB donor masses can be understood as follows. For a given initial donor mass both the mass of the initial convective core[1] and the donor mass after fast Case A mass transfer barely depend on the initial orbital period (fig. F.3 of Sen et al., 2022). This can be seen in Fig. 4.2, where we find for an initial donor mass of $20M_{\odot}$ a donor mass after fast Case A of $10.9M_{\odot}$ for a small initial orbital period (top panels) and for a wider Case A system (bottom panels) we get $10.5M_{\odot}$. In both models the initial convective core mass was $11.0M_{\odot}$ and the convective core masses just before the onset of mass transfer were $8.5M_{\odot}$ and $7.0M_{\odot}$, as expected since the extend of the convective core shrinks during main-sequence evolution and the mass transfer happens later during hydrogen burning for the wider system. During the fast Case A phase the mass of the convective core decreases abruptly, namely by $2.6M_{\odot}$ for the close system and by $1.1M_{\odot}$ for the wide system. The extent of the abrupt shrinking (in mass) depends on how early the Case A

[1] This includes the overshooting region above and not just the MESA output `mass_conv_core`.

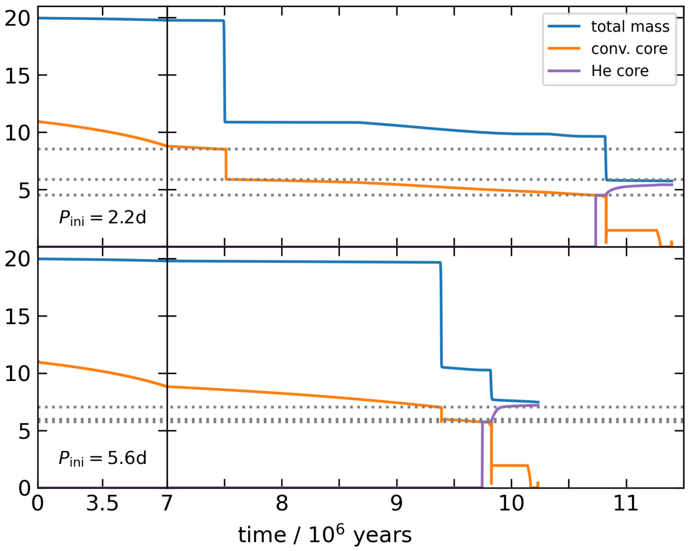

Figure 4.2: Evolution of the total mass, the convective core mass, and the helium core of the donor model with an initial mass of $20M_\odot$ with a companion of initially $14M_\odot$ and an initial orbital period of $10^{0.35}$ d = 2.2 d (top panels) and $10^{0.75}$ d = 5.6 d (bottom panels). We indicate the mass of the convective core at the onset of mass transfer, just after the fast Case A, and at central hydrogen depletion by grey lines.

mass transfer occurs i.e. on the initial orbital period of the binary. The shorter the initial orbital period, the greater is the shrinking in terms of mass. This period dependent jump in the convective core mass is the first reason for the period dependence in the post-Case AB mass. Over the whole model set, it takes values from $0.8M_\odot$ to $2.6M_\odot$

Since the remaining central hydrogen burning time is larger for the donor in the closer system (3.3 but only $0.4 \cdot 10^6$ years for the wide system), the mass of the donor's convective core decreases even more. During the slow Case A phase, the donor transfers mass on a nuclear timescale, wherefore the donor in the close system loses more mass. In the example in Fig. 4.2, the donor mass at central hydrogen depletion is $9.6M_\odot$ for the close and $10.3M_\odot$ for the wide system. This causes the mass of the convective core to become even smaller, which forms the second reason for the period dependency. At central hydrogen depletion, the convective cores has shrunken by $1.4M_\odot$ since end of fast Case A for the close system and by only $0.2M_\odot$ for the wide system. Over the whole model set, this effect can shrink the convective core up to $5M_\odot$ for the closest and heaviest systems. For light donors, both effect are equally important, since for close and wide systems the difference in mass change of the convective core for the first effect is about $1M_\odot$ as it is for the second one, while for heavier donors, the second one dominates. Finally, that mass of the convective core at hydrogen exhaustion determines the mass of the helium core, which then determines the mass of the donor after Case AB mass transfer.

Fig. 4.3 shows in its top and middle panels the duration of Case A mass transfer as a function of initial donor mass and initial orbital period. We find that the duration is larger for initially closer orbits, since donor stars in close orbits fill their Roche lobe earlier and thus more of the central hydrogen burning time remains for the donor in its mass-reduced state. Furthermore, the duration of Case A mass transfer increases weakly

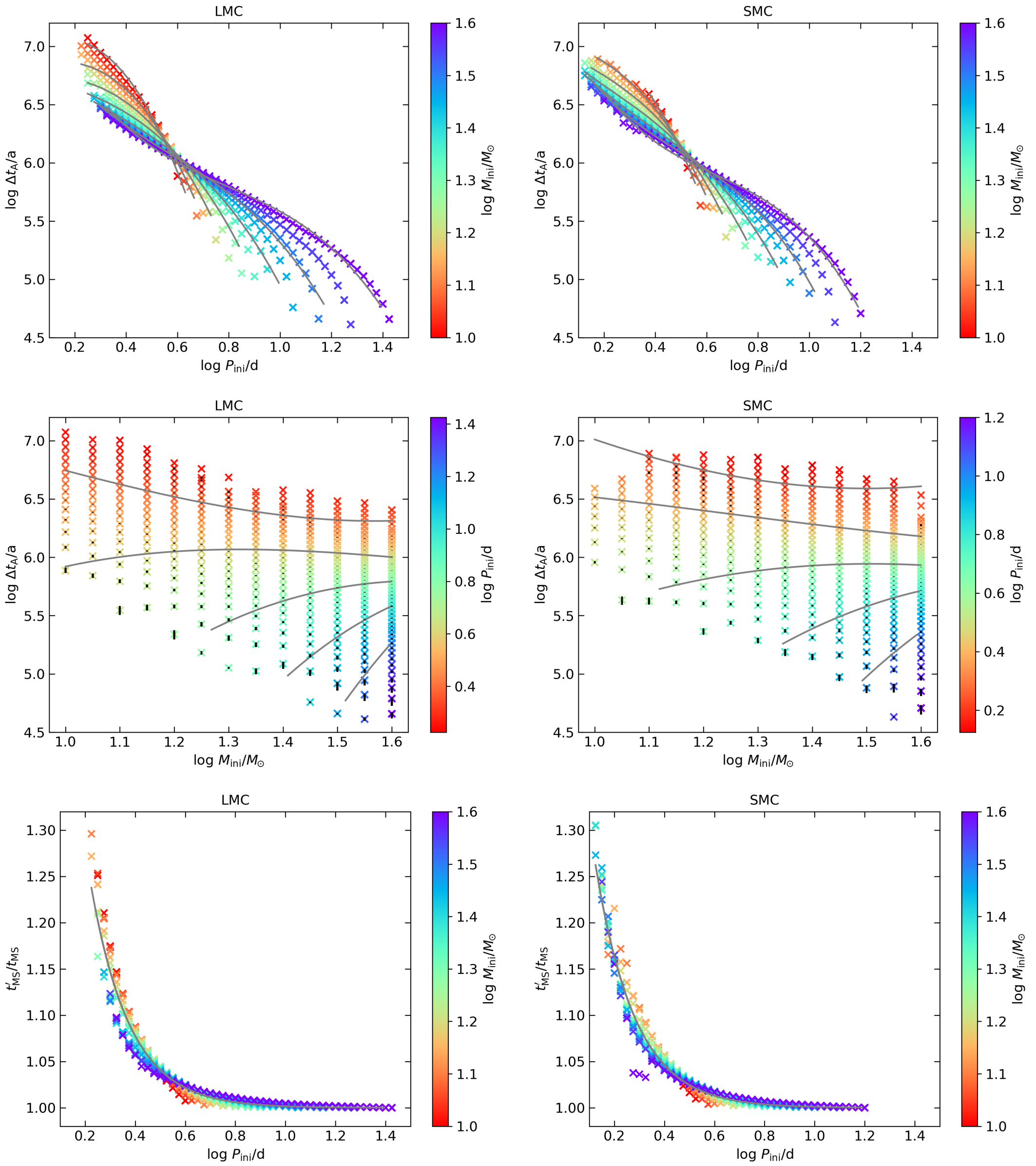

Figure 4.3: Duration of Case A mass transfer (Δt_A) in logarithmic years as functions of initial orbital period P_{ini} with the initial donor mass M_{ini} colour coded (top) and as functions of the initial donor mass, where models with the same initial orbital period are indicated with the same colour (middle). The bottom panels show the ratio of the Case A donor core hydrogen burning lifetime t'_{MS} to the core hydrogen burning lifetime t_{MS} of a single star of the same initial mass, as a function of the initial orbital period and in the top plots we indicted in black its interquartile range. Each cross represents the median value of Δt_A across different initial mass ratios. In the top plot we indicted in black the first and third quartile. Grey lines indicate our best fit to the data. The panels on the left show LMC models and on the right is SMC.

with increasing initial mass for initial orbital periods above about $10^{0.5\cdots0.6}$ d and decreases for lower initial periods. This means a stronger decrease in duration of mass transfer with initial orbital period for smaller initial donor masses. For our lowest masses ($10M_\odot$) with the closest orbits, we find durations for Case A mass transfer of about 10^7 years. Interestingly for both metallicities the Case A duration is about 10^6 years around initial orbital periods around $10^{0.5\cdots0.6}$ d independently of initial donor mass. From the middle plots one can see that the differences in Case A duration between the two metallicities are small and mainly arise from the initial masses and periods where Case A mass transfer is stable. In particular, the upper left corner of the middle panel of Fig. 4.3 contains models for the LMC grid, but not for the SMC grid. It also shows through the interquartile range that the impact of the initial mass ratio is very small.

In the bottom plot of Fig. 4.3, we show the ratio of the core hydrogen burning lifetime of the Case A donor t'_MS in units of the core hydrogen burning lifetime of a single star of the same initial mass t_MS. We find that in this representation a strong non-linear correlation to the initial orbital period. The lifetime increases for smaller initial orbital period. This is not unexpected as systems with lower initial orbital period undergo RLO earlier, have thus a larger hydrogen fraction in the core after the fast part of the mass transfer and are less massive and therefore keep core hydrogen burning for a longer time. We find increases in lifetime of up to 30% for the closest systems. For larger initial orbital periods, the lifetime increase becomes zero as the upper orbital period for Case A mass transfer is reached. For the the $10M_\odot$-models this happens around an initial period of $10^{0.6}$ d and for the $40M_\odot$-models around $10^{1.4}$ d (LMC) and $10^{1.2}$ d (SMC), respectively. The bottom panels show that for the same initial orbital period, the lifetime increase is larger for the larger metallicity.

We found that if we would normalise the data so that we would show the lifetime increase as a function between minimum and maximum of period where Case A mass transfer occurs, they would not lie as neatly on one curve as shown here. Using the orbital period as the independent quantity for Fig. 4.1 and 4.3 may seem to be an arbitrary choice, but we found that only with that the data fall onto one single curve. Using the relative age of the donor at beginning of the mass transfer compared to the age of central hydrogen exhaustion of a single star of same initial mass or the central hydrogen content at beginning of the mass transfer as the independent quantity, did not yield such unique curves. For practical application, we provide these data with fits in Appendix C.1.

4.3.2 Analytic fits

Before we provide fits for the donor mass after Case AB mass transfer and the duration of Case A mass transfer, we are going to give mass dependent boundaries of initial periods in which Case A occurs and within which our fits are valid. We find that the lower period limit P_min for a Case A mass transfer which leads to donor stripping is well described by a parabola

$$\log P_\mathrm{min} = a + b \cdot (\log M_\mathrm{ini} - c)^2 \tag{4.1}$$

with $(a, b, c) = (0.240 \pm 0.001, 0.270 \pm 0.134, 1.04 \pm 0.13)$ for the LMC and $(a, b, c) = (0.114 \pm 0.012, 1.72 \pm 0.27, 1.37 \pm 0.02)$ for the SMC. On the other hand the upper period limit for Case A mass transfer P_max, which is also the boundary towards Case B, is also well described by a parabola

$$\log P_\mathrm{max} = a + b \cdot (\log M_\mathrm{ini} - c)^2 \tag{4.2}$$

with $(a, b, c) = (0.619 \pm 0.022, 1.87 \pm 0.21, 0.957 \pm 0.039)$ for the LMC and $(a, b, c) = (0.535 \pm 0.019, 1.31 \pm 0.13, 0.897 \pm 0.040)$ for the SMC.

We find third order polynomials f well fitting to describe the dependency of the donor mass M_AB after Case AB mass transfer and its duration Δt_A on the initial donor mass M_ini and the initial orbital period P_ini.

We define $m = \log M_{\rm ini}/M_\odot$ and $p = P_{\rm ini}/{\rm d}$. With that the polynomials can be written as

$$\begin{aligned} f(m,p) = &a_{30}m^3 + a_{20}m^2 + a_{10}m + \\ &a_{03}p^3 + a_{02}p^2 + a_{01}p + \\ &a_{21}m^2p + a_{12}mp^2 + a_{11}mp + a_{00}. \end{aligned} \tag{4.3}$$

The coefficients a_{ij} of the fit are given in Table 4.1 for both metallicities. The root-mean-square relative deviation between model data and fit is in all cases smaller than 3% and the maximum relative deviation reaches about 15% for the worst outlier. We conclude that our fit describes the data well. We indicated the fits in Fig. 4.1 and 4.3 (top and middle) with grey lines for selected values of the colour coordinate, which confirms that they match well.

Table 4.1: Fit coefficients a_{ij} found for Eq. 4.3. The last rows show root-mean-square relative deviation $\delta_{\rm rms}$ and the maximum relative deviation $\delta_{\rm max}$ between fit and data.

	LMC		SMC	
	$f(m,p) = \log \Delta t_{\rm A}$	$f(m,p) = M_{\rm AB}$	$f(m,p) = \log \Delta t_{\rm A}$	$f(m,p) = M_{\rm AB}$
a_{30}	0.958 ± 0.187	20.5 ± 1.2	0.356 ± 0.212	18.8 ± 1.7
a_{20}	1.95 ± 0.67	-56.1 ± 4.2	1.83 ± 0.80	-53.0 ± 6.5
a_{10}	-8.84 ± 0.81	53.2 ± 5.1	-6.30 ± 1.03	51.1 ± 8.4
a_{03}	-2.14 ± 0.04	9.83 ± 0.27	-3.27 ± 0.06	25.9 ± 0.5
a_{02}	-18.8 ± 0.3	8.46 ± 1.6	-15.0 ± 0.3	25.2 ± 2.3
a_{01}	-6.27 ± 0.32	6.03 ± 2.02	-5.71 ± 0.42	10.0 ± 3.4
a_{21}	-11.4 ± 0.3	19.1 ± 1.8	-7.88 ± 0.29	36.7 ± 2.4
a_{12}	14.9 ± 0.2	-24.4 ± 1.3	13.3 ± 0.23	-55.7 ± 1.9
a_{11}	19.0 ± 0.6	-13.5 ± 3.8	13.1 ± 0.7	-32.3 ± 5.5
a_{00}	12.9 ± 0.3	-18.0 ± 2.1	11.3 ± 0.5	-16.8 ± 3.7
$\delta_{\rm rms}$	0.7%	2.0%	0.6%	2.7%
$\delta_{\rm max}$	5.6%	11.0%	5.3%	14.4%

Next, we consider the donor mass after Case AB $M_{\rm AB}$ in units of the donor mass after Case B $M_{\rm B}$. We found a power law of the form

$$\frac{M_{\rm AB}}{M_{\rm B}} = 1 - a \cdot \left(\frac{P_{\rm ini}}{\rm d}\right)^b \tag{4.4}$$

well fitting. We find $(a,b) = (0.841 \pm 0.007, -1.253 \pm 0.007)$ for the LMC and $(a,b) = (0.657 \pm 0.008, -1.487 \pm 0.016)$ for the SMC. The root mean square relative deviation between data and fit are 3% and 4% for LMC and SMC. The maximum relative deviation has relative high values of 15% and 24%. They can be explained with the neglection of mass dependence and the wavy structure in the period dependence (consider e.g. the purple sequence in Fig. 4.1, bottom). For the SMC data the deviation is so strong as they do not fall so well on a single curve due to the jump between post-Case B mass and highest post-Case AB mass. The fit is shown in Fig. 4.1 (bottom) in grey.

Finally, we give a fit for the relative increase in core hydrogen burning lifetime $t'_{\rm MS}/t_{\rm MS}$ again in form of a power law

$$\frac{t'_{\rm MS}}{t_{\rm MS}} = 1 + a \cdot \left(\frac{P_{\rm ini}}{\rm d}\right)^b. \tag{4.5}$$

We found $(a, b) = (1.003 \pm 0.010, -2.779 \pm 0.011)$ for the LMC and $(a, b) = (0.577 \pm 0.005, -2.741 \pm 0.015)$ for the SMC best fitting. The root mean square relative deviation between data and fit are 0.6% and 0.7% and the maximum relative deviation has values of 5% and 7% for LMC and SMC. The latter is impacted by the three outliers around $P_{\mathrm{ini}} \approx 10^{0.3}$ d. A visual inspection of the fit in Fig. 4.3 (bottom, grey line) shows that it does not trace the mass dependence perfectly, i.e. that donors with lower initial mass reach unity at lower orbital periods, but such small deviations can safely be disregarded.

The fits for the post-Case AB mass and the lifetime increase are independent of initial donor mass. This suggests that our results may be applicable outside of the considered donor mass range. To test that, we compared our fits to additional detailed models. For the LMC we used models from the extensions of the LMC grid by Pauli et al. (2022), and for the SMC models of our grid outside of the adopted mass range. We show in Table 4.2 the parameters of the models and compare the outcomes of Case A. We find that the typical deviation between fit and detailed model is less then 10%. Only the lifetime of the $5M_\odot$ SMC model and the post-Case AB mass of the $70M_\odot$ LMC model deviate more than that. The typical deviation is comparable with the deviations within the analysed models in Sect. 4.3.1 and thus we conclude that our fits are also applicable outside of their original mass range, at least as long the models have similar structure (i.e. a convective core and a radiative envelope).

Table 4.2: Test of our fits against models outside the used mass range ($10M_\odot$ to $40M_\odot$). Columns 6 and 7 give the post-Case AB mass and the hydrogen burning lifetime from the detailed models, while columns 8 and 9 show the results of our fits (eq. 4.4 and 4.5) calculated from columns 1 to 5. The first two models are with LMC metallicity, the other with SMC metallicity.

$M_{\mathrm{ini}}/M_\odot$	q_{ini}	$P_{\mathrm{ini}}/\mathrm{d}$	$M_{\mathrm{B}}/M_\odot$	$t_{\mathrm{MS}}/\mathrm{a}$	$M_{\mathrm{AB}}/M_\odot$ (detailed models)	$t'_{\mathrm{MS}}/\mathrm{a}$ (detailed models)	$M_{\mathrm{AB}}/M_\odot$ (our fit)	$t'_{\mathrm{MS}}/\mathrm{a}$ (our fit)
50	0.7	$10^{0.45}$	28	$4.5 \cdot 10^6$	22	$4.6 \cdot 10^6$	22	$4.8 \cdot 10^6$
70	0.65	$10^{0.55}$	45	$3.7 \cdot 10^6$	32	$3.8 \cdot 10^6$	37	$3.8 \cdot 10^6$
5.0	0.85	$10^{0.3}$	1.3	$1.0 \cdot 10^8$	1.0	$1.8 \cdot 10^8$	1.0	$1.1 \cdot 10^8$
6.3	0.8	$10^{0.125}$	1.8	$6.1 \cdot 10^7$	0.9	$8.2 \cdot 10^7$	1.0	$7.8 \cdot 10^7$
6.3	0.8	$10^{0.425}$	1.8	$6.1 \cdot 10^7$	1.5	$6.2 \cdot 10^7$	1.5	$6.3 \cdot 10^7$
50	0.7	$10^{0.55}$	29	$4.5 \cdot 10^6$	26	$4.6 \cdot 10^6$	26	$4.6 \cdot 10^6$
50	0.7	$10^{0.7}$	29	$4.5 \cdot 10^6$	27	$4.5 \cdot 10^6$	27	$4.5 \cdot 10^6$
80	0.7	10^1	56	$3.5 \cdot 10^6$	52	$3.5 \cdot 10^6$	55	$3.5 \cdot 10^6$

4.4 Discussion

4.4.1 Impact of the initial mass ratio and the accretion efficiency

We have see in Sect. 4.3.1, that the post-Case AB mass and the duration of Case A mass transfer are nearly independent of the initial mass ratio (Fig. 4.1 top panels and Fig. 4.3 middle panels). This result is further reinforced by the small deviation between data and fits in Sect. 4.3.2, since the fits do not consider the initial mass ratio and are still very good. We can explain the insensibility of our results to the initial mass ratio by considering each of the three phases of the RLO individually. The onset of interaction at a fixed orbital period happens more or less at the same donor radius, and thus donor age, nearly independent of mass ratio (about a factor of 2 in orbital period over the relevant regime, Eggleton, 1983; Marchant and Bodensteiner, 2023). The end of the first fast phase of mass transfer is determined by the interplay between the radius evolution of the donor star and the evolution of its Roche radius. The former is a question of stellar physics and the latter mainly depends on the orbital period and is again only a weak function of mass ratio. This is in opposition to Giannone et al. (1968), who predicted larger mass loss from the donor for smaller initial mass ratios (their fig. 6 in particular). The slow Case A phase is determined by the nuclear evolution of the donor star, on which the accretor star has no impact. Finally, in Case AB mass transfer, which is very similar to Case B, the donor loses mass until its helium core ignites on which the companion has also no impact. All this is in agreement with fig. F.3 to F.5 of Sen et al. (2022).

It may appear that our model grid has the shortcoming that we lose generality by assuming a certain mass transfer evolution during RLO. As the secondary star accretes matter until it reaches critical rotation, tidal forces cause a wide range of mass transfer efficiencies (Sen et al., 2022, fig. F.2). The mass transfer efficiency controls the orbital evolution of the binary through the scheme of isotropic re-emission (Soberman et al., 1997) and thus the size of the donor's Roche lobe. Thus one wonder whether our results are only valid for these assumptions. It turns out however, that the accretion efficiency only has a limited effect on the outcome of Case A mass transfer. Consider the $40M_\odot$ models of the LMC grid. They show a clear structure in accretion efficiency (Sen et al., 2022, fig. F.2). When we consider an initial period of $10^{0.6}$ d, we find for an initial mass ratio of 0.9 an overall accretion efficiency of about 80%, and for an initial mass ratio of 0.55 an accretion efficiency of 30%. Yet in both cases the donor mass after the mass transfer about $18M_\odot$ ($18.6M_\odot$ for the first and $17.5M_\odot$ for the latter), which is a strong indication that the accretion efficiency is a subdominant factor. In fact, it turns out, that in Fig. 4.1 (top) the slightly larger interquartile range due to different initial mass ratios in the mid-period regime is caused by the transition from high to low accretion efficiency. (Compare the periods with a larger interquartile range to fig. F.2 of Sen et al. (2022).) This should also cause the light wiggle in the model data in e.g. Fig. 4.1 around a period of about $10^{0.5}$ d. Hence we can quantify the impact of varying accretion efficiency and argue that its effect is small for the whole of both model grids.

4.4.2 Metallicity dependence

In Sect. 4.1, we have found that the exponent b of the power-law describing the ratio of post-Case A mass to post-Case B mass is smaller for the smaller metallicity. This means that this ratio increases slower with initial orbital periods for the smaller metallicity. However, the smaller offset a in the power-law causes the curve of the smaller metallicity to lie on top of the other in the considered period range. Therefore we conclude that the donor mass after Case A compared with the mass after Case B is larger for smaller metallicities, given the same initial orbital period, and thus models with Galactic metallicity might be even lighter after Case A mass transfer. This can be qualitatively understood by the fact that donor radii at zero-age main-sequence are larger and at higher metallicities and will fill their Roche lobe earlyer during hydrogen burning. Thus they deviate stronger from Case B evolution.

For the increase in the core hydrogen burning lifetime, we found for both metallicities about same exponent in the power-law fit, namely about -2.8, and that the offset a is larger for the larger metallicity. Therefore the lifetime increase for the same initial orbital period is larger for the larger metallicity. This fits with the smaller post-Case AB mass for the larger metallicity. Again, we can extrapolate to Galactic metallicity and expect an even stronger lifetime increase.

4.4.3 Other work

The models we analysed in this work were already compared to observations. Sen et al. (2022) analysed LMC and Milky Way Algol binaries, which are believed to be a product of Case A mass transfer, with the LMC grid and found a good agreement. Sen et al. (2023) used an extension of the LMC grid by Pauli et al. (2022) to explain so called revered Algols in the Tarantula Nebula. Wang et al. (2020), Wang et al. (2022) and Wang et al. (2023) found a good agreement of their SMC models with the morphology of Hertzsprung-Russell diagrams, in which systems in slow Case A mass transfer contribute to an extended main-sequence turnoff and blue stragglers.

To calculate the outcome of Case AB mass transfer, several schemes have been adopted in the literature. The BSE-code (Hurley et al., 2002) and its derivatives `binary_c` (Izzard et al., 2004; Izzard et al., 2006, 2009; Schneider et al., 2015) and COMPAS (Stevenson et al., 2017; Riley et al., 2022) determine the post-Case AB donor mass by removing the minimal mass necessary to keep the donor within its Roche-lobe. This process seems to be based on single star models which neglects the more complex structure (in particular the large helium enriched layer) of a model undergoing Case A mass transfer. Romero-Shaw et al. (2023) proposed a simple approximation for the post-Case AB donor mass by multiplying the post-Case B donor mass by the relative age of the donor at the beginning of mass transfer. We show in Fig. C.1, that their method can lead to mismatches of up to 60%. Giannone et al. (1968) follows a more sophisticated approached using generalised main-sequences (stationary models with a particular total mass, central helium abundance and core mass). However, their figure 6 shows a clear dependency of the donor mass after fast Case A on the initial mass ratio, which is in contradiction with our results from detailed models. The ComBinE-code of Kruckow et al. (2018) use the same approach as for Case B to evaluate Case A. They assume that the donor is reduced to its helium core mass. We show in this work that this assumption can be inaccurate to varying degrees, as for core hydrogen burning models, no helium core can be defined and therefore rely on the helium mass in the convective core. For the duration of Case A they use the thermal timescale, which strongly underestimates its real duration.

4.5 Conclusions and outlook

In this study we analysed large grids of detailed massive binary evolution models to provide simple recipes for the donor mass after Case AB mass transfer and for the duration of Case A mass transfer. We found that these two quantities are nearly independent of the initial mass ratio of the binary. For the post-Case AB donor mass relative to the post-Case B donor mass, and for the ratio of core hydrogen burning lifetime compared to that of a single star, we found that power laws (Eq. 4.4 and 4.5) describe the models well. The main sequence lifetime of Case A donors exceed that of single stars or Case B donors of the same initial mass by up to 30%. This extension depends on the initial orbital period, but is insensitive to the initial donor mass (Fig. 4.3, bottom). The donor mass after Case AB can be up to 50% smaller than after a corresponding Case B mass transfer (Fig. 4.1, bottom). We predict lighter donors after mass transfer and a larger lifetime increase at higher metallicities for given initial orbital periods. We found that our results are independent of the employed mass transfer efficiency, and found evidence that our results are also valid outside the considered mass range.

The significance of these corrective effect of our new method will be strongly dependent on the specific considered binary population. It will naturally be pronounced for a predicted Algol population, as these objects are undergoing slow Case A mass transfer which is usually neglected in rapid binary evolution codes. While the overall supernova rate in the nearby Universe is perhaps not significantly affected, the occurrence of these events will be delayed by up to 30% due to the longer core hydrogen burning time and a longer lifetime of the lighter stripped donor.

The predicted lower donor masses may have an even stronger effect, in particular for initial orbital period distributions which are skewed towards short initial orbital periods. As favoured by the initial mass function, of all supernova progenitors our mass correction will strongly affect that part of the parameter space where most neutron stars are born. Even donor stars with initial masses as high as $16M_{\odot}$ may form white dwarfs (Wellstein et al., 2001). In essence, the number of electron capture supernovae will be reduced. The same applies to black holes, but the vicariously generated neutron stars will not compensate the loss to white dwarfs. Consequently, the number of high mass X-ray binaries is expected to decrease, but only for super-giant X-ray binaries which reside in close orbits, in contrast to Be/X-ray binaries which tend to be the outcome of Case B evolution. The corrected mass of the supernova progenitor might affect the predicted neutron star birth kick which may change the fate of the binary. The impact on the predictions for gravitational wave sources is non-trivial, but the reduced donor masses could lead to less stellar remnant mergers.

While the qualitative effects of Case A mass transfer are described in the literature, this work quantifies them such that they can be implemented into rapid binary population synthesis codes. They can be used to update the predictions of gravitational wave event rates for different classes of stellar remnants, and they could also be important for the predicted number of double white dwarf binaries in the Milky Way that LISA can detect. In a forthcoming paper we will use our recipe in a rapid binary population synthesis of the post-mass transfer massive star population of the SMC.

Acknowledgements. PM acknowledges support from the FWO senior postdoctoral fellowship No. 12ZY523N. KS was funded by the National Science Center (NCN), Poland under grant number OPUS 2021/41/B/ST9/00757.

CHAPTER **5**

Exploring the boundary between stable mass transfer and L_2-overflow in close binary evolution

C. Schürmann[1] and N. Langer[1,2]

[1] Argelander-Institut für Astronomie, Universität Bonn, Auf dem Hügel 71, 53121 Bonn, Germany
[2] Max-Planck-Institut für Radioastronomie, Auf dem Hügel 69, 53121 Bonn, Germany

Submitted to *Astronomy & Astrophysics*. (At the time of publication of this thesis, this chapter is published as Schürmann and Langer (2024), *Astronomy & Astrophysics* **691** A174, DOI 10.1051/0004-6361/202450354.)

Author contributions. CS computed the stellar models, analysed them and wrote the first draft. NL helped to interpret the results and reviewed the draft.

Abstract

The majority of massive stars reside in binary systems, which are expected to experience mass transfer during their evolution. However, so far the conditions under which mass transfer leads to a common envelope, and thus possibly to a merging of both stars, are not well understood. Main uncertainties arise from the possible swelling of the mass gainer, and from angular momentum loss from the binary system, during non-conservative mass transfer. We have computed a dense grid of detailed models of stars accreting mass at constant rates, to determine their radius increase due to their thermal disequilibrium. While we find that models with faster than thermal timescale accretion generally expand, this expansion remains quite limited in the intermediate mass regime even for accretion rates which exceed the thermal timescale accretion rate by a factor of 100. Our models of massive accretion stars expand to extreme radii under those conditions. When the accretion rate exceed the Eddington accretion rate, our models expand rapidly. We have derived analytical fits to the radius evolution of our models and a prescription for the boundary between stable mass transfer and L_2-overflow for arbitrary accretion efficiencies. We then apply our results to grids of binary models adopting various constant mass transfer efficiencies and angular momentum budgets. We find that the former parameter has the stronger effect on the outcome of the Roche lobe overflow. Our results are consistent with

detailed binary evolution models, and often lead to a smaller initial parameter space for stable mass transfer than other recipes in the literature. We use this method to investigate the origin of the Wolf-Rayet stars with O star companions in the Small Magellanic Cloud, and find that the efficiency of the mass transfer process which lead to the formation of the Wolf-Rayet star was likely below 50%.

Key words. stars: evolution – binaries: general – binaries: close – stars: massive – stars: Wolf-Rayet

5.1 Introduction

Binary stars play a key role in stellar physics, since most massive stars, which enrich the universe with elements and shape star forming galaxies by their energy output, are part of a binary system (Vanbeveren et al., 1998; Sana et al., 2012; Moe and Di Stefano, 2017), which may lead to powerful phenomena like X-ray pulsars (Tauris and van den Heuvel, 2006) and gravitational wave events (Tauris and van den Heuvel, 2023). Interacting binaries are an important site of stellar nucleosynthesis (de Mink et al., 2009b; Margutti and Chornock, 2021) and those of low mass are possible progenitors of Type Ia supernovae, which are essential for mapping the Universe (Riess et al., 1998; Schmidt et al., 1998; Perlmutter et al., 1999).

Close binaries will sooner or later interact (Sana et al., 2012), but what the outcome is when one component fills its Roche lobe is still under debate (Langer, 2012; Marchant and Bodensteiner, 2023). A Roche-lobe overflow (RLO) where material is transferred steadily from one star to the other (e.g. Kippenhahn and Weigert, 1967) is believed to lead to a stripped star in form of a hot sub-dwarf (Bodensteiner et al., 2020a; Shenar et al., 2020a) or a Wolf-Rayet (WR) star (Langer, 1989; Wellstein et al., 2001) and a mass gainer which was spun up to fast rotation if the tides are negligible (de Mink et al., 2013; Wang et al., 2020), observable as a Be star (Rivinius et al., 2013). If the RLO is dynamical unstable or the two components evolve into contact, a common envelope is formed which may be ejected (Kruckow et al., 2016) or drives the system towards a stellar merger (Ivanova et al., 2013; Schneider et al., 2019). Even if such a scenario is avoided, it is unclear how much of the material lost by the donor star is accreted by its companion (de Mink et al., 2007) and how much angular momentum the ejected material drains from the system (Soberman et al., 1997).

Several studies in the literature address these questions. A classical approach is to determine the mass-radius exponent of stellar models, which was done by e.g. Hjellming and Webbink (1987) for polytropes, and for more realistic stellar models by Hjellming (1989a) and Hjellming (1989b) and most recently by Ge et al. (2010, 2015, 2020). Wellstein et al. (2001) examine the formation of contact in conservative detailed binary evolution models. Langer et al. (2020), Wang et al. (2020) and Sen et al. (2022) determine the accretion efficiency by letting the accretor take on mass until it reaches critical rotation and use an energy criterion to determine the outcome of a RLO.

Kippenhahn and Meyer-Hofmeister (1977) and Neo et al. (1977) showed that the accretor expands if the inflow of matter is too fast (see also Ulrich and Burger, 1976; Flannery and Ulrich, 1977; Packet and De Greve, 1979; Fujimoto and Iben, 1989). If this expansion is large enough that the accretor also fills its Roche-lobe, one expects the formation of a common envelope, and after further expansion that material leaves the binary at the second Lagrange point (L_2-overflow), which is expected to lead to the merger of the two stars as the expelled material drains a large amount of angular momentum from the system (Nariai and Sugimoto, 1976). Pols et al. (1991) inferred from the work of Kippenhahn and Meyer-Hofmeister (1977) that the accretor does not expand significantly as long as its accretion rate remains smaller than ten times its thermal timescale accretion rate. This approach is commonly used in many binary population studies (e.g. Hurley et al., 2002; Shao and Li, 2014, 2016; Vigna-Gómez et al., 2018; van Son et al., 2022), where the mass gain of the accretor is often limited by the thermal timescale accretion rate when the mass transfer rate exceeds this value (see

Portegies Zwart and Verbunt (1996) and Toonen et al. (2012) for a more detailed approach). Other works do not consider the reaction of the accretor, and adopt more ad hoc merger criteria (e.g. Belczynski et al., 2002, 2008; Kruckow et al., 2018).

In the last decades powerful codes like the one of Eggleton (1971, 1972), Eggleton et al. (1973) and Eggleton (1973), BEC (Heger et al., 2000; Yoon et al., 2006; Brott et al., 2011), the Brussels codes STAREVOL and BINSTAR (Siess et al., 2000; Palacios et al., 2006; Siess, 2006; Siess and Arnould, 2008; Davis et al., 2013; Deschamps et al., 2013; Siess et al., 2013), and MESA (Paxton et al., 2011, 2013, 2015, 2018, 2019) were developed for the detailed modelling of both single and binary stars. However, even today it is still a large effort to model a complete stellar population with these one-dimensional approaches. Therefore rapid population synthesis codes have been developed, which approximate the evolution of binary systems either by analytic fits (e.g. Hurley et al., 2002) or by interpolation of precalculated single star models (e.g. Kruckow et al., 2018). Thus, it is one aim of this study to provide a practical and efficient method to determine the outcome of a RLO without the need for detailed modelling.

Our study consists of two parts. In Sect. 5.2, we analyse a generic set of accreting detailed single star models to find an accurate and practical description of their radius evolution, as function of the relevant parameters. The second part (Sect. 5.3) is dedicated to the application of our results to grids of binary models, which we also compare to observation. Throughout the paper, we will compare our simplified models with detailed binary evolution models.

5.2 Accretion on main-sequence stars

5.2.1 Method

We calculated detailed single-star models of Small Magellanic Cloud (SMC) metallicity with initial chemical compositions as in Brott et al. (2011, their tables 1 and 2, i.e. $Z_{\rm SMC} = 0.0021$) and custom-built OPAL opacities (Iglesias and Rogers, 1996) in line with these abundances. The initial masses $M_{\rm i}$ of the models are 1, 1.5, 2, 3, 5, 7, 10, 15, 20, 30, 50, 70, and $100 M_\odot$, and we assumed various constant accretion rates $\dot{M}$ (see Fig. 5.1 top, D.1, and D.2), using MESA version 10108 (Paxton et al., 2011, 2013, 2015, 2018). We applied the Ledoux criterion for convection and used standard mixing-length theory with $\alpha_{\rm ml} = 1.5$. We followed Schootemeijer et al. (2019) and Hastings et al. (2021) and used semiconvection with $\alpha_{\rm sc} = 10$ and a mass-dependent step-overshooting. We assume thermohaline mixing following Cantiello and Langer (2010) with $\alpha_{\rm th} = 1$. We simplify our models by treating them as non-rotating. After the stellar models have relaxed onto the main-sequence, they are subjected to a constant accretion of material that carries the same entropy as the model's uppermost mass shell. We let the models accrete until they have quintupled in mass, at which point we terminate the calculations.

5.2.2 Results

Behaviour of accreting main-sequence star models

We show the tracks of our $5 M_\odot$-models in the Hertzsprung–Russell diagram (HRD) in Fig. 5.1 (top), which are typical for our model grid. We have indicated the different adopted accretion rates by colour. The corresponding diagram for the other initial masses are given in Fig. D.1 and D.2. In the bottom panel we show the radius evolution as a function of the models' mass M up to its maximum radius.

The stellar models with the lower accretion rates follow a common pattern. At the onset of accretion they briefly evolve to the left of the zero-age main-sequence (ZAMS) as a hydrodynamic response to the accretion

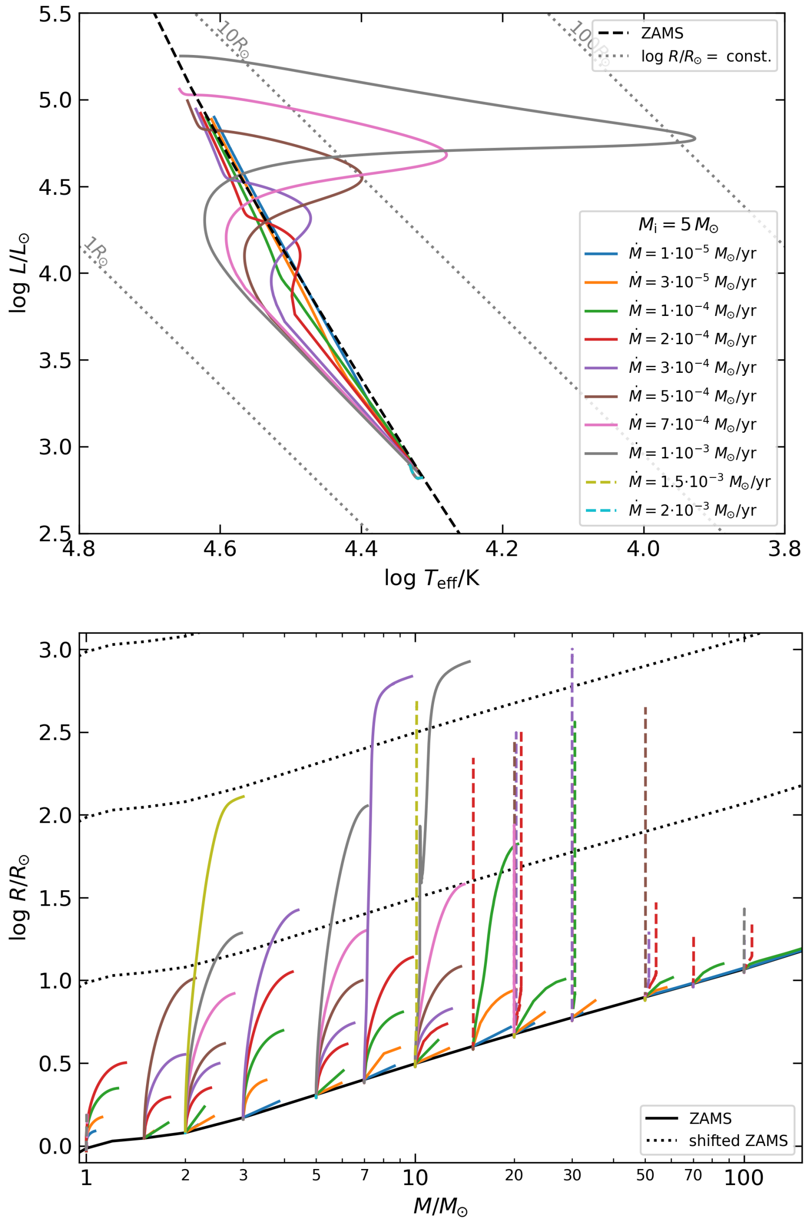

Figure 5.1: Evolution of our accreting single star models. Top: Evolution of the $5M_{\odot}$-models in the HRD for different accretion rates (indicated by colour). Stably swelling models are shown with solid lines and unstable models with dashed lines. We also show the ZAMS (black) and various lines of constant radius (grey). Bottom: Radius of accreting models as a function of mass. For each initial mass the colours are the same as in the corresponding HRDs (top panel, Fig. D.1 and D.2). Models that become unstable are indicated by dashed lines. Some are so short that they are hardly visible. The ZAMS radius is shown in black.

only to rapidly increase their radius R thereafter (unless for the smallest accretion rates). The increase in radius is larger for higher accretion rates. After reaching a maximum radius $R_{\max}$ at a mass $M_{R=R_{\max}}$ the models contract again towards the ZAMS. From there they evolve along the ZAMS as they still accrete material. We call these models stable models or models with stable swelling.

The two models with the highest accretion rates of Fig. 5.1 (top, yellow and cyan lines) show a different evolution from the stable models, as their lines so short that they are barely visible in the two plots. In fact, these models barely accrete any mass and terminate shortly after the onset of the accretion due to numerical problems, as the time step becomes unreasonably small. We call these models unstable models or models with unstable swelling.

We observe the same patterns for the models of other masses (Fig. D.1 and D.2). The larger the accretion rate, the larger is the maximum radius of the models, and beyond a certain accretion rate the models terminate due to numerical problems. For initial masses above $10 M_\odot$, the unstable models show a large increase in radius before they terminate (Fig. 5.1, bottom, dashed lines). This extends the interpretation of the unstable models to the description that, above a certain accretion rate, a small increase in mass causes the star to expand by a very large amount. Consider, for instance, the models with an initial mass of $15 M_\odot$ in Fig. 5.1 (bottom). From $1 \cdot 10^{-3}\, M_\odot/\mathrm{yr}$ (blue) to $3 \cdot 10^{-3}\, M_\odot/\mathrm{yr}$ (green) the swelling becomes stronger, but at an accretion rate of $6 \cdot 10^{-3}\, M_\odot/\mathrm{yr}$ (red) the mass-radius-curve becomes nearly vertical. Furthermore, for initial masses above $10 M_\odot$ we find that with increasing mass a stable radius increase becomes less possible, and from $30 M_\odot$ on the models either accrete stably along the ZAMS or become unstable.

Between the stable and unstable regimes we find three borderline models: $2 M_\odot$ with $\dot{M} = 2 \cdot 10^{-4}\, M_\odot/\mathrm{yr}$, $7 M_\odot$ with $\dot{M} = 2 \cdot 10^{-3}\, M_\odot/\mathrm{yr}$, and $10 M_\odot$ with $\dot{M} = 2.5 \cdot 10^{-3}\, M_\odot/\mathrm{yr}$. These models have in common (in contrast to the other stable ones) that they reach their maximum radius as red (super) giants, and that their tracks in the HRD depict a lower curvature at maximum radius. In Fig. 5.1 (bottom) we see that the three borderline models reach the largest radii of all stable models of the same initial mass, and show a plateau in this. We assume that the unstable models would show the same behaviour as the borderline models if they could be calculated further, which is supported by the binary models presented in Sect. 5.2.3.

We can understand whether a model accretes stably or not by considering the Eddington accretion rate, given by

$$\dot{M}_{\mathrm{Edd}} = \frac{4\pi c R}{\kappa}, \tag{5.1}$$

where c is the speed of light, R is the stellar radius and κ the opacity (Webbink, 1985; Tauris and van den Heuvel, 2023). By assuming $R \propto M^{0.6}$, which fits our ZAMS models well (Kippenhahn et al., 2013) and $\kappa = 0.34\,\mathrm{cm^2/g}$, which is a good approximation for $M > 10 M_\odot$, we find

$$\dot{M}_{\mathrm{Edd}} \approx \left[1.2 \cdot 10^{-3}\, M_\odot/\mathrm{yr}\right] \cdot \left(\frac{M}{M_\odot}\right)^{0.6} \tag{5.2}$$

In Fig. 5.2 we show the initial mass and the adopted accretion rate of our models. The blue continuous line shows the Eddington accretion rate and the dashed line assumes an opacity of twice the electron-scattering value, which approximates the total opacity in the outer envelope of our models. The latter matches well to the boundary between the stable and the unstable models. This means, that our models become unstable if the accretion rate exceeds the Eddington accretion rate of the accretor. This may be so because the material at the surface of a star close to its Eddington limit is barely bound. Sanyal et al. (2015, 2017) found that such stars can inflate to large radii, and therefore it appears likely that they are pushed close to their Hayashi line (see Sect. 5.2.3 and 5.3.1).

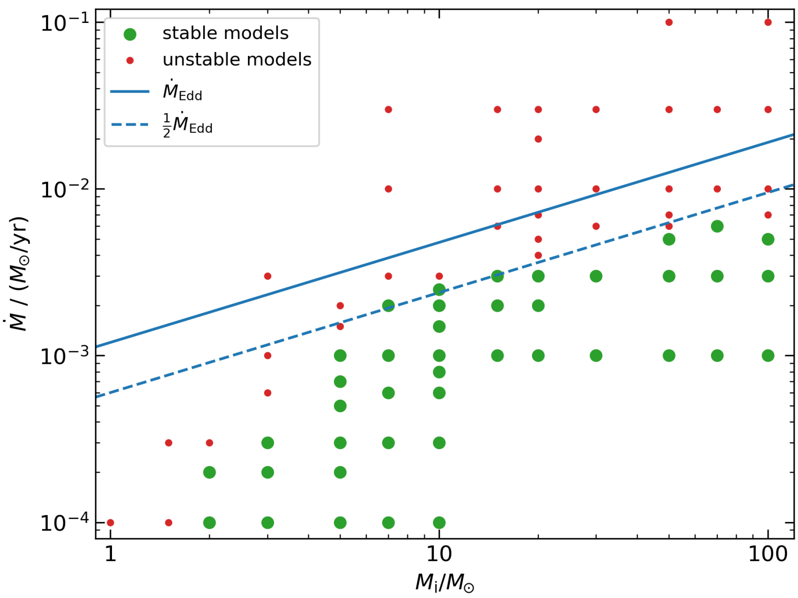

Figure 5.2: Initial mass and adopted accretion rate for our stable (green) and unstable (red) models. Not all models are shown as we focus on the boundary between stable and unstable models at high masses. The blue lines indicate the Eddington accretion rate assuming electron-scattering opacity.

Analytic fits

To provide a description of the response of the stellar models to accretion, Fig. 5.3 shows a synopsis of our models. We express the accretion rate in terms of the logarithmic ratio

$$t = \log \frac{\tau_{\rm KH}}{\tau_{\dot{M}}} \tag{5.3}$$

of the thermal timescale $\tau_{\rm KH}$ and the mass gain timescale $\tau_{\dot{M}}$ at the onset of accretion, which are defined as

$$\tau_{\rm KH} = \frac{3GM^2}{4RL}, \tag{5.4}$$

$$\tau_{\dot{M}} = \frac{M}{\dot{M}}, \tag{5.5}$$

where L is the luminosity and G is the gravitational constant (Hansen et al., 2004; Kippenhahn et al., 2013). We find that the boundary between stable and unstable models can be described by two simple lines, which are given by

$$t_{\rm max} = \begin{cases} 1.65 + 3\log(M_{\rm i}/M_\odot), & M_{\rm i} < 2M_\odot \\ 3 - 1.5\log(M_{\rm i}/M_\odot), & M_{\rm i} > 2M_\odot. \end{cases} \tag{5.6}$$

For masses above $2M_\odot$ we find that our models become more unstable with increasing initial mass. Models below that show the opposite trend. Also, the closer a model of a given initial mass is to the boundary, the larger is its maximum radius. For a fixed t, the maximum radius is minimal around $M_{\rm i} = 2M_\odot$. Near the boundary,

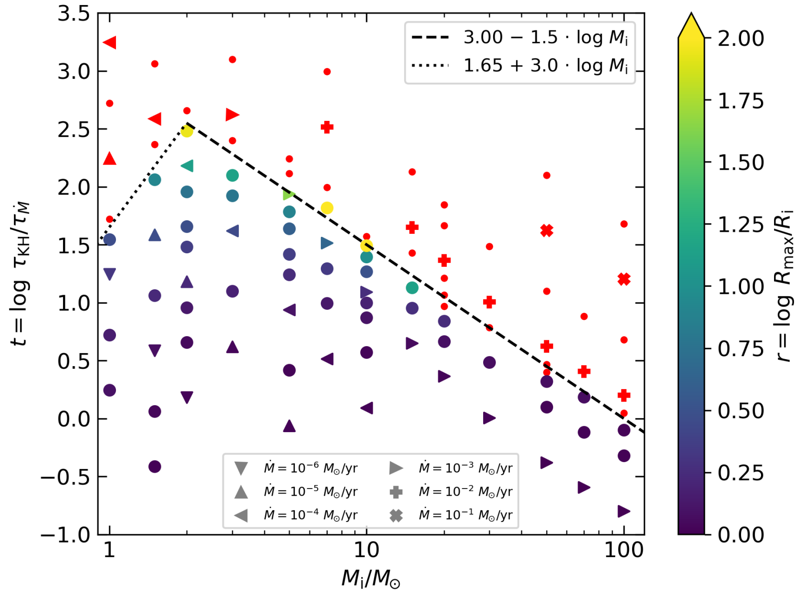

Figure 5.3: Maximum radius of accreting models as a function of initial mass and the ratio of thermal and mass transfer timescales. Unstable models are shown in red. Special symbols are used for selected accretion rates. The two black lines distinguish between stable and unstable models.

Table 5.1: Parameters found for Eq. 5.7 and 5.8 as well as the root-mean-square relative deviation δ_{rms} and the maximum relative deviation δ_{max}.

	Eq. 5.7	Eq. 5.8
a	5.44 ± 0.53	0.0709 ± 0.0149
b	2.38 ± 0.27	0.185 ± 0.011
c	–	1.028 ± 0.020
δ_{rms}	0.62	0.04
δ_{max}	1.98	0.11

the maximum radii are up to 100 times larger than the ZAMS radii. For models with $t = \log \tau_{KH}/\tau_{\dot{M}} < 0$ the swelling is negligible.

In order to incorporate our results into a rapid binary population synthesis code, we fitted simple functions to the logarithmic radius increase $r = \log R_{max}/R_i$ and the mass increase to reach the maximum radius $m = M_{R=R_{max}}/M_i$ as functions of the initial mass M_i and the logarithmic timescale ratio t. For the function r we require that $r(t = 0) = 0$ and that it reaches values of 2 at the boundary towards the unstable models, which roughly corresponds to the radius increase of the three borderline models (1.9, 2.3, 2.3). While a systematic search for the mass dependent borderline accretion rate is possible, the exact value is not important for practical applications.

We find a good fit for R_{max} with the function

$$r(\log M_i, t) = 2 \cdot \frac{\exp\left[(a \log M_i + b)\frac{t}{3-1.5\log M_i}\right] - 1}{\exp\left[a \log M_i + b\right] - 1}, \quad 0 < t < t_{max}, \tag{5.7}$$

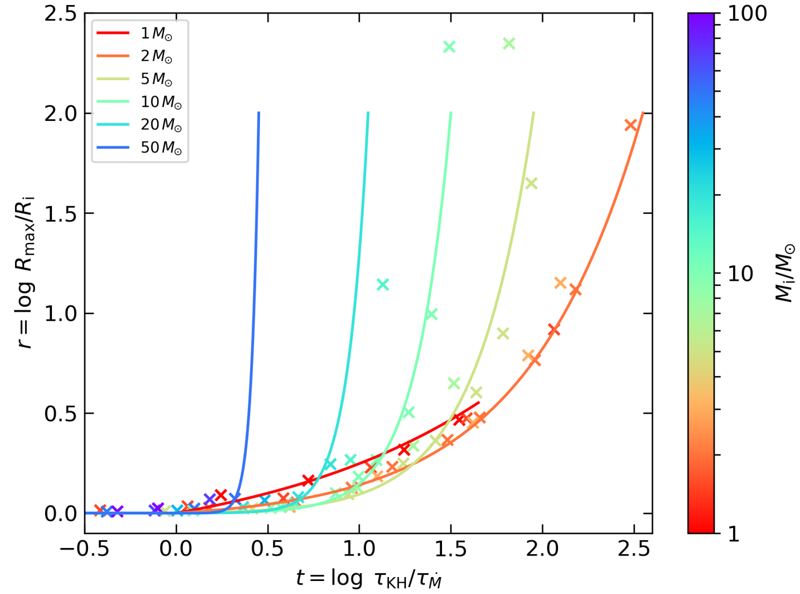

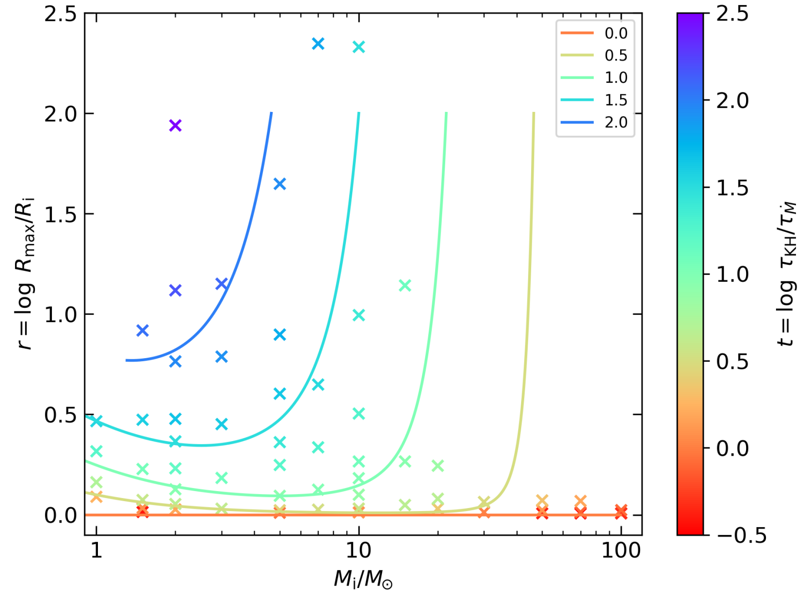

Figure 5.4: Logarithmic radius increase r of accreting models as a function of initial mass and the ratio of thermal and mass transfer timescale together with our fit (lines) for selected initial masses (top) and for selected timescale ratios (bottom).

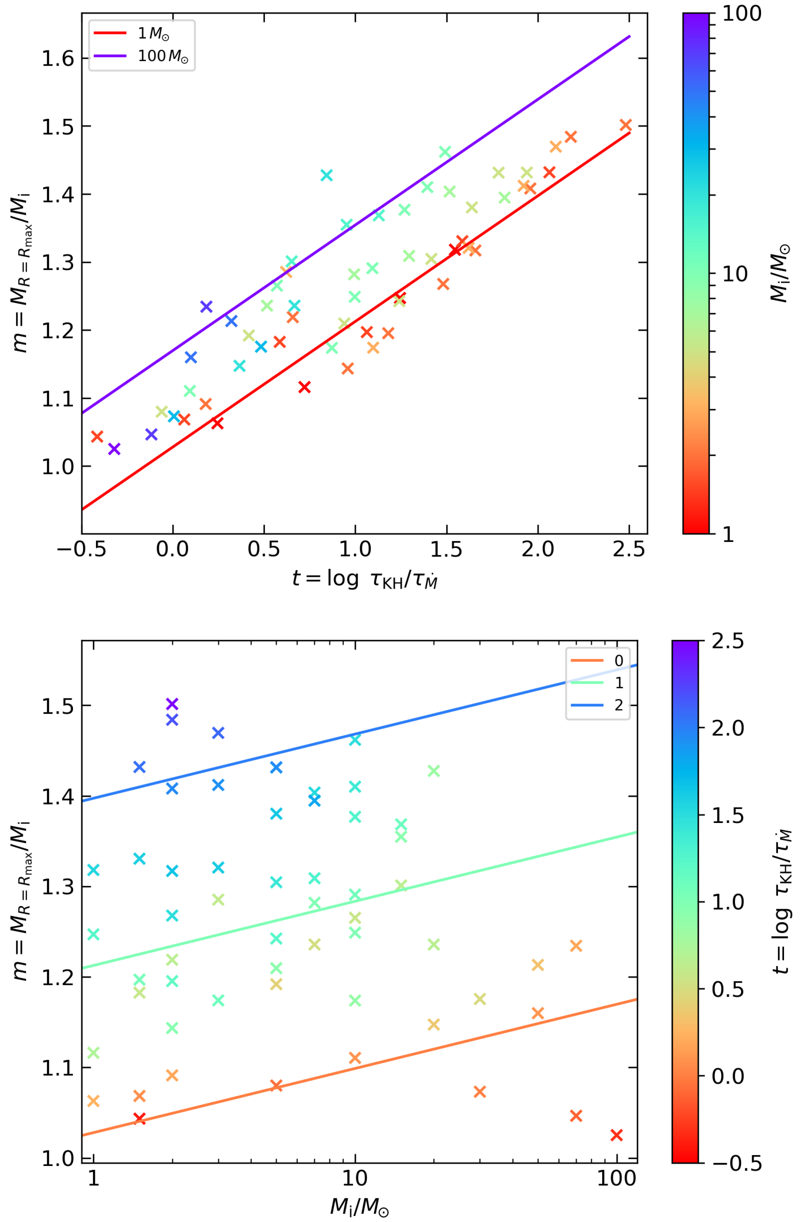

Figure 5.5: Mass at which accreting models reach their largest radius as a function of initial mass and the ratio of thermal and mass-transfer timescale together with our fit for selected initial masses (top) and for selected timescale ratios (bottom).

with the parameters a and b given in Table 5.1. Note that t is not divided by t_{max} as in Eq. 5.6, but only by the second line of the formula. We show the values of the detailed models as well as our fit function in Fig. 5.4. The data and the fit are in good agreement, as the root-mean-square relative deviation[1] and the maximum relative deviation of R_{max} and $M_{R=R_{max}}$ are reasonably small (Table 5.1).

For the mass at the maximum radius, we find the linear function given by

$$m(\log M_i, t) = a \log M_i + bt + c, \quad 0 < t < t_{max}, \tag{5.8}$$

fits well. The parameters a, b, c are listed in Table 5.1. The values of the detailed models and the fit are shown in Fig. 5.5.

5.2.3 Discussion

In this section we discuss the uncertainties of our prescription (Sect. 5.2.3) and compare it with detailed binary models (Sect. 5.2.3) and previous works (Sect. 5.2.3).

Uncertainties

In our models we have omitted stellar rotation for simplicity. However, rotation is a ubiquitous phenomenon observed in stars (Maeder and Meynet, 2000; Langer, 2012). It has several effects on stars. First of all, there is the deformation of the stellar surface due to the centrifugal force (e.g. Kippenhahn et al., 2013). This effect can increase the equatorial radius by a factor of up to 1.5. This number is within the uncertainty of our prediction for the accretion induced swelling (Sect. 5.2.2). Moderate rotation does not alter stellar evolution much (Brott et al., 2011; Choi et al., 2016), so the expected corotation in close binaries (de Mink et al., 2009a) and the fast rotating branch of the main sequence (Dufton et al., 2013; Wang et al., 2020) are not affected.

On the other hand it is generally accepted that mass transfer leads to a spin-up of the accretor star to close to critical rotation (de Mink et al., 2013). Packet (1981) showed, that only a small amount of matter is required to spin up the star, if tidal breaking (Zahn, 1977) is not acting. Therefore, the accretors in all but the closest mass transferring binaries can be expected to rotate rapidly (Wang et al., 2020; Sen et al., 2022). Due to the centrifugal force, the equatorial radius of a rapid rotator is increased by up to 50% (Gagnier et al., 2019). While this is a moderate radius increase compared to the accretion induced inflation discussed above, it adds to the uncertainties in the boundary between stable and unstable mass transfer.

It is likely that the mass gainer's accretion rate in mass transferring binaries is not constant but varies with time. For a strongly varying accretion rate, the assumption we will make for Eq. 5.9 would be no longer valid. In the models of Langer et al. (2020), Wang et al. (2020) and Sen et al. (2022), the effective accretion rate varies because it depends on the rotation rate of the mass gainer. A variation of the mass transfer rate may also be induced by the evolution of the Roche lobe radius, even though only mildly so, as the Roche radius varies only weakly with the mass ratio Ge et al. (2015). On the other hand, strong oscillations of the mass transfer and accretion rate appear unlikely, such that focusing on the time interval with the most efficient accretion may yield a valid approximation.

We have assumed that the material arriving at the accretor has the same entropy as its surface. This assumption is justified for accretion rates below the thermal timescale accretion rate, i.e. for $t < 0$ (Eq. 5.3), since in this case any excess energy will be radiated away quickly Paxton et al. (2015). For $t > 0$, the impact of the accretion stream (Ulrich and Burger, 1976; Shaviv and Starrfield, 1988), or boundary layer heating

[1] (fit–data)/data

in the case of disk accretion onto a sub-critically rotating star (e.g. Steinacker and Papaloizou, 2002), may deposit hot material onto the star faster than the extra heat can be drained. The energy released by these processes is related to the gravitational energy gain of the infalling matter (which we neglect), and will thereby be comparable, but not greatly exceeding the energy released by the gravitational compression of the star by the weight of the accreted mass (which we include). We therefore do not expect a qualitative impact of these effects on our results.

Finally, we note that we have explored the effects of accretion on the upper main sequence, and that our results can not be extrapolated into the regime of low mass main sequence stars. Zhao et al. (2024) have shown that low mass main sequence stars with deep convective envelopes, as well as fully convective main sequence stars, undergo in fact shrinkage upon accretion, even for accretion rates which exceed the thermal timescale accretion rate by many orders of magnitude.

Comparison with detailed binary models

To validate our results, we compare our fits with detailed binary models undergoing RLO calculated with MESA (see Sect. 5.2.1). The adopted initial masses and initial periods are listed in Table 5.2. We use the same physical assumptions as in Sect. 5.2.1, and the structure of both binary components is calculated in parallel with the evolution of the orbit. The models are assumed to be non-rotating, as we are not interested in the radius increase due to this effect. We assumed a constant accretion efficiency of $\varepsilon = 50\%$, and that the ejected material carries the specific angular momentum of the accretor (Soberman et al., 1997). We have used the mass transfer scheme `roche_lobe`. To be able to measure the maximum accretor radius, we allow the accretor to overfill its L_2-volume without losing mass or terminating the calculation.

The mass-radius evolution of the accretors with initially $10M_\odot$ is shown in Fig. 5.6 together with estimates according to Eq. 5.7 and 5.8 based on the maximum mass transfer rate of the models (×-symbols). In general we find satisfactory agreement. Typically we miss the maximum radius by no more than a factor of 2. Models #2 (orange) and #3 (green) stay at large and relatively constant radii for a while, similar to the borderline models mentioned in Sect. 5.2.2. They also swell unstably according to Eq. 5.7 and 5.8. Models #4, #8, #12 are not shown because the calculations terminated due to numerical problems (time step limit) shortly after the onset of RLO. Typically, our recipe yields smaller accretor radii than in detailed calculations, making it a rather conservative estimate of L_2-overflow.

There are two main reason for the differences between our approach and the detailed models. Our fitting function (Sect. 5.2.2) is very steep, and thus small uncertainties can lead to large changes in the resulting maximum radius. This could be improved with a denser model grid and a refined fit. Second, the accretion rate imposed by the donor is time dependent and a notable deposition of material on the mass gainer before the maximum mass transfer rate is reached could change our prediction. Considering a time dependent mass transfer rate is beyond the scope of our approach.

Comparison with previous work

Numerical experiments for accreting stars have been carried out by Kippenhahn and Meyer-Hofmeister (1977) and Neo et al. (1977). They arrive at the same qualitative result as our study, namely that the maximum stellar radii increase as the accretion rate increases. If we compare the tracks in our HRDs with those of Kippenhahn and Meyer-Hofmeister (1977, their fig. 1-3) and Neo et al. (1977, fig. 1), we find that the evolutionary tracks of Neo et al. (1977), like ours, intersect each other for a given initial mass, but those of Kippenhahn and Meyer-Hofmeister (1977) do not. On the other hand, we find similarities between both fig. 4 of Kippenhahn

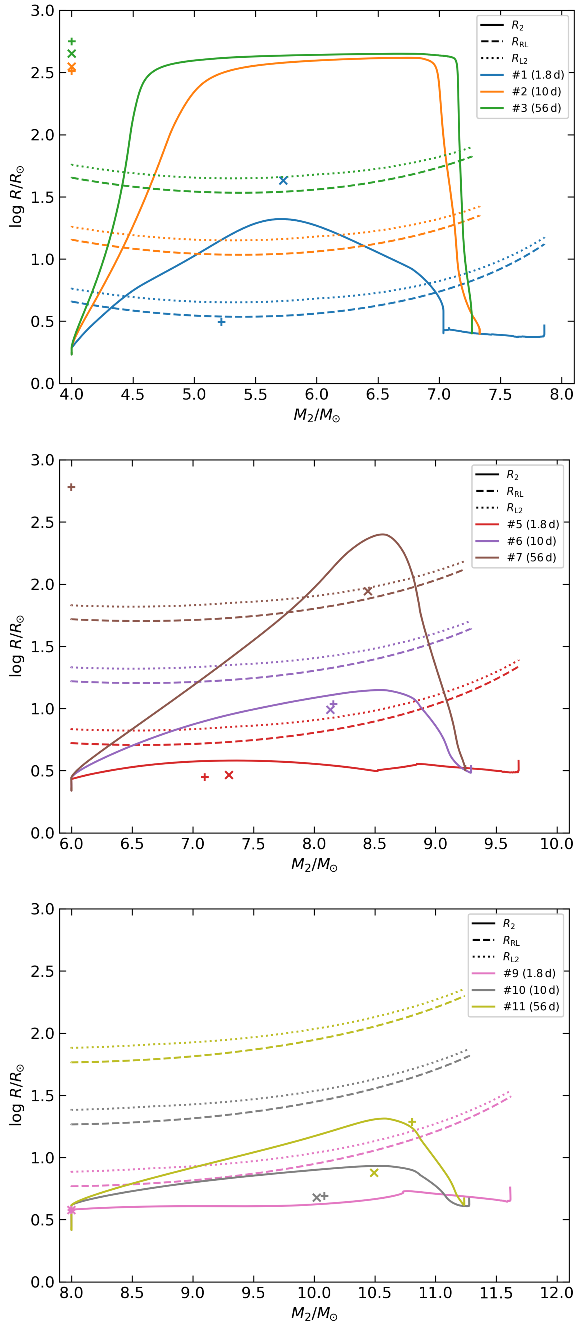

Figure 5.6: Mass-radius evolution (solid line) of detailed accretor models for different initial periods (colour) and initial accretor masses (top $4M_\odot$, middle $6M_\odot$, bottom $8M_\odot$). The donor always has an initial mass of $10M_\odot$. The size of the accretor's Roche-lobe and L_2-sphere are shown as dashed and dotted lines. We have used ×-symbols to indicate the maximum of the mass-radius curve ($R_{\max}, M_{R=R_{\max}}$) according to Eq. 5.7 and 5.8, based on the maximum mass transfer rate of the detailed model. The +-symbols indicate the same, but for an estimate of the mass transfer rate based on the conditions just before the RLO (Eq. 5.9). If a symbol is placed at a high radius but at the initial mass of the model, the model is expected to swell unstably and the radius is the Hayashi radius (see Sect. 5.3.1).

Table 5.2: Initial masses M_{1i} and M_{2i} and initial orbital periods P_i of our detailed binary models and the case of RLO through which they pass. We distringuish between Case B with a donor with radiative (Br) and convective (Bc) envelope. The maximum mass transfer rates of the detailed binary models (ε = 50%) are given as well. We display the outcomes of the RLO according to the detailed binary models (Sect.5.2.3), the radius estimate using the maximum mass transfer rate of the detailed binary models (× in Fig. 5.6), the radius estimate based on Eq. 5.9 (+ in Fig. 5.6), and the outcome from Sect. 5.3.2. We qualify the stability of the swelling and the occurrence of L_2-overflow (L_2O), contact, or neither (donor stripping).

#	$M_{1i}/M_\odot$	$M_{2i}/M_\odot$	P_i/ d	Case	max $\log \dot{M}$/ $M_\odot$/yr	outcome det. model	outcome with $\max(\dot{M})$	outcome with Eq. 5.9	outcome of Sect. 5.3.2
1	10	4	1.8	A	−3.22	stable, L_2O	stable, L_2O	stable, stripping	L_2O
2	10	4	10	Br	−2.92	unstable, L_2O	unstable, L_2O	unstable, L_2O	L_2O
3	10	4	56	Br	−2.71	unstable, L_2O	unstable, L_2O	unstable, L_2O	L_2O
4	10	4	316	Bc	–	no solution	unstable, L_2O	unstable, L_2O	L_2O
5	10	6	1.8	A	−3.82	stable, stripping	stable, stripping	stable, stripping	stripping
6	10	6	10	Br	−3.04	stable, stripping	stable, stripping	stable, stripping	stripping
7	10	6	56	Br	−2.75	stable, L_2O	stable, contact	unstable, L_2O	L_2O
8	10	6	316	Bc	–	no solution	unstable, L_2O	unstable, L_2O	L_2O
9	10	8	1.8	A	−4.30	stable, stripping	stable, stripping	stable, stripping	stripping
10	10	8	10	Br	−3.07	stable, stripping	stable, stripping	stable, stripping	stripping
11	10	8	56	Br	−2.75	stable, stripping	stable, stripping	stable, stripping	L_2O
12	10	8	316	Bc	–	no solution	unstable, L_2O	unstable, L_2O	L_2O
13	30	12	1.8	A	−2.42	unstable, L_2O	stable, L_2O	stable, stripping	stripping
14	30	12	10	Br	−1.96	unstable, L_2O	unstable, L_2O	unstable, L_2O	L_2O
15	30	12	56	Br	−2.24	unstable, L_2O	unstable, L_2O	unstable, L_2O	L_2O
16	30	12	316	Br	−2.18	unstable, L_2O	unstable, L_2O	unstable, L_2O	L_2O

and Meyer-Hofmeister (1977) and fig. 4 of Neo et al. (1977) and our Fig. 5.1 (bottom), not only in shape of the tracks but also in terms of critical accretion rate. Neo et al. (1977) find that an accretion rate greater than $4 \cdot 10^{-3}\,M_\odot/\mathrm{yr}$ is required for a $20M_\odot$ model to be unstable. We find a slightly lower rate of $3 \cdot 10^{-3}\,M_\odot/\mathrm{yr}$. Similarly, for the $5M_\odot$ and the $10M_\odot$ models, we also find slightly lower critical accretion rates compared to Kippenhahn and Meyer-Hofmeister (1977). The differences could be caused by the used opacities, first because the old models did not include the iron-peak opacity and secondly we used a lower metallicity, which also enters the opacity and thus the Eddington limit.

Pols et al. (1991) and Pols and Marinus (1994) state that the response of the accretor becomes important when the thermal timescale is ten times larger than the accretion timescale, i.e. for $t = 1$. In contrast, we find that the radius of the accretor already deviates from equilibrium when the accretion timescale is equal to the thermal timescale ($t = 0$) and the swelling becomes unstable at $t = t_{\mathrm{max}}$. Our t_{max} is mass dependent in contrast to their mass independent limit of $t = 1$. However, these studies and subsequent work (e.g. Shao and Li, 2014; Schneider et al., 2015; Shao and Li, 2016) assume that the unstable swelling leads to a reduced accretion efficiency and only to a merger if the ejected angular momentum is high enough.

Recently, a similar studies were put forward by Zhao et al. (2024) and Lau et al. (2024), who calculated accreting models at Solar metallicity. Their models behave qualitatively similar to our models. However, a close inspection reveals that our models swell less for the same accretion rate. For example, our $5M_\odot$-model with $\dot{M} = 10^{-3}\,M_\odot/\mathrm{yr}$ reaches about $120R_\odot$, while that of Lau et al. (2024, $Z = 0.0142$) swells to around $500R_\odot$ and that of Zhao et al. (2024, $Z = 0.02$) reached about $600R_\odot$. This behaviour may relate to the metallicity dependence of the opacity (cf. Sect. 5.2.2). A higher metallicity increases the opacity, which in turn decreases the Eddington accretion rate. This means that for increasing metallicity the boundary between stable and unstable accretion moves to smaller timescale ratios t. The magnitude of the shift is hard to estimate from the combined model data. The $5M_\odot$-model of Zhao et al. (2024) with $\dot{M} = 10^{-3}\,M_\odot/\mathrm{yr}$ appears to be what we consider a borderline model, our comparable model accretes stably and our $5M_\odot$-model with $\dot{M} = 1.5 \cdot 10^{-3}\,M_\odot/\mathrm{yr}$ is unstable. Form that we can estimate that the shift of the boundary between stable and unstable accretion may be less than 0.2 dex when going from SMC to Solar metallicity. Lau et al. (2024) analysed their models, but fit their results different parameters, so a direct comparison is difficult. However, two common features are the double-exponential behaviour of the stably accreting models on the accretion rate, and that more massive models are more sensitive to the accretion rate. Other model assumption, such as core overshooting and the mixing-length parameter, may also have an impact.

5.3 Predictions for L_2-overflow

In this Section, we apply our model for the swelling of the accretor star to model grids of binary systems. We follow the evolution of the accretor radius and of its Roche radius. We then determine the conditions under which the accretor overfills its Roche lobe, leading at first to contact and with further overfilling to an L_2-overflow. We assume that the latter leads to a merger of the two stars (Nariai and Sugimoto, 1976).

5.3.1 Method

We model the binary systems in our grid based on detailed non-rotating single star models computed with MESA version 10108 (Paxton et al., 2011, 2013, 2015, 2018). The initial masses are 8, 10, 15, 20, 30, 50, 70, and $100M_\odot$, and the physical assumptions are identical to those in Sect. 5.2.1, unless otherwise stated. We use overshooting ($\alpha_{\mathrm{ov}} = 0.33$) and semiconvection ($\alpha_{\mathrm{sc}} = 1$) as in Wang et al. (2020) to avoid central helium ignition in the Hertzsprung gap (Schootemeijer et al., 2019), as the following Case C behaves differently than

Case B mass transfer, and to better compare our results with Wang (2022). We ran our models until central helium depletion and used them to model the evolution of the donor star. For the accretor star, we assume no evolution, which is justified for mass ratios away from unity, and interpolate between the ZAMS models to build a binary grid for each donor mass with mass ratios from 0.1 to 0.95 in steps of 0.05 and orbital periods from $10^{-0.5}\,\mathrm{d} \approx 0.3\,\mathrm{d}$ to $10^{3.5}\,\mathrm{d} \approx 3000\,\mathrm{d}$ in steps of 0.25 dex.

For each combination of initial donor mass $M_{1\mathrm{i}}$, initial accretor mass $M_{2\mathrm{i}}$ and initial orbital period, we determine the Roche radius of the donor using the fit formula from Eggleton (1983). If the Roche radius is equal to the stellar radius of a hydrogen core-burning donor model (RLO Case A), we calculate the post-RLO donor mass $M_{1\mathrm{f}}$ according to Eq. 4.4. If the Roche radius is equal to the stellar radius of a hydrogen shell-burning model (RLO Case B) or a helium-burning model (RLO Case C), we use the helium core-mass of the donor as the post-RLO donor mass $M_{1\mathrm{f}}$.

Next we determine the logarithmic timescale-ratio t (Eq. 5.3). The thermal timescale of the accretor star is given by Eq. 5.4 using the ZAMS values. The mass-transfer timescale can be calculated using Eq. 5.5. $\dot{M}_2$ is given by by $-\varepsilon \dot{M}_1$, which in turn can be estimated by $\dot{M}_1 \approx (M_{1\mathrm{f}} - M_{1\mathrm{i}})/\tau_{\mathrm{KH1}}$. The mass transfer efficiency ε is assumed to be constant during the RLO and is a free parameter. Thus we find

$$t \approx \log\left(\frac{M_{2\mathrm{i}}^2}{M_{1\mathrm{i}}^2} \cdot \frac{R_{1\mathrm{i}} L_{1\mathrm{i}}}{R_{2\mathrm{i}} L_{2\mathrm{i}}} \cdot \varepsilon \cdot \frac{M_{1\mathrm{i}} - M_{1\mathrm{f}}}{M_{2\mathrm{i}}}\right). \tag{5.9}$$

For $t < 0$, the accretor remains in thermal equilibrium, as discussed in Sect. 5.2, and we describe its radius evolution during the RLO by linearly interpolating $\log R_{2\mathrm{i}}$ to $\log R_{2\mathrm{f}}$ between $M_{2\mathrm{i}}$ and the final secondary mass $M_{2\mathrm{f}}$, where we take the radius of a ZAMS model of mass $M_{2\mathrm{f}}$ for $R_{2\mathrm{f}}$. For $0 < t < t_{\mathrm{max}}$ (Eq. 5.6), we determine the parameters r and m (Eq. 5.7 and 5.8). We model the time-dependent accretor radius linearly from $\log R_{2\mathrm{i}}$ at $M_{2\mathrm{i}}$ to $\log R_{\mathrm{max}} = \log R_{2\mathrm{i}} + r$ at $M_{R=R_{\mathrm{max}}} = mM_{2\mathrm{i}}$, and from $\log R_{\mathrm{max}} = \log R_{2\mathrm{i}} + r$ to $\log R_{2\mathrm{f}}$ between $M_{R=R_{\mathrm{max}}} = mM_{2\mathrm{i}}$ and $M_{2\mathrm{f}}$. We chose this piece-wise linearity in $\log R$ due to the rough piece-wise linear behaviour shown in Fig. 5.6. For $t > t_{\mathrm{max}}$, we assume that the accretor swells until it reaches the Hayashi lines. We model these by assuming a fixed effective temperature of $\log T_{\mathrm{eff}}/\,\mathrm{K} = 3.6$ and by adopting an additional luminosity given by

$$L_{\mathrm{gr}} = \frac{1}{2}\frac{GM_{2\mathrm{i}}\dot{M}_{2\mathrm{i}}}{R_{2\mathrm{i}}}, \tag{5.10}$$

which accounts for the gravitational energy release of the accreted matter. In general, we use this to limit the accretor radius. We have thus derived a model for the accretor radius under accretion as a function of the current accretor mass.

Similar to the mass transfer efficiency ε, the angular momentum budget of an RLO is not well understood. To describe it, we use the formalism of Soberman et al. (1997), which allows an analytical analysis of certain angular momentum budgets. In addition to their parameters α, the fraction of mass lost from the donor leaving the system with the specific orbital angular momentum of the donor, and β, the mass fraction lost from the donor leaving the system with the accretor's specific orbital angular momentum, we introduce η for the material ejected with the specific orbital angular momentum of the binary system. These quantities are related as $\varepsilon = 1 - \alpha - \beta - \eta$. Soberman et al. (1997) introduces a parameter A to describe the enhancement of the angular momentum loss at the donor by spin-orbit coupling. We will use it as a general parameter to scale the angular momentum loss and also introduce B and H as scaling factors for the angular momentum loss similar to A. This leads the three angular momentum evolution exponents in Soberman et al. (1997)

eqs. (25) to (27) taking the form

$$\mathscr{A}_w = A\alpha, \tag{5.11}$$

$$\mathscr{B}_w = \frac{A\alpha + B\beta - H\eta}{1-\varepsilon}, \tag{5.12}$$

$$\mathscr{C}_w = \frac{A\alpha\varepsilon + B\beta/\varepsilon - H\eta}{1-\varepsilon}. \tag{5.13}$$

We use eq. (28) from Soberman et al. (1997) to determine the system's semi-major axis as a function of the accretor mass, expressed by the mass ratio. With this, we use the formula of Eggleton (1983) to calculate the Roche radius of the accretor R_{RL2} over the course of the RLO and eq. (3.1) and (3.2) from Marchant Campos (2018) to find the L_2equivalent-radius R_{L2}[2]. Finally, we calculate the maximum of $\log(R_2/R_{\mathrm{RL2}})$ and $\log(R_2/R_{\mathrm{L2}})$ during the RLO as a function of initial mass ratio and initial orbital period for fixed donor mass, mass transfer efficiency and angular momentum budget. The sign of these tells us whether the accretor remains within its Roche lobe or whether contact or even a L_2-overflow occurs.

5.3.2 Results

In Fig. 5.7 we show the maximum ratio of the accretor radius to its Roche radius over the course of the RLO for a $10M_\odot$ (top) and a $30M_\odot$ (bottom) donor for a mass transfer efficiency of 50%, assuming that the ejected material carries the specific orbital angular momentum of the accretor, as a function of initial mass ratio and initial orbital period. Red dots indicate that the accretor is growing larger than its Roche lobe, and blue dots are for accretors that remain within their Roche lobe. In the $10M_\odot$-model, we find that for low initial orbital periods and mass ratios greater than about 0.5, the accretor avoids filling its Roche lobe and the system does not evolve to contact. For higher periods and lower mass ratios we get the opposite. Contact is also expected for very low orbital periods below about 0.3 d, but this region is almost completely excluded due to the donor RLO at ZAMS. A similar pattern is observed for the L_2-overflow, which is not unexpected since the L_2-radius is not larger than about 30% of the Roche radius.

We can explain why the accretors in low mass ratio systems tend to evolve to contact by using the thermal timescale of the accretor. The smaller the mass ratio, the smaller the accretor mass and luminosity, hence a larger accretor thermal timescale and a larger logarithmic timescale ratio t, since no changes have been made to the donor. The tendency for systems with large orbital periods to develop contact can be understood by the thermal timescale of the donor. A larger orbit implies a larger donor radius at the start of RLO, which implies a smaller donor thermal timescale and thus a larger mass transfer rate, resulting in a larger logarithmic timescale ratio t.

For the adopted angular momentum budget (material leaving the system carries the same specific angular momentum as the accretor), we find Case A and Case B systems that can avoid contact. The cyan line, which marks RLO at ZAMS, indicates the lower period limit for meaningful binary evolution. We expect the accretor not to overfill its Roche lobe in systems with orbital periods above 3000 d, indicated by the dotted lines in the upper right-hand corner, since this period corresponds roughly to the largest radius possible for our Hayashi-line models (Eq. 5.10). However, this is hardly relevant as the donor is barely expected to grow large enough in radius to initiate a RLO as such high initial orbital period.

Moving to the $30M_\odot$ donor, we find that that the contact avoidance region is smaller compared to the $10M_\odot$ model. In particular, almost no Case B system can avoid contact. It is a general trend that we observe that as

[2] Technically, $L_2$and L_3 flip when the mass ratio inverts. Therefore one has to evaluate eq. (3.1) to find L3.

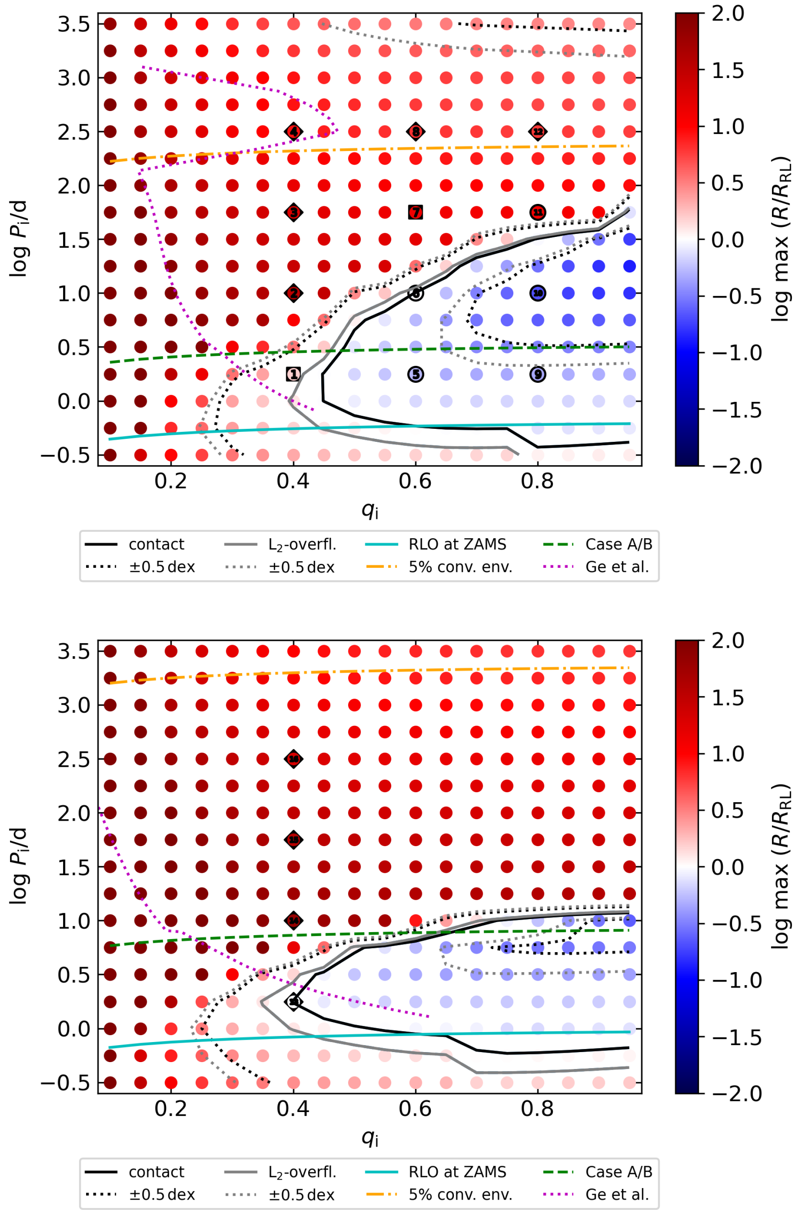

Figure 5.7: Maximum ratio of the accretor radius to its Roche radius over the course of the RLO as a function of initial mass and initial orbital period in our simulated binary systems. Red means that the accretor star swells to become larger than its Roche lobe, and blue indicates that it remains within its Roche lobe. The black line marks the boundary between these, and in grey we show the boundary for the L_2-radius instead of the Roche radius. The dotted black and grey lines indicate a shift of ±0.5 dex in the two boundaries. The initial donor masses are $10M_\odot$ (top) and $30M_\odot$ (bottom), the mass transfer efficiency is 50%, and we assume that the ejected material carries the specific orbital angular momentum of the accretor ($\alpha = \eta = 0$, $\beta = -\varepsilon$, $B = 1$). We show the region where RLO at ZAMS is expected (cyan solid line), the boundary between Case A and Case B (green dashed line), the onset of the donor convective envelope (orange dot-dashed line), and the critical mass ratio according to Ge et al. (2010, 2015, 2020, pink dotted line). Systems marked with numbers and black symbols are those for which we have computed detailed models, see Table 5.2. Black circles indicate stable swelling without contact formation, squares stand for stable swelling but L_2-overflow, and diamonds indicate unstable swelling with L_2-overflow.

the donor mass increases, a smaller number of systems avoid contact. We explain this with Fig. 5.3. Higher donor masses imply higher accretor masses. For higher accretor masses, t_{max} approaches zero, shrinking the contact avoidance region.

In Fig. 5.8 we show only the boundary between contact and non-contact models, but for varying accretion efficiencies. At the highest efficiency, the contact avoidance region is the smallest and it grows with decreasing efficiency. This can be understood from Eq. 5.9, where $t \propto \log \varepsilon$. For the assumed angular momentum budget, we also find a limiting case given by completely non-conservative mass transfer (pink line). It indicates that for a fixed orbital period, systems with more extreme mass ratios than given by this line can not avoid contact, and that this contact is caused by the orbital evolution of the system and not by the swelling of the accretor.

Figs. D.3 to D.5 show the same as Fig. 5.8, but with different assumptions about the amount of angular momentum of the ejected material. If it carries twice the specific orbital angular momentum of the accretor (Fig. D.3 left), the main difference from the original case is that the boundary for unavoidable contact has moved to the right. If the ejected material carries the donor specific orbital angular momentum (Fig. D.4 left), this boundary exists only towards small initial periods. The pattern remains that a higher mass transfer efficiency implies more contact systems. If twice this angular momentum is ejected (Fig. D.4 right), for most mass transfer efficiencies at low donor mass, most Case A mass transfers lead to contact. If the ejected material carries the binary's specific orbital angular momentum once or twice (Fig. D.5), a mixture of the above cases occurs. If no angular momentum is lost (Fig. D.3 right), the patterns resemble the case where the ejected material carries the specific orbital angular momentum of the donor.

5.3.3 Discussion

In this Section we describe the uncertainties of our model (Sect. 5.3.3), compare it with detailed binary models in Sect. 5.3.3, apply our recipe to the WR stars in the SMC (Sect. 5.3.3), and compare our work with previous publications in Sect. 5.3.3.

Uncertainties

We have already described the uncertainties in modelling the swelling of the accretor in Sect. 5.2.3. Besides that, for the model of the binary system, the most important uncertainty is probably that we have neglected the nuclear evolution of the accretor. This assumption is only realistic for systems with mass ratios not close to unity, where the nuclear evolution of the more massive star is much faster than that of the companion. If this is not the case, stellar models predict that both the radius and luminosity of the star will have increased at the onset of accretion, and thus the thermal timescale of the accretor has decreased. This causes the logarithmic timescale ratio t to be smaller given the same accretion rate. We therefore expect the accretor to expand less, which should increase the region of contact avoidance region in Fig. 5.7 for mass ratios close to unity by shifting its upper boundary upwards.

The lack of nuclear evolution of the accretor also causes our models to avoid a reverse mass transfer and a mass transfer on post-main-sequence models. This is important for mass ratios very close to unity and/or Case A systems. If both stars have similar masses, the accretor star can complete its central hydrogen burning during or after the RLO, which is expected to result in a merger (Wellstein et al., 2001; Sen et al., 2022). For a Case A RLO this is much more likely, even for mass ratios not very close to unity, since this type of mass transfer proceeds on the nuclear timescale (Pols, 1994; Wellstein et al., 2001; Sen et al., 2022). A comparison of our Fig. 5.7 with the yellow shaded area of fig. A.4 (left) of Wang (2022) suggests that at least half of the systems in the contact-avoiding region of Case A should undergo this effect.

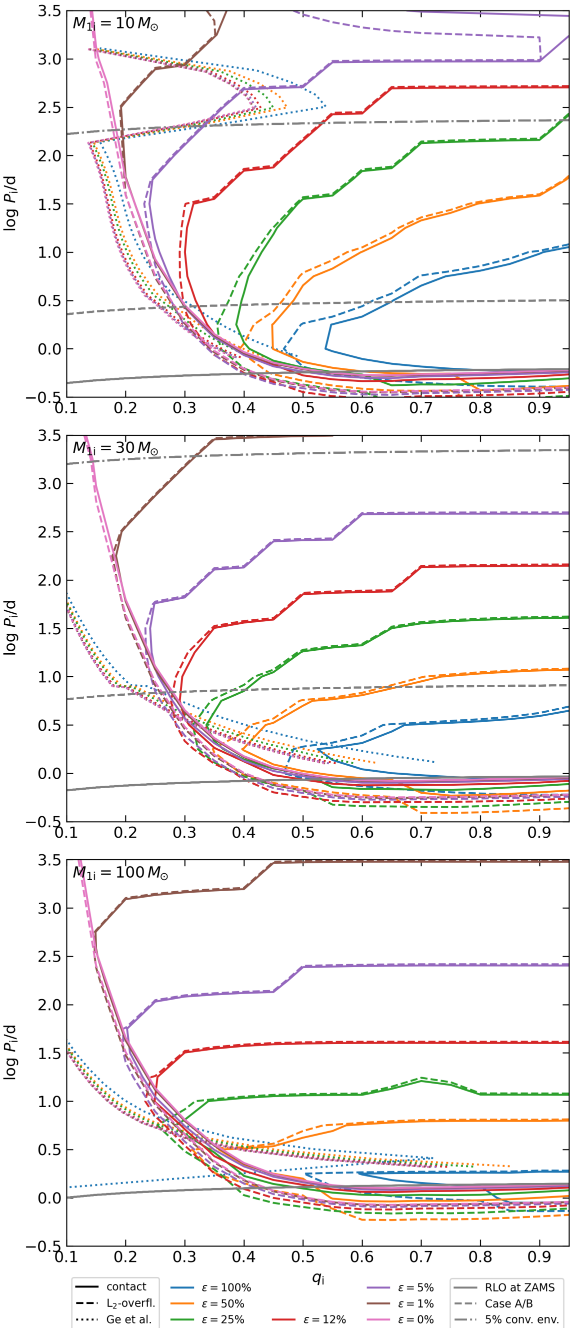

Figure 5.8: Boundary between the contact-developing and the contact-avoiding models for different initial donor masses (from top to bottom 10, 30, and 100$M_\odot$) assuming the ejected material carries the accretor's specific orbital angular momentum (i.e. $\alpha = \eta = 0$, $\beta = -\varepsilon$, $B = 1$). Colours indicate the assumed mass transfer efficiency. Dashed lines show the boundary of L$_2$-overflow and dotted lines the critical mass ratio for dynamical timescale mass transfer derived from Ge et al. (2010, 2015, 2020).

Our adopted values for semiconvection and overshooting avoid central helium ignition in the Hertzsprung-gap (Schootemeijer et al., 2019; Klencki et al., 2020, 2022). These works and other recent studies such as Hastings et al. (2021) favour models which avoid the red supergiant stage during core helium burning. Early central helium ignition would convert most of our Case B systems to Case C systems, if they reach the required radius, or lead to helium ignition during the RLO, which may cause its termination. The formation of blue loops starting from a red supergiant is unproblematic, as the radius evolution beyond the Hertzsprung gap is slow enough to make helium ignition during RLO is unlikely.

In this work we have restricted ourselves to angular momentum budgets that can be described by analytical formulae, because these were easy to implement. In a real binary the ejection of material from the binary may be a complex hydrodynamical process and thus the angular momentum budget could be more complex than the formalism of Soberman et al. (1997). However, we have analysed the limiting case where no angular momentum leaves the system (Fig. D.3 right). On the other hand, if the angular momentum loss is much larger than assumed here, say of the order of an L_2-overflow, we expect the system to undergo a rapid merger.

Our results were found using stellar models with SMC metallicity. In Sect. 5.2.3, we found evidence that with higher metallicity, the accretor swells more. A larger maximum accretor radius means that the system is more likely to evolve into contact, and thus the contact-avoidance regions in Fig. 5.8 should become smaller. This means that at larger metallicities the products of stable mass transfer could be less, and common envelope or merger products could be more likely. Other parameters, such as the choice of the overshooting and the mixing length parameter, should also affect the result.

Comparison with detailed binary models

In Fig. 5.6 we have indicated by +-symbols the maximum of the mass-radius curve when using Eq. 5.9 with the parameters of the detailed models at the onset of RLO. They agree well with the ×-symbols, which are based on the actual mass transfer rate of the detailed models, except for models #1 (blue), #7 (brown) and #11 (yellow). For the latter two this is unproblematic because the binary is very wide and the maximum radius is either much larger (#7) or much smaller (#11) than the Roche radius. Fig. 5.6 also supports our assumption that unstably swelling models can be assumed to reach the Hayashi lines. Models #2 and #3 swell to a radius similar to the one indicated by the position of the +-symbols. Only a small mass accretion ($0.5 M_\odot$ and $1 M_\odot$ respectively) is required to achieve this.

In Fig. 5.7 we have shown the initial-mass–initial-period combination for which we have computed detailed MESA binary models with black symbols. Whether they evolve into contact or avoid it can be predicted well by our method. Systems that remain in thermal equilibrium or swell stably but do not overfill their Roche lobe are marked with circles. Indeed, models #5, #6, #9, and #10 are in the contact avoidance region. However, model #6 is near the boundary and model #11 deviates from our prediction, likely because the accretor in our simplified models does not undergo nuclear evolution before RLO, see Sect. 5.3.3. Models #1 and #7 are computed to swell stably but still overfill L_2(squares), which is indeed confirmed in Fig. 5.7. Unstable swelling and subsequent L_2-overflow is observed in models #2 and #3 and expected to occur in models #4, #8 and #12, all marked by diamonds and all in the contact forming region. For the $30 M_\odot$-donor, models #14, #15, and #16 behave as predicted. Model #13 swells unstably and undergoes L_2-overflow, but our recipe predicts that it will just fill its Roche lobe. As the function we found for r (Eq. 5.7) is quite steep, especially at high masses (see Fig. 5.4), it is not unexpected that such mismatches occur at the boundaries.

Table 5.3: Mass estimates and orbital parameters of the four WR+O systems in the SMC. The superscript indicates the method on which the estimate is based (ΔRV = radial velocity variation, lum = Luminosity, $\mathrm{d}X/\mathrm{d}Q$ = hydrogen gradient, SpT = spectral type, gr = surface gravity)

	AB 3	AB 6	AB 7	AB 8
P_{orb}/ d	$10.053(5)^{(f)}$	$6.5384(4)^{(g)}$	$19.5600(5)^{(h)}$	$16.633(9)^{(i)}$
$q^{\Delta\mathrm{RV}}$	$-^{(f)}$	$2.23(9)^{(g)}$	$1.94(6)^{(h)}$	$2.85(20)^{(i)}$
$M_{\mathrm{WR}}^{\mathrm{lum}}/M_\odot{}^{(a)}$	29^{+2}_{-2}	26^{+7}_{-5}	37^{+6}_{-5}	40^{+7}_{-6}
$M_{\mathrm{WR}}^{\mathrm{d}X/\mathrm{d}Q}/M_\odot{}^{(b)}$	28	$20\ldots30^{(c)}$	34	–
$X_{\mathrm{H,WR}}{}^{(d)}$	0.25(5)	0.25(5)	0.15(5)	$0^{+0.15}$
$M_{\mathrm{O}}^{\mathrm{SpT}}/M_\odot{}^{(d)}$	20^{+20}_{-5}	41^{+10}_{-10}	44^{+26}_{-9}	61^{+14}_{-25}
$M_{\mathrm{O}}^{\mathrm{gr}}/M_\odot{}^{(d)}$	13^{+70}_{-10}	61^{+60}_{-30}	30^{+55}_{-19}	70^{+210}_{-52}
$M_{\mathrm{1i}}^{\mathrm{lum}}/M_\odot{}^{(e)}$	50^{+5}_{-5}	47^{+10}_{-7}	65^{+10}_{-10}	80^{+15}_{-15}
$M_{\mathrm{1i}}^{\mathrm{SpT}\,\wedge\,\Delta\mathrm{RV}}/M_\odot{}^{(e)}$	–	35^{+5}_{-5}	45^{+20}_{-7}	47^{+8}_{-15}
$M_{\mathrm{1i}}^{\mathrm{gr}\,\wedge\,\Delta\mathrm{RV}}/M_\odot{}^{(e)}$	–	50^{+40}_{-20}	32^{+43}_{-15}	$50^{+?}_{-30}$

Notes. The superscripts indicate the method used to estimate the masses. [(a)] Shenar et al. (2016, 2018) using the mass-luminosity relation from Gräfener et al. (2011). [(b)] Schootemeijer and Langer (2018), since their method requires $X_{\mathrm{H,WR}} > 0$, no mass could be determined for AB 8. [(c)] Schootemeijer (priv. comm.) [(d)] Shenar et al. (2016, 2018) [(e)] Based on $M_{\mathrm{WR}}^{\mathrm{lum}}/M_\odot$, $X_{\mathrm{H,WR}}$ and the profiles of Schootemeijer et al. (2019). The mass for AB 8 is a lower limit. [(f)] Foellmi et al. (2003), no mass ratio could be determined. [(g)] Shenar et al. (2018) [(h)] Niemela et al. (2002) [(i)] Bartzakos et al. (2001) and St-Louis et al. (2005)

Comparison with the SMC binary WR stars

It is instructive to compare our results with the WR stars of the SMC. Indeed, it is proposed that WR stars can form by binary interaction (e.g. Shenar et al., 2020b; Pauli et al., 2022). The SMC contains twelve WRs, five of which are known binaries (Foellmi et al., 2003; Foellmi, 2004; Shenar et al., 2016, Schootemeijer et al. subm.). One of them, AB 5, is a double WR star, which makes it unsuitable for the following analyses. Following Schootemeijer and Langer (2018), we can add the initial mass ratio and initial orbital period of the remaining WR+O systems (AB 3, AB 6, AB 7, and AB 8) to diagrams like Fig. 5.8. We can calculate the initial orbital period from the observed orbital period, if the current and initial mass ratios are known and the angular momentum budget is fixed (Sect. 5.3.1 and Soberman et al., 1997). To determine the current mass ratio, we can rely on radial velocity variations (Foellmi et al., 2003; Shenar et al., 2016, 2018, Schootemeijer et al. subm.) or on mass estimates of the two stars. Shenar et al. (2016, 2018) estimate the mass of the O star in two ways. One mass estimate is derived from the spectral type, and the other is derived from the surface gravity. Unfortunately, these estimates typically have significant uncertainties. The WR masses from Shenar et al. (2016, 2018), based on the mass-luminosity relation of Gräfener et al. (2011) agree well with those from Schootemeijer and Langer (2018). Thus for each system we can adopt two of the three observed properties (mass ratio, WR mass, O-star mass) and calculate the third. Furthermore, we can use the WR masses together with their hydrogen surface abundance to estimate the initial masses of the WR progenitor using the models of Schootemeijer et al. (2019) with overshooting and semiconvection as suggested by Hastings et al. (2021). Finally, assuming a mass transfer efficiency ε, we can calculate the initial O star mass $M_{2\mathrm{i}} = M_{\mathrm{O}} - \varepsilon \cdot (M_{1\mathrm{i}} - M_{\mathrm{WR}})$ and find the initial mass ratio and initial orbital period. We have summarised the adopted values in Table 5.3.

We show the resulting initial configurations of AB 7 in Fig. 5.9. We find the initial donor mass of this system to be about $50M_\odot$ for all three estimates of the WR mass. Based on the five different mass estimates for the WR and the O star, we have placed the system several times in the diagram. We also vary the assumed mass transfer efficiency (colour). Comparing the proposed initial parameters of the systems with the corresponding contact boundary, we find that some values of the mass transfer efficiency lead to unrealistic results.

The case of conservative evolution (blue) places the system into the contact forming side of the diagram for all five methods. This means that under this assumption the system must have experienced contact or L_2-overflow, which we have argued leads to a merger and not to the stripping of the envelope of the WR progenitor. On the other hand, only initial mass ratios below unity are meaningful. This is fulfilled for all five methods except the one based on the WR mass derived from the mass-luminosity relation and the spectroscopic mass ratio, for which we find initial mass ratios above unity for mass transfer efficiencies $> 25\%$. All other methods yield initial configurations for the fully non-conservative case (pink) that are on the contact-avoiding side.

A closer inspection of the diagram reveals that for $\varepsilon > 50\%$ (orange) there are only unrealistic solutions (i.e. q_i and P_i values are located in the L_2-overflow region) and for $\varepsilon < 5\%$ (purple) there are only realistic ones (i.e. q_i and P_i values located in the contact-avoiding region and $q_i < 1$). For $\varepsilon = 12\%$ (red), the mass estimate based on the mass-luminosity relation and the surface gravity is in the merger region and for $\varepsilon = 25\%$ (green) also the estimate with mass-luminosity relation and spectral type. This suggests that the mass transfer efficiency for AB 7 was less than 50%, may be as low as 5%. A similar analysis for AB 3 yields $\varepsilon < 1 \ldots 5\%$, for AB 6 $\varepsilon < 50\%$, and for AB 8 $\varepsilon < 25\%$ (Fig. D.6).

Assuming other angular momentum budgets give similar results. In general, the ejection of more specific orbital angular momentum requires a lower mass transfer efficiency to obtain realistic initial configurations. Furthermore, we find that in almost all scenarios it was a Case A RLO that formed AB 6, AB 7, and AB 8 (initial configuration below the grey dashed line) while AB 3 was likely formed in Case B. This fits to the fact that we found it to have the lowest mass transfer efficiency of the analysed systems, as in close binary systems tides are expected to increase the mass transfer efficiency (e.g. Sen et al., 2022). Also all four systems are stable according to the criterion of Ge et al. (2010, 2015, 2020) (initial configurations above the dotted lines). Unfortunately, the discrepancy between the different methods to estimate the stellar masses and the large errors of some of them makes a final judgement difficult. More constraining observations would be desired.

Comparison with previous work

The question under what conditions an RLO will lead to a stripped star and avoid a merger or a common envelope has been addressed by many authors. The classical approach is to compare the mass-radius indices of the donor and the Roche lobe. This is equivalent to asking whether the donor radius shrinks faster or slower under mass loss than its Roche radius. The most recent work on this topic is Ge et al. (2010, 2015, 2020), who calculate mass-radius exponents $\tilde{\zeta}_{\rm ad}$ for donor stars of all evolutionary phases and also give critical mass ratios for conservative evolution. From their mass-radius exponents, we have derived critical mass ratios for all mass transfer efficiencies using eq. (62) of Soberman et al. (1997)[3], as suggested by the authors, and plotted them as pink lines in Fig. 5.7 and as dotted lines in Figs. 5.8 and D.3 to D.5. They indicate that dynamical mass transfer is initiated to their left, probably leading to a merger or common envelope. In most cases, the critical mass ratios lie within the regions where we predict contact and L_2-overflow to occur. Dynamical mass transfer only affects contact-avoiding systems with low accretion efficiencies or with high

[3] Eq. (30) (and eq. (31)), which needs to be evaluated here, has a typo. The last term should have εq in the numerator instead of q.

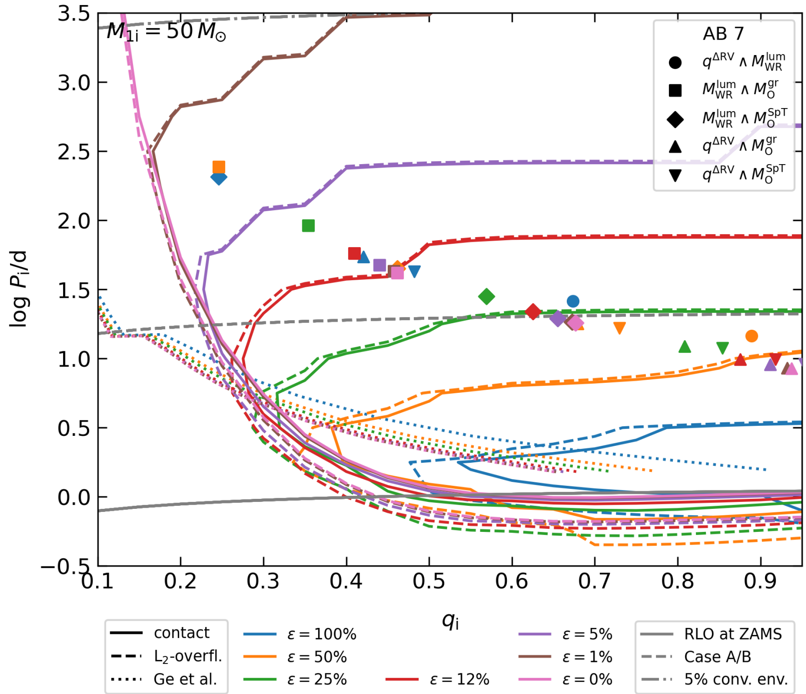

Figure 5.9: Same as Fig. 5.8, but for a $50M_\odot$ donor star. The symbols indicate possible initial configurations for AB 7. The shapes of the symbols indicate whether we have estimated the O star mass with the mass ratio from radial velocity variations and the WR mass from its luminosity (circle), estimated the mass ratio with the surface-gravity mass of the O star and the luminosity mass of the WR star (squares), with the spectral-type mass of the O star and the luminosity mass of the WR star (diamonds), estimated the WR mass the the mass ratio and the surface-gravity mass of the O star (triangles up), or the the mass ratio and the spectral-type mass (triangles down). See also Table 5.3.

donor mass systems and short orbital periods. This means that our criterion – the swelling of the accretor and subsequent contact and L_2-overflow – is often stronger in deciding for or against a stable RLO. Still, both criteria need to be checked.

Wellstein et al. (2001) approach the occurrence of contact systems by computing a small grid of detailed binary models assuming conservative mass transfer. They distinguish three contact formation mechanisms. Their q-contact (contact due to higher mass transfer rates and/or larger thermal timescales of the secondary) is similar to what we observe in our grid. We cannot model what Wellstein et al. (2001) call delayed contact ,i.e. an initially stable mass transfer, which turns unstable during the widening of the orbit since the mass donor's mass-radius exponent increases, because our mass transfer rate is not resolved in time. However, we observe in our models, that in close and very unequal systems the secondary reaches its maximum radius at lower mass ($M_{R=R_{\max}} = mM_{2i}$) than in wide and more equal systems. Finally, premature and reverse contact does not occur in our study, as we do not assume nuclear evolution of the secondary. We can compare fig. 12 of Wellstein et al. (2001) with our Fig. 5.8 (top, conservative case). While they are qualitatively similar, Wellstein et al. (2001) have a larger Case B region with contact avoidance and a smaller corresponding region with Case A region. This could come from the fact that although fast Case A and Case B take place on a thermal timescale, this is only the order of magnitude. Their duration in detailed binary models differs by a factor of a few. In agreement with them, we find the shrinking of the contact avoidance regions and the increasing dominance of Case A with mass.

Langer et al. (2020), Wang et al. (2020) and Sen et al. (2022) use an energy criterion to determine the stability of the RLO. If the combined luminosity of the two stars is large enough to unbind the unaccreted material from the system, a merger will be avoided. They determine the amount of accretion by allowing the accretor to accrete until it reaches critical rotation. This leads to accretion efficiencies of less than 5% for a Case B mass transfer and up to 50% for in Case A (Sen et al., 2022). Although these detailed models are able to indicate a merger by an L_2-overflow, their accretion efficiencies are so low that L_2-overflows only happens at very low initial orbital periods. The energy criterion however predicts a much larger number of systems to undergo unstable RLO, which cover all the unstable models according to our criterion. Thus, its in general the energy criterion which decides for or against a stable RLO. We compare our Fig. 5.8 with Fig. A.4 (right) and A.9 (right) of Wang (2022) because they have the same donor mass, metallicity and angular momentum budget. While for the $10M_{\odot}$-models Wang (2022) finds the region of stable mass transfer to take on a triangular shape between 5 and 100 d up to a mass ratio of about 0.65 and a few Case A systems up to a mass ratio of 0.8 to avoid contact (see also fig. B.1 in Langer et al. (2020)), we find a much larger area if the accretion efficiency is below 50%. Our shape of the contact-avoiding regions is also very different, especially since we find one but Wang (2022) find two separate regions. Its upper limit is given by the onset of convection in the donor. To allow the same number of systems to survive, we would have to set the mass transfer efficiency to about 100%, which would however be centred on systems with close orbits. Comparing the $30M_{\odot}$-models, we see that our contact-avoiding regions have shrunk, but in Wang (2022) they have increased by a large amount. Almost all Case B systems and half of the Case A systems avoid contact. To allow the same number of systems to survive, we would have to set our mass transfer efficiency to about 5%.

Schneider et al. (2015) use fixed critical mass ratios for each Case A and B to decide as the merger criterion, but limit the accretion by the thermal timescale of the accretor (Hurley et al., 2002). In the language of our work, $\varepsilon = 1$ if $t < 1$, and if t would be greater than 1, ε is adjusted so that $t = 1$. For a $10M_{\odot}$-donor this leads to fig. 1 of Schneider et al. (2015), where Case A yields a stripped donor star for mass ratios greater than 0.56, not so different from our work, but their Case B is split into a conservative case for high mass ratios and low orbital periods, and a highly non-conservative case otherwise. The line between these cases roughly corresponds to our line between contact and contact avoidance, but differs because our t_{max} is mass-dependent and we let the accretor swell. For higher donor masses Schneider et al. (2015) find that the region of conservative mass transfer shrinks slightly (as does our contact-avoidance region), but the dividing line becomes an extended transition region (their $20M_{\odot}$ models in fig. 19).

Henneco et al. (2024) analyse which initial binary configurations lead to a merger or common envelope evolution by calculating detailed binary models up to $20M_{\odot}$. Since rotation limited accretion is assumed, their mass transfer efficiency is about 50% for Case A and about 15% for Case B mass transfer. Thus, they find in agreement with our work, that Case A systems with low initial mass ratios evolve towards a merger due to the swelling of the accretor. Because of the low mass-transfer efficiency in their models, it is likely that the evolution of the mass-radius exponents of the donor stars rather than the accretor swelling leads to contact in their Case B systems with extreme initial mass ratios. They also find Case A systems at initial mass ratios close to unity as merger candidates, which we do not find because we do not model the nuclear evolution of the accretor.

Lau et al. (2024) assume that the formation of contact leads to non-conservative mass transfer, which may cause a merger if the ejected material carries a high enough specific angular momentum, while we assume this in the first place. Similar to our results about WR stars, they find that in high mass X-ray binaries and gravitational wave sources a non-conservative mass transfer is likely.

5.4 Conclusion and outlook

Our work sheds new light on the question in which part of the initial binary parameter space the merging of the two stars can be avoided during their first mass transfer phase. When assuming a fixed mass transfer efficiency, the answer to this question depends on the swelling of the mass accreting star, and on the evolution of the orbital separation during the mass transfer. The former can be well computed by detailed binary evolution models, for which, however, it is difficult to scan through the rather unconstrained accretion and angular momentum loss efficiencies. Therefore, we develop a theoretical framework in which we first derive analytic approximations for the radius evolution of accreting main-sequence stars based on detailed models (Eqs. 5.7 and 5.8), which we then use to predict the part of the initial binary parameter space in which merging can be avoided, as function of the chosen accretion efficiency and angular momentum loss parameter.

We derived regions in the initial-mass-ratio–initial-orbital-period–plane in which the binary models evolve into L_2-overflow, potentially leading to a merger, and the regions where the binaries avoid contact and develop a fully stripped donor with a main-sequence companion. We find that only very few models evolve into contact and avoid L_2-overflow. We have tested and compared our binary evolution approach with detailed binary evolution models, for which we find reasonable agreement, but we find rather significant differences compared to simple merger criteria often used in rapid binary evolution calculations. Our models predict a larger fraction of binaries to merge compared with most previous studies, even at the low metallicity of the Small Magellanic Cloud. For larger metallicities, we expect the mass gainers to swell more, which would result in more mergers.

We have applied our results to interpret the observations of the WR+O stars observed in the Small Magellanic Cloud. We found that the mass transfer process which has produced these binaries must have been inefficient, with a mass transfer efficiency of 50% or less, and as low as 1% for one particular system.

We have developed a fast and powerful method to determine the outcome of a Roche-lobe overflow, which often provides stronger constraints than the classical approach of comparing mass-radius exponents. We found that while the angular momentum loss parameter is not unimportant, the mass transfer efficiency is the more influential parameter. Our approach is suitable to be used in rapid population synthesis calculations, for which it is possible to avoid several of the simplifications made here, in particular neglecting the nuclear evolution of the mass gainer. In a forthcoming paper we will use our recipe in a rapid binary population synthesis of the post-mass transfer massive star population of the SMC.

Acknowledgements. The authors would like to thank Pablo Marchant for allowing us to use his MESA framework, and the members of the Bonn Stellar Physics Group for the fruitful discussions.

CHAPTER 6

Populations of evolved massive binary stars in the Small Magellanic Cloud II: Predictions from the rapid binary evolution code ComBinE

C. Schürmann[1] X.-T. Xu[1], N. Langer[1,2], M. Kruckow[3,4], C. Wang[5]

[1] Argelander-Institut für Astronomie, Universität Bonn, Auf dem Hügel 71, 53121 Bonn, Germany
[2] Max-Planck-Institut für Radioastronomie, Auf dem Hügel 69, 53121 Bonn, Germany
[3] Département d'Astronomie, Université de Genève, Chemin Pegasi 51, CH-1290 Versoix, Switzerland
[4] Gravitational Wave Science Center (GWSC), Université de Genève, CH-1211 Geneva, Switzerland
[5] Max-Planck-Institut für Astrophysik, Karl-Schwarzschild-Str. 1, 85748 Garching, Germany

In preparation. (At the time of publication of this thesis, an updated version of this chapter is submitted to *Astronomy & Astrophysics* and is available as pre-print as Schürmann et al. (2025), arXiv:2503.23878.)

Author contributions. CS updated the ComBinE-code originally developed by MK, performed the data analysis and wrote this article. XTX performed the companion study in parallel based on models calculated by CW. CS, XTX, and NL interpreted the results.

Abstract

The evolution of massive stars plays a crucial role in astrophysics, but is subject to large uncertainties. This is amplified by the fact that most massive stars prefer to reside in binaries, whose evolution is much more complex. The mass-transfer efficiency is a major uncertainty in binary physics, together with the angular momentum budget and the condition for stable mass transfer. We use the rapid population synthesis code ComBinE to generate stellar model populations under the assumption of different constant mass-transfer efficiencies. We combine this parameter with a new model to decide on the stability of mass transfer based on the response of the accretor to the incoming matter. By varying the mass-transfer efficiency, we compare the resulting populations with observations of Be stars, Be/X-ray binaries, and Wolf-Rayet stars, and find a mass-dependent mass-transfer efficiency. We use this to generate a fiducial population of post-interaction binaries. We predict the properties of massive main-sequence stars with stellar remnants as companions, in good agreement with observations of Be/X-ray binaries and other objects. We find that there must be a large unobserved population of OB type stars with black hole companions, consisting of two sub-populations. One may appear as SB1 systems and the other is highlighted by the fast rotation and hydrogen emission lines of the star. A companion study using a grid of detailed binary models comes to a similar conclusion. A multi-epoch observation of the massive stars in the Small Magellanic Cloud would be able to reveal this population, test the differences between the two studies, and help to constrain major uncertainties in massive binary evolution.

Key words. stars – massive stars – Be stars – BeXB – SMC – black holes – neutron stars – Wolf-Rayet stars

6.1 Introduction

Stars are the actors of the cosmic theatre and massive stars are the protagonists. Not only do they entertain us with spectacular events like supernovae and gamma-ray bursts, but they also breed heavy elements (Kippenhahn et al., 2012) and shape the evolution of galaxies (Hopkins et al., 2014). It is well established, that massive stars prefer to reside in binary systems (Sana and Evans, 2011). These systems are the origin of even more fascinating phenomena such as X-ray binaries and gravitational wave mergers (Tauris and van den Heuvel, 2023), but our understanding of them is far from complete (e.g. Langer, 2012, 2022).

The two components of a binary star can be cast by a large variety of living or dead stars, so binaries can be watched at almost all energies of the electromagnetic spectrum. The most common and best understood are binary main-sequence stars (Langer, 2012; Tauris and van den Heuvel, 2023), as they are visually bright and long-lived. They are also the longest known kind of binary system (Michell, 1767; Mayer, 1778; Herschel, 1803). In contrast, binaries consisting of two stellar remnants (SR) were found only shortly after the discovery of the first radio pulsar (Hewish et al., 1968; Hulse and Taylor, 1975). The companion of such a pulsar is in most cases a white dwarf (WD) or another neutron star (NS) (Manchester et al., 2005; Tauris et al., 2012). Systems consisting of a star and a SR were observed even before binary SRs, most notably Sirius and its WD companion (Bessel, 1844a). With the advent of X-ray astronomy the first X-ray binaries consisting of a star and an accreting neutron star or black hole (BH) were discovered (e.g. Tauris and van den Heuvel, 2006). The most recent addition to this zoo are double BHs and BH+NS systems, first seen by LIGO (Abbott et al., 2016, 2017).

All these binary species can be understood in terms of Fig. 6.1 (e.g. Tauris and van den Heuvel, 2006). It shows a simplified evolutionary scheme from a zero-age main-sequence binary through several intermediate stages to a gravitational wave merger. However, not every massive binary star leads to such an event, as the system may break up in a supernova (SN) and release its stars (Tauris and Takens, 1998), or the two stars may merge into a single object before ending their lives (Podsiadlowski et al., 1992; Langer, 2012; de Mink et al., 2014). A critical step in this evolutionary scheme is the Roche-lobe overflow (RLO), where matter is transferred from one star, commonly called the ”donor”, to the other, known as the ”accretor” (Kippenhahn and Weigert, 1967). In the first RLO the heavier star is usually the donor, because it burns its fuel faster and expands first. This can happen either during its main-sequence phase (Case A) or during shell burning (Case B, Kippenhahn and Weigert, 1967). The physical details of the RLO are not well understood, in particular under what conditions it is stable (Webbink, 1985), what fraction of the material lost by the donor is deposited on the accretor (de Mink et al., 2007), and how much angular momentum the ejected material removes from the system (Soberman et al., 1997).

A stable RLO is thought to result in the almost complete removal of the hydrogen-rich envelope of the donor. Although this stripped star may retain a thin hydrogen layer, it is commonly referred to as a helium star (HeS). The accretor receives mass, which rejuvenates the star, and gains spin angular momentum. Packet, 1981 showed that only a small amount of accreted material is needed to bring the accretor close to critical rotation, where the centrifugal forces equal the star's gravity (Rivinius et al., 2013). The critical rotation rate $\omega_{\rm cr}$ and the critical rotation velocity $v_{\rm cr}$ are given by

$$\omega_{\rm cr} = \sqrt{\frac{GM}{R_{\rm eq,cr}^3}}, \quad v_{\rm cr} = \omega_{\rm crit} R_{\rm eq,cr} \tag{6.1}$$

where M is the mass of the star and $R_{\rm eq,crit}$ is its critical equatorial radius (de Mink et al., 2013). Assuming Roche geometry (Kippenhahn et al., 2012) one finds

$$R_{\rm eq,cr} = \frac{3}{2} R_{\rm p}, \tag{6.2}$$

where $R_{\rm p}$ is the (unchanged) polar radius.

When such a star rotates close to its critical rotation, it ejects matter from its surface, forming a decretion disk around its equator. This disk emits non-thermal radiation, in particular Balmer emission lines. These, together with the rotationally broadened absorption lines of the star, can explain the Be star phenomenon (Porter and Rivinius, 2003; Rivinius et al., 2013). However, it is possible that either the mass loss (and thus angular momentum loss) or tidal forces end the Be-phase and the star becomes a normal OB star again, or that strong stellar winds remove the disk. It can happen that the HeS expands so much that it initiates a second mass transfer, which we will call a Case (A)BC[1]. The duration of the OBe+HeS phase is limited by the lifetime of the HeS, which ends its life shortly afterwards and becomes a SR. The subsequent phase (OB+SR) is the focus of this work, as it is the second best observable phase, since it has a main-sequence star and an inert SR.

This formation channel of Be stars by binary interaction is not undisputed, but is supported by the fact that no Be stars with main-sequence companions are observed (Bodensteiner et al., 2020b) and on the other hand Be stars with hot subdwarf (sdOB, the observational counterpart to light HeSs, Wang et al., 2021), WD (Zhu et al., 2023) and NS (Tauris and van den Heuvel, 2006) companions are well known. However, only a few Be+sdOB and Be+WD systems have been discovered, because the light and faint companion is difficult to detect. Be+NS systems often appear as Be/X-ray binaries (BeXB), because the NS accretes material from the disk and releases X-ray emission. Another proposed formation process of Be stars is single star evolution, which has recently been studied by Ekström et al. (2008) and Hastings et al. (2020).

The success of this picture raises the question of the unobserved configurations. In particular, since many massive stars with NS companions are known, one would assume that similar Be star systems with BH companions exist. Today, only one such system has been proposed (MWC 656, Casares et al., 2014), but its nature is not undisputed (Rivinius et al., 2022; Janssens et al., 2023). On the other hand, three supergiant/X-ray binaries with BHs (Cyg X-1, LMC X-1, and M33 X-7) are well observed (Orosz et al., 2007, 2009, 2011; Miller-Jones et al., 2021; Ramachandran et al., 2022) and even a source with an X-ray quiet black hole is known (VFTS 243, Shenar et al., 2022). Therefore, an objective of this study is to answer whether it is possible to form OBe+BH systems and to predict their properties. After the OBe+SR phase, the system can evolve by a common envelope ejection (Ivanova et al., 2013; Kruckow et al., 2016) into a binary BH or a double NS, which may undergo a gravitational wave merger (Fig. 6.1). The OB+SR phase is therefore an important intermediate step in understanding the evolution of binary stars.

[1] ”A” is used if a Case A mass transfer has occurred. We use ”BC” instead of the commonly used ”BB” because the donor star is helium burning, which is commonly marked by a ”C”

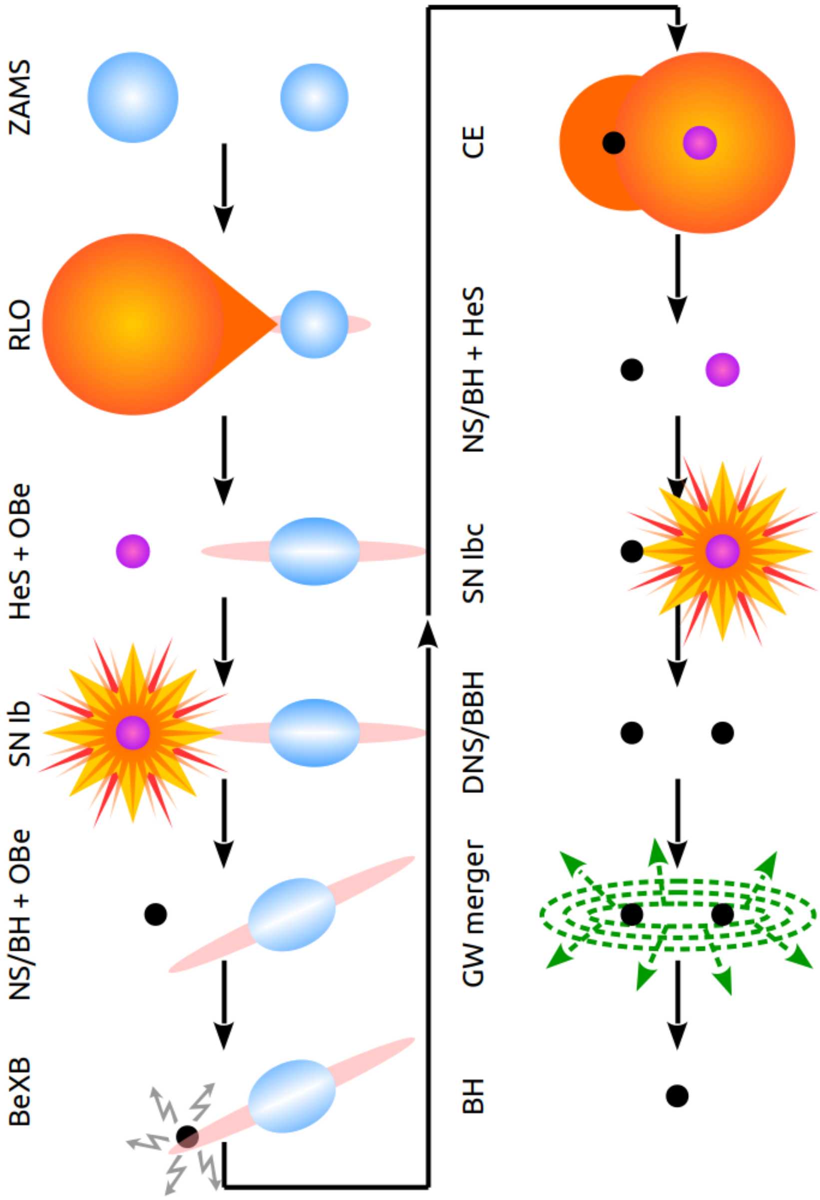

Figure 6.1: A schematic typical evolutionary path from ZAMS to BBH as shown in Kruckow et al. (2018). We focus on the BH+OBe phase. ZAMS = zero age main-sequence, RLO = Roche-lobe overflow, HeS = helium star, OBe = O/B type emission-line star, SN = supernova, NS = neutron star, BH = black hole, BeXB = Be X-ray binary, CE = common envelope, DNS = double neutron star, BBH = binary black hole, GW = gravitational wave.

In this study we focus on stars in the Small Magellanic Cloud (SMC). As a low metallicity satellite galaxy of the Milky Way it is a distinctive environment. Its metallicity of about one fifth of the solar value (Venn, 1999; Korn et al., 2000; Hunter et al., 2008) corresponds to $z \approx 3$ (Kewley and Kobulnicky, 2007). Low metallicities are interesting because the aforementioned events (supernovae, gamma-ray bursts and gravitational waves) originate predominately in low metallicity environments (Abbott et al., 2019; Abbott et al., 2023b). Being located at a distance of about 60kpc, it is still possible to observe individual stars. Another advantage of the SMC are the weaker stellar winds caused by the low metallicity (Abbott, 1982; Kudritzki et al., 1987; Mokiem et al., 2007). Lower winds imply a lower loss of angular momentum, so we expect Be stars to be more numerous and of higher mass, and hence a higher success rate in finding OBe+BH systems.

Our study is closely related to Xu (2024), who investigate the same types of objects using detailed stellar models, while we use rapid binary evolution. Our work is structured as follows. Sect. 6.2 describes our methods for simulating systems consisting of a hydrogen-burning star with a SR. In Sect. 6.3 we describe how the outcome of the binary evolution code depends on the initial parameters of the binary. In Sect. 6.4 we use different physical assumptions to generate artificial populations and compare them with observational properties to determine a fiducial set of assumptions. The population based on these fiducials is analysed in detail in Sect. 6.5. In Sect. 6.6 we compare our results with observations and with previous work. A summary of our conclusions is given in Sect. 6.7.

6.2 Method

We investigate the OB+SR population of the SMC with the Monte Carlo based rapid binary population synthesis code ComBinE which was first introduced by Kruckow et al. (2018). In this Section we describe how this code operates.

6.2.1 The rapid binary population synthesis code ComBinE

Evolving both binary components simultaneously, ComBinE is based on tabulated detailed single star models, in contrast to other binary population synthesis codes, which treat stellar evolution using fitting formulae. This allows for a fast exchange and modular use of the underlying stellar models. Compared to detailed codes like MESA (Paxton et al., 2019, and references therein), ComBinE is much faster and enables the user to generate large model populations of different underlying binary physics in a small amount of time. Also in contrast to MESA, it follows a system's evolution through a SN event, is able to treat a common envelope phase and, in contrast to other rapid binary population synthesis codes, uses envelope binding energies calculated from stellar models rather than constant values of the envelope's binding energy (Kruckow et al., 2016).

The dense grid of detailed stellar models is currently available for Milky Way, Large Magellanic Cloud, SMC, and IZwicky 18 metallicity and features both hydrogen-rich and HeS models. The models were calculated with BEC (Yoon et al., 2010, and references therein) using the same stellar physics as Brott et al. (2011) with initial masses from 0.5 to $100 M_{\odot}$. For the application in ComBinE, the following quantities were extracted and tabulated: total stellar mass, age, photospheric radius, core mass (see Sect. 6.2.2 for the updated definition), luminosity, effective temperature, two versions of the λ-parameter describing the binding energy of the envelope, and (new to this version of ComBinE, see Sect. 6.2.2) the carbon core mass and the concentration factor. For hydrogen-rich models, the time of central hydrogen exhaustion is saved, too. Within this grid using initial mass and age as independent quantities, the current values of the remaining eight dependent quantities are interpolated linearly. The same HeS tracks are used for all metallicities but their were rescaled by the wind mass loss rate according to Hainich et al. (2015). While we are aware that detailed stellar models predict a small hydrogen layer to remain on the HeS and that the size of this layer has a large impact on the stellar radius (Laplace et al., 2020), we neglect it for simplicity.

To initialise a binary star model, ComBinE draws the initial primay mass from an initial mass function. We use a Kroupa-like function with a high mass slope of $\alpha = 2.3$ (Salpeter, 1955; Massey et al., 1995) within the range of 3 to $100 M_{\odot}$. The lower limit takes care that we consider all relevant stars to meaningfully compare the companions of NS to stars of similar mass and the upper limit is the mass of the most massive stellar model we have. The mass of the secondary is derived from a mass ratio distribution

$$f_q = \frac{\mathrm{d}N}{\mathrm{d}q} \propto q^{\kappa} \tag{6.3}$$

and the initial separation from a orbital period distribution

$$f_{\log P} = \frac{\mathrm{d}N}{\mathrm{d}\log P} \propto (\log P)^{\pi}. \tag{6.4}$$

To model the SMC, we rely on four sets of observationally inferred values of κ and π. These are Sana et al. (2012) based on Galactic O stars ($\kappa = -0.1, \pi = -0.55$), Sana et al. (2013) based on LMC O stars ($\kappa = -1.0, \pi = -0.45$), Dunstall et al. (2015) based on LMC early B type stars ($\kappa = -2.8, \pi = 0.0$), and flat distributions which were observed by Kobulnicky et al. (2014) in the Cygnus OB2 association, but we will treat this mostly as an academic example. Note that these distributions might not be independent (Moe and Di Stefano, 2017). While the lower orbital period limit is given naturally by RLO at ZAMS, one needs to be careful about the upper limit. We choose to only consider orbital periods up to $10^{3.5}\,\mathrm{d} \approx 3162\,\mathrm{d}$, as this is the range considered by Sana et al. (2012), Sana et al. (2013), and Dunstall et al. (2015). As they note that 50% to 70% of massive stars have orbital periods below that value and this upper limit coincides roughly with the maximum orbital period for RLO (see Sect. 6.3), the remaining fraction of stars is either single or in wide non-interacting binaries, rendering them effectively single for our purposes. For this study, we assume a fraction of interacting binaries of 100%. We assume our systems to be circular, as tidal effects will circularise the orbit before the onset of RLO (Zahn, 1977). As we implemented stellar rotation (see Sect. 6.2.3), it is also possible to choose the initial rotation of the models. We allow for no rotation, a bimodal distribution as in Dufton et al. (2013), synchronised (as in Langer et al., 2020) and a flat equatorial rotation distribution between zero and a user determined value. In this study we restrict ourselves to initially synchonised stars, as tidal interaction predict this to be archived during evolution towards RLO (Zahn, 1977). We used the same stellar models for all rotation rates, which is justified for stars not to close to critical rotation (Brott et al., 2011).

After a system is initialised, it is evolved by ComBinE until only SRs remain. In practice this means the code determines the time until the radius of one model becomes larger than the Roche radius according to the formula of Eggleton (1983), which marks the onset of a RLO, or the end of the stellar evolution, after which a SN is modelled. For the intermediate time, the orbital period is adjusted to account for mass loss and the rotational velocity evolves as described in Sect. 6.2.3.

If one of the two stars is destined to overfill its Roche lobe, the stability of the RLO is evaluated. We updated the applied criteria and list them in Sect. 6.2.2. In case of stable mass transfer, ComBinE employs the analytical descriptions of Soberman et al. (1997) to describe the change in orbital period. For this study, we assume that all ejected mass carries the same specific orbital angular momentum as the accretor. We assume that the mass-transfer efficiency is constant throughout the RLO and tread it as a free parameter, whose value we are going to vary in this study. After the end of the mass transfer, ComBinE searches the stellar model grid for a new model for the accretor with matching core mass and total mass. Since the envelope mass increased, the new model appears younger compared to the old model (rejuvenation). The donor is assumed to become a HeS. In case of a Case (A)BC RLO when the donor is already a HeS, we assume an instant SN after the RLO. Like for the accretor, a new model is calculated from the stellar grid, but this time based on the HeS models. The duration of a Case B mass transfer is assumed to be of the order of a thermal timescale. For the duration of Case A mass transfer and the donor mass thereafter see Sect. 6.2.2. All unstable RLOs are checked whether a common envelope ejection is possible. For our study this scenario can be neglected and the two models merge as described in Sec. 6.2.2.

When the end of a stellar track is reached, a SR is formed. Depending on the structure this is either a WD, NS or BH. If the helium core mass exceed $6.6M_{\odot}$, we assume a BH is formed (Sukhbold et al., 2018). We assume that the complete carbon core and 80% of the helium layer above end up in the black hole and we reduce that mass by 20% to account for the release of gravitational energy (Kruckow et al., 2018, and references therein). If the mass of the carbon core is above $1.435M_{\odot}$ a NS is formed by core collapse SN (CCSN) and if it is between $1.37M_{\odot}$ and $1.435M_{\odot}$ we assume an electron capture SN (ECSN) as calculated by Tauris et al. (2015). The NS masses are around $1.3M_{\odot}$ with the detailed formulae given in Kruckow et al. (2018). If the carbon core is lighter than $1.37M_{\odot}$, a WD is formed which inherits the progenitor's carbon core mass as its total mass.

From the velocity distribution of pulsars it is known that a SN imposes a natal kick on them. For ECSN our standard assumption is a uniformly distributed kick between 0 and 50 km/s (Podsiadlowski et al., 2004; Dessart et al., 2006; Kitaura et al., 2006). For CCSN we use a Maxwell-Boltzmann distribution of the kick velocity w

$$f_w(w) = \sqrt{\frac{54}{\pi}} \frac{w^2}{w_{\mathrm{rms}}^3} \exp\left(-\frac{3}{2}\frac{w^2}{w_{\mathrm{rms}}^2}\right) \tag{6.5}$$

with a root-mean-square velocity w_{rms} of 265 km/s for H-rich progenitors (Hobbs et al., 2005), 120 km/s for HeS (Tauris and Bailes, 1996; Coleiro and Chaty, 2013; Tauris et al., 2017) and 60 km/s for SN after Case (A)BC (Kruckow et al., 2018). Following Tauris et al. (2017) and Kruckow et al. (2018), we assume that 20% of the stripped systems receive a kick of 200 km/s. We vary these assumptions by running one scenario without SN kicks and one with only root-mean-square velocities of 265 km/s. We refer to this scenarios as "fiducial", "no kick" and "Hobbs". It is unknown if BHs receive a birth kick (Nelemans et al., 1999; Janka, 2013; Repetto and Nelemans, 2015; Mandel, 2016). Therefore we use two extreme scenarios, either no kick or a flat kick distribution between 0 and 200 km/s (Kruckow et al., 2018). Table 6.1 summarises the SN kicks. We use the results of Tauris and Takens (1998) to calculate the post-SN orbit or, if the binary breaks up, the centre-of-mass velocities of the two components.

To generate a stellar model population, a specified number of binaries is calculated. Each system is assigned an age according to a predefined distribution function. For this study we restrict ourselves to a flat age distribution, i.e. a constant star formation rate. We assume a value in the SMC of $0.05M_{\odot}$/a (Harris and Zaritsky, 2004; Rubele et al., 2015; Hagen et al., 2017; Rubele et al., 2018; Schootemeijer et al., 2021). The parameters of each system at its assigned age are saved. To convert the number of modelled systems into the predicted number of binary systems, we sum the total simulated stellar mass M_{tot} accounting for the additional masses $< 3M_{\odot}$, calculate from that and the width of the age distribution the simulated star formation rate, and compare that to the desired star formation rate to find a conversion factor.

6.2.2 Updates to ComBinE: single stars, mergers and Case A

We implemented several updates to ComBinE. This sections deals with the more minor ones.

Table 6.1: SN types, their kick velocity distribution and characteristic velocities for the fiducial scenario. For CCSN we distinguish between hydrogen-rich models, HeS, and models exploding at the end of Case (A)BC mass transfer.
*Stripped models have a 20% probability of receiving a higher kick ($w_{\mathrm{rms}} = \sqrt{3} \cdot 200\,\mathrm{km/s}$).

SN type	distribution	char. velocity
ECSN	flat	$w \in [0, 50]\,\mathrm{km/s}$
CCSN H-rich	Maxwellian	$w_{\mathrm{rms}} = \sqrt{3} \cdot 265\,\mathrm{km/s}$
CCSN HeS*	Maxwellian	$w_{\mathrm{rms}} = \sqrt{3} \cdot 120\,\mathrm{km/s}$
CCSN Case (A)BC*	Maxwellian	$w_{\mathrm{rms}} = \sqrt{3} \cdot 60\,\mathrm{km/s}$
BH formation	flat	$w = 0$

Compared to Kruckow et al. (2018) we use a new definition of the core mass M_{c}, which reads $M_{\mathrm{c}} = M - M_{\mathrm{H}}/X_{\mathrm{env}}$, where M is the total mass of the model, M_{H} is the model's hydrogen mass and X_{env} is the hydrogen mass fraction above the mass coordinate with a hydrogen mass fraction $X_{\mathrm{thr}} = 0.2X_{\mathrm{s}} + 0.8X_{\mathrm{c}}$, where X_{s} and X_{c} are the values at the surface and in the centre. In the previous version the mass coordinate at which $X = 0.1$ was used, which lead to inconsistencies for hydrogen burning models. The new definition turned out to be a better predictor for the stripped stellar mass. Another change is that the carbon core mass of the hydrogen-rich models is now considered, too, to better predict the SN properties and the remaining lifetime of the HeS.

ComBinE is now able to treat single stars. This is necessary because up to 30% of massive stars may not be part of a binary system or do not interact and a notable fraction of binary stars merges to a single star throughout their live (Podsiadlowski et al., 1992; de Mink et al., 2014). While the true nature of a stellar merger is complicated, we simplify the process by assuming that 10% of the stellar mass is lost in the process (de Mink et al., 2013). The model of the merger process rejuvenates according to its central helium content. We assume that the merger process lasts until the star has reached thermal equilibrium, e.i. about one thermal timescale. Following Schneider et al. (2019) we set the rotation rate of the product to 10% of the critical rotation. ComBinE is neither able to model the changed surface abundance patterns nor the expected magnetic fields of the merger product.

In the previous version, it was assumed that the duration of Case A mass transfer and the final mass of the donor star could be modelled in the same manner as for Case B. We improved the treatment by adopting the results of Ch. 4, namely implementing fit formulae for these two quantities depending on the initial donor mass and the initial orbital period. It turned out that both quantities are independent of the initial mass ratio.

It is an open question under which condition the two binary components in a RLO remain separated or merge to one object (Webbink, 1985). Examples for proposed criteria are the radius evolution of the models and the Roche lobe (Ge et al., 2010, 2015, 2020), the ability of the system to eject the non accreted material (Marchant Campos, 2018; Xu, 2024), limits in mass ratio (de Mink et al., 2014), or thermal equilibrium limited accretion (Hurley et al., 2002). In this study we use the results of Ch. 5 and check if the accretor overfills its outer Lagrange point during accretion. Following Ch. 5 we model both the evolution of the size of the L_2-sphere and the radius evolution of the accretor, which depends on the mass dependent ratio of the accretor's thermal timescale and the mass transfer timescale of the system, modelled by the donor's thermal timescale and the mass-transfer efficiency. If the accretor grows larger than the L_2-sphere, we assume an instable mass transfer.

There are further conditions under which we need to assume that the RLO is unstable. The first condition is accretion onto a hydrogen-rich model after central hydrogen exhaustion as such accretors expand fast. Thus

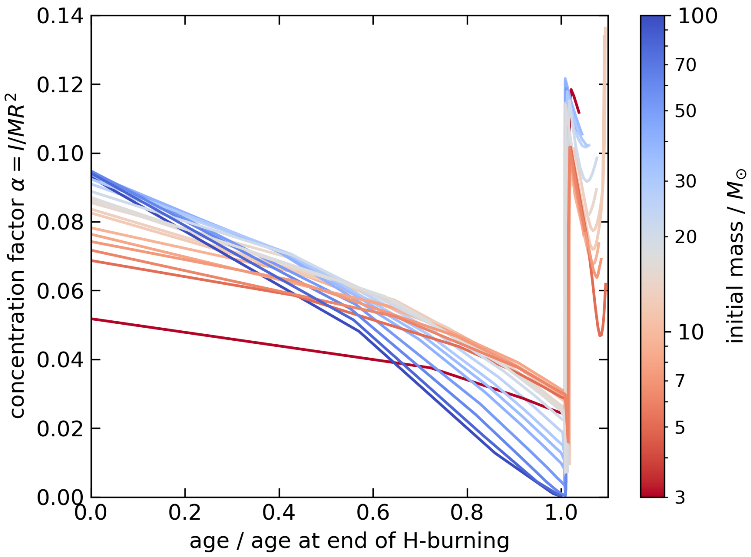

Figure 6.2: Evolution of the concentration factor of our SMC models. The abscissa is scaled in units of hydrogen burning time.

a contact system forms, which is believed to be unstable and merge fast. We assume a similar fate if mass is transferred onto a HeS, as a hydrogen envelope of 10 to 50% of the stellar mass produces a bloated star (Kippenhahn et al., 2012) leading to a contact configuration as above. This fate can be challenged, if the accretion efficiency is small enough to keep the accretor within its Roche lobe. We assume that mass transfer is not stable if the donor has developed a convective envelope. However this approach is challenged by Ge et al. (2010, 2015, 2020) for binaries with mass ratios close to unity. Lastly it is assumed for technical reasons that systems with mass ratios < 0.1 merge immediately.

In case of a HeS donor we employ the same criteria and an additional lower period limit (Tauris et al., 2015). We did not use the criterion of Dewi and Pols (2003) by which the donor is assumed to become convective if it is lighter than some threshold mass leading to a merger. However it turned out that if the hydrogen rich RLO is successful, Case (A)BC is successful, too.

6.2.3 Updates to ComBinE: rotation

We implemented stellar rotation into ComBinE. We decided to use the angular velocity ω of the star to describe rotation in our code as it can be applied to calculate the Roche-limit of the star and is linked the the star's spin angular momentum $S = I\omega$, which is a conserved quantity if tides and mass loss are negligible. I is the stars moment of inertia, which we added to the tabulated single star models ComBinE relies on in form of the concentration factor $\alpha = I/MR^2$. A homogeneous sphere would have $\alpha = 0.4$ and if its density would increase towards the centre one finds $\alpha < 0.4$. We show the concentration factor of our stellar models in Fig. 6.2. Even though a rotating star deforms, leading to a change of moment of inertia, we assume this effect is of second order and use the single star moment of inertia in this work.

Knowing a star's angular velocity, one can calculate its rotational velocity at the equator $v_{\rm rot}$ by multiplication with the star's equatorial radius $R_{\rm eq}$. Since the star deforms due to rotation, the equatorial radius can be up to

1.5 times larger than the polar radius R_p, which remains almost equal to the non-rotating radius. The ratio of the equatorial radius to the polar radius is a function of $\omega/\omega_\mathrm{cr} \in [0,1)$, where ω_cr is the critical angular velocity of the model before it breaks up due to the centrifugal forces at the equator being larger than gravity. One finds

$$\omega_\mathrm{cr} = \sqrt{\frac{GM(1-\Gamma)}{(1.5R_\mathrm{p})^3}}, \tag{6.6}$$

where Γ is the Eddington factor (Kippenhahn et al., 2012). Following Rivinius et al. (2013) the radius ratio is

$$\frac{R_\mathrm{eq}}{R_\mathrm{p}} = 3\frac{\omega_\mathrm{cr}}{\omega}\sin\left(\frac{1}{3}\arcsin\left(\frac{\omega}{\omega_\mathrm{cr}}\right)\right), \tag{6.7}$$

where we simplified their expression. The rotational deformation does not lead to an earlier RLO, since we assume that before Roche-lobe filling the model's rotation synchronises to the orbit, which leads to only mild radius ratios of a factor of about 1.1.

Using this, we can trace the rotation of a stellar model over its evolution given an initial rotation and assuming the same nuclear evolution as for a single star model. If there is neither mass loss nor tides, the angular velocity of the next time step is given by

$$\omega' = \omega\frac{\alpha}{\alpha'}\frac{M}{M'}\left(\frac{R}{R'}\right)^2 \tag{6.8}$$

following from conservation of angular momentum assuming a rigid rotator. We marked the quantities of the next time step with a prime and left those of the previous time step unmarked. For main-sequence model the assumption of rigid rotation is well enough fulfilled, but after central hydrogen exhaustion models clearly rotate differentially (e.g. Yoon et al., 2010; Schürmann et al., 2022). We are not able to trace differential rotation meaningfully with our means and resign from computing it from there on. Also, the rotational decoupling process between core and envelope is not trivial, as Schürmann et al. (2022) showed.

If stellar winds become important, the change of spin angular momentum is

$$\dot{S} = \frac{2}{3}\dot{M}\omega R^2 \tag{6.9}$$

neglecting deformation and assuming isotropic winds (Georgy et al. (2011), see however Hastings et al. (2023)). The wind mass loss rate $\dot{M}$ can be calculated from our tabulated stellar models. Following Langer (1998), wind mass loss is amplified by rotation in form of $\dot{M}_\mathrm{amp} = x\dot{M}$ with

$$x = \left(1 - \frac{v_\mathrm{rot}}{v_\mathrm{cr}}\right)^{-0.43} \tag{6.10}$$

for $v_\mathrm{rot}/v_\mathrm{cr} \in (0, 0.8)$. Since this expression diverges for $v_\mathrm{rot}/v_\mathrm{cr} \to 1$, we extrapolate it linearly by assuming the slope of Eq. 6.10 at $x = 0.8$ giving

$$x = 4.3\frac{v_\mathrm{rot}}{v_\mathrm{cr}} - 1.44. \tag{6.11}$$

With that we can write

$$\frac{\dot{S}}{S} = \frac{2x}{3\alpha}\frac{\dot{M}}{M} \tag{6.12}$$

leading to

$$\omega' = \omega \frac{\alpha}{\alpha'} \left(\frac{M}{M'}\right)^{1-\frac{2x}{3\alpha}} \left(\frac{R}{R'}\right)^2 . \tag{6.13}$$

In a binary system the stars are subject to tides. To account for this we calculate the synchronisation timescales τ_{sync} of the models as Hurley et al. (2002) eq. 44 for hydrogen burning models with radiative envelopes ($M > 1.2M_{\odot}$) and eq. 27 for hydrogen burning models with convective envelopes ($M < 1.2M_{\odot}$), see also Hut (1981). For more evolved stars we do not calculate tides due to the reasons mentioned above. This gives us

$$\omega' = (\omega - \Omega) \exp\left(-\frac{\Delta t}{\tau_{\text{sync}}}\right) + \Omega \tag{6.14}$$

with Ω as the angular velocity of the orbit, e.g. Detmers et al. (2008). Eq. 6.13 and 6.14 applied after one another give than the models's angular velocity at the next time step. Since the orbital angular momentum of a model is much larger than its spin angular momentum, we can neglect changes of the orbit due to tides.

If this scheme leads to a model spinning over-critically, e.g. $\omega > \omega_{\text{cr}}$, we let the model lose additional mass at its equator. As the specific spin angular momentum there is ωR^2 (notice that in contrast to Eq. 6.9 the factor $\frac{2}{3}$ disappears) and thus $\Delta S = \Delta M \omega R^2$. We can assume that the mass loss to bring the model down to critical rotation is small, as Packet (1981) showed that large changes in stellar rotation require only small changes in mass, and therefore the change of radius is small to, we write $\Delta S = \alpha M R^2 \Delta\omega$. Equating these two expressions gives the extra mass loss to bring a model from rotating over-critically back to sub-critical rotation is

$$\frac{\Delta M}{M} = \alpha \cdot \left(1 - \frac{\omega}{\omega_{\text{cr}}}\right). \tag{6.15}$$

It is generally assumed that accretion leads to the spin-up of stars. We calculate the accreted angular momentum depending whether or not an accretion disk forms by calculating

$$R_{\text{min}} = 0.0425 a \sqrt[4]{q + q^2}, \quad 0.0667 \leq q \leq 15, \tag{6.16}$$

a is the semi-major axis, see Lubow and Shu (1975), Ulrich and Burger (1976) and Paxton et al. (2015). If the accretor is larger than this value, we assume ballistic accretion with a specific angular momentum of $\sqrt{1.7 G M R_{\text{min}}}$ and other wise accretion from a Keplerian rotating disk at its equator and thus with a specific angular momentum of $\sqrt{GMR}$, where M and R refer to the accretor's mass and radius. We let the models at most rotate critically and assume that additional material brings no angular momentum with it (see Paczynski, 1991; Popham and Narayan, 1991; de Mink et al., 2013, for a discussion). An alternative view, where the accretion is limited by the accretors spin-up (Petrovic et al., 2005; Marchant Campos, 2018), is investigated in Xu (2024).

6.3 Binary evolution depending on initial mass ratio and orbital period

Before we construct artificial populations from our binary models, we need to understand how different initial masses, mass ratios, orbital periods and mass-transfer efficiencies affect the evolution of a binary in our code. Therefore we drew 10^4 binary models with uniform distribution in mass ratio q and logarithmic orbital period $\log P$ for several fixed primary masses and mass-transfer efficiencies, and evolved them. We classify the evolutionary path until either just after the first SN or the merger of the system, and colour the q–$\log P$ plane according to the nearest model. We differentiate between different reasons for unstable mass transfer and the

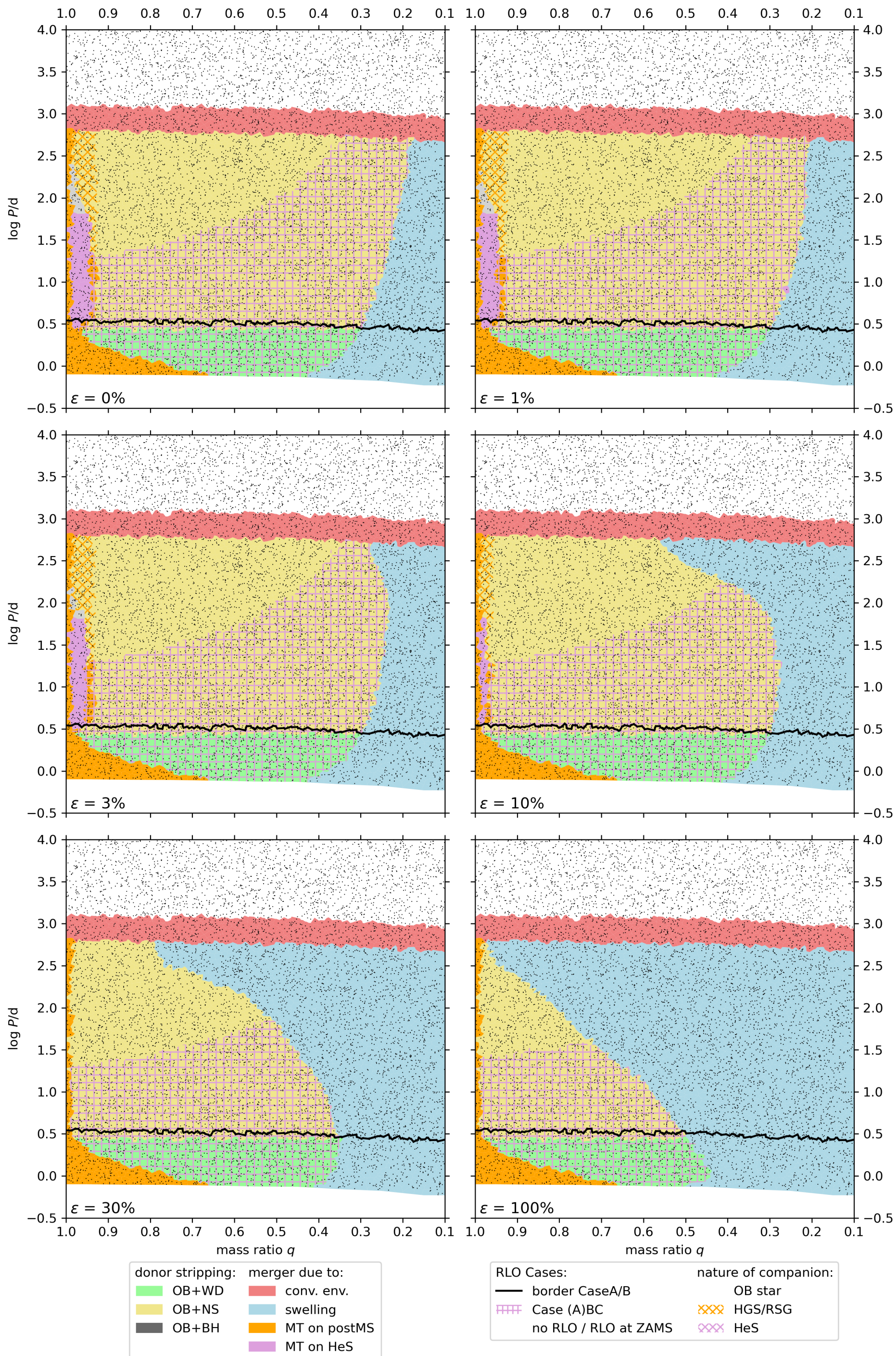

Figure 6.3: Evolution of binary systems with a primary mass of $10 M_{\odot}$ until one componant ends its life or the merger of the system as a function of initial orbital period P and initial mass ratio q for different accretion efficiencies ε. Each black dot represents one model system ($N = 10^4$). We have coloured the plane according to the result of the closest model (Voronoi diagram). In addition, we mark the boundary between RLO Case A and B, the occurrence of a Case (A)BC RLO, and the nature of the companion star if it is not an OB star, but a hydrogen-rich after core hydrogen burning (HGS/RSG) or HeS. White regions are those with no RLO or RLO at ZAMS. The boundary to the latter region is much smoother than the others, as ComBinE does not produce systems overflowing at ZAMS, so we estimated the boundary by eye. Grey systems are undefined.

nature of the SR and its companion star after stable mass transfer and the first SN. In Fig. 6.3 we show that for an initial mass of $10M_\odot$ and Appendix E.1 contains similar diagrams for other masses. For simplicity, we assume no SN kick.

In Fig. 6.3 we find that most of the systems evolve to OB+NS systems (yellow) for low accretion efficiencies and merge because of accretor swelling and subsequent L_2-overflow (blue) in case of high accretion efficiencies. At high orbital periods we expect mergers due to the donor star developing a convective envelope (red) and at even wider orbits no RLO takes place at all (white). A large fraction of systems experience a Case (A)BC mass transfer (+-like pink hatching). Only wide systems do not, as the HeS is not able to fill such a large Roche lobe. Very close systems which untergo Case A mass transfer end up as OB+WD systems (green) unless the mass ratio is too close to unitiy (orange). In this case the slow phase of the mass transfer lasts so long that the accretor ends hydrogen burning, expands and fills its Roche lobe. So, a double contact system is formed which we assume will merge fast.

Systems with mass ratios close to unity show very different fates depending on the precise value of the mass ratio. Those closest to $q = 1$ merge due to mass transfer on a post main-sequence star as for Case A mentioned in the previous paragraph (orange). Here, the accretor ends hydrogen burning while accreting. For slightly lower mass ratios the system merges due to mass transfer onto a HeS (pink). In this case, the donor was able to loose its complete envelope but the former accretor initiates a reverse RLO shortly after that and before the HeS can end its life. This fate is only present for orbital periods below $\sim 10^{1.7}$ d as for wider orbits the initially less massive star cannot fill its Roche lobe any more. This initially more massive star rather becomes a SR while its companion is beyond hydrogen burning (×-like orange hatching). In some models (light grey) both SN happen at the same time (due to the finite temporal resolution of the code). For even lower mass ratios we find mergers due to mass transfer on hydrogen-rich core hydrogen exhausted models again as now the accretor has ended hydrogen burning when a Case BC mass transfer happens. This fate happens only for periods below $\sim 10^{1.3}$ d as above the HeS cannot fill its Roche lobe so the companion of the SR will be a hydrogen exhausted model again. This behaviour is most prominent for low mass-transfer efficiencies as rejuvenation is weak.

The region with mergers due to accretion on a HeS is very interesting as there may be the possibility of stable mass transfer. If the accretion efficiency is high, the initially less massive star transfers its envelope onto the initially more massive one, swapping the two stars' roles of OB star and HeS. However Kippenhahn et al. (2012) predicts that HeS with a hydrogen layer with mass fraction 0.1 to 0.5 should expand to become red giants. So, this channel would probably lead to a merger. However, if the accretion efficiency is low, the initially less massive model looses its envelope becoming a HeS while the initially more massive one does not accrete and expand, remaining being a HeS. So a wide system of two HeS can be formed. Even if the mass transfer is unstable, we found that it is possible that a common envelope is ejected by the HeS yielding a system consisting of two close HeSs. The analysis of these evolutionary paths is unfortunately beyond the scope of this work, but may be the origin of the double WR star SMC AB 5. If we assume a current mass of $50M_\odot$ for both components (Schootemeijer and Langer, 2018, their acual mass ratio is 0.935) and initial masses of $80M_\odot$ (using the models from Schootemeijer et al., 2019), than we have an initial mass ratio of almost 1, after the first mass transfer $q \approx 1.6$ and after the second one $q \approx 1$ (completely non-conservative mass transfer). Following Soberman et al. (1997), the first mass transfer increases the period by a factor of 2.014 and the second one by 1.144. Thus with the current orbital period of 19.6 d, the initial period would have been 8.51 d = $10^{0.93}$ d, which is a value at the lower end of this behaviour in our models (Fig. E.10).

If we consider higher donor masses, we find that Case (A)BC RLOs soon disappear from the evolution as the HeSs do not grow to large radii for higher masses. The regions where mergers occur only shift slightly. Around masses of $20M_\odot$ the donor becomes a BH (dark grey). For even higher masses we find that the

Case A/B boundary shifts to higher orbital periods and that the merger region at $q \approx 1$ becomes larger as the mass-lifetime exponent decreases.

Comparing these diagrams to the predictions of Ch. 5, we find about the same boundary between donor stripping and merger, as expected. We also find that our models merge at low periods and high mass ratios and strip the donor at high periods and high mass ratios. This difference is, as we have already predicted in Ch. 5, due to our consideration of the evolution of the accretor. Compared to Xu (2024), we predict mergers only at mass ratios far from unity if the accretion efficiency is not too high. Only for very high values, systems at intermediate mass ratios and high periods merge. The models of Xu (2024) merge for intermediate mass ratios at low periods (independently for Case A and B), as they use a completely different criterion to decide the stability of a mass transfer. As we show in Sect. 6.5, this leads to strong differences for the period distributions of BeXB and OB+BH systems.

6.4 Influence of the accretion efficiency on artificial populations

In this Section, we present results of our simulations which are weighted by initial mass, mass ratio and orbital period distributions. We compare different mass ratio and orbital period exponents κ and π as described in Sect. 6.2. We also employ the different kick scenarios and vary the accretion efficiency from 10% to 100% in steps of 10% with additional values of 5%, 3%, 2%, and 1%. Each simulation contains 10^7 binary models and is scaled such to a star-formation rate of $0.05 M_\odot$/a. We extract the number of selected types of stars and binary systems (O type stars, OB stars, Be stars, BeXBs, WR+O systems) and compare them to the observed numbers in Fig. 6.4.

The four panels in Fig. 6.4 are ordered in such a way that one can easily identify the impact of the initial binary parameters. The two panels on the left side have rather flat mass ratio distribution ($\kappa \approx 0.0$) but the mass ratio distributions of the panels to the right are skewed towards more unequal systems ($\kappa = -2.8$ and -1.0). The upper panels both have a flat period distribution ($\pi = 1.0$), while for the two lower panels, close systems are preferred ($\pi \approx 0.5$).

We calculate the number of O stars by classifying all models with an effective temperature greater than 31600 K as such. The margin of error derives from varying this number by one spectral class, i.e. 30350 K and 32900 K (Schootemeijer et al., 2021). The observed number of about 400 is the estimate corrected by completeness from Schootemeijer et al. (2021). The numbers of OB and Be stars only includes stars brighter than $G_{pb} = -3$, which is the completion limit of Schootemeijer et al. (2022). We used a distance modulus of 18.91 (Hilditch et al., 2005) and calculated the absolute magnitude following Schootemeijer et al. (2021). We classify all hydrogen burning models as Be stars if they spin faster than 0.95 times their critical rotational velocity (Townsend et al., 2004). The observed numbers of OB and Be stars are from Schootemeijer et al. (2022). For the Be stars we indicate a margin of error by including all hydrogen-burning models after RLO (dash-dotted line) and merger products (blue shading) in that number. We classify a model as WR star if it is a HeS with a luminosity larger than $10^{5.6} L_\odot$ (Shenar et al., 2020b) and compare them to the four WR+O systems in the SMC (Shenar et al., 2016, 2018). The margin of error is the Poisson counting uncertainty, i.e. ± 2. Finally we classify a model as BeXB, if it contains a Be star according to the definition from above and a NS. 107 BeXBs are known in the SMC Haberl and Sturm (2016, living version `https://www.mpe.mpg.de/heg/SMC`) with the dimmest having a magnitude of 16.9.

For all initial distributions in Fig. 6.4, we identify a clear overproduction of O stars. This however not unexpected as this dearth was already discussed by Schootemeijer et al. (2021). The total number of bright OB stars is consistent with the observations and deviates less than a factor 1.5. Both quantities are almost

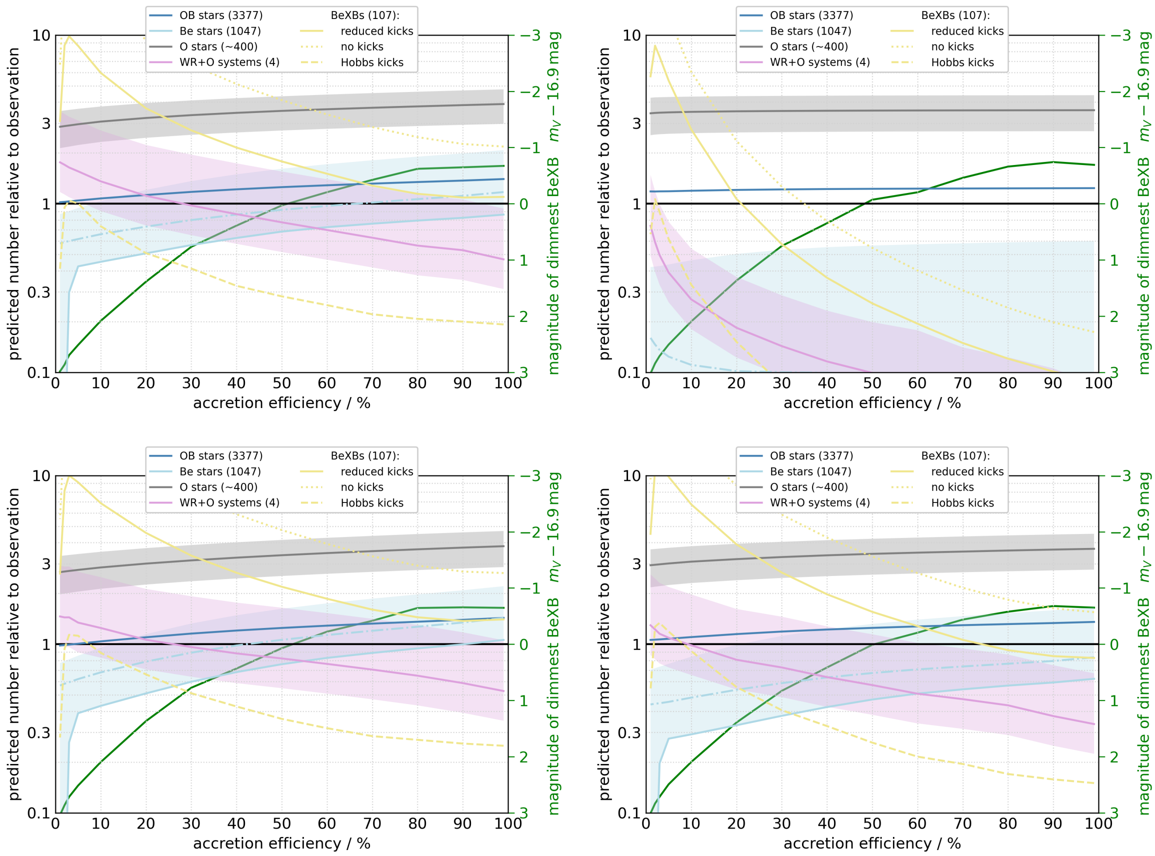

Figure 6.4: Predicted number of selected types of stars and binary systems relative to the observed number (given in parentheses) as a function of accretion efficiency. We indicate margins of error by shading (see text) and show the result for three different kick scenarios for BeXB. In addition, the magnitude of the dimmest synthetic BeXB relative to the dimmest observed one is shown in green with labelling on the right-hand side of the diagram. The initial binary distributions are flat (top left), according to Sana et al. (2012, bottom left), Sana et al. (2013, bottom right), and Dunstall et al. (2015, top right).

independent of the accretion efficiency. The predicted number of WR+O stars agrees for the flat distributions, Sana et al. (2012) and Sana et al. (2013) in a wide range of accretion efficiencies with the best match at 10%. For the Dunstall et al. (2015) distribution, only accretion efficiencies below 5% yield an agreement between simulations and observations. Thus, the number of WR+O systems is unaffected by reasonable variation of the initial period distribution but depends more on the mass ratio distribution. More extreme initial mass ratios lead to more mergers reducing the number of systems. For all initial distributions, we find that the WR+O number decreases with increasing accretion efficiencies. This comes from the larger merger area in Fig. 6.3 and the reduced lifetime of the accretor.

Similarly, we find a less BeXBs at high accretion efficiencies for the same reason. Only for very small accretion efficiencies we observe the opposite trend, since in this case not enough mass is transfered to the accretor which then does not spin fast enough to become a Be star. We predict most BeXBs for the no-kick scenario and least for the Hobbs scenario, as stronger kicks break up the systems more easily. A steeper mass ratio distribution ($\kappa = 0 \rightarrow -1$, lower left to lower right panel in Fig. 6.4) decreases the number of BeXBs due to more systems merging and a steeper period distribution ($\pi = 0 \rightarrow 0.5$, top panels to bottom panels) increases the number of systems especially at high accretion efficiencies as wide systems merge there more often (Fig. 6.3).

A higher accretion efficiency causes the magnitude of the dimmest BeXB to be smaller, as expected for a heavier accretor. This behaviour is independent of the initial mass ratio and orbital period distribution as it does not consider the number but only the occurrence of such systems. For Be stars we find that their number increases with larger accretion efficiency. While a lifetime effect might be present, here the assumed magnitude limit comes into play. A larger accretion efficiency pushed more accretors over the magnitude limit than a lower accretion efficiency. We find more Be stars for steeper period distributions and flatter mass ratio distributions. For the Dunstall et al. (2015) distributions the curve showing the number of Be stars is outside the range of the plot, i.e. this distribution underestimates the number of Be stars by more than a factor of 10. Only the Sana et al. (2012) distribution reproduces the observed number of Be stars and only at very high accretion efficiencies.

If we allow post-RLO systems which our tidal evolution broke down or merger products to appear as Be stars, only the Dunstall et al. (2015) cannot be brought in agreement with the observations. However when doing this one should also consider all OB+NS systems as BeXB, which would lead to an overproduction of BeXBs. Another approach would be to vary the star-formation rate in such a way that it takes a higher value when the Be star progenitors are born. However it turns out that this is at the same age when the BeXB progenitors were born, so their number would be lifted, too. Thus either merger products or single star evolution needs to be considered to explain all Be stars.

In the simulations based on the flat and Sana et al. (2012, 2013) distributions the line for the number of BeXBs and for the magnitude of the dimmest meet at an accretion efficiency of 60% to 75% close to the desired observed level. Thus we can conclude that during the formation of BeXBs the accretion efficiency was rather high. The flat and the Sana et al. (2012) distribution can reproduce the WR+O systems at all accretion efficiencies with a preference for low values but the Sana et al. (2013) distributions only at low ones. Therefore we propose that WR+O system evolved with a low accretion efficiency, meaning that this quantity is a function of stellar mass. We assume in the following that the mass to be considered is the accretor mass, as we assume that this is the place in the system where the material is ejected. LMC stars are probably a better proxy for SMC stars than MW stars, and so we choose the Sana et al. (2013) distributions as our fiducial set. The median initial mass of the WR companions is $35 M_\odot$ in our models and $7 M_\odot$ for the OB stars in BeXBs.

We decide to vary the accretion efficiency linearly between these two accretor masses M_{A}, which yields

$$\varepsilon = 1.21 - 0.72 \log M_{\mathrm{A}}, \quad 7M_{\odot} \leq M_{\mathrm{A}} \leq 35M_{\odot} \tag{6.17}$$

and take the boundary values of 0.6 and 0.1 outside that range. The median mass of accretors in OB+BH progenitors turns out to lie with $15M_{\odot}$ somewhere in between causing an typical accretion efficiency of about 30% in such systems.

In Fig. 6.5 (top) we present the absolute number of OBe stars with certain companions including those which were unbound from their NS in the SN for the distributions from Sana et al. (2013), see Fig. E.12 for other initial distributions. We only consider HeS heavier than $2.55M_{\odot}$ which is a rough limit between WD and NS formation. The numbers reach a maximum at accretion efficiencies of 3% as for larger values the accretors becomes heavier and thus live shorter and the lowest accretion efficiencies do not spin up the accretor to a OBe star. The number of of OBe+HeS does not drop as steeply as the others as it is in general the HeS which ushers in the end of the phase. While a stronger (weaker) SN kick reduces the number of OBe+NS=BeXB systems, the number of unbound systems is increased (decreased). We find that the BH kick can unbind a substantial number of systems reducing their number by a factor of two. We predict 10 to 200 OBe+BH systems. For an accretion efficiency of 30% we predict 50 of them.

Fig. 6.5 (bottom) shows those OB star models which are not rotating fast engough to be classified as emission-line stars. Again the numbers shrink with larger accretion efficiency. At low efficiencies we find a sharp spike due to the inability to become OBe systems at all. The OB+BH systems show a different slope than the other spieces. This may be due to the lower exponent if the mass-lifetime relation for massive stars. Furthermore the SN kicks affect these systems less than the OBe systems since non-OBe stars originate generally from closer and more strongly bound systems. We expect about 150 OB+BH stars from this source.

6.5 Results of the model with mass dependent accretion efficiency

In this Section, we present the properties of our fiducial simulation, i.e. where the accretion efficiency is a function of accretor mass according to Eq. 6.17, with the initial mass ratio and orbital period distributions of Sana et al. (2013) and the SN kicks as in Table 6.1. In the following, we will often differentiate between OBe stars, i.e. main-sequence OB type stars with Balmer emission lines, and regular OB stars, i.e. main-sequence OB type stars without emission lines. For this analysis we rerun our fiducial model with 10^8 binary models.

6.5.1 Companions of SMC OB stars

In Fig 6.6 (left) we show the predicted companions of hydrogen-burning heavy SMC models after RLO as a function of stellar mass. This Figure includes system which became unbound during the SN event, but excludes merger products, single stars and binary stars before interaction. We find five types of companions in such systems, each occurring typically in a certain mass range. HeSs can be found over the whole mass spectrum. This is not surprising, as they are the immediate outcome of stable RLOs. They make up about 20% of OB star companions. In both the low and the high mass regime this fraction turns out to be larger, namely up to 30%. Less than half of their OB star companions are expected to be emission-line stars with a shrinking fraction towards higher masses.

Up to a OB star mass of $14M_{\odot}$ WDs can be found as companions. The OB star is in general an emission-line star. This may be a consequence of Case (A)BC RLO where the accretor is spun up a second time. The

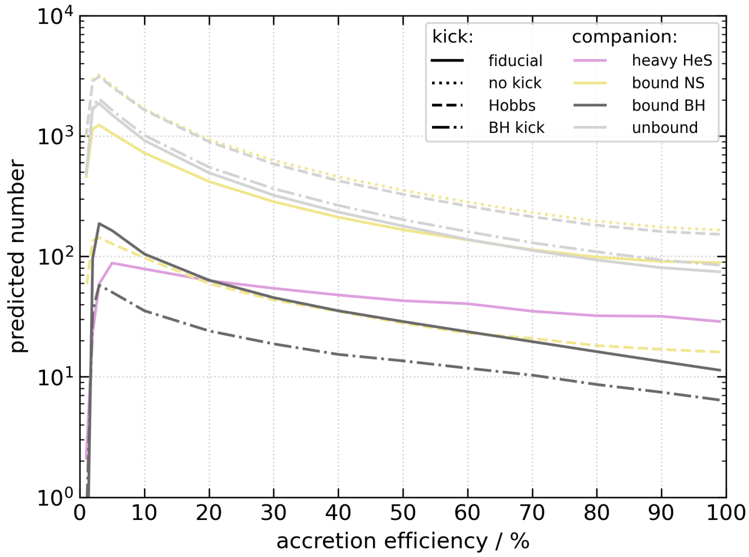

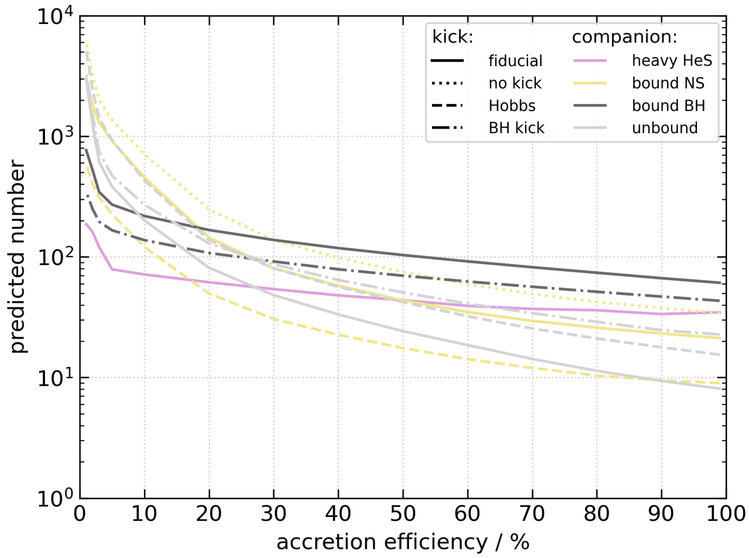

Figure 6.5: Predicted number of OBe star (top) and regular OB star (bottom) companions indicated by colour and different kick scenarios indicated by line style as a function of accretion efficiency for the initial distributions of Sana et al. (2013).

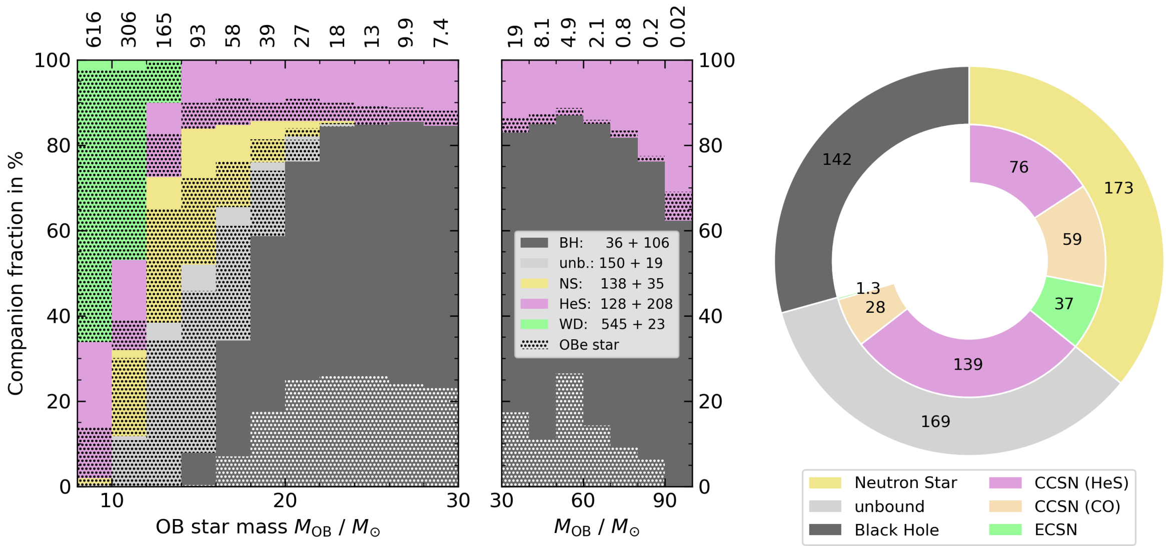

Figure 6.6: Left: Predicted companion fraction of heavy ($M > 8M_\odot$) main-sequence SMC stars after RLO in percent as a function of stellar mass, including systems where the companion (generally a NS) was unbound during the SN and excluding merger products. Models that we expect to appear as emission-line stars are marked with black/white dots. Above each mass bin we give the total number of systems in that bin. The total number of each companion type is given in the legend, distinguishing between emission-line stars (first number) and normal OB stars (second number). Right: Fractions of compact companions of OB stars and their type of the progenitor SN type with the respective predicted numbers.

forming WD is not able to brake the OB star as strongly as the HeS, as it is less massive and the orbit is wider. While WD companions are expected to be the dominant companion type of post-interaction binaries, this prediction changes fast, if one considers massive enough companions. NSs, which appear at OB star masses of $8M_\odot$ supersede the WDs around $12M_\odot$. The NS companion fraction is largest around $15M_\odot$ and becomes zero only above about $24M_\odot$. The ratio of normal OB stars to OBe stars with NS companions increases towards higher masses. In contrast to the WDs, we predict a notable amount of normal OB stars as Case (A)BC is not that relevant, especially at high masses. Unbound systems can be found at the same OB star masses as NS companions as they share the same evolutionary past. Unbound OB stars have a larger OBe fraction than systems with NSs, since they are not subject to synchronising tides of the NS. In agreement with observations, we predict 138 NS+OBe systems which we expect to appear as BeXBs in observations. Additionally, we find 35 normal OB stars with NS companions, which may or may not become SGXBs depending on the stellar and orbital properties.

Lastly, for OB star masses higher than $14M_\odot$, we expect BH companions. They become the majority companions above $18M_\odot$ and reach a constant fraction of 80% from $22M_\odot$ on. Only at the highest companion masses ($> 70M_\odot$), the fraction of BHs decreases slightly. Only a minority ($\sim 30\%$) of BHs has an OBe companion and this number decreases with OB star mass. The reason are the strong tides imposed by the heavy BH on to the star, which grow with mass. At such high masses, angular momentum loss by wind becomes important, too. We predict for the SMC a total number of 150 OB+BH binaries for this scenario without BH kick. 36 of them should have an emission line companions making them relatively easy to detect. Additionally we expect 106 normal OB+BH systems, which may appear as SB1 binaries. Janssens et al.

(2022) predicts that a large fraction of OB+BH systems should be identifiable as such. This result has large consequences for observational campaigns.

Fig. 6.6 (right) shows the companion fraction for systems with NSs or BHs and unbound systems together with the SN type. Bound NS systems, unbound NS systems, and BH systems occur in roughly the same frequency. The most dominant SN type is the CCSN from a HeS progenitor (pink), which make up about 60% of all SN. About 3/4 of them unbind the NS from the system. In CCSN after Case (A)BC RLO most NS remain bound because the kick velocity is smaller than for a HeS progenitor. ECSN, which have the smallest kick, in general do not lead to a disruption. They make up less then 1% of the unbound systems. In this scenario no BH is unbound from the system as we did not assume a kick at BH formation.

6.5.2 Masses of OB stars and their companions

In Fig. 6.7, we show the predicted masses of the components of bound and unbound OB+NS systems and OB+BH systems. We find stellar masses (top row) from 9 to $100 M_\odot$. In different mass ranges different companion types dominate. We find NS companions for stars with 9 to $22 M_\odot$ and BHs from 14 to $100 M_\odot$. Systems which broke up due to the SN kick follow the same patterns as NS systems, with slightly heavier OB stars as the former peak around $13 M_\odot$, while the latter reach their maximum at $12 M_\odot$. OB stars with BH companions have their mode at $20 M_\odot$.

We can understand the mass distributions considering the assumed binary physics. We find the lightest NS progenitors to have an initial mass of about $10 M_\odot$. Such a star has according to our models a $3 M_\odot$ helium core at core hydrogen exhaustion, thus $7 M_\odot$ are lost from the donor during the mass transfer. The mass-transfer efficiency is around 60% in this mass range and the minimum mass ratio for stable mass transfer is about 0.5 (see Fig. 6.3), which yields a lower limit of $5 M_\odot$ for the initial mass of the accretor and therefore a minimum mass of $9 M_\odot$ for the OB star as seen in Fig. 6.7 (top). Similarly the upper limit and the ranges of the BH companions can be understood.

Fig. 6.7 (top right) shows Case A and B separately. We find that almost all regular OB stars evolved through Case A since in close orbits tidal forces are more efficient in braking the star. Systems tend to disrupt more frequently in Case B which is due to the lower binding energy in wide orbits. In Case A the mass distributions are slightly wider. This is caused by orbital period dependent mass loss of the donor star (see Ch. 4). Since the main-sequence becomes wider for larger mass in our stellar model set, the preference for BH systems to evolve through Case A is not surprising.

The lower panel of Fig. 6.7 show the mass distribution of the BH companions. They range from 4 to $32 M_\odot$ and show a slope $\mathrm{d}\log N/\mathrm{d}M_{\mathrm{BH}}$ of about -0.05. The minimum BH mass derives from the minimum mass of a HeS to form a BH, which is $6.6 M_\odot$ (Sect. 6.2). We assume that the whole carbon core (about half the HeS's mass) and 80% of the helium envelope collapse to the BH. As 20% of the mass is released as gravitational binding energy, we get 4.8 for the minimum mass. The upper mass limit, about $30 M_\odot$, can be found similarly by taking away 50% of the initial mass of a $100 M_\odot$ star, our upper limit, to get the mass of the collapsing HeS.

The BH masses depict interesting differences between RLO Case A and B (Fig. 6.7, bottom right). While the mass distribution of Case A BHs shows the same slope as the total population, for Case B $\mathrm{d}\log N/\mathrm{d}M_{\mathrm{BH}}$ is with -0.1 twice as large. We attribute this to the widening of the main-sequence for increasing stellar mass. As already mentioned, Case B BHs tend to have in general OBe companions, while those are rare for Case A BHs. For them, we find a large dip of OBe companions around $12 M_\odot$, which we cannot explain, but hardly matters as it would increase the number of emission line companions only by 4 to 5, if one would remove the dip by drawing a straight line over it. BHs which formed after a Case B RLO do not reach the

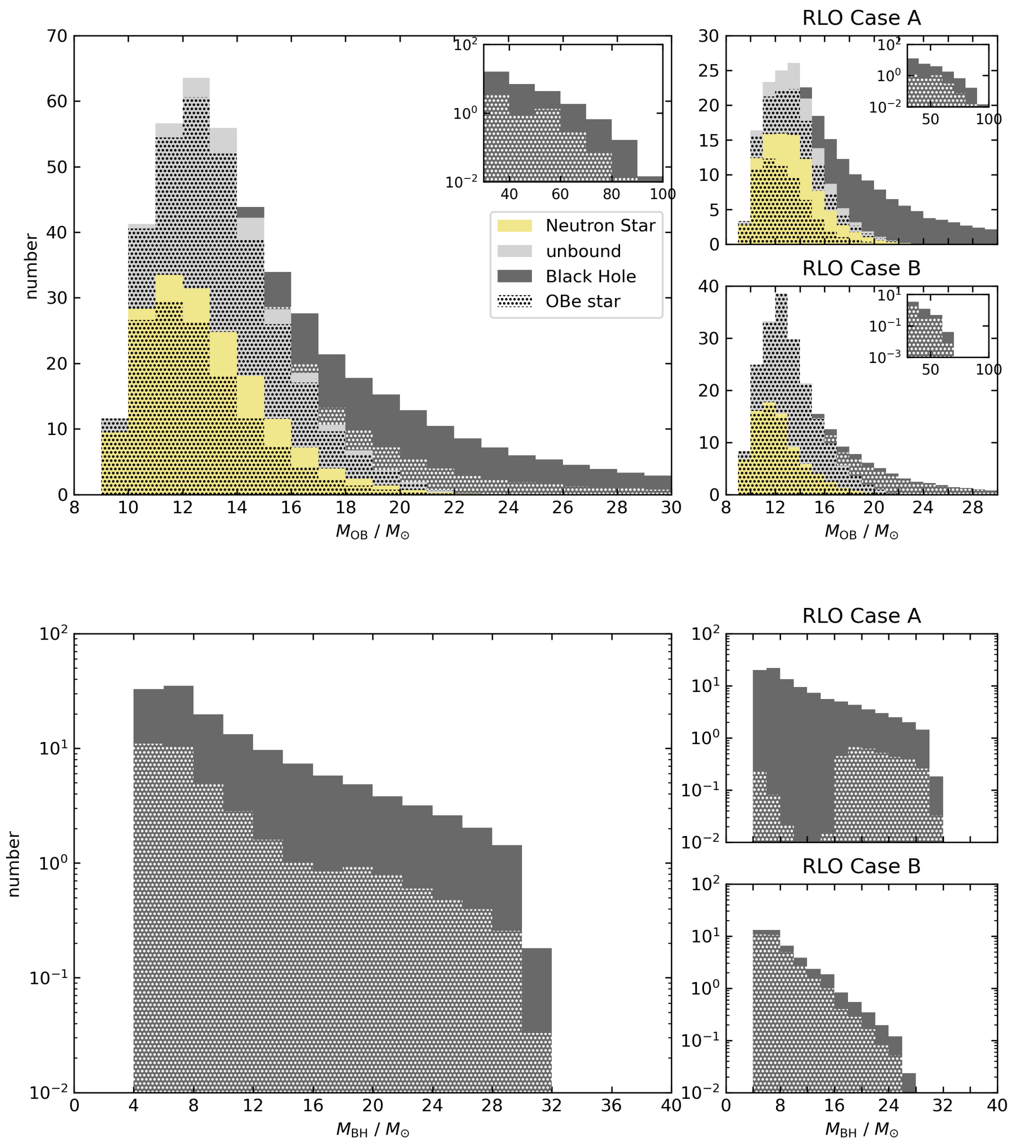

Figure 6.7: Predicted masses of the components of massive binary systems after RLO and the formation of a SR. Top row: OB star masses coloured according to their companion type and marked with dots if we expect an emission-line star. The inlays in the upper right corners focus on the upper mass end. Bottom row: BH masses with dots in case of an OBe companion. Left: Total numbers. Right: Case A RLO (top) and B (bottom) separately.

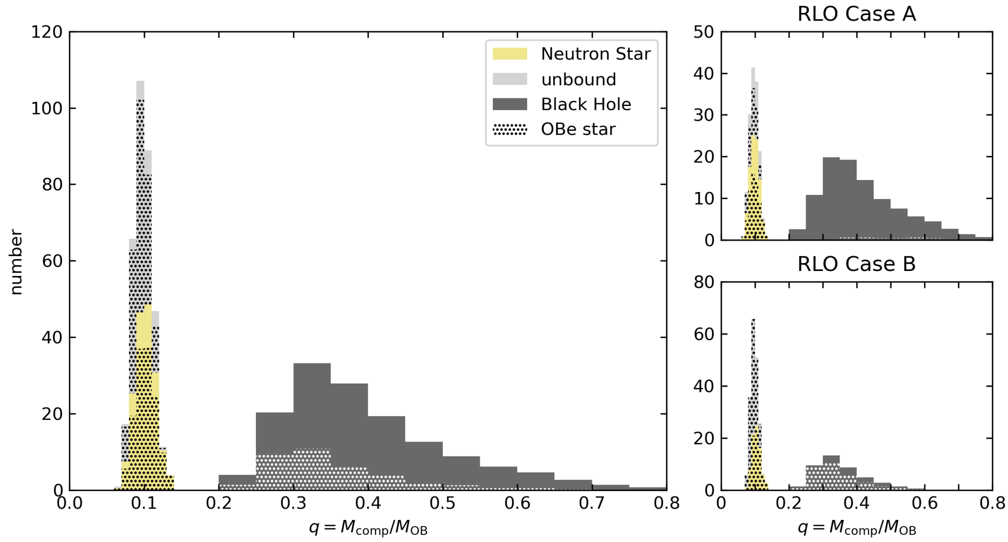

Figure 6.8: Predicted mass ratios ($M_{\mathrm{SR}}/M_{\mathrm{OB}}$) of massive binary systems after RLO and SN, including systems unbound by the SN. (The step size is 0.01 for NSs and 0.05 for BHs.) Left: Total numbers. Right: Case A RLO (top) and B (bottom) separately.

same maximum mass as those from Case A because our stellar models above $80M_\odot$ did not evolve beyond central hydrogen exhaustion.

In Fig. 6.8 we show the mass ratio $q = M_{\mathrm{SR}}/M_{\mathrm{OB}}$ of our OB+SR systems. We find values from 0.05 to 0.15 for NS companions and 0.2 to 0.8 for BH companions. As expected, NSs dominate the lower mass ratio regime and BHs the higher mass ratios. BHs whose progenitors evolved through Case A mass transfer reach masses almost as great as their companions star. The distributions for NS can be understood with the values of Fig. 6.7 and a typical NS mass of $1.3M_\odot$. For OB+BH systems this is more complex, as the BH mass is a function of initial stellar mass and the mass of the OB star depends on the accretion efficiency, which is a function of the accretor mass (Eq. 6.17).

For a better understanding of the mass distributions, we give Fig. 6.9. The distribution in the main panel can be described as being framed by four lines. At first there are the upper and lower BH masses as discussed previously. As we have shown in this Section, one can divide the BH mass by 0.36 to estimate its initial stellar mass. Secondly, the population is limited to the left by a diagonal line following $q \approx 1$. This is the maximum mass ratio discussed in the previous paragraph. These systems stem from those with the initially most extreme mass ratios $q_0 \approx 0.3$. Take for instance the upper left corner with $M_{\mathrm{BH}} \approx 30M_\odot$ and $M_{\mathrm{OB}} \approx 30M_\odot$. The initial BH progenitor mass was about $100M_\odot$ and the initial accretor mass about $25M_\odot$, since the accretion efficiency is small at high masses. The systems in the lower left corner on the other hand ($M_{\mathrm{BH}} \approx 6M_\odot$ and $M_{\mathrm{OB}} \approx 10M_\odot$) had initial masses of about $15M_\odot$ and $6M_\odot$ due to the higher accretion efficiency.

The systems at the right side of Fig. 6.9 are bounded by a line of $q \approx 0.2 \ldots 0.3$ and come from systems with a mass ratio initially close to unity. They explain the lower boundary of OB+BH mass ratios in Fig. 6.8. Here, however, effects of Case A mass transfer come into play. Take for example a system with initial masses of $15M_\odot$ and $14M_\odot$. If the donor loses half of its mass of which about a third (Eq. 6.17) is gained by the accretor, the OB star would have $16M_\odot$, but the diagram shows accretors as heavy as $22M_\odot$ in the lower right

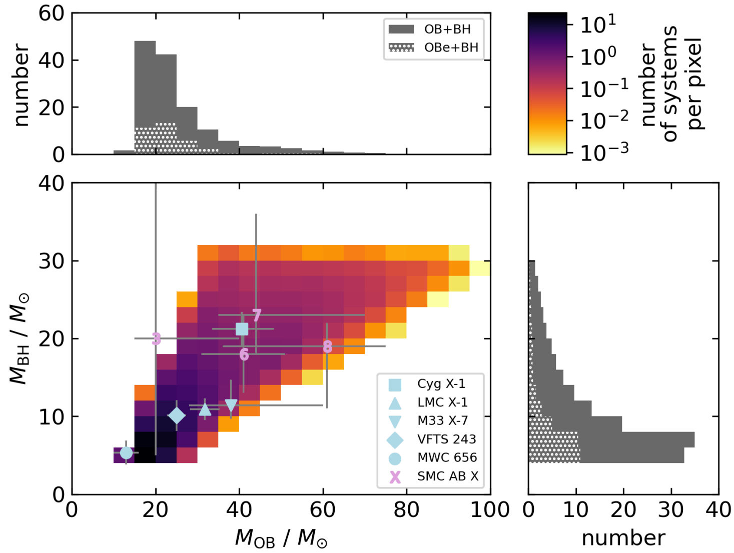

Figure 6.9: Predicted masses of OB+BH systems. The lower left panel shows the number of systems in the mass-mass plane in logarithmic colouring, and the other panels are projections of this onto an axis, i.e. the distribution of OB masses (upper left) and BH masses (lower right), where emission-line stars are marked by white dots. We also show the masses of all known BH+OB systems and the masses of the SMC WR+O systems.

corner of the population. This is due to the fact, that donors which evolve though Case A mass transfer can lose more than half of their mass, especially if a Case ABC mass transfers strips them even further, reducing the mass of the BH and increasing the mass of the OB star. The difference between Case A and B is well visible in the right panels of Fig. 6.8. For the density of systems per pixel in Fig. 6.9 we note, that the number of systems decreases for larger BH masses, but is fairly constant for varying OB masses. The former derives from the initial mass function and the latter from the near flat initial mass ratio distribution. This means it is more likely to find a $30M_\odot$ OB star with a $15M_\odot$ BH than with a $30M_\odot$ BH, but it is about equally likely for a $20M_\odot$ BH to have a $30M_\odot$ and a $50M_\odot$ OB companion.

6.5.3 Luminosities, temperatures and magnitudes

Closely related to the stellar mass is the luminosity. Hence it is straightforward to consider the Hertzsprung-Russell diagrams (HRD) of our predicted populations in Fig. 6.10. It is expected that fast rotating stars redden due to the von Zeipel-theorem. We are not able to include this effect in our analysis as our models are fixed and rather show the non-rotational effective temperature. We show the companions of the BHs in the upper panel of Fig. 6.10. They have luminosities from $10^{4.5}L_\odot$ to $10^{6.5}L_\odot$ and display temperatures from 25 kK to 50 kK corresponding to O and the earliest B type stars. For the most massive companions, the main-sequence broadens a lot leading the temperatures as low as 10 kK. Their contribution is, as one can see in the upper panels, negligible.

The HRDs for the companions of NSs (Fig. 6.10 middle) and those stars which became unbound during the SN (bottom) are as expected very similar. Their luminosities are between $10^4L_\odot$ and $10^5L_\odot$ and their temperatures range from 20 kK to 40 kK which may appear as late O and early B type stars. Comparing the

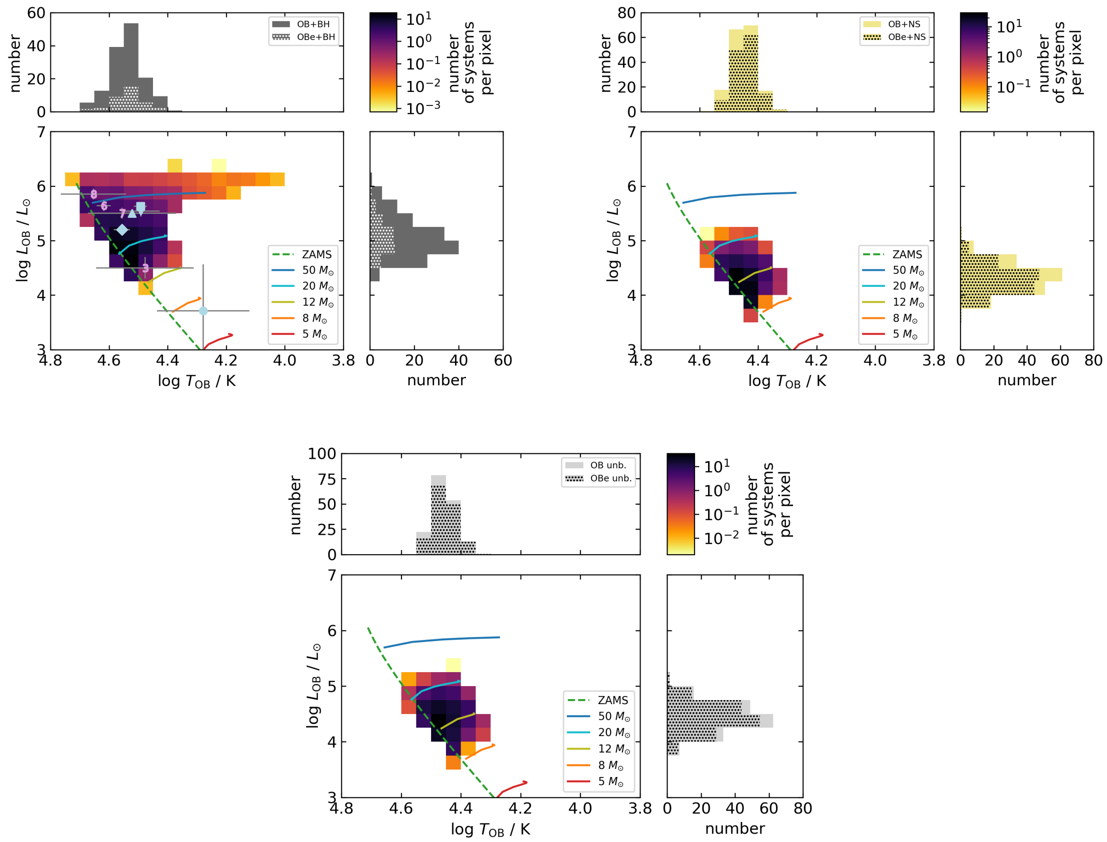

Figure 6.10: Predicted HRD positions of OB stars with a BH (left), NS (right) and unbound companions (bottom) in logarithmic colouring together with selected model tracks and the zero-age main-sequence (ZAMS). We include values from all observed OB+BH systems and the O star of SMC WR+O systems (see Fig. 6.9 for the symbols). The top and right panels show the temperature and luminosity distributions, with predicted emission-line stars highlighted by dotting.

population the the model tracks, one can see that they lie between the $8M_{\odot}$- and the $20M_{\odot}$-track in agreement with the results of Sect. 6.5.2.

To make a meaningful comparison of our simulations with the observations we estimate the V-band magnitudes of our OB star models by using the recipe from Schootemeijer et al. (2021) to calculate magnitudes from luminosity and effective temperature. We show the results in Fig. 6.11. There, the slope of the expected OBe stars $\mathrm{d}\log N/\mathrm{d}m_{\mathrm{V}}$ of about 0.55 until a magnitude of 12, where their number drops significantly, while the number of all post RLO systems continues to follow the same slope. A difference already appears around $m_{\mathrm{V}} = 14$. The magnitudes we find for OB+NS binaries reach from 13 to 17 with a maximum around 15.5. The distribution is skewed towards dimmer stars. BeXBs are slightly more common at larger magnitudes. BHs can be found around stars brighter than 16th magnitude. Thire distribution is flatter and less skewed than the OB+NS distribution.

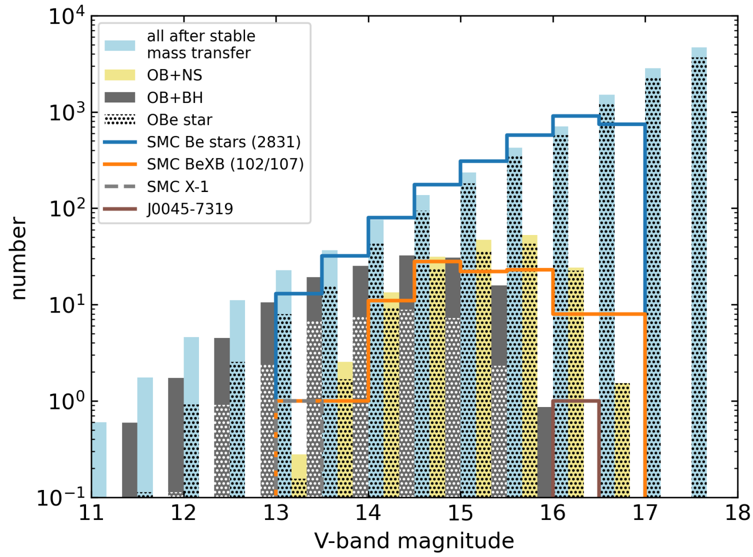

Figure 6.11: Predicted and observed distribution of V-band magnitudes. The blue bars show the magnitudes of all OB star models (i.e. with HeS, WD, NS, and BH companion and unbound systems) after stable mass transfer. OBe candidates are marked with dots. As observations we show the SMC OBe magnitudes distribution from Schootemeijer et al. (2022), the magnitudes of BeXBs from Haberl and Sturm (2016, living version `https://www.mpe.mpg.de/heg/SMC`), SMC X-1 and J0045-7319.

6.5.4 Rotation of OB(e)-stars

Fig. 6.12 shows two different measures for the rotation of the OB star. The upper panel shows the equatorial rotational velocity $v_{\rm rot}$ in km/s and the lower panel that relative to the critical velocity $v_{\rm cr}$. We assume an inclination of 90°. Form the former we find velocities from 25 up to almost 700 km/s in a bimodal distribution. The first peak is near 50 km/s and the second one is around 550 km/s, which is much broader for BH companions than for NS and unbound systems. Similarly the low velocity peak is stronger for BHs than the high velocity peak while for the other two species the high velocity peak is clearly the dominant one. At 350 km/s the velocity distribution has a discontinuity, especially for NS and unbound systems, coinciding with the occurrence of the formation of emission-line stars. This becomes much clearer in the bottom panel. All potential OBe star lie on the right side of $v_{\rm rot}/v_{\rm cr} = 0.95$ and form an extremely strong peak. Due to the variance of the critical velocity it was broadened in the upper diagram. The low velocity peak remains broad and also a clear gap between the two modes is present (0.6 to 0.95).

The panels on the right of Fig. 6.12 indicate Case A and B. Systems which evolved through Case B only belong to the high velocity peak and are OBe stars. Only a negligible fraction of them has $v_{\rm rot}/v_{\rm cr} < 0.95$. Thus we can understand this peak as those stars which were spun up by accretion unaffected by tides. The Case A systems are more complex. While one group exisists at high velocities, which corresponds to wide Case A evaluations similar to Case B, the low rotational velocity peak is only produces through Case A RLO. It is due to synchronising tides that the peak is so broad as the range of orbital periods after RLO leads to a range of synchronous rotational velocities. BH systems are more strongly affected by this as BHs are more massive and thus induces stronger tides than NSs.

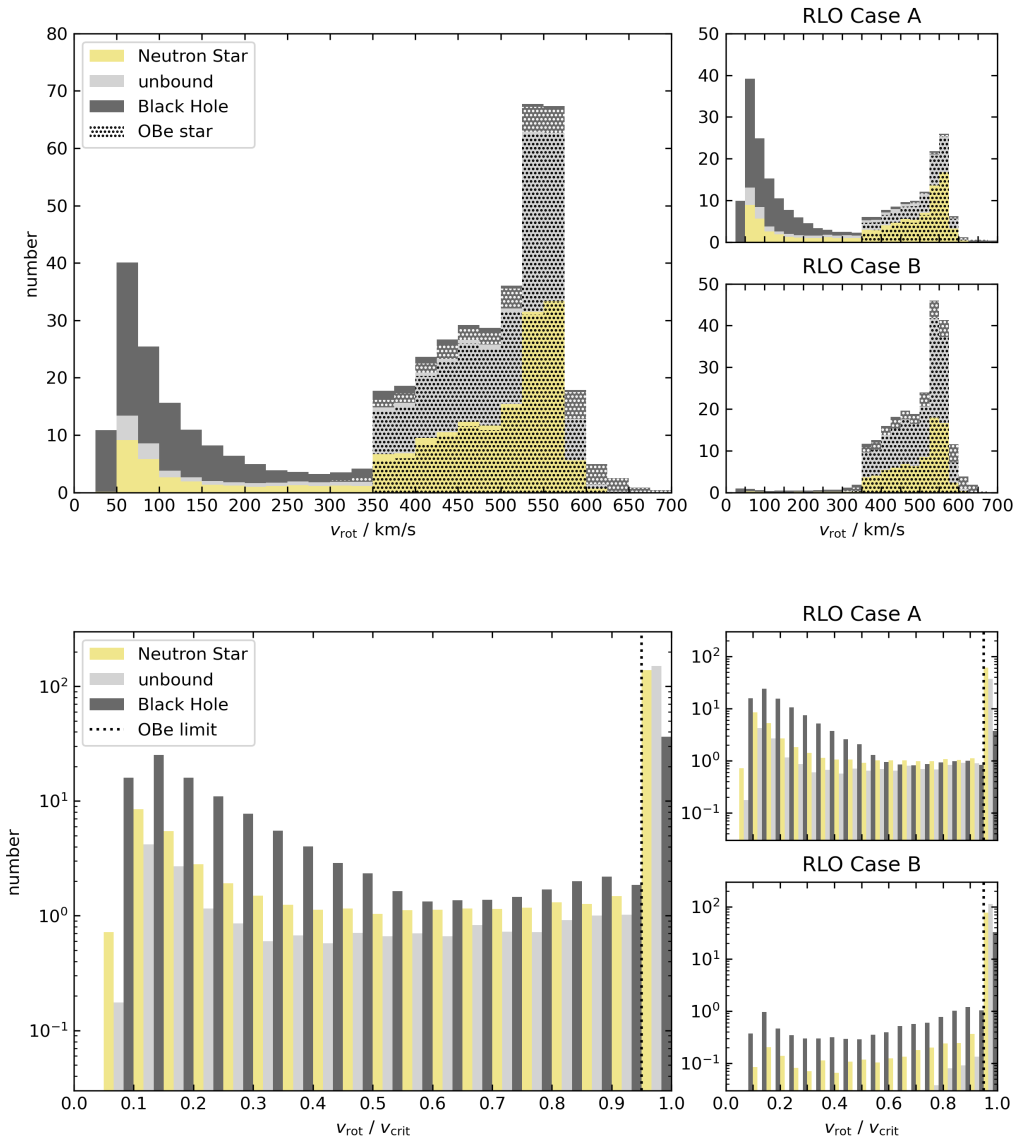

Figure 6.12: Same as Fig. 6.7 but for the equatorial rotational velocity of the OB star (top row) and the ratio of rotational to critical velocity of the OB star (bottom row). Our criterion for an emission-line star is indicated by the dotted line.

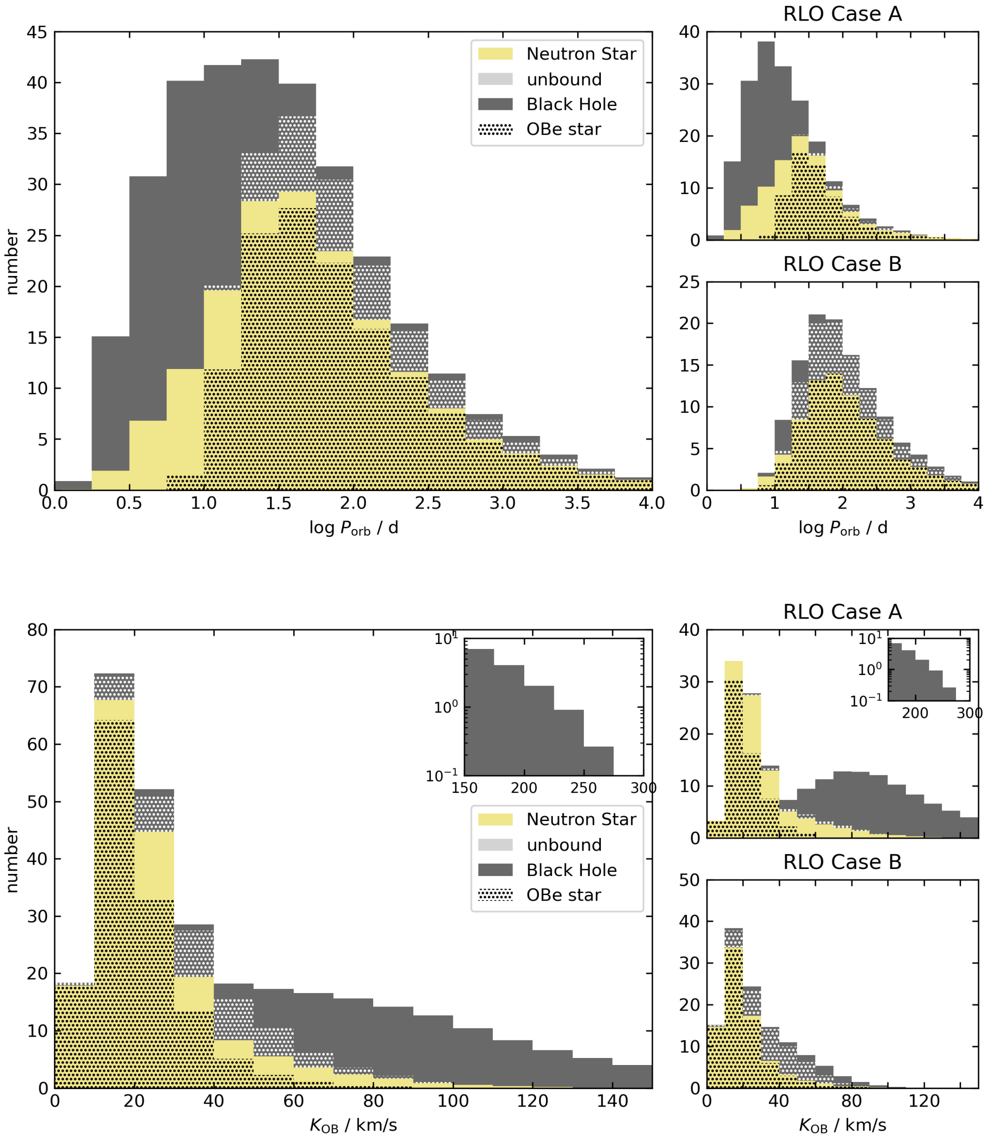

Figure 6.13: Same as Fig. 6.7 but for the orbital period (top row) and the orbital velocity semi-amplitude of the OB star (bottom row).

6.5.5 Orbital parameters

For the systems which remain bound after the formation of the SR, we can analyse their orbital properties. Fig. 6.13 (top) shows the orbital period. For both BH and NS systems we find orbital periods ranging from 1 d up to 1000 d. Most NS systems can be found with 30 d while BH systems orbit slightly faster with the mode at 10 d. Both populations' numbers decrease towards higher periods because of the initial period distribution which prefers close systems and, in case for the NS systems where the accretion efficiency was higher, the reduced stability of mass transfer at greater periods. We find normal OB stars to dominate at low periods because here tides are effective braking the rotation of the star, and OBe stars to dominate in wide orbits where tides are weak. The transition from normal OB to OBe stars happens between 10 d and 30 d. The NSs' transition happens closer to the lower end and the BHs' near the upper end. As expected, Case A systems tend to show lower and Case B system tend to show larger orbital periods.

A histogram of expected orbital velocity semi-amplitude of the OB star

$$K_{\mathrm{OB}} = \frac{M_{\mathrm{SR}}}{M_{\mathrm{SR}} + M_{\mathrm{OB}}} \sqrt{\frac{G(M_{\mathrm{SR}} + M_{\mathrm{OB}})}{a \cdot (1 - e^2)}}, \tag{6.18}$$

where a is the semi-major axis and e is the eccentricity, can be found in Fig. 6.13 (bottom). Note that we show the maximally possible semi-amplitude and not the projection onto the sky-plane, i.e. an inclination of 90° and with an argument of periastron of 90°. OB stars with NS companions reach velocities up to 100 km/s, but peak at 20 km/s. The companions of BHs show a much broader distribution between 10 km/s and 250 km/s. OB stars in BH systems are typically faster than in NS systems, because of the high BH mass compared to NSs, and are so diverse in velocity semi-amplitude because of the broad mass distribution of BHs. Again, OB stars with a large semi-amplitude tend to be normal OB stars as they are orbits is close and tides are braking the stellar rotation. While the distributions for Case A and B look similar for the NS, they clearly differ for the BHs, as the high velocity contribution comes from the Case A systems.

Fig. 6.14 focuses on the orbital properties of our OB+BH binaries. In the upper left panel we find, in agreement with Fig. 6.7 and 6.13 that systems with masses around $20 M_\odot$ and velocity semi-amplitudes from 25 to 150 km/s are preferred. Only the widest systems, those with low orbit velocities, become OBe stars. The upper right corner is empty as their progenitors would have initially overfilled their Roche lobe. The intend at high velocities and low masses is due to the progenitor after Case A being to light to form a BH. The upper right panel shows a somewhat narrow relation between orbital period and velocity semi-amplitude, which is due to Kepler's law. In the lower left panel the combined distribution of orbital period and OB mass is shown. Both quantities are highly skewed and peak at low values. Towards high masses and periods a wide plane can be found. The upper right corner is empty because such system are very rare due to the initial distributions. Systems with low periods and high masses are avoided as such systems would overfill their Roche-lobe initially. Finally, the lower right panel depicts orbital period and eccentricity. This quantity only assumes values between 0.05 and 0.2 and strongly peaks at 0.1. The reason is our BH formation formalism. As 20% of the helium envelope is lost, the BH progenitor loses some of its momentum, which translates to a non-zero eccentricity (Tauris and Takens, 1998). Varying the mass loss or imposing a kick on the BH would change the resulting eccentricity dramatically. Note however that our prescription does not account for the continuous circularisation of the orbit due to tides after the SN, so the real eccentricity may be lower. Nevertheless the eccentricity distribution of wide OB+BH systems could be a probe for BH kicks.

We show a combined histogram of rotational and orbital velocity of OB+BH systems in Fig. 6.15. We find that the OB+BH populations divides clearly in two sub-groups. The somewhat larger group can be found at low rotational (< 200 km/s) and medium to high orbital (> 50 km/s) velocities. These systems evolved through Case A RLO and are normal OB stars. Systems with high rotational (> 300 km/s) and low orbital (~ 50 km/s) velocities form the second group. They are in general emission-line stars. This has an important consequence for the observational search for BHs. We find that on one site high radial velocity variations in SB1 systems and on the other site that OBe stars are a predictor of BH companions.

The orbital properties, namely period and eccentricity, for OB+NS binaries are shown in in Fig. 6.16. We do not treat mass ratio and orbital velocity here because they are rather uninteresting as the NS mass is strongly confined and the OB stars' velocities are very low due the low NS mass. The upper panel shows

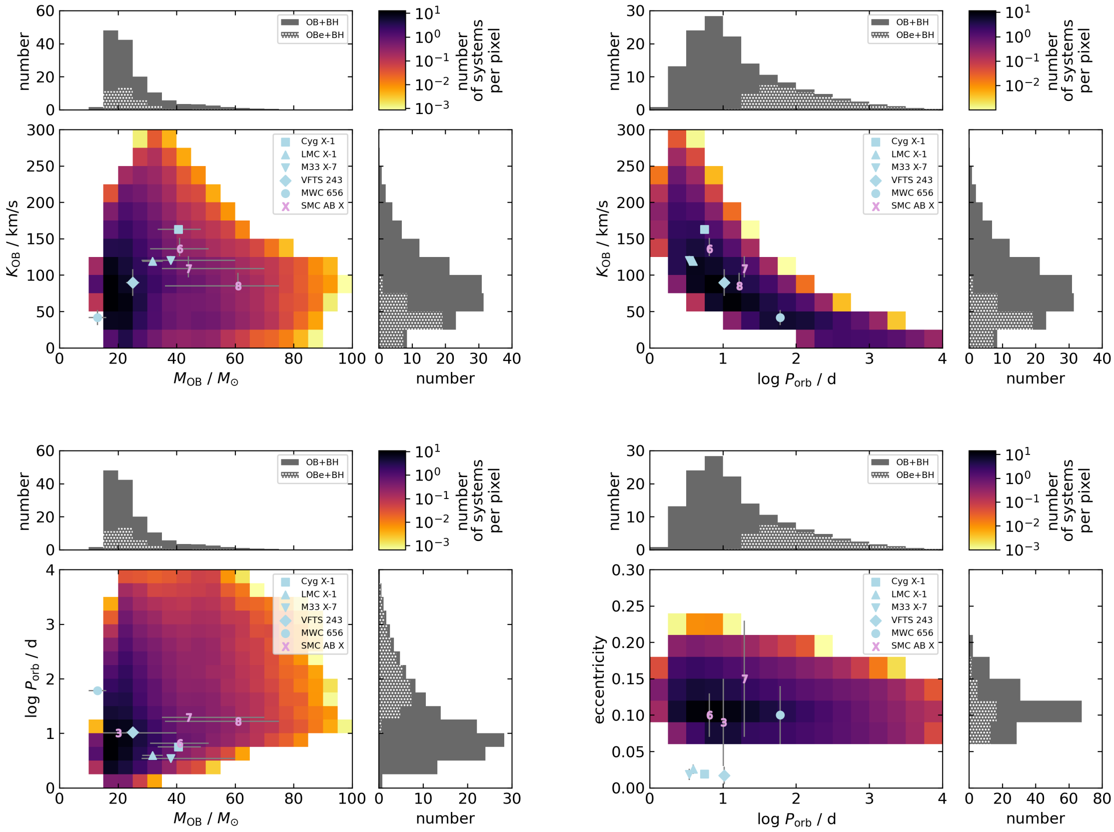

Figure 6.14: Predicted orbital properties of OB+BH systems with measurements of all known OB+BH and SMC WR+O systems, as in Fig. 6.9. Top left: OB mass–velocity semi-amplitude plane. Top right: orbital period–velocity semi-amplitude plane. Bottom left: OB mass–orbital period plane. Bottom right: orbital period–eccentricity plane.

a 2d histogram of period and eccentricity. The eccentricities follow a very broad distribution covering all values from 0 to 1 and the periods' mode is, as discussed above, between 10 and 100 d. The combined distribution has accordingly a large main feature at these values. A notable exception is a preference for large orbital periods at high eccentricities and an avoidance of high eccentricities at low orbital periods. This is not surprising as such a combination would lead to Roche-lobe overfilling periastron distances. While emission-line stars are more frequent at large orbital periods, we find no dependency on eccentricity.

In the middle and lower panel of Fig. 6.16, we show the period and eccentricity distribution coloured according to the SN type which formed the NS. CCSN from a HeS, CCSN after a Case (A)BC RLO and ECSN have slightly different typical orbital periods, increasing in that order. This means systems with a stronger kick lead to lower orbital periods, which may sound counter-intuitive but can be explained with wider orbits being more likely to unbind than close orbits. Furthermore, CCSN from a HeS progenitor are the only species which yields a notable amount of regular OB stars as tidal breaking before the SN is only possible here. In case of a CCSN after Case (A)BC RLO the OB star was just spun-up again and system which undergo a ECSN and are close enough for effective tidal braking also experience such a mass transfer. The eccentricities of systems which evolved through ECSN show the smallest eccentricities and those which

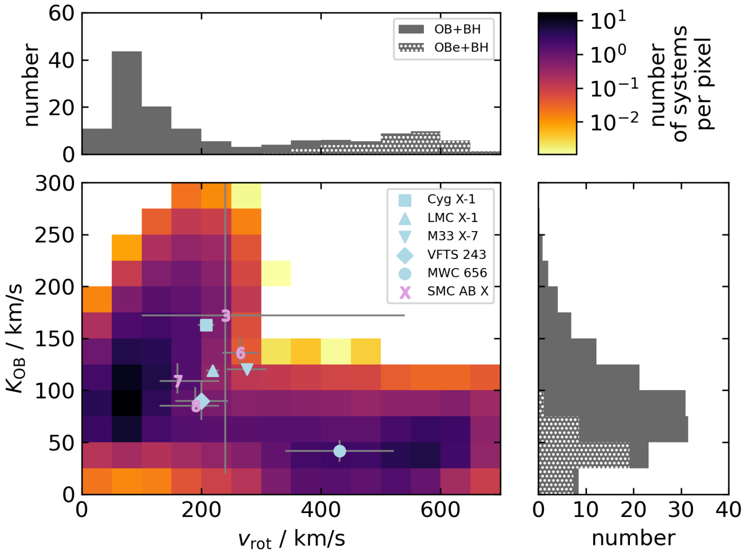

Figure 6.15: Same as Fig. 6.9, but for the rotational velocity and the orbital velocity semi-amplitude.

experienced a CCSN from a HeS the largest. This also reflects the magnitude of the SN kick as larger kick velocities lead to more eccentric systems. As mentioned above we did not employ continuous tidal induced circularisation of the orbit which may affect the eccentricity distribution.

6.5.6 Systemic velocity

Because a SN kick changes the momentum of the system, we are able to predict the space velocity $v_{\mathrm{OB}}^{3\mathrm{D}}$ of our OB systems and ejected OB stars as we do in Fig. 6.17. We find that NS systems (yellow) have the broadest distribution from 0 to up to 100 km/s. Even more striking is that this distribution is bimodal with one narrow maximum at 10 km/s and a wide one at 40 km/s. Inspecting the lower left panel we see that the second peak comes exclusively from CCSN with a HeS progenitor. As they have the largest kick velocities leading to the large space velocities. CCSN after Case (A)BC RLO and ECSN lead to lower space velocities in agreement with the strength of their kicks. NS systems with the largest space velocities tend not to be OBe stars. This is due to the fact that the pre-SN orbital velocity leaves an imprint on the space velocity (Tauris and Takens, 1998). Thus we can follow that they come from initially close binaries which explains the absence of fast rotation. The panels on the top right support that Case A produces faster systems.

For unbound systems we find the most common space velocity just above 10 km/s. They again reach up to almost 100 km/s but do not have the bimodality of their bound counterparts. BH systems show a unimodal distribution, too. However it does not extend to such high velocities and peaks 20 km/s. Their velocities are, as for the eccentricities, not due to a kick but due to mass loss during BH formation.

In the lower right panel of Fig. 6.17 we show a 2d histogram of spacial and rotational velocities of all OB+SR systems, whether bound or unbound. We find similarly to Fig. 6.15 two populations. First, there are systems with high rotational (> 300 km/s) and relatively low spatial velocity (peak at 10 km/s), which are the Case B and wide Case A systems. Then there are systems with low rotational (~ 100 km/s) and higher

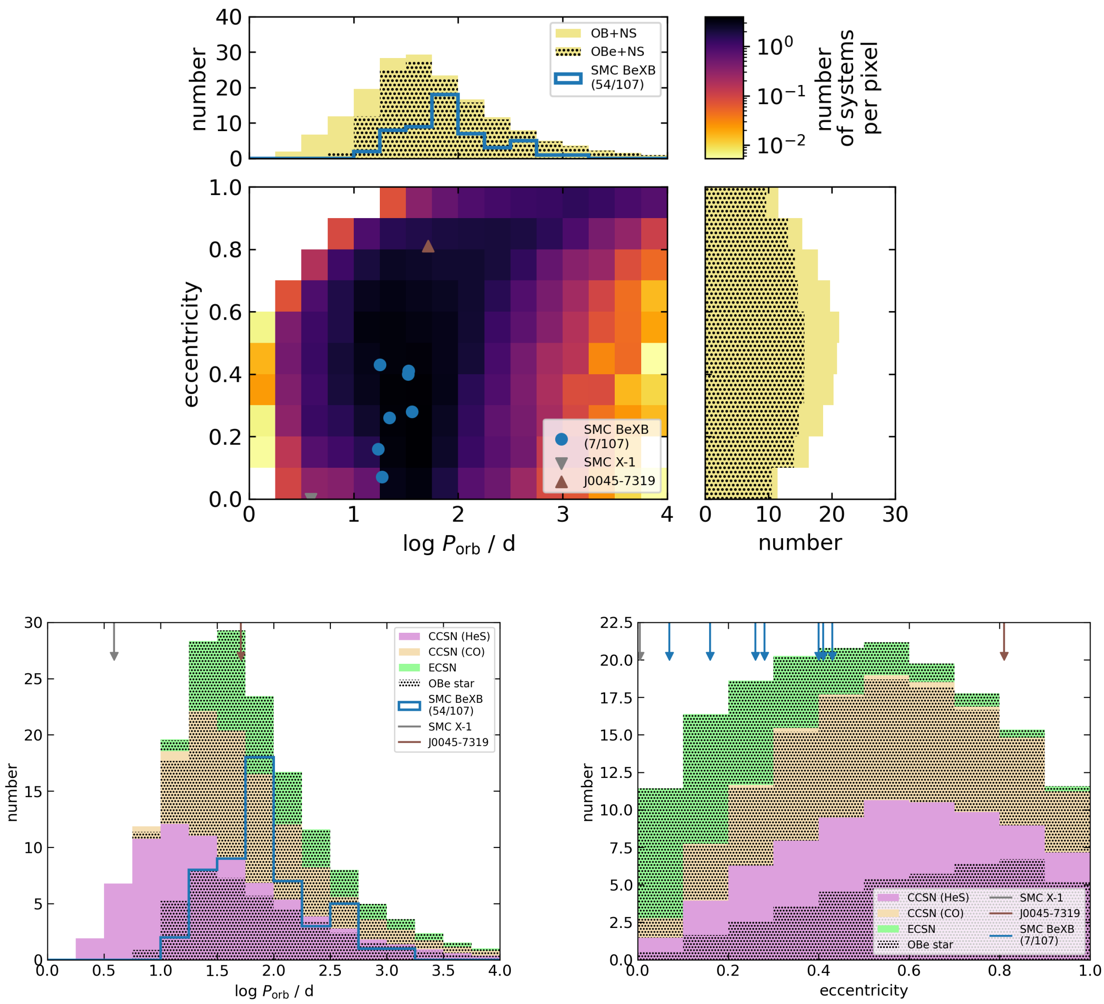

Figure 6.16: Predicted orbital properties of OB+NS with observations of the SMC BeXBs, SMC X-1, and J0045-7319, as in Fig. 6.9. Top: orbital period–eccentricity plane. Left: orbital period coloured by SN-type. Right: eccentricity coloured by SN-type.

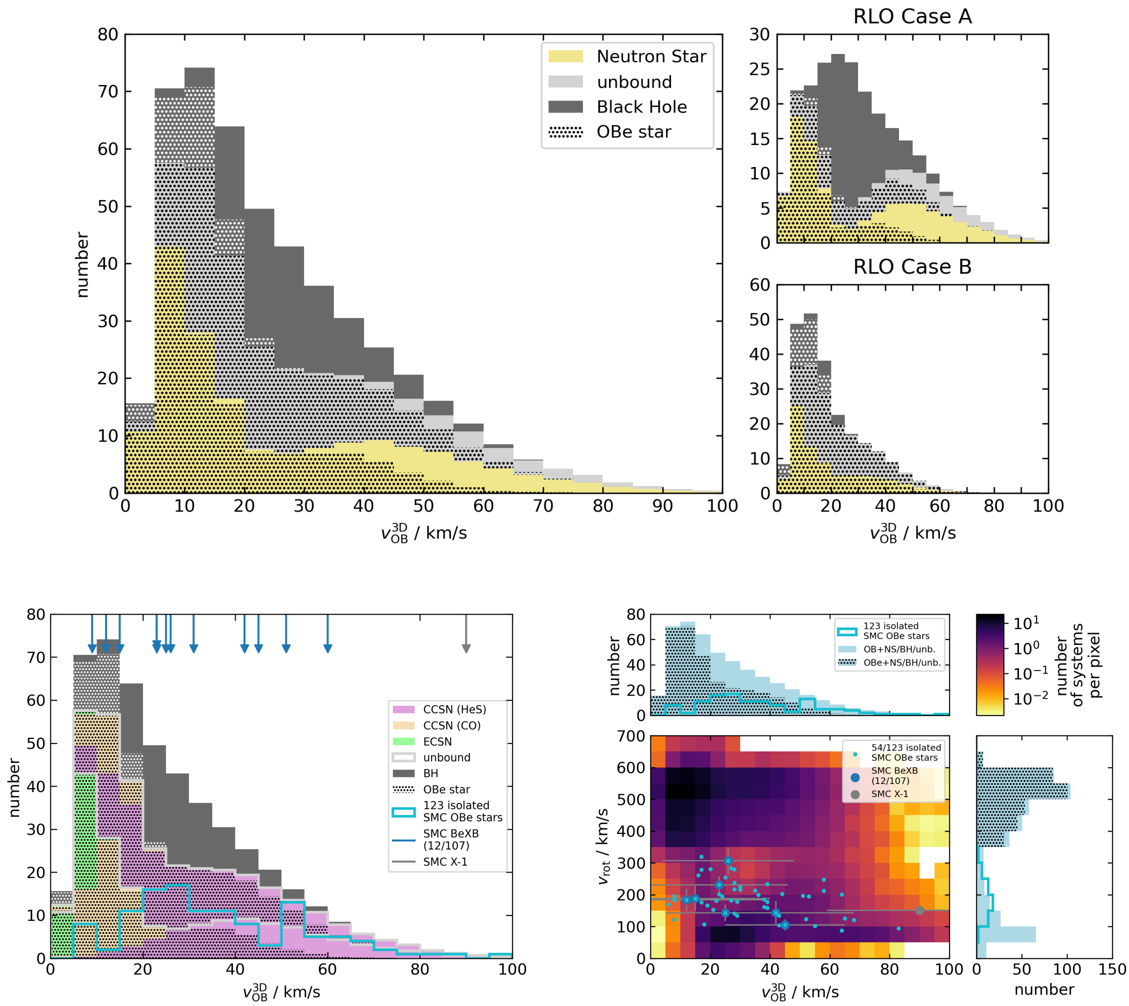

Figure 6.17: Top: Same as Fig. 6.7 but for the space velocity of the OB star. Bottom left: Space velocity coloured by SN-type with observation of the transverse velocities of isolated SMC OBe stars, BeXBs, and SMC X-1. Bottom right: Systemic velocity and rotational velocity of OB stars with bound and unbound NS and BH companions as in Fig. 6.9 and the same observational data as in the left panel. The median error of the transverse velocities is 23 km/s.

spacial velocities (mode at 20 km/s). These are the narrow Case A systems where tidal locking is relevant which inherited their fast orbital velocity as systemic velocity.

6.5.7 Wolf-Rayet stars

We assume, following Shenar et al. (2020b), that a HeS with a luminosity above $5.6 L_{\odot}$ appears as a WR-star. We show the properties of our simulated O+WR systems in Fig. 6.18. As usual we label O star which rotate faster than 95% their critical rotation as OBe stars, even though the WR or O star wind may prevent the formation of a disk or slow the O star's rotation down. WR+WR and WR+SR systems are beyond the scope of this work.

The upper left panel shows the luminosities of the two components. While the number of WRs decreases towards higher values as expected from the initial mass function, the luminosities of the O stars are more symmetrical, but still screw. In the 2d histogram, the population forms a rough triangle since more luminous and thus more massive WRs have more massive and luminous companions. The K_{WR}–K_{OB} diagram (lower right panel of Fig. 6.18) shows that the orbital velocity semi-amplitudes are in good correlation. This is not surprising as both stars have roughly the same mass. Low velocities, especially for the OB star are somewhat preferred but a notable amount of stars still shows values above 200 km/s.

In the two panels on the right side of Fig. 6.18 we investigate the relation between the OB star's rotational velocity to the orbital properties. We expect orbital periods from 1 d to 1000 d with a preference for short periods around 10 d. Velocity semi-amplitudes range up to 450 km/s, but most common are values of about 100 km/s. As for the OB+BH systems we find a bimodality in the rotation rate of the OB star, but a less pronounced one. The two 2d histograms show again a distribution with two peaks, one for the close systems where tidal braking slowed the OB star down and one for the wide systems where the OB star could keep most of its spin angular momentum.

6.6 Discussion

In this Section, we discuss the main uncertainties of our results (Sect. 6.6.1), compare our results with observations (Sect. 6.6.2), with the companion study by Xu (2024, Sect. 6.6.3), and with previous work (Sect. 6.6.4).

6.6.1 Uncertainties

Stability of mass transfer and accretion efficiency

The key uncertainty of this study is the condition under which a RLO is stable and leads to a stripped donor and under which the system mergers. We used the proposition of Ch. 5 to link that to the swelling of the accretor star to the accretion efficiency, which forms the second key uncertainty. Several other conditions have been proposed in the literature. Most prominent is the comparison of the radius evolution of the Roche lobe under mass loss with the adiabatic radius evolution of the donor, most recently investigated by Ge et al. (2010, 2015, 2020). These studies find a period dependent minimum mass ratio for donor stripping, which itself has a minimum for a $10 M_{\odot}$ donor around $q = 0.15$ and decreases for higher masses. In Ch. 5 we discussed that those condition is in general more restrictive than the one of Ge et al. (2010, 2015, 2020). While we assume that donors with a deep convective envelope always result in a unstable mass transfer, aforementioned

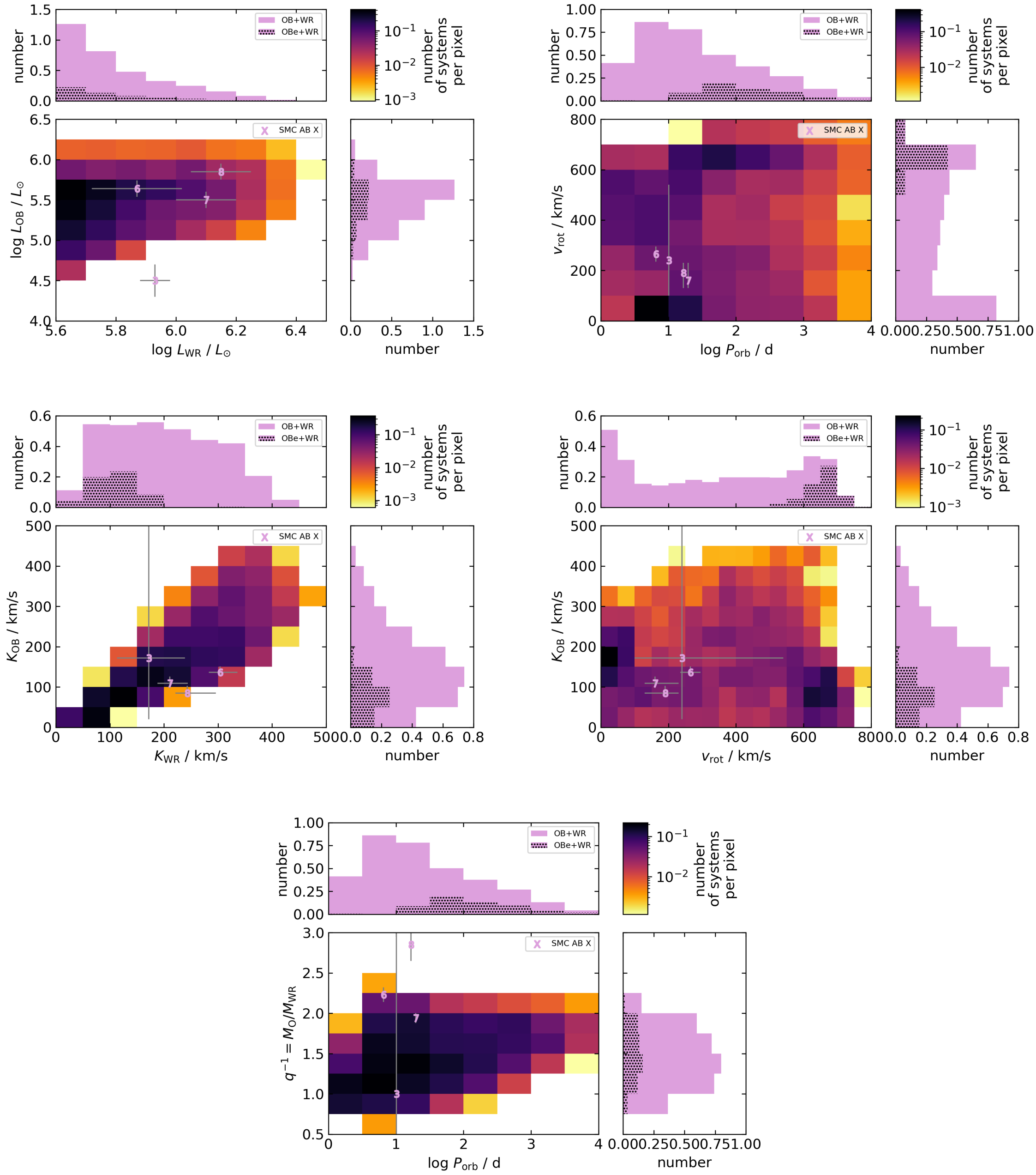

Figure 6.18: Predicted properties of WR+O systems with observations of the SMC WR+O systems (Foellmi et al., 2003; Shenar et al., 2016, 2018), in the same manner as Fig. 6.9. Top left: luminosity-luminosity plane. Top right: orbital period–rotational velocity plane. Middle left: orbital velocity semi-amplitude plane. Middle right: orbital velocity semi-amplitude–rotational velocity plane. Bottom: orbital period–mass ratio plane.

studies find that mass transfer might be stable for systems close to a mass ratio of unity (see also Ercolino et al., 2023).

An other physically motivated approach was undertaken by Marchant Campos (2018), whose method was also used by Xu (2024). They stop the deposition of material onto the accretor if it starts to rotate critically. If then the combined luminosity of the two stars is large enough to drive the non-accreted material out of the system, the mass transfer is regarded as stable. The comparison of our Fig. 6.3 with their Fig. 2, A.1 and A.2 shows a drastic difference. This will be further discussed in Sect. 6.6.3.

Studies (e.g. Pols et al., 1991; Hurley et al., 2002; Schneider et al., 2015; Renzo et al., 2019) use fixed minimal mass ratios for stable mass transfer for each Case A and B to decide as the merger criterion, but limit the accretion by the thermal timescale of the accretor, whereby the accretion efficiency becomes a function of period and mass ratio. Details on that are discussed in Sect. 6.6.4.

Case A RLO

Case A mass transfer takes place on the nuclear timescale of the donor and comprises three phases of different structure, which determine the evolution of the stellar masses (Wellstein et al., 2001). The adopted scheme based on the results of Ch. 4 might be too simplistic as their underlying models are restricted to a certain set of assumptions of binary physics. Furthermore we do not resolve the mass transfers phases in detail but jump after a reasonable amount of time directly to the OB+HeS phase. While we are not interested at the models configuration as an Algol system during the mass transfer (e.g. Sen et al., 2021), the detailed evolution may have an imprint on the outcome and the subsequent OB+SR phase, especially at initial mass ratios smaller than about 0.5, where the orbit shirks a lot during RLO (Ch. 4).

Stellar models

Our predictions rely on the assumed underlying stellar models. A key uncertainty lies in the HeS models. They influence the evolution of our systems by two ways. At first there is their lifetime which determines when a SR forms. This can have an influence on whether a reverse mass transfer occurs. Second, the radius evolution determines if and when a Case (A)BC RLO takes place. This is important as the assumed SMC HeS models are extrapolated from Milky Way models (Kruckow et al., 2018) and, most importantly, a thin remaining hydrogen layer was not considered in modelling these stars. As Laplace et al. (2020) have shown, the radius evolution of stripped stars has a noticeable effect on the final fate of the system. The occurrence of Case (A)BC mass transfer changes not only the orbital period of the system (Soberman et al., 1997), but also impacts the SN kick (Sect. 6.2) and determines the final mass of the SR.

An other uncertainty of the stellar models lies in envelope inflation. Sanyal et al. (2015) showed that stellar models heavier than about $40 M_\odot$ can exceed the local Eddington limit in their envelope, which leads to a large increase in radius and to a convective envelope. As we assume unstable mass transfer for a donor with a deep convective envelope, including this effect into our models could drastically reduce the production of massive HeS by binary stripping and consequently the formation of WR+O and BH+OB systems.

Formation of Be stars

In this study we followed Townsend et al. (2004) and assumed that models with $v_{\rm rot}/v_{\rm cr} > 0.95$ appear as Be stars. It is however neither clear if this is the right value nor whether in general a condition in terms of

v_{rot}/v_{cr} is appropriate. Rivinius et al. (2013) summarises that the average v_{rot}/v_{cr} of Be stars is around 0.85[2] and the minimum v_{rot}/v_{cr} around 0.77. More recent studies confirmed that Be stars can rotate substantially sub-critical (Zorec et al., 2016; Balona and Ozuyar, 2020; El-Badry et al., 2022; Dufton et al., 2022). On the other hand, interferometric observations of α Eri (Domiciano de Souza et al., 2003, 2012) obtained near-critical rotation.

While fast rotation is likely a necessary criterion for a star to become a Be star it seems not to be a sufficient condition, as the example of α Leo shows (McAlister et al., 2005). It rotates with $v_{rot}/v_{cr} = 0.86$ faster than the aforementioned minimum while it is not a Be star but only of spectral type Bn. Several other condition for a rotating star to become a Be star such as pulsations and magnetic fields are discussed in Rivinius et al. (2013).

Our simulations yielded that almost all accretors, which rotated faster than $v_{rot}/v_{cr} = 0.5$ after mass transfer, rotated with at least $v_{rot}/v_{cr} = 0.95$. Thus the number of Be stars will change only weakly if we would change our limit from 0.95 (Townsend et al., 2004) to a lower value as 0.77 (Rivinius et al., 2013). A further condition which might needs to be fulfilled by a star to become a Be star may reduce the number of Be stars in our study. This is problematic as our predicted total number is already below the observations (see Sect. 6.4). Similarly, there might exist conditions under which a star becomes a Be star which do not involve binary evolution.

BH kick

In Sect. 6.5, we assumed the most optimistic scenario, namely that the BH receives no birth kick, and thus we find that BH+OB systems do not unbind in our study. In the pessimistic scenario (flat distribution between 0 km/s and 200 km/s, Sect. 6.4) we found that their number was reduced by a factor of about two. No consensus about the natal kick has been reached in the literature. Many observational works analysing the position and kinematics of low-mass X-ray binaries argue in favour of a high kick scenario (Podsiadlowski et al., 2002; Gualandris et al., 2005; Willems et al., 2005; Fragos et al., 2009; Repetto et al., 2012), while others argue for a low kick (Nelemans et al., 1999; Mandel, 2016). Repetto and Nelemans (2015) even finds clues for both scenarios depending on the systems. Fryer et al. (2012) and Shao and Li (2014, 2019, 2020, 2021) use for their population syntheses an approach by which the kick of the initially formed NS is reduced by fallback prior to the BH formation. From the detailed modelling site, Janka (2013) is able to explain high BH kicks by an asymmetric SN with fallback. Rahman et al. (2022) on the other hand proposes a mechanism for a low BH kick based on hydrodynamical simulations while Chan et al. (2020) can produce, also with hydrodynamical simulations, both low and high kicks depending on the explosion energy. See Janka et al. (2022) for a recent discussion.

The BH kick does not only affect the total number of OB+BH systems, but also the distributions of orbital parameters such as period and 3D velocity (Tauris and Takens, 1998). With the two extreme assumptions we used, we probably have covered the parameter space well enough. We reproduced Fig. 6.6, 6.14 (lower right), and 6.17 (lower left) with a strong BH kick in Fig. 6.19. About a third of the BH systems unbinds and we only expect 15 OBe+BH systems and 69 regular OB+BH systems. Especially the systems with OBe stars break appart as they are wider then those with regular OB stars. The eccentricity distribution of the unbound systems is flat, but avoid systems with an eccentricity below 0.1. The current observations seem to prefer a weak or no kick at BH formation.

[2] We converted the $W = v_{rot}/v_{orb}$ of Rivinius et al. (2013) to $\Upsilon = v_{rot}/v_{cr}$ using their eq. 8 and 11.

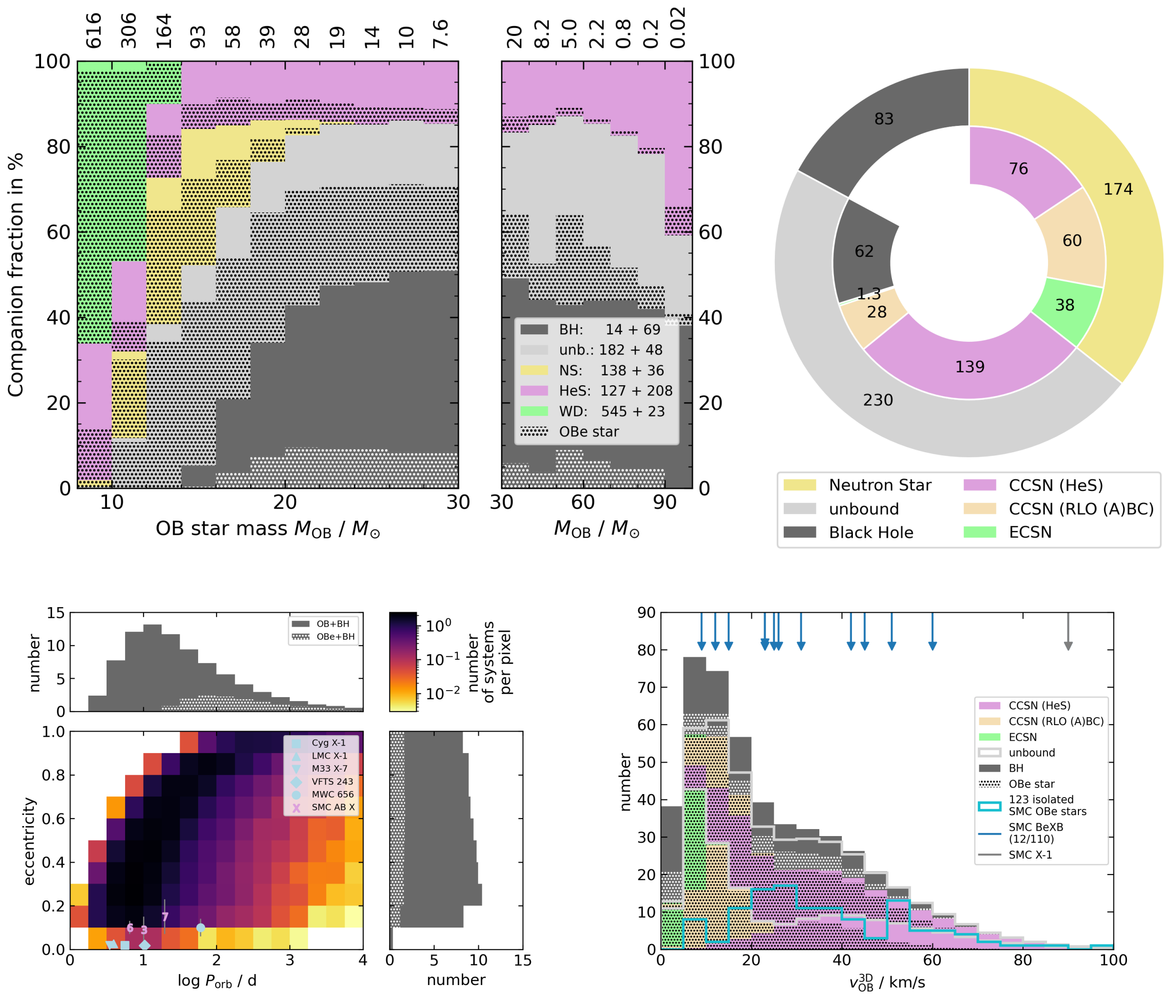

Figure 6.19: Same as Fig. 6.6, 6.14 (lower right), and 6.17 (lower left), but with a BH kick.

6.6.2 Comparison with observations

In this Section we compare our predicted distribution to observations of SMC systems and suitable proxies. We focus here on systems with BH or NS companions and their directly observable properties.

BH systems

No OB+BH system was so far observed in the SMC. Therefore we rely on OB+BH systems of other galaxies and WR+OB systems, which are believed to evolve to OB+BH systems (Langer, 2012), as proxies. The OB+BH systems in question are Cyg X-1 (Orosz et al., 2011; Miller-Jones et al., 2021), LMC X-1 (Orosz et al., 2009), M33 X-7 (Orosz et al., 2007; Ramachandran et al., 2022), VFTS 243 (Shenar et al., 2022), and MWC 656 (Casares et al., 2014; Rivinius et al., 2022; Janssens et al., 2023, the true nature is under debate). For the WR+O systems, we rely on Shenar et al. (2016) and Shenar et al. (2018) and references therein. For all analysed quantities, we calculate and discuss the un-inclined values.

In Fig. 6.9 we can see that our predictions and the observed masses cover the same ranges. (We assume the WR mass as BH mass.) MWC 656 is at the extreme low mass end of both components. However we find that the observations are roughly equally distributed over the predicted are. This is not surprising due to a possible luminosity bias and the fact that far more systems than only the WR systems, which populate the high mass end, evolve into OB+BH systems.

In Fig. 6.14 (top left) we find the observed systems to cluster around a velocity semi-amplitude of 100 to 150 km/s. The reason may be the difficulty in observing systems with lower values. In the top right panel we find that the observations follow the shape of the predicted population. Furthermore the occurrence of emission line companions matches. Only MWC 656 lies in the region where we expect OBe stars (high period, low orbital velocity) and it is the only known BH+OBe candidate. As predected, we find a typical orbital period of around 10 d.

The bottom right panel of Fig. 6.14 is interesting as we predicted the OB+BH systems' eccentricities to range from 0.05 to 0.20 but find that the observed OB+BH systems have values clearly below this, with the sole exception of MWC 656. The reason may be tidal circularisation in close orbits. Even more interesting is that the WR+O systems from the SMC have a non-zero eccentricities while we would expect a perfectly circular orbit after RLO.

All observed BH/WR+OB systems (but MWC 656) are observed to have relatively similar orbital (~ 120 km/s) and rotational velocities (~ 200 km/s) of the OB star (Fig. 6.15). The cluster is very close the our predicted subpopulation of BH+OB systems. The only difference is that our predictions have their maximal rotational velocity at ~ 100 km/s. This may be due to an overestimate of tidal or wind braking in our models or due to a different stellar structure. We can conclude that these systems likely evolved through Case A mass transfer. MWC 656 however seems to belong to the OB+BH sub-population at high rotation. Indeed this system harbours an emission-line star matching the predictions. Thus MWC 656 might be the tip of the iceberg of yet undiscovered BH+OBe systems.

Fig. 6.10 offers an important counterargument to the nature of MWC 656. While all other BH/WR+OB systems can be observed with temperatures and luminosities in well agreement with observations, MWC 656 lies clearly outside our population of OB+BH systems. This may be due to uncertainties in our BH formation criterion or a different mass-transfer efficiency, but we rather see as a support for the claim of Rivinius et al. (2022) and Janssens et al. (2023) that MWC 656 harbours a subdwarf instead of a BH.

BeXBs, SMC X-1 and J0045–7319

Haberl and Sturm (2016, living version `https://www.mpe.mpg.de/heg/SMC`) report 107 BeXBs in the SMC. They give V-band magnitudes for 102 and orbital periods for 54 of them. Townsend et al. (2011) and Coe and Kirk (2015) list eccentricities for seven BeXBs. Next to the BeXBs two other systems with a NS are found in the SMC. These are the super-giant X-ray binary SMC X-1 (van der Meer et al., 2007) and the pulsar/B-type star binary J0045–7319 (Bell et al., 1995; Kaspi et al., 1996; Manchester et al., 2005). Magnitude, orbital period and eccentricity are well known for them. We included these values in Fig. 6.11 and 6.16.

The V-band magnitude of BeXBs covers the same range as our simulation (Fig. 6.11), but the distributions have slightly different shapes. SMC X-1 lies at the bright end of our distribution and J0045–7319 at the dim end, while we would have rather expected such systems without emission lines over the whole range of magnitudes.

The orbital period distribution of BeXBs behaves with values above 10 d like the artificial one (Fig. 6.16). Both samples spread out over several decades and show a clear maximum. The differences, especially the large number of BeXBs with periods between 56 and 100 d may be due to sampling. The period of J0045–7319 is close to the mode of the model's, however it is not a Be star like almost all of our systems at such a period. SMC X-1 has with 3.89 d the shortest orbital period. At such a value we would expect a super-giant X-ray binary according to our model.

If we consider eccentricities we find a notable difference between our work and the observations. While we predict a wide symmetrical distribution for the BeXB, the observations range only up to 0.5. This may be due to an observational bias against high eccentricities. The high eccentricity of J0045–7319 and the near zero one of SMC X-1 fit to our model. In Fig. 6.16 (top) we find that all observations lie where we predict the largest density of systems. The only exception is SMC X-1, which may be explained by our ignorance towards tidal circularisation. The mass ratios of SMC X-1 (0.068 ± 0.010) and J0045–7319 (0.16 ± 0.03) are at the edges of our predictions (Fig. 6.8). The deprojected rotational velocity of the optical counterpart of J0045–7319 is 163 ± 21 km/s and fits to the predictions for OBs star in Fig. 6.12.

Spatial velocities

In Fig. 6.17 we have added local transverse velocities of 123 isolated SMC OBe stars from Dorigo Jones et al. (2020). For most of these observations the binary status is unknown, but since Bodensteiner et al. (2020b) found evidence that such systems are post-interaction systems, we assume this and compare them with our OB+SR systems (including unbound accretors). The observations likely also contain OB+HeS systems for which we expect no local spatial velocity as they did not receive a SN kick. Twelve of them have a counterpart in the BeXB table of Haberl and Sturm (2016) wherefore we highlight them as well as SMC X-1. Dorigo Jones et al. (2020) also provide rotational velocities for 54 of their systems. Notice that the observations are projected velocities but our simulations are not.

The velocity range of observed and simulated systems agree well, while the shape of the distributions are different (Fig. 6.17 bottom left). Our data are more strongly skewed towards lower velocities, which one would rather expect from the observations due to projection effects. A possible explanation is an observational bias agaist slow moving systems and the relativly large uncertainties. (The median error of the local transverse velocity is 32 km/s.) The BeXBs on the other hand seem to follow the simulated distribution more closely as they only reach 45 km/s. However the system with the largest observed projected velocity is already moving as fast as the fastest (not projected) artificial BeXB candidates. SMC X-1 is with 90 km/s in agreement with our OBs+NS systems.

In the bottom right panel of Fig. 6.17 we find that the bulk of the observations shows lower rotational velocities than we predict. All of the observed OBe star lie in the part of the diagram where we predict normal OB stars. This may be due to several effects. First, we did not consider a possible inclination in our simulation. While this will shift may of our systems to lower rotational velocities it does not empty the upper part of the diagram completely. Second, the observations may underestimate the rotational velocity at the equator as this region cools by the von Zeipel-theorem and thus dims (Townsend et al., 2004). Finally, we may have underestimated the effects of tidal and wind braking.

Wolf-Rayet stars

Finally we consider the WR+O binares in the SMC of which four are known (Shenar et al., 2016, 2018). Additionally, thee are apparent single WR stars which may harbour a hidden BH (Xu, 2024), but these systems are beyond the scope of this work as well as the WR+WR system AB 5 (see however Sect. 6.3). The WR population in the SMC is thought to be complete. We use the values given by Shenar et al. (2016) for AB 3, AB 7, and AB 8 and by Shenar et al. (2018) for AB 6.

Fig. 6.18 (top left) shows that AB 6, 7, and 8 have luminosities as predicted, while the OB-luminosity of AB 3 does not match. In the other three panels we find the observations only cover a certain subspace of our simulations. While the orbital periods align with the maximum of the simulations (about 10 d), the observations are not distributed as broadly as the models. The same is true for the velocity semi-amplitude distribution (bottom left panel). From that distribution we can interfer that our models predict the same mass ratios as observe. We find also a mismatch in the rotational velocities of the OB stars. The observations lie closely toghethrer in the brought trough between the two expected maxima (right panels in Fig. 6.18). Perhaps our rotation scheme (tides, winds, structural evolution) does brake down for stars with so high masses and/or the inflation of the OB star significantly changes its radius and thus its rotational velocity.

6.6.3 Comparison with detailed binary models

In this Section we compare our results to that of Xu (2024), which is a companion study with the same aims but a different approach. While we did used a rapid binary population synthesis code to generate a large range of model populations, Xu (2024) use a given set of detailed MESA binary models. Besides that, the major differences between the two works are, first, that our models accretion during RLO is not limited to the achievement of critical rotation of the accretor but is gauged to the observed number of BeXBs ans WR+O systems. Second, Xu (2024) uses a luminosity crieterion to decide whether a RLO is stable or leads to a stellar merger, while we rely on the occurrence of a L_2-overflow by the swelling of the accretor. The major consequence is that the q–$\log P$ diagram of the two approaches look very different (our Fig. 6.3 and Sect. E.1 and their Fig. 2, A.1 and A.2). While these diagrams in the work of Xu (2024) the region where donor stripping occurs has the shape of two triangles with stable mass transfer up to smaller mass ratios at high orbital periods, in our work the transition between Case A and B is continuous and if systems merge they tend to be those at high orbital periods and mass ratios away from unity. Furthermore a smaller fraction of our models merge if we chose a small accretion efficiency but we can enlarge the region of expected mergers by assuming an more efficient mass transfer.

By direct comparison of our Fig. 6.6 and Fig. 3 of Xu (2024), we find that they predict an overall smaller number of OB+SR systems. Also their number in each mass bin is smaller than ours. The different companion types are also differently distributed over the OB star masses. Their OB stars up to $8M_\odot$ and $30M_\odot$ have WD and NS companions, respectively. The NS with such massive companions evolved through Case A mass transfer which may cause difference in final fate as MESA models the internal structure of the stripped star detailed. On the other hand, stars as light as $6M_\odot$ harbour NSs and BHs in their study, while our lowest masses are $8M_\odot$ and $14M_\odot$. This may come from the higher accretion efficiency we assume. Furthermore, the ratio of OB+NS to OB+BH systems of Xu (2024) is smaller than ours, probably due to the large number of systems with small donor masses merging in the work of Xu (2024). We also note that Xu (2024) finds a larger ratio of OBe to normal OB stars, probably due to the larger chance to merger for closer systems.

The impact of the different assumptions for mass-transfer efficiency and stable mass transfer as a function of mass ratio and orbital period can be explain the major differences between our results and those of Xu (2024). While Xu (2024) predicts more BH systems than we do, we predict more NS systems than Xu (2024), because under the assumptions of Xu (2024) more low mass systems merge during RLO while we have slightly more merger for BH progenitors as well as a shorter lifetime due to the more massive companions caused by a larger mass-transfer efficiency.

A strong feature of the merger criterion of Xu (2024) is the bi-modality of the orbital period (their Fig. 5), which is not present in our Fig. 6.16. The range of orbital period is similar nevertheless. This prediction is easily testable and the current data seems to support our approach.

In our model, the accretion efficiency is only a function of accretor mass, but in Xu (2024), it can depend on both masses and the orbital period. This may be the cause of several differnces between our results, such as the the larger spread of OB masses for a fixed BH mass (our Fig. 6.9 and their Fig. 9) and the larger range of luminosities of NS and BH companions and stronger overlap of the populations (our Fig. 6.10 and their Fig. 8) in Xu (2024). Overall Xu (2024) predicts less massive stars in OB+BH systems due to their lower accretion efficiency. This also causes the mass ratio of OB+BH systems be larger in the model of Xu (2024).

An interesting and testable difference can be found in our Fig. 6.14 and Fig. 9 of Xu (2024). We predict the lower left corner in the $M_{\rm OB}$–$P_{\rm orb}$ diagram much stronger populated than Xu (2024) does. In our Fig. 6.13 and Fig. E.3 of Xu (2024) one can find accordingly the lack of close normal OB+BH systems. It may be explained with the fact that our merger criterion lets more systems with initially short periods and extreme ass ratios survive at low ($\sim 15M_\odot$, the lowest BH progenitor initial mass) initial donor masses. It should be a straight forward task to determine if these systems should be X-ray bright.

ComBinE and MESA rely on the same theory when it comes to the treatment of tides. However the execution is different due to the design of the cores. Our Fig. 6.12 and Fig. E.4 of Xu (2024) therefore show interesting differences. The population at low rotational velocities is missing in Xu (2024). Whether this is due to the implementation of tides or the merger criterion is unclear. We find also that the high rotation peak is broader in the model of Xu (2024) which is probably due to the implementation of rotational evolution. In our work this peak is only very weak for the BH companions. Xu (2024) has also almost no normal OB+NS systems and Case B systems do not have $v_{\rm rot}/v_{\rm cr}$ below 0.8 in general.

For the NS, we find that Xu (2024) predict a slightly flatter eccentricity distribution but the tendency to have higher eccentricities for the largest periods remains (our Fig. 6.16 and their Fig. 7). For the SN types, we find about the same tendencies with less CCSN after Case (A)BC in Xu (2024), which may be caused by the ability of the HeS to expand due to the presence of a hydrogen shell. It is also interesting to note that Xu (2024) do not find velocity semi-amplitudes larger than 40 km/s in OB+NS systems (our Fig. 6.13 and their Fig. E.3).

Lastly, we compare our results of the WR+O systems. Both our studies find a similar WR luminosity function, however differences in the orbital properties emerge. Our WR velocity semi-amplitude distribution is almost flat, but Xu (2024) prefers low values. Similarly, our period distribution shows a clear maximum while theirs is rather flat even though it has a maximum at low periods. These differences are unexpected since at such high masses we have assumed a low accretion efficiency (10%), relatively close to typical values (5%) of Xu (2024). Furthermore the regions of donor stripping in the q–$\log P$ diagrams look rather similar as both our merger criteria do not show a strong impact.

6.6.4 Comparison with earlier work

In the last three decades many population synthesis studies of X-ray binaries and/or Be stars (e.g. Meurs and van den Heuvel, 1989; Waters et al., 1989; Pols et al., 1991; Tutukov and Yungel'Son, 1993; Dalton and Sarazin, 1995; Iben et al., 1995; Portegies Zwart, 1995; Portegies Zwart and Verbunt, 1996; van Bever and Vanbeveren, 1997; Raguzova and Lipunov, 1998; Terman et al., 1998; Van Bever and Vanbeveren, 2000; Raguzova, 2001; Lü et al., 2011; Shao and Li, 2014; Zuo et al., 2014; Renzo et al., 2019; Vinciguerra et al., 2020; Misra et al., 2023; Liu et al., 2024) have been conducted. While many of them focused on the X-ray output, we discuss here those who focus on aspects of binary evolution.

A popular approach in the past was to use a mass ratio dependent mass-transfer efficiency, as Pols et al. (1991), Portegies Zwart (1995) or Portegies Zwart and Verbunt (1996) did. Typical is a high efficiency for systems with mass ratios close to unity and low values for rather unequal systems with a narrow transition zone. This description is in general not able to reproduce the mass (or spectral type) distribution of BeXBs, as B stars as light as $2M_\odot$ are predicted. SN kicks are not able to regulate that sufficiently (Portegies Zwart, 1995). Rephrasing of this criterion into a thermally limited accretion (Portegies Zwart and Verbunt, 1996) leads to the same problem. Many studies (e.g. Pols et al., 1991) introduce an ad hoc minimal mass ratio for stable mass transfer of about 0.3 to 0.5 to remove systems with light companions. Portegies Zwart (1995) identified with the specific angular momentum of the ejected material a further key parameter, which they used to regulate which binaries evolve to BeXBs. They found that the larger the specific orbital angular momentum of the ejected material the larger is the minimal mass ratio for donor stripping. This was confirmed by van Bever and Vanbeveren (1997) and Terman et al. (1998). More recently, Shao and Li (2014) tested three models within the stable RLO channel to examine the formation of Be stars by binary interaction. They could best explain the observed mass and orbital period distribution of OB+NS systems neither with the rotation limited accretion model nor with the thermally limited accretion model but only with the model with 50% mass-transfer efficiency, for which the authors found in contrast to the other two models no physical motivation. Lastly, Vinciguerra et al. (2020) studies a combination of three fixed mass-transfer efficiencies and three models for the loss of angular momentum. Each combination resulted in a certain minimal mass ratio for successful donor stripping. With that, they confirmed the earlier findings about the minimum mass ratio, the need for a moderate mass-transfer efficiency and notable angular momentum loss from the system. All these findings are in line with the results of our study and furthermore we are able to connect the minimal mass ratio for stable mass transfer with the accretion efficiency by a physical mechanism. In general our results for distribution functions of parameters of BeXBs agree with previous work and differences can easily be explained by the underlying physics.

Several studies address the number of BeXBs. Vinciguerra et al. (2020) found that their mechanism under-predicts their number and need to invoke a time dependent star formation rate. They need to do this since many of their systems unbind during the SN because the authors do not use reduced SN kicks for HeS as we do. Shao and Li (2014) and Renzo et al. (2019) report for the same reason a larger ratio between bound and unbound NS than we do. That SN kicks regulate the number of BeXBs was also found by Portegies Zwart and Verbunt (1996), Raguzova and Lipunov (1998) and Renzo et al. (2019). Raguzova and Lipunov

(1998) furthermore showed that the magnitude of the kick does not change the shape of the orbital period distribution and only slightly the shape of the eccentricity distribution.

We were not able to explain the number of Be stars in the SMC with binary evolution. The literature shows no consensus on the question how important this channel is for their formation. While e.g. Pols et al. (1991) find that no more then 60% of them can come from the binary channel, Shao and Li (2014) can explain all Be stars by binary evolution. Hastings et al. (2020) found that single star evolution is not able to explain the observed number of Be stars in open clusters, but binary evolution might be able to (Hastings et al., 2021).

We identified further characteristics shared by our and previous studies: In general 20% of mass gainers of all masses are predicted to have a HeS companion (Portegies Zwart, 1995; van Bever and Vanbeveren, 1997). Several further studies (Tutukov and Yungel'Son, 1993; Terman et al., 1998; Shao and Li, 2014, e.g.) found that the common envelope channel is not relevant for the formation of BeXBs. Tides are the reason why OB+NS systems with small orbital periods do not evolve to BeXBs (Raguzova and Lipunov, 1998) and circularise close systems which we neglected (Terman et al., 1998; Shao and Li, 2014). Renzo et al. (2019) identified that the minimum mass ratio for successful donor stripping and the mass-transfer efficiency impact the velocity distribution of unbound stars.

Several studies make predictions about the yet unobserved OBe+BH population. Raguzova and Lipunov (1999) predicted orbital period and eccentricities in agreement with our results, even though they require the BH progenitors have initial masses of at least $50 M_{\odot}$. Shao and Li (2014) predicts OB(e)+BH binaries for their rotationally limited and their semi-conservative model but not for their thermally limited accretion model as in the latter the OBe stars become too massive. In the former two models the OBe+BH populations have different OB masses. They compare well to our model (e.g. Fig. 6.14) as our effective accretion efficiency for BHs lies in between their two models. Their ratio of OBe+NS and OBe+BH systems is larger than ours as they do not consider O stars as emission-line stars. Shao and Li (2019) predict the Galactic population of BHs with normal star companions assuming a rotationally limited mass-transfer efficiency. Their model B, which is similar to our scenario with BH kicks, yields relatively similar results, while differences in the companions masses are smaller by a factor of 2 (probably due to the lower accretion efficiency) and the period distribution appears to be flatter than ours. While they did not consider whether the accretor becomes a OBe star, they predict a large number of OB+BH systems. Their follow-up study (Shao and Li, 2020) treats the possibility of these systems to become X-ray binaries. They predict a large number of OBe+BH systems in the Galaxy. Their orbital periods are as in our results roughly larger than 10 d and the OB masses are lower for the mentioned reasons. Ther ratio of normal OB+BH to OBe+BH systems is about 1:4 in contrast with our result of 4:1. Langer et al. (2020) predicted the LMC's OB+BH population with a MESA binary grid similar to Xu (2024) with rotation limited accretion and the same luminosity limit for stable mass transfer. Thus their OB stars are lighter than in our study and the period distribution is bimodal due to the same reason as for Xu (2024). Therefore, we refer to our discussion about the work of Xu (2024) in Sect. 6.6.3. On the other site, the lack of BeXBs with BH accretors is an open question in the literature and several mechanisms are proposed why such systems are not observed. Raguzova (2001) proposed that a luminous blue variable phase occurs to the BH progenitor before the RLO. By the strong winds of that phase the BH progenitor loses so much mass before collapse that a RLO is prevented and its companions does not become an emission-line star. This idea breaks apart if the companion can evolve to a Be star by single star evolution. Zhang et al. (2004) argue that these BHs would not accrete material from the disk. Their argument is based on the results from Podsiadlowski et al. (2003) that BH binaries prefer short orbital periods, which is challenged by our and other results. Belczynski and Ziolkowski (2009) find evolutionary arguments, why BeXBs with BHs are suppressed. This study however relies heavily on a common envelope ejection, which was found to be unrealistic for the formation of BeXBs (Shao and Li, 2014). Langer et al. (2020) suggest that the BH progenitor is a WR star whose wind has removed the Be disk. Finally, we compare our WR+O population to those of Pauli et al. (2022), even though their study focuses on the LMC. Compared to their Fig. 5 to 7, we find a larger period range but our mass ratio distribution is narrower. We share the preference for systems with a period of 10 d and O stars as massive or up to 50% heavier than the WR star with them.

In Sect. 6.4 we reported evidence for a mass-dependent mass-transfer efficiency with more massive accretors accreting a smaller fraction of the lost donor mass than less massive accretors. Throughout the literature we found evidence supporting this claim, both from theoretical and observational studies. Bodensteiner et al. (2018) found evidence for non-conservative evolution through infrared nebulae for O to A typ stars. Sarna (1993) reports a mass-transfer efficiency for the late B type star β Per of 60%. For the early B type star φ Per, Raguzova (2001) states that the mass-transfer efficiency during its formation could not have been non-conservative. Similarly, Pols (2007) and Schootemeijer et al. (2018) report an accretion efficiency for that object of more than 70% and more than 75%, respectively. For LB-1, an object at a similar stellar mass, Shao and Li (2021) and Schürmann et al. (2022) report a moderately non-conservative evolution and for β Lyr A Brož et al. (2021) found close to conservative mass transfer. Wang et al. (2021) states that the mass-transfer efficiency in their Be+sdOB systems was close to 100%. For G0 to B1 type Algols, Nelson and Eggleton (2001) find conservative mass transfer fitting and hints that OB type Algols may bee non-conservative. Figueiredo et al. (1994), de Mink et al. (2007), van Rensbergen et al. (2006) and van Rensbergen et al. (2008) confirmed that. For HMXBs, Dalton and Sarazin (1995) found an mass-transfer efficiency of about 30%, and for BeXBs, Vinciguerra et al. (2020) found an mass-transfer efficiency of at least 30% while Shao and Li (2014) found an accretion efficiency of 50% to agree with observations. On the other hand, Hastings et al. (2021) derived from Be stars in coeval populations a highly non-conservative mass transfer. At higher masses, Renzo and Götberg (2021) find an accretion efficiency for the late O type star ζ Oph of about 30%. For even more massive stars, namely O+WR systems, in agreement with each other, Petrovic et al. (2005), Shao and Li (2016) and our Ch. 5 identified these systems to be highly non-conservative (10...25%). While certainly a period dependency for the mass-transfer efficiency is reported (de Mink et al., 2007; Sen et al., 2021) which occults the picture, a trend for lower mass-transfer efficiency at higher mass seems to emerge. We can only speculate about its origin, maybe stellar winds play a role, as the wind of very massive stars could blow parts of the material lost from the donor out of the system. If so, we would expect a metallicity dependent mass-transfer rate similar to the metallicity dependence of stellar winds (Langer, 2012; Vink, 2022). As a last remark, our mass dependent accretion efficiency implies a mass dependent minimal mass ratio for donor stripping. Such an effect was also found by Hastings et al. (2021) from Be stars in star clusters.

6.7 Conclusions

In this study we used the rapid binary population synthesis code ComBinE to examine the properties of OB+SR systems in the SMC. We used a novel prescription for the swelling of the accretor during RLO to decide whether mass transfer is stable and the donor is stripped to a HeS or the system merges into a single star. In this approach, the mass-transfer efficiency is the key free parameter that controls which systems survive the RLO. We found that this criterion gives rise to specific sets of initial binary parameters that produce binary systems that host a SR, and so specific numbers of them. To constrain the mass-transfer efficiency, we gauged the number of systems produced by the population synthesis against the observed numbers of Be stars, BeXBs, and WR+O systems and found a preference for moderate to high mass-transfer efficiencies at low accretor masses, and low values thereof at high masses. Implicit evidence for this can be found throughout the literature.

We used the mass-dependent accretion efficiency to predict the properties of massive OB stars with SR as their companion. In agreement with Langer et al. (2020) and Xu (2024) we found strong evidence for a large but unobserved population of OB+BH systems. For the SMC we predict about 150 OB+BH systems, of which we expect 36 to show emission lines in their spectra. We predict two sub-populations, namely close systems with small rotation but medium to large orbital velocities, which may appear as SB1 systems, and wide systems with small orbital velocities but large rotation velocities, which may appear as OBe stars, in agreement with Langer et al. (2020) and Xu (2024). However the mass-transfer stability criterion we used leads to important differences in the distribution functions, e.g. in the orbital period, which makes aspects of the assumed binary physics testable with observations.

We also found that our simulations can explain well the observed properties of Be stars and BeXBs of the SMC and OB+BH systems. The picture for O stars with WR companions and runaway stars is more complex, since we neglect some formation channels. For them, the LMC is a fruitful new target for a follow-up study, since it hosts a larger number of WR stars and has a higher metallicity, which may cause a shift in the mass-dependent accretion efficiency. We predict that the eccentricity of OB+BH systems is a good test for the occurrence of a kick at BH formation, and conclude from current observational data that a weak or no kick is more likely.

The detection of these OB+BH systems, either as SB1 systems or as OBe systems, e.g. by multi-epoch spectroscopy, will help to reduce the uncertainties in massive binary evolution. If it turns out that such a population does not exist, this will be an exciting challenge for the massive star community, as evolutionary pathways to suppress these systems but allow close binary black holes would be needed. Future work based on this will be able to more accurately predict the properties of pulsars in binary systems, possible WR+SR systems, and gravitational wave mergers, and to understand the contribution of binary evolution to them.

CHAPTER 7

Summary and outlook

In this thesis we have studied aspects of massive binary evolution from the zero-age main-sequence to the formation of the first stellar remnant. This was necessary because massive stars, preferably in binary systems, are the key constituents of the Universe. With them, even though they are rare, we can understand where X-ray sources come from, why supernovae can be seen, how heavy elements were formed, and how the Universe was re-ionised.

We carried out two population synthesis studies, each with different assumptions about binary physics and using different computational methods. In the first study (Ch. 2), we used detailed binary models, weighted by their birth probability and lifetime, to produce a population of OB-type stars with black hole companions. We assumed that during a mass transfer phase, the binary can avoid merging into a single star if the combined luminosity of both stars is powerful enough to remove material from the system that cannot be accreted, since it is assumed that accretion is only possible until the accretor has not reached critical rotation. In the second study (Ch. 6), we generated model systems using a Monte Carlo approach and evolved them using tabulated single-star models. For binary interaction phases we used semi-analytic prescriptions. To make this work, we had to develop new such prescriptions, namely for the description of rotation, for the outcome of mass transfer during core hydrogen burning, and for the condition for stable mass transfer.

In Ch. 3 we have tested the mechanisms of angular momentum transport in stars with the aim of predicting the spin of stellar remnants. We have analysed stellar models with purely hydrodynamical and with magnetic angular momentum transport and compared them with the Galactic B-type star LB-1, which consists of a Be star and a stripped star that has recently lost most of its envelope and is now revealing the rotation of its former interior. We find that only magnetic angular momentum transport can reproduce the observed rotational velocities of LB-1 and of subdwarfs in binary systems. This magnetic transport removes angular momentum from the stellar core during central hydrogen burning and early shell burning, keeping the star rotating as a rigid body until central hydrogen depletion, and preventing the core from rotating at extremely high speeds. During the transition to core helium burning, the rotation rates of the core and envelope decouple and from then on evolve independently from each other. We found that the angular momentum in the stellar core is comparable between single and binary star models. Our results allow us to model the rotation of main-sequence stars as a rigid body.

Close binary systems that undergo mass transfer during core hydrogen burning are difficult to model with rapid binary population synthesis codes. This is because the donor star continues its slow nuclear timescale evolution during mass transfer. Since such systems are favoured by the initial period distribution, ignoring them or treating them similarly to Case B mass transfer systems would introduce a large number of inaccuracies. We have therefore developed a new prescription in Ch. 4 to accurately predict the final donor mass and the duration of mass transfer. After analysing two grids of binary models at the metallicities of the Large and Small Magellanic Clouds, we found that shorter initial orbital periods lead to lighter donors at the end of mass transfer and to a longer duration of core hydrogen burning. This is because in narrow systems the size of the convective core shrinks more during the fast Case A mass transfer than in wide systems, and because in narrow systems the slow Case A mass transfer lasts longer, so more mass is lost. Case A mass transfer takes longer in narrow systems because the donor is less evolved. This result has direct implications for the type of stellar remnant the donor becomes, as this depends on the progenitor mass, and when the first supernova occurs. Since small initial orbital periods and low initial masses are favoured, this result has a major implications for the number of neutron stars and black holes in binaries.

We have developed a new criterion for deciding whether the mass transfer in an interacting binary is stable in Ch. 5, based on the expansion of the accretor star under accretion. While this behaviour has been known for about 50 years (Kippenhahn and Meyer-Hofmeister, 1977; Neo et al., 1977), research has mainly focused on the response of the donor star to mass loss (Webbink, 1985; Ge et al., 2010, 2015, 2020). If, during the mass transfer, the accreting star expands enough to fill its Roche lobe, a contract system is formed and soon after, after a little more expansion, matter can leave the system through the L_2-point, removing a large amount of angular momentum from the system. This leads to a decay of the orbit and a possible merger of the binary into a single star. From detailed models of accreting stars, we have developed a criterion for the expansion of the accretor. If the mass-transfer rate is below the thermal accretion rate, the accretor can remain in thermal equilibrium and does not expand. If the accretion rate is above the thermal rate, the accretor star cannot incorporate the incoming material fast enough, leading to a moderate expansion. Finally, if the accretion rate is above the Eddington accretion rate, the accretor expands rapidly and becomes almost fully convective. Combining this result with the evolution of the orbit under mass transfer, we derive combinations of initial masses and orbital periods for stable mass transfer or L_2-overflow. The only free parameter in this recipe is the mass-transfer efficiency. We have applied our model to the Wolf-Rayet stars in the Small Magellanic Cloud and found that the mass-transfer efficiency in these systems was likely to be less than 50%.

With the above result, we were able to perform rapid population syntheses of massive binaries, but since the mass-transfer efficiency remained a free parameter, we generated a grid of population syntheses and compared the resulting numbers of Wolf-Rayet–O-type star binaries and Be/X-ray binaries with observations. We found that the Be/X-ray population can only be explained with a moderate to high mass-transfer efficiency, while the Wolf-Rayet binaries require a low value. This leads to the conclusion that this quantity is mass dependent, with low values for high masses and high values for low masses. The detailed population synthesis of Ch. 2 at Large Magellanic Cloud metallicity, the rapid one of Ch. 6, and the detailed companion study reported in Ch. 6, both as Small Magellanic Cloud metallicity, come to a common conclusion. There is a large yet unobserved population of OB-type stars with black hole companions. Since this holds for both metallicities, it is likely that such a population can also be found in the Milky Way. Notably, this result is independent of the assumed physics of mass transfer. While the different studies predict differences in the distribution functions for key binary parameters, which can be easily tested by observations, we find that black hole–OB-type star systems can be identified either as rapid rotators, appearing as Be stars, with moderate radial-velocity variations, or as nitrogen-enriched stars with large radial-velocity variations. Uncovering this population will constrain many uncertainties in the evolution of massive binary stars. If it turns out that this population does not exist, its absence would pose a serious but exciting challenge to the stellar modelling community.

Further studies are needed to determine the mass-transfer efficiency and possibly the angular momentum budget during the RLO. Valuable target populations are Algol stars, Wolf-Rayet–O-type star binaries (Shenar et al., 2019) and hot subdwarfs with Be star companions (Wang et al., 2021). These populations have the advantage that no supernova has introduced more uncertainties, so only the effects of the mass-transfer phase can be studied. While recently Sen et al. (2022, 2023) investigated heavy Algols with a grid of detailed binary models, a broader approach using different mass-transfer efficiencies and various mass ranges is necessary, since we have argued in Ch. 6 that it is possible that the mass-transfer efficiency is mass dependent. Such a project requires an extension of the existing ComBinE-code, as it is not yet able to model the properties of binary stars during nuclear timescale mass transfer, or to account for Wolf-Rayet stars formed from the single-star channel. In this context, the result of Schootemeijer et al. (2024) that the single Wolf-Rayet stars in the Small Magellanic Cloud are truly single and do not host X-ray quiet black holes needs to be addressed. As these systems are a predicted intermediate stage in the formation of close binary black holes, their absence is challenging. Finally, the in Ch. 6.3 proposed evolutionary path for the double Wolf-Rayet star SMC AB 5 needs to be tested.

The result of Ch. 6 that the mass-transfer efficiency is mass dependent needs to be explained. While three-dimensional hydrodynamic simulations will certainly be needed to fully reveal the evolution during mass transfer, perhaps this behaviour can be understood in terms of stellar winds that could blow material out of the system. Indeed, it is known that very massive stars have the strongest winds, and that these winds are stronger at higher metallicities (Langer, 2012; Vink, 2022). Thus, we might expect that in high metallicity environments, lower mass-transfer efficiencies occur at lower masses. Testing this hypothesis requires a population synthesis study similar to that in Ch. 6 at a range of metallicities and stellar masses.

In contrast to detailed codes such as MESA (Paxton et al., 2011, 2013, 2015, 2018, 2019), the rapid population synthesis code ComBinE is able to model binary evolution through a common envelope evolution. This has opened up the possibility of studying the formation of close binary black holes (Kruckow et al., 2018), but still needs to be tested against evolutionary pathways with fewer steps. A possible test bed for this could be hot subdwarf stars with low-mass companions, which are either white dwarfs or main-sequence stars. The latter configuration has either long or short orbital periods and is thought to have evolved by stable RLO or common envelope ejection, respectively (Podsiadlowski et al., 2008; Heber, 2009). A population synthesis of such systems could potentially shed more light on the conditions under which mass transfer is stable and how to determine the outcome of a common envelope ejection. Although these stars are in the low-mass regime, their analysis could also provide insights into the evolution of massive stars.

To test the common envelope evolution in high-mass stars, low-mass X-ray binaries could be a valuable target for binary population synthesis. It is proposed that these systems, initially consisting of a massive and a low-mass star, first evolved through a common envelope, after which the initially more massive star underwent a supernova explosion to become a neutron star or a black hole (Tauris and van den Heuvel, 2023). While the formation of the stellar remnant introduces a number of uncertainties into the evolutionary modelling, the population properties of the low-mass X-ray binary population may shed light on the conditions under which a common envelope of a massive star can be ejected (Ivanova et al., 2013; Kruckow et al., 2016).

There are many other questions about the evolution of massive stars that can be addressed by population synthesis: Are supernova kicks or close encounters in dense stellar systems more important for runaway stars? Can we predict the P–$\dot{P}$ diagram of pulsars or the spin of black holes from stellar evolution models? Do the statistics of supernova types agree with predictions from binary evolution? What are the products of stellar mergers? Why are no pulsars with black hole or helium star companions observed? …

Overall, we have shown that binary population synthesis is a powerful tool for stellar astrophysics. In the coming years, it will be able to expand our understanding of massive stars, and so more knowledge is nigh(t).

Bibliography

Abbott, B. P., R. Abbott, T. D. Abbott et al. (2016), *Observation of Gravitational Waves from a Binary Black Hole Merger*, Physical Review Letters **116** 061102.

Abbott, B. P., R. Abbott, T. D. Abbott et al. (2017), *GW170817: Observation of Gravitational Waves from a Binary Neutron Star Inspiral*, Physical Review Letters **119** 161101.

Abbott, B. P., R. Abbott, T. D. Abbott et al. (2019), *GWTC-1: A Gravitational-Wave Transient Catalog of Compact Binary Mergers Observed by LIGO and Virgo during the First and Second Observing Runs*, Physical Review X **9** 031040.

Abbott, D. C. (1982), *The theory of radiatively driven stellar winds. II. The line acceleration.*, The Astrophysical Journal **259** 282.

Abbott, R., T. D. Abbott, F. Acernese et al. (2023a), *GWTC-3: Compact Binary Coalescences Observed by LIGO and Virgo during the Second Part of the Third Observing Run*, Physical Review X **13** 041039.

– (2023b), *Population of Merging Compact Binaries Inferred Using Gravitational Waves through GWTC-3*, Physical Review X **13** 011048.

Aerts, C., J. Christensen-Dalsgaard and D. W. Kurtz (2010), *Asteroseismology*, Springer-Verlag.

Aguilera-Dena, D. R., B. Müller, J. Antoniadis et al. (2023), *Stripped-envelope stars in different metallicity environments. II. Type I supernovae and compact remnants*, Astronomy & Astrophysics **671** A134.

Almeida, L. A., H. Sana, W. Taylor et al. (2017), *The Tarantula Massive Binary Monitoring. I. Observational campaign and OB-type spectroscopic binaries*, Astronomy & Astrophysics **598** A84.

Anderson, W. (1929), *Gewöhnliche Materie und strahlende Energie als verschiedene „Phasen“ eines und desselben Grundstoffes*, Zeitschrift für Physik **54** 433.

Baade, W. and F. Zwicky (1934), *Remarks on Super-Novae and Cosmic Rays*, Physical Review **46** 76.

El-Badry, K., C. Conroy, E. Quataert et al. (2022), *Birth of a Be star: an APOGEE search for Be stars forming through binary mass transfer*, Monthly Notices of the Royal Astronomical Society **516** 3602.

Balona, L. A. and D. Ozuyar (2020), *TESS observations of Be stars: a new interpretation*, Monthly Notices of the Royal Astronomical Society **493** 2528.

Banyard, G., H. Sana, L. Mahy et al. (2022), *The observed multiplicity properties of B-type stars in the Galactic young open cluster NGC 6231*, Astronomy & Astrophysics **658** A69.

Bartzakos, P., A. F. J. Moffat and V. S. Niemela (2001), *Magellanic Cloud WC/WO Wolf-Rayet stars - II. Colliding winds in binaries*, Monthly Notices of the Royal Astronomical Society **324** 33.

Beals, C. S. (1929), *On the nature of Wolf-Rayet emission*, Monthly Notices of the Royal Astronomical Society **90** 202.

Belczynski, K., T. Bulik, I. Mandel et al. (2013), *Cyg X-3: A Galactic Double Black Hole or Black-hole-Neutron-star Progenitor*, The Astrophysical Journal **764** 96.

Belczynski, K., V. Kalogera and T. Bulik (2002), *A Comprehensive Study of Binary Compact Objects as Gravitational Wave Sources: Evolutionary Channels, Rates, and Physical Properties*, The Astrophysical Journal **572** 407.

Belczynski, K., V. Kalogera, F. A. Rasio et al. (2008), *Compact Object Modeling with the StarTrack Population Synthesis Code*, The Astrophysical Journal Supplement Series **174** 223.

Belczynski, K. and J. Ziolkowski (2009), *On the Apparent Lack of Be X-Ray Binaries with Black Holes*, The Astrophysical Journal **707** 870.

Bell, J. F., M. S. Bessell, B. W. Stappers et al. (1995), *PSR J0045-7319: A Dual-Line Binary Radio Pulsar*, The Astrophysical Journal Letters **447** L117.

Bellm, E. C., S. R. Kulkarni, M. J. Graham et al. (2019), *The Zwicky Transient Facility: System Overview, Performance, and First Results*, Publications of the Astronomical Society of the Pacific **131** 018002.

Bessel, F. W. (1844a), *On the variations of the proper motions of Procyon and Sirius*, Monthly Notices of the Royal Astronomical Society **6** 136.

Bessel, F. W. (1838), *Bestimmung der Entfernung des 61sten Sterns des Schwans*, Astronomische Nachrichten **16** 65.

– (1844b), *Über Veränderlichkeit der eigenen Bewegungen der Fixterne*, Astronomische Nachrichten **22** 145.

Bethe, H. A. (1939), *Energy production in stars*, Physical Review **55** 434.

Blaauw, A. (1961), *On the origin of the O- and B-type stars with high velocities (the "run-away" stars), and some related problems*, Bulletin of the Astronomical Institutes of the Netherlands **15** 265.

Bodensteiner, J., D. Baade, J. Greiner and N. Langer (2018), *Infrared nebulae around bright massive stars as indicators for binary interactions*, Astronomy & Astrophysics **618** A110.

Bodensteiner, J., T. Shenar, L. Mahy et al. (2020a), *Is HR 6819 a triple system containing a black hole?. An alternative explanation*, Astronomy & Astrophysics **641** A43.

Bodensteiner, J., T. Shenar and H. Sana (2020b), *Investigating the lack of main-sequence companions to massive Be stars*, Astronomy & Astrophysics **641** A42.

Bolton, C. T. (1971), "The Spectrum of HDE 226868 = Cyg X-1 (?).", *Bulletin of the American Astronomical Society*, vol. 3 458.

Braun, H. and N. Langer (1995), *Effects of accretion onto massive main sequence stars.*, Astronomy & Astrophysics **297** 483.

Brott, I., S. E. de Mink, M. Cantiello et al. (2011), *Rotating massive main-sequence stars. I. Grids of evolutionary models and isochrones*, Astronomy & Astrophysics **530** A115.

Brož, M., D. Mourard, J. Budaj et al. (2021), *Optically thin circumstellar medium in the β Lyr A system*, Astronomy & Astrophysics **645** A51.

Burbidge, E. M., G. R. Burbidge, W. A. Fowler and F. Hoyle (1957), *Synthesis of the Elements in Stars*, Reviews of Modern Physics **29** 547.

Burrows, A. and D. Vartanyan (2021), *Core-collapse supernova explosion theory*, Nature **589** 29.

Burrows, A., J. Hayes and B. A. Fryxell (1995), *On the Nature of Core-Collapse Supernova Explosions*, The Astrophysical Journal **450** 830.

Byrne, C. M., E. R. Stanway, J. J. Eldridge et al. (2022), *The dependence of theoretical synthetic spectra on α-enhancement in young, binary stellar populations*, Monthly Notices of the Royal Astronomical Society **512** 5329.

Cannon, A. J. and E. C. Pickering (1901), *Spectra of bright southern stars photographed with the 13-inch Boyden telescope as part of the Henry Draper Memorial*, Annals of Harvard College Observatory **28** 129.

Cantiello, M. and N. Langer (2010), *Thermohaline mixing in evolved low-mass stars*, Astronomy & Astrophysics **521** A9.

Casares, J., I. Negueruela, M. Ribó et al. (2014), *A Be-type star with a black-hole companion*, Nature **505** 378.

Chaboyer, B. and J.-P. Zahn (1992), *Effect of horizontal turbulent diffusion on transport by meridional circulation.*, Astronomy & Astrophysics **253** 173.

Chan, C., B. Müller and A. Heger (2020), *The impact of fallback on the compact remnants and chemical yields of core-collapse supernovae*, Monthly Notices of the Royal Astronomical Society **495** 3751.

Chandrasekhar, S. (1931), *The Maximum Mass of Ideal White Dwarfs*, The Astrophysical Journal **74** 81.

Choi, J., A. Dotter, C. Conroy et al. (2016), *Mesa Isochrones and Stellar Tracks (MIST). I. Solar-scaled Models*, The Astrophysical Journal **823** 102.

Clausius, R. (1870), *Ueber einen auf die Wärme anwendbaren mechanischen Satz*, Annalen der Physik **217** 124.

Coe, M. J. and J. Kirk (2015), *Catalogue of Be/X-ray binary systems in the Small Magellanic Cloud: X-ray, optical and IR properties*, Monthly Notices of the Royal Astronomical Society **452** 969.

Coleiro, A. and S. Chaty (2013), *Distribution of High-mass X-Ray Binaries in the Milky Way*, The Astrophysical Journal **764** 185.

Crowther, P. A. (2007), *Physical Properties of Wolf-Rayet Stars*, Annual Review of Astronomy and Astrophysics **45** 177.

Crowther, P. A., S. M. Caballero-Nieves, K. A. Bostroem et al. (2016), *The R136 star cluster dissected with Hubble Space Telescope/STIS. I. Far-ultraviolet spectroscopic census and the origin of He II λ1640 in young star clusters*, Monthly Notices of the Royal Astronomical Society **458** 624.

Dalton, W. W. and C. L. Sarazin (1995), *High-Mass X-Ray Binary Populations. I. Galactic Modeling*, The Astrophysical Journal **440** 280.

Davis, P. J., L. Siess and R. Deschamps (2013), *Mass transfer in eccentric binary systems using the binary evolution code BINSTAR*, Astronomy & Astrophysics **556** A4.

De Greve, J.-P. and C. De Loore (1977), *The Evolution of Massive Close Binaries. V: Systems Containing Primaries with Masses between* $10M_{\odot}$ *and 15* $M_{\odot}$, Astrophysics and Space Science **50** 75.

de Kool, M. (1990), *Common Envelope Evolution and Double Cores of Planetary Nebulae*, The Astrophysical Journal **358** 189.

de Mink, S. E., M. Cantiello, N. Langer et al. (2009a), *Rotational mixing in massive binaries. Detached short-period systems*, Astronomy & Astrophysics **497** 243.

de Mink, S. E., N. Langer, R. G. Izzard et al. (2013), *The Rotation Rates of Massive Stars: The Role of Binary Interaction through Tides, Mass Transfer, and Mergers*, The Astrophysical Journal **764** 166.

de Mink, S. E., O. R. Pols and R. W. Hilditch (2007), *Efficiency of mass transfer in massive close binaries. Tests from double-lined eclipsing binaries in the SMC*, Astronomy & Astrophysics **467** 1181.

de Mink, S. E., O. R. Pols, N. Langer and R. G. Izzard (2009b), *Massive binaries as the source of abundance anomalies in globular clusters*, Astronomy & Astrophysics **507** L1.

de Mink, S. E., H. Sana, N. Langer et al. (2014), *The Incidence of Stellar Mergers and Mass Gainers among Massive Stars*, The Astrophysical Journal **782** 7.

Deschamps, R., L. Siess, P. J. Davis and A. Jorissen (2013), *Critically-rotating accretors and non-conservative evolution in Algols*, Astronomy & Astrophysics **557** A40.

Dessart, L., A. Burrows, C. D. Ott et al. (2006), *Multidimensional Simulations of the Accretion-induced Collapse of White Dwarfs to Neutron Stars*, The Astrophysical Journal **644** 1063.

Detmers, R. G., N. Langer, P. Podsiadlowski and R. G. Izzard (2008), *Gamma-ray bursts from tidally spun-up Wolf-Rayet stars?*, Astronomy & Astrophysics **484** 831.

Dewi, J. D. M. and O. R. Pols (2003), *The late stages of evolution of helium star-neutron star binaries and the formation of double neutron star systems*, Monthly Notices of the Royal Astronomical Society **344** 629.

Domiciano de Souza, A., M. Hadjara, F. Vakili et al. (2012), *Beyond the diffraction limit of optical/IR interferometers. I. Angular diameter and rotation parameters of Achernar from differential phases*, Astronomy & Astrophysics **545** A130.

Domiciano de Souza, A., P. Kervella, S. Jankov et al. (2003), *The spinning-top Be star Achernar from VLTI-VINCI*, Astronomy & Astrophysics **407** L47.

Dorigo Jones, J., M. S. Oey, K. Paggeot et al. (2020), *Runaway OB Stars in the Small Magellanic Cloud: Dynamical versus Supernova Ejections*, The Astrophysical Journal **903** 43.

Dufton, P. L., N. Langer, P. R. Dunstall et al. (2013), *The VLT-FLAMES Tarantula Survey. X. Evidence for a bimodal distribution of rotational velocities for the single early B-type stars*, Astronomy & Astrophysics **550** A109.

Dufton, P. L., D. J. Lennon, J. I. Villaseñor et al. (2022), *Properties of the Be-type stars in 30 Doradus*, Monthly Notices of the Royal Astronomical Society **512** 3331.

Dunstall, P. R., P. L. Dufton, H. Sana et al. (2015), *The VLT-FLAMES Tarantula Survey. XXII. Multiplicity properties of the B-type stars*, Astronomy & Astrophysics **580** A93.

Eddington, A. S. (1916), *On the radiative equilibrium of the stars*, Monthly Notices of the Royal Astronomical Society **77** 16.

– (1917), *On the radiative equilibrium of the stars*, Monthly Notices of the Royal Astronomical Society **77** 596.

– (1920), *The internal constitution of the stars*, The Observatory **43** 341.

– (1924), *On the relation between the masses and luminosities of the stars*, Monthly Notices of the Royal Astronomical Society **84** 308.

Eggleton, P. P. (1983), *Aproximations to the radii of Roche lobes.*, The Astrophysical Journal **268** 368.

Eggleton, P. P., J. Faulkner and B. P. Flannery (1973), *An Approximate Equation of State for Stellar Material*, Astronomy & Astrophysics **23** 325.

Eggleton, P. P. (1971), *The evolution of low mass stars*, Monthly Notices of the Royal Astronomical Society **151** 351.

– (1972), *Composition changes during stellar evolution*, Monthly Notices of the Royal Astronomical Society **156** 361.

– (1973), *A numerical treatment of double shell source stars*, Monthly Notices of the Royal Astronomical Society **163** 279.

Ekström, S., G. Meynet, A. Maeder and F. Barblan (2008), *Evolution towards the critical limit and the origin of Be stars*, Astronomy & Astrophysics **478** 467.

Eldridge, J. J. (2017), "Population Synthesis of Massive Close Binary Evolution", *Handbook of Supernovae*, ed. by A. W. Alsabti and P. Murdin 671.

Eldridge, J. J., E. R. Stanway, L. Xiao et al. (2017), *Binary Population and Spectral Synthesis Version 2.1: Construction, Observational Verification, and New Results*, Publications of the Astronomical Society of Australia **34** e058.

Eldridge, J. J., R. G. Izzard and C. A. Tout (2008), *The effect of massive binaries on stellar populations and supernova progenitors*, Monthly Notices of the Royal Astronomical Society **384** 1109.

Emden, R. (1907), *Gaskugeln: Anwendungen der mechanischen Wärmetheorie auf kosmologische und meteorologische Probleme*, BG Teubner.

Ercolino, A., H. Jin, N. Langer and L. Dessart (2024), *Interacting supernovae from wide massive binary systems*, Astronomy & Astrophysics **685** A58.

Ercolino, A., H. Jin, N. Langer and L. Dessart (2023), *Interacting supernovae from wide massive binary systems*, arXiv e-prints arXiv:2308.01819.

Evans, C. J., W. D. Taylor, V. Hénault-Brunet et al. (2011), *The VLT-FLAMES Tarantula Survey. I. Introduction and observational overview*, Astronomy & Astrophysics **530** A108.

Figueiredo, J., J. P. De Greve and R. W. Hilditch (1994), *OB-type binaries : models versus observations.*, Astronomy & Astrophysics **283** 144.

Flannery, B. P. and R. K. Ulrich (1977), *On the origin of Centaurus X-3 and related binary X-ray sources.*, The Astrophysical Journal **212** 533.

Flannery, B. P. and E. P. J. van den Heuvel (1975), *On the origin of the binary pulsar PSR 1913+16.*, Astronomy & Astrophysics **39** 61.

Foellmi, C. (2004), *Another single hydrogen-rich Wolf-Rayet star in the SMC?*, Astronomy & Astrophysics **416** 291.

Foellmi, C., A. F. J. Moffat and M. A. Guerrero (2003), *Wolf-Rayet binaries in the Magellanic Clouds and implications for massive-star evolution - I. Small Magellanic Cloud*, Monthly Notices of the Royal Astronomical Society **338** 360.

Fowler, R. H. (1926), *On dense matter*, Monthly Notices of the Royal Astronomical Society **87** 114.

Fragos, T., B. Willems, V. Kalogera et al. (2009), *Understanding Compact Object Formation and Natal Kicks. II. The Case of XTE J1118 + 480*, The Astrophysical Journal **697** 1057.

Fragos, T., J. J. Andrews, S. S. Bavera et al. (2023), *POSYDON: A General-purpose Population Synthesis Code with Detailed Binary-evolution Simulations*, The Astrophysical Journal Supplement Series **264** 45.

Fraunhofer, J. (1823), *Kurzer Bericht von den Resultaten neuerer Versuche über die Gesetze des Lichtes, und die Theorie derselben*, Annalen der Physik **74** 337.

Fraunhofer, J. (1817), *Bestimmung des Brechungs-und des Farbenzerstreungs-Vermögens verschiedener Glasarten, in Bezug auf die Vervollkommnung achromatischer Fernröhre*, Denkschriften der königlichen Akademie der Wissenschaften zu München **5** 193.

– (1821), *Neue Modifikation des Lichts durch Gegenseitige Einwirkung und Beugung der Strahlen, und Gesetze Derselben*, Denkschriften der königlichen Akademie der Wissenschaften zu München **8** 1.

Fryer, C. L., K. Belczynski, G. Wiktorowicz et al. (2012), *Compact Remnant Mass Function: Dependence on the Explosion Mechanism and Metallicity*, The Astrophysical Journal **749** 91.

Fujimoto, M. Y. and J. Iben Icko (1989), *Behavior of Low-Mass, Main-Sequence Stars in Response to Accretion*, The Astrophysical Journal **341** 306.

Gagnier, D., M. Rieutord, C. Charbonnel et al. (2019), *Critical angular velocity and anisotropic mass loss of rotating stars with radiation-driven winds*, Astronomy & Astrophysics **625** A88.

Gaia Collaboration, A. Vallenari, A. G. A. Brown et al. (2023), *Gaia Data Release 3. Summary of the content and survey properties*, Astronomy & Astrophysics **674** A1.

Ge, H., M. S. Hjellming, R. F. Webbink et al. (2010), *Adiabatic Mass Loss in Binary Stars. I. Computational Method*, The Astrophysical Journal **717** 724.

Ge, H., R. F. Webbink, X. Chen and Z. Han (2015), *Adiabatic Mass Loss in Binary Stars. II. From Zero-age Main Sequence to the Base of the Giant Branch*, The Astrophysical Journal **812** 40.

Ge, H., R. F. Webbink, X. Chen and Z. Han (2020), *Adiabatic Mass Loss in Binary Stars. III. From the Base of the Red Giant Branch to the Tip of the Asymptotic Giant Branch*, The Astrophysical Journal **899** 132.

Georgy, C., G. Meynet and A. Maeder (2011), *Effects of anisotropic winds on massive star evolution*, Astronomy & Astrophysics **527** A52.

Giacconi, R., H. Gursky, E. Kellogg et al. (1971), *Discovery of Periodic X-Ray Pulsations in Centaurus X-3 from UHURU*, The Astrophysical Journal Letters **167** L67.

Giacconi, R., H. Gursky, F. R. Paolini and B. B. Rossi (1962), *Evidence for x Rays From Sources Outside the Solar System*, Physical Review Letters **9** 439.

Giannone, P., K. Kohl and A. Weigert (1968), *Entwicklung in engen Doppelsternsystemen IV*, Zeitschrift für Astrophysik **68** 107.

Gies, D. R., J. Bagnuolo William G., E. C. Ferrara et al. (1998), *Hubble Space Telescope Goddard High Resolution Spectrograph Observations of the Be + sdO Binary φ Persei*, The Astrophysical Journal **493** 440.

Gingerich, O. (2013), "The Critical Importance of Russell's Diagram", *Origins of the Expanding Universe: 1912-1932*, ed. by M. J. Way and D. Hunter, vol. 471, Astronomical Society of the Pacific Conference Series 205.

Götberg, Y., S. E. de Mink, J. H. Groh et al. (2018), *Spectral models for binary products: Unifying subdwarfs and Wolf-Rayet stars as a sequence of stripped-envelope stars*, Astronomy & Astrophysics **615** A78.

Gräfener, G., J. S. Vink, A. de Koter and N. Langer (2011), *The Eddington factor as the key to understand the winds of the most massive stars. Evidence for a Γ-dependence of Wolf-Rayet type mass loss*, Astronomy & Astrophysics **535** A56.

Gualandris, A., M. Colpi, S. Portegies Zwart and A. Possenti (2005), *Has the Black Hole in XTE J1118+480 Experienced an Asymmetric Natal Kick?*, The Astrophysical Journal **618** 845.

Gurzadyan, G. A. (1997), *The Physics and Dynamics of Planetary Nebulae*, Springer-Verlag.

Haberl, F. and R. Sturm (2016), *High-mass X-ray binaries in the Small Magellanic Cloud*, Astronomy & Astrophysics **586** A81.

Hagen, L. M. Z., M. H. Siegel, E. A. Hoversten et al. (2017), *Swift Ultraviolet Survey of the Magellanic Clouds (SUMaC) - I. Shape of the ultraviolet dust extinction law and recent star formation history of the Small Magellanic Cloud*, Monthly Notices of the Royal Astronomical Society **466** 4540.

Hainich, R., D. Pasemann, H. Todt et al. (2015), *Wolf-Rayet stars in the Small Magellanic Cloud. I. Analysis of the single WN stars*, Astronomy & Astrophysics **581** A21.

Halm, J. (1911), *Stars, motion in space, etc. Further considerations relating to the systematic motions of the stars*, Monthly Notices of the Royal Astronomical Society **71** 610.

Han, Z.-W., H.-W. Ge, X.-F. Chen and H.-L. Chen (2020), *Binary Population Synthesis*, Research in Astronomy and Astrophysics **20** 161.

Hansen, C. J., S. D. Kawaler and V. Trimble (2004), *Stellar interiors : physical principles, structure, and evolution*.

Harris, C. R., K. J. Millman, S. J. van der Walt et al. (2020), *Array programming with NumPy*, Nature **585** 357, URL: `https://doi.org/10.1038/s41586-020-2649-2`.

Harris, J. and D. Zaritsky (2004), *The Star Formation History of the Small Magellanic Cloud*, The Astronomical Journal **127** 1531.

Hastings, B., N. Langer and J. Puls (2023), *A model of anisotropic winds from rotating stars for evolutionary calculations*, Astronomy & Astrophysics **672** A60.

Hastings, B., N. Langer, C. Wang et al. (2021), *Stringent upper limit on Be star fractions produced by binary interaction*, Astronomy & Astrophysics **653** A144.

Hastings, B., C. Wang and N. Langer (2020), *The single star path to Be stars*, Astronomy & Astrophysics **633** A165.

Hayashi, C. and R. Hoshi (1961), *The Outer Envelope of Giant Stars with Surface Convection Zone*, Publications of the Astronomical Society of Japan **13** 442.

Heber, U. (2009), *Hot Subdwarf Stars*, Annual Review of Astronomy and Astrophysics **47** 211.

Heger, A., C. L. Fryer, S. E. Woosley et al. (2003), *How Massive Single Stars End Their Life*, The Astrophysical Journal **591** 288.

Heger, A. and N. Langer (2000), *Presupernova Evolution of Rotating Massive Stars. II. Evolution of the Surface Properties*, The Astrophysical Journal **544** 1016.

Heger, A., N. Langer and S. E. Woosley (2000), *Presupernova Evolution of Rotating Massive Stars. I. Numerical Method and Evolution of the Internal Stellar Structure*, The Astrophysical Journal **528** 368.

Heger, A., S. E. Woosley and H. C. Spruit (2005), *Presupernova Evolution of Differentially Rotating Massive Stars Including Magnetic Fields*, The Astrophysical Journal **626** 350.

Helmholtz, H. v. (1854), *Ueber die Wechselwirkung der Naturkräfte...* Verlag von Gräfe & Unzer.

Henneco, J., F. R. N. Schneider and E. Laplace (2024), *Contact tracing of binary stars: Pathways to stellar mergers*, Astronomy & Astrophysics **682** A169.

Henyey, L. G., R. Lelevier and R. D. Levee (1959a), *Evolution of Main-Sequence Stars.*, The Astrophysical Journal **129** 2.

Henyey, L. G., R. Lelevier and R. D. Levée (1955), *The Early Phases of Stellar Evolution*, Publications of the Astronomical Society of the Pacific **67** 154.

Henyey, L. G., L. Wilets, K. H. Böhm et al. (1959b), *A Method for Automatic Computation of Stellar Evolution.*, The Astrophysical Journal **129** 628.

Herschel, W. (1803), *Account of the Changes That Have Happened, during the Last Twenty-Five Years, in the Relative Situation of Double-Stars; With an Investigation of the Cause to Which They Are Owing*, Philosophical Transactions of the Royal Society of London Series I **93** 339.

Hertzsprung, E. (1911), *Ueber die Verwendung photographischer effektiver Wellenlaengen zur Bestimmung von Farbenaequivalenten*, Publikationen des Astrophysikalischen Observatoriums zu Potsdam **63**.

– (1919), *Bemerkungen zur Statistik der Sternparallaxen*, Astronomische Nachrichten **208** 89.

Hewish, A., S. J. Bell, J. D. H. Pilkington et al. (1968), *Observation of a Rapidly Pulsating Radio Source*, Nature **217** 709.

Hilditch, R. W., I. D. Howarth and T. J. Harries (2005), *Forty eclipsing binaries in the Small Magellanic Cloud: fundamental parameters and Cloud distance*, Monthly Notices of the Royal Astronomical Society **357** 304.

Hills, J. G. (1983), *The effects of sudden mass loss and a random kick velocity produced in a supernova explosion on the dynamics of a binary star of arbitrary orbital eccentricity. Applications to X-ray binaries and to the binarypulsars.*, The Astrophysical Journal **267** 322.

Hjellming, M. S. (1989a), *ALGOLS as Limits on Binary Evolution Scenarios*, Space Science Reviews **50** 155.

Hjellming, M. S. and R. F. Webbink (1987), *Thresholds for Rapid Mass Transfer in Binary System. I. Polytropic Models*, The Astrophysical Journal **318** 794.

Hjellming, M. S. (1989b), *Rapid Mass Transfer in Binary Systems.*, PhD thesis: University of Illinois, Urbana-Champaign.

Hobbs, G., D. R. Lorimer, A. G. Lyne and M. Kramer (2005), *A statistical study of 233 pulsar proper motions*, Monthly Notices of the Royal Astronomical Society **360** 974.

Hopkins, P. F., D. Kereš, J. Oñorbe et al. (2014), *Galaxies on FIRE (Feedback In Realistic Environments): stellar feedback explains cosmologically inefficient star formation*, Monthly Notices of the Royal Astronomical Society **445** 581.

Hoyle, F. and R. A. Lyttleton (1942), *On the internal constitution of the stars*, Monthly Notices of the Royal Astronomical Society **102** 177.

Hoyle, F. and M. Schwarzschild (1955), *On the Evolution of Type II Stars.*, The Astrophysical Journal Supplement Series **2** 1.

Huggins, W. and W. A. Miller (1864), *On the Spectra of Some of the Fixed Stars*, Philosophical Transactions of the Royal Society of London Series I **154** 413.

Hulse, R. A. and J. H. Taylor (1975), *Discovery of a pulsar in a binary system.*, The Astrophysical Journal Letters **195** L51.

Hunter, I., D. J. Lennon, P. L. Dufton et al. (2008), *The VLT-FLAMES survey of massive stars: atmospheric parameters and rotational velocity distributions for B-type stars in the Magellanic Clouds*, Astronomy & Astrophysics **479** 541.

Hunter, J. D. (2007), *Matplotlib: A 2D graphics environment*, Computing in Science & Engineering **9** 90.

Hurley, J. R., O. R. Pols and C. A. Tout (2000), *Comprehensive analytic formulae for stellar evolution as a function of mass and metallicity*, Monthly Notices of the Royal Astronomical Society **315** 543.

Hurley, J. R., C. A. Tout and O. R. Pols (2002), *Evolution of binary stars and the effect of tides on binary populations*, Monthly Notices of the Royal Astronomical Society **329** 897.

Hut, P. (1981), *Tidal evolution in close binary systems.*, Astronomy & Astrophysics **99** 126.

Iben Icko, J., A. V. Tutukov and L. R. Yungelson (1995), *A Model of the Galactic X-Ray Binary Population. I. High-Mass X-Ray Binaries*, The Astrophysical Journal Supplement Series **100** 217.

Iglesias, C. A. and F. J. Rogers (1996), *Updated Opal Opacities*, The Astrophysical Journal **464** 943.

Ivanova, N., S. Justham, X. Chen et al. (2013), *Common envelope evolution: where we stand and how we can move forward*, The Astronomy and Astrophysics Review **21** 59.

Izzard, R. G., L. M. Dray, A. I. Karakas et al. (2006), *Population nucleosynthesis in single and binary stars. I. Model*, Astronomy & Astrophysics **460** 565.

Izzard, R. G., E. Glebbeek, R. J. Stancliffe and O. R. Pols (2009), *Population synthesis of binary carbon-enhanced metal-poor stars*, Astronomy & Astrophysics **508** 1359.

Izzard, R. G. and G. M. Halabi (2018), *Population synthesis of binary stars*, arXiv e-prints arXiv:1808.06883.

Izzard, R. G., C. A. Tout, A. I. Karakas and O. R. Pols (2004), *A new synthetic model for asymptotic giant branch stars*, Monthly Notices of the Royal Astronomical Society **350** 407.

Jacoby, G. H., D. A. Hunter and C. A. Christian (1984), *A library of stellar spectra.*, The Astrophysical Journal Supplement Series **56** 257.

Janka, H.-T. (2013), *Natal kicks of stellar mass black holes by asymmetric mass ejection in fallback supernovae*, Monthly Notices of the Royal Astronomical Society **434** 1355.

Janka, H.-T., A. Wongwathanarat and M. Kramer (2022), *Supernova Fallback as Origin of Neutron Star Spins and Spin-kick Alignment*, The Astrophysical Journal **926** 9.

Janssens, S., T. Shenar, N. Degenaar et al. (2023), *MWC 656 is unlikely to contain a black hole*, Astronomy & Astrophysics **677** L9.

Janssens, S., T. Shenar, H. Sana et al. (2022), *Uncovering astrometric black hole binaries with massive main-sequence companions with Gaia*, Astronomy & Astrophysics **658** A129.

Karttunen, H., P. Kröger, H. Oja et al. (2017), *Fundamental Astronomy*, Springer-Verlag.

Kaspi, V. M., M. Bailes, R. N. Manchester et al. (1996), *Evidence from a precessing pulsar orbit for a neutron-star birth kick*, Nature **381** 584.

Kewley, L. and H. A. Kobulnicky (2007), *The Metallicity History of Disk Galaxies*, Astrophysics and Space Science Proceedings **3** 435.

Kippenhahn, R. and E. Meyer-Hofmeister (1977), *On the radii of accreting main sequence stars.*, Astronomy & Astrophysics **54** 539.

Kippenhahn, R., S. Temesváry and L. Biermann (1958), *Sternmodelle I. Die Entwicklung der Sterne der Population II. Mit 6 Textabbildungen*, Zeitschrift für Astrophysik **46** 257.

Kippenhahn, R. and A. Weigert (1967), *Entwicklung in engen Doppelsternsystemen I. Massenaustausch vor und nach Beendigung des zentralen Wasserstoff-Brennens*, Zeitschrift für Astrophysik **65** 251.

Kippenhahn, R., A. Weigert and A. Weiss (2012), *Stellar Structure and Evolution*.

– (2013), *Stellar Structure and Evolution*, Springer-Verlag.

Kirchhoff, G. (1859), *Ueber den Zusammenhang zwischen Emission und Absorption von Licht und. Wärme*, Monatsberichte der Akademie der Wissenschaften zu Berlin 783.

– (1861), *Untersuchungen über das Sonnenspektrum und die Spectren der Chemischen Elemente*, Abhandlungen der königlich Preussischen Akademie der Wissenschaften zu Berlin 63.

– (1862), *Untersuchungen über das Sonnenspektrum und die Spectren der Chemischen Elemente*, Abhandlungen der königlich Preussischen Akademie der Wissenschaften zu Berlin 227.

– (1863), *Untersuchungen über das Sonnenspektrum und die Spectren der Chemischen Elemente*, Abhandlungen der königlich Preussischen Akademie der Wissenschaften zu Berlin 225.

Kitaura, F. S., H.-T. Janka and W. Hillebrandt (2006), *Explosions of O-Ne-Mg cores, the Crab supernova, and subluminous type II-P supernovae*, Astronomy & Astrophysics **450** 345.

Klencki, J., A. Istrate, G. Nelemans and O. Pols (2022), *Partial-envelope stripping and nuclear-timescale mass transfer from evolved supergiants at low metallicity*, Astronomy & Astrophysics **662** A56.

Klencki, J., G. Nelemans, A. G. Istrate and O. Pols (2020), *Massive donors in interacting binaries: effect of metallicity*, Astronomy & Astrophysics **638** A55.

Kobulnicky, H. A., D. C. Kiminki, M. J. Lundquist et al. (2014), *Toward Complete Statistics of Massive Binary Stars: Penultimate Results from the Cygnus OB2 Radial Velocity Survey*, The Astrophysical Journal Supplement Series **213** 34.

Kopal, Z. (1959), *Close binary systems*, Chapman & Hall.

Korn, A. J., S. R. Becker, C. A. Gummersbach and B. Wolf (2000), *Chemical abundances from Magellanic cloud B stars*, Astronomy & Astrophysics **353** 655.

Kroupa, P. (2001), *On the variation of the initial mass function*, Monthly Notices of the Royal Astronomical Society **322** 231.

Kroupa, P., C. A. Tout and G. Gilmore (1993), *The Distribution of Low-Mass Stars in the Galactic Disc*, Monthly Notices of the Royal Astronomical Society **262** 545.

Krtička, J., S. P. Owocki and G. Meynet (2011), *Mass and angular momentum loss via decretion disks*, Astronomy & Astrophysics **527** A84.

Kruckow, M. U., T. M. Tauris, N. Langer et al. (2016), *Common-envelope ejection in massive binary stars. Implications for the progenitors of GW150914 and GW151226*, Astronomy & Astrophysics **596** A58.

Kruckow, M. U., T. M. Tauris, N. Langer et al. (2018), *Progenitors of gravitational wave mergers: binary evolution with the stellar grid-based code COMBINE*, Monthly Notices of the Royal Astronomical Society **481** 1908.

Krzeminski, W. (1974), *The Identification and UBV Photometry of the Visible Component of the Centaurus X-3 Binary System*, The Astrophysical Journal Letters **192** L135.

Kudritzki, R. P., A. Pauldrach and J. Puls (1987), *Radiation driven winds of hot luminous stars. II. Wind models for O-stars in the Magellanic clouds.*, Astronomy & Astrophysics **173** 293.

Landau, L. D. (1932), *To the Stars theory*, Phys. Zs. Sowjet **1** 285.

Lane, H. J. (1870), *On the theoretical temperature of the sun, under the hypothesis of a gaseous mass maintaining its volume by its internal heat, and depending on the laws of gases as known to terrestrial experiment*, American Journal of Science **2** 57.

Langer, N. (1989), *Standard models of Wolf-Rayet stars.*, Astronomy & Astrophysics **210** 93.

– (1991), *Evolution of massive stars in the Large Magellanic Cloud : models with semiconvection.*, Astronomy & Astrophysics **252** 669.

– (1998), *Coupled mass and angular momentum loss of massive main sequence stars*, Astronomy & Astrophysics **329** 551.

– (2012), *Presupernova Evolution of Massive Single and Binary Stars*, Annual Review of Astronomy and Astrophysics **50** 107.

– (2022), *Open questions in massive star research*, arXiv e-prints arXiv:2209.04165.

Langer, N., K. J. Fricke and D. Sugimoto (1983), *Semiconvective diffusion and energy transport*, Astronomy & Astrophysics **126** 207.

Langer, N., C. Schürmann, K. Stoll et al. (2020), *Properties of OB star-black hole systems derived from detailed binary evolution models*, Astronomy & Astrophysics **638** A39.

Laplace, E., Y. Götberg, S. E. de Mink et al. (2020), *The expansion of stripped-envelope stars: Consequences for supernovae and gravitational-wave progenitors*, Astronomy & Astrophysics **637** A6.

Laplace, E., S. Justham, M. Renzo et al. (2021), *Different to the core: The pre-supernova structures of massive single and binary-stripped stars*, Astronomy & Astrophysics **656** A58.

Lau, M. Y. M., R. Hirai, I. Mandel and C. A. Tout (2024), *Expansion of Accreting Main-sequence Stars during Rapid Mass Transfer*, The Astrophysical Journal Letters **966** L7.

Ledoux, P. (1947), *Stellar Models with Convection and with Discontinuity of the Mean Molecular Weight*, The Astrophysical Journal **105** 305.

Lennon, D. J., P. L. Dufton, J. I. Villaseñor et al. (2024), *Rotational synchronisation of B-type binaries in 30 Doradus*, arXiv e-prints arXiv:2405.17608.

Lennon, D. J., J. Maíz Apellániz, A. Irrgang et al. (2021), *Hubble spectroscopy of LB-1: Comparison with B+black-hole and Be+stripped-star models*, Astronomy & Astrophysics **649** A167.

Lipunov, V. M., K. A. Postnov and M. E. Prokhorov (1996), *The Scenario Machine: restrictions on key parameters of binary evolution.*, Astronomy & Astrophysics **310** 489.

Liu, B., N. S. Sartorio, R. G. Izzard and A. Fialkov (2024), *Population synthesis of Be X-ray binaries: metallicity dependence of total X-ray outputs*, Monthly Notices of the Royal Astronomical Society **527** 5023.

Liu, J., H. Zhang, A. W. Howard et al. (2019), *A wide star-black-hole binary system from radial-velocity measurements*, Nature **575** 618.

Lockyer, J. N. (1887), *Researches on the Spectra of Meteorites. A Report to the Solar Physics Committee*, Proceedings of the Royal Society of London Series I **43** 117.

– (1915), *Notes on Stellar Classification*, Nature **94** 618.

Longair, M. S. (2006), *The Cosmic Century*, Cambridge University Press.

Lorimer, D. R. and M. Kramer (2004), *Handbook of Pulsar Astronomy*, vol. 4, Cambridge University Press.

St-Louis, N., A. F. J. Moffat, S. Marchenko and J. M. Pittard (2005), *FUSE Observations of the SMC 16 day Wolf-Rayet Binary Sanduleak 1 (WO4+O4): Atmospheric Eclipses and Colliding Stellar Winds*, The Astrophysical Journal **628** 953.

Lü, G.-L., C.-H. Zhu and Z.-J. Wang (2011), *Population synthesis of high mass X-ray binaries*, Research in Astronomy and Astrophysics **11** 327.

Lubow, S. H. and F. H. Shu (1975), *Gas dynamics of semidetached binaries.*, The Astrophysical Journal **198** 383.

Mac Low, M.-M. and R. S. Klessen (2004), *Control of star formation by supersonic turbulence*, Reviews of Modern Physics **76** 125.

Maeder, A. and G. Meynet (2004), *Stellar evolution with rotation and magnetic fields. II. General equations for the transport by Tayler-Spruit dynamo*, Astronomy & Astrophysics **422** 225.

Maeder, A. (2009), *Physics, Formation and Evolution of Rotating Stars*, Springer-Verlag.

Maeder, A. and G. Meynet (2000), *The Evolution of Rotating Stars*, Annual Review of Astronomy and Astrophysics **38** 143.

Manchester, R. N., G. B. Hobbs, A. Teoh and M. Hobbs (2005), *The Australia Telescope National Facility Pulsar Catalogue*, The Astronomical Journal **129** 1993.

Mandel, I. (2016), *Estimates of black hole natal kick velocities from observations of low-mass X-ray binaries*, Monthly Notices of the Royal Astronomical Society **456** 578.

Marchant, P. and J. Bodensteiner (2023), *The Evolution of Massive Binary Stars*, arXiv e-prints arXiv:2311.01865.

Marchant Campos, P. (2018), *The impact of tides and mass transfer on the evolution of metal-poor massive binary stars*, PhD thesis: Rheinische Friedrich-Wilhelms-Universität Bonn, URL: `http://hdl.handle.net/20.500.11811/7507`.

Margutti, R. and R. Chornock (2021), *First Multimessenger Observations of a Neutron Star Merger*, Annual Review of Astronomy and Astrophysics **59** 155.

Massey, P., C. C. Lang, K. Degioia-Eastwood and C. D. Garmany (1995), *Massive Stars in the Field and Associations of the Magellanic Clouds: The Upper Mass Limit, the Initial Mass Function, and a Critical Test of Main-Sequence Stellar Evolutionary Theory*, The Astrophysical Journal **438** 188.

Maury, A. C. and E. C. Pickering (1897), *Spectra of bright stars photographed with the 11-inch Draper Telescope as part of the Henry Draper Memorial.*, Annals of Harvard College Observatory **28** 1.

Mayer, C. (1778), *Gründliche Vertheidigung neuer Beobachtungen von Sternwarte entdecket worden sind Fixsterntrabanten, welche zu Mannheim auf der kurfürstlichen*.

McAlister, H. A., T. A. ten Brummelaar, D. R. Gies et al. (2005), *First Results from the CHARA Array. I. An Interferometric and Spectroscopic Study of the Fast Rotator α Leonis (Regulus)*, The Astrophysical Journal **628** 439.

Menon, A., N. Langer, S. E. de Mink et al. (2021), *Detailed evolutionary models of massive contact binaries - I. Model grids and synthetic populations for the Magellanic Clouds*, Monthly Notices of the Royal Astronomical Society **507** 5013.

Meurs, E. J. A. and E. P. J. van den Heuvel (1989), *The number of evolved early-type close binaries in the galaxy.*, Astronomy & Astrophysics **226** 88.

Michell, J. (1767), *An Inquiry into the Probable Parallax, and Magnitude of the Fixed Stars, from the Quantity of Light Which They Afford us, and the Particular Circumstances of Their Situation, by the Rev. John Michell, B. D. F. R. S.*, Philosophical Transactions of the Royal Society of London Series I **57** 234.

Miller-Jones, J. C. A., A. Bahramian, J. A. Orosz et al. (2021), *Cygnus X-1 contains a 21-solar mass black hole—Implications for massive star winds*, Science **371** 1046.

Misra, D., K. Kovlakas, T. Fragos et al. (2023), *X-ray luminosity function of high-mass X-ray binaries: Studying the signatures of different physical processes using detailed binary evolution calculations*, Astronomy & Astrophysics **672** A99.

Moe, M. and R. Di Stefano (2017), *Mind Your Ps and Qs: The Interrelation between Period (P) and Mass-ratio (Q) Distributions of Binary Stars*, The Astrophysical Journal Supplement Series **230** 15.

Mokiem, M. R., A. de Koter, J. S. Vink et al. (2007), *The empirical metallicity dependence of the mass-loss rate of O- and early B-type stars*, Astronomy & Astrophysics **473** 603.

Montanari, G. (1671), *Sopra la sparizione d'alcune stelle et altre novità celesti*, Prose de Signori Accademici Gelati di Bologna 369.

Nariai, K. and D. Sugimoto (1976), *Unstable Mass Outflow from a Binary System*, Publications of the Astronomical Society of Japan **28** 593.

Nelemans, G., T. M. Tauris and E. P. J. van den Heuvel (1999), *Constraints on mass ejection in black hole formation derived from black hole X-ray binaries*, Astronomy & Astrophysics **352** L87.

Nelson, C. A. and P. P. Eggleton (2001), *A Complete Survey of Case A Binary Evolution with Comparison to Observed Algol-type Systems*, The Astrophysical Journal **552** 664.

Neo, S., S. Miyaji, K. Nomoto and D. Sugimoto (1977), *Effect of Rapid Mass Accretion onto the Main-Sequence Stars*, Publications of the Astronomical Society of Japan **29** 249.

Niemela, V. S., P. Massey, G. Testor and S. Giménez Benítez (2002), *The massive Wolf-Rayet binary SMC WR7*, Monthly Notices of the Royal Astronomical Society **333** 347.

O'Connor, E. and C. D. Ott (2011), *Black Hole Formation in Failing Core-Collapse Supernovae*, The Astrophysical Journal **730** 70.

Oke, J. B. and M. Schwarzschild (1952), *Inhomogeneous Stellar Models. I. Models with a Convective Core and a Discontinuity in the Chemical Composition.*, The Astrophysical Journal **116** 317.

Oppenheimer, J. R. and H. Snyder (1939), *On Continued Gravitational Contraction*, Physical Review **56** 455.

Oppenheimer, J. R. and G. M. Volkoff (1939), *On Massive Neutron Cores*, Physical Review **55** 374.

Orosz, J. A., J. E. McClintock, J. P. Aufdenberg et al. (2011), *The Mass of the Black Hole in Cygnus X-1*, The Astrophysical Journal **742** 84.

Orosz, J. A., J. E. McClintock, C. D. Bailyn et al. (2007), *Dynamical Evidence for a Black Hole in the Eclipsing X-ray Binary M33 X-7*, The Astronomer's Telegram **977** 1.

Orosz, J. A., D. Steeghs, J. E. McClintock et al. (2009), *A New Dynamical Model for the Black Hole Binary LMC X-1*, The Astrophysical Journal **697** 573.

Özel, F. and P. Freire (2016), *Masses, Radii, and the Equation of State of Neutron Stars*, Annual Review of Astronomy and Astrophysics **54** 401.

Packet, W. (1981), *On the spin-up of the mass accreting component in a close binary system*, Astronomy & Astrophysics **102** 17.

Packet, W. and J. P. De Greve (1979), *Accretion onto ZAMS stars: application to beta Lyrae and remarks on X-ray binaries.*, Astronomy & Astrophysics **75** 255.

Paczynski, B. (1991), *A Polytropic Model of an Accretion Disk, a Boundary Layer, and a Star*, The Astrophysical Journal **370** 597.

Paczyński, B. (1966), *Evolution of Close Binaries. I.*, Acta Astronomica **16** 231.

– (1971), *Evolution of Single Stars. IV. Helium Stars*, Acta Astronomica **21** 1.

Palacios, A., C. Charbonnel, S. Talon and L. Siess (2006), *Rotational mixing in low-mass stars. II. Self-consistent models of Pop II RGB stars*, Astronomy & Astrophysics **453** 261.

Pauli, D., N. Langer, D. R. Aguilera-Dena et al. (2022), *A synthetic population of Wolf-Rayet stars in the LMC based on detailed single and binary star evolution models*, Astronomy & Astrophysics **667** A58.

Pauli, W. (1925), *Über den Zusammenhang des Abschlusses der Elektronengruppen im Atom mit der Komplexstruktur der Spektren*, Zeitschrift für Physik **31** 765.

Paxton, B., L. Bildsten, A. Dotter et al. (2011), *Modules for Experiments in Stellar Astrophysics (MESA)*, The Astrophysical Journal Supplement Series **192** 3.

Paxton, B., M. Cantiello, P. Arras et al. (2013), *Modules for Experiments in Stellar Astrophysics (MESA): Planets, Oscillations, Rotation, and Massive Stars*, The Astrophysical Journal Supplement Series **208** 4.

Paxton, B., P. Marchant, J. Schwab et al. (2015), *Modules for Experiments in Stellar Astrophysics (MESA): Binaries, Pulsations, and Explosions*, The Astrophysical Journal Supplement Series **220** 15.

Paxton, B., J. Schwab, E. B. Bauer et al. (2018), *Modules for Experiments in Stellar Astrophysics (MESA): Convective Boundaries, Element Diffusion, and Massive Star Explosions*, The Astrophysical Journal Supplement Series **234** 34.

Paxton, B., R. Smolec, J. Schwab et al. (2019), *Modules for Experiments in Stellar Astrophysics (MESA): Pulsating Variable Stars, Rotation, Convective Boundaries, and Energy Conservation*, The Astrophysical Journal Supplement Series **243** 10.

Payne, C. H. (1925), *Stellar Atmospheres; a Contribution to the Observational Study of High Temperature in the Reversing Layers of Stars.*, PhD thesis: Radcliffe College.

Perlmutter, S., G. Aldering, G. Goldhaber et al. (1999), *Measurements of Ω and Λ from 42 High-Redshift Supernovae*, The Astrophysical Journal **517** 565.

Petrovic, J., N. Langer and K. A. van der Hucht (2005), *Constraining the mass transfer in massive binaries through progenitor evolution models of Wolf-Rayet+O binaries*, Astronomy & Astrophysics **435** 1013.

Pickering, E. C. (1890a), *On the spectrum of zeta Ursae Majoris*, The Observatory **13** 80.

Pickering, E. C. (1890b), *The Draper Catalogue of stellar spectra photographed with the 8-inch Bache telescope as a part of the Henry Draper memorial*, Annals of Harvard College Observatory **27** 1.

Pickering, E. C. (1912), *Distribution of stellar spectra*, Annals of Harvard College Observatory **56** 1.

Pignatari, M., R. Gallino, M. Heil et al. (2010), *The Weak s-Process in Massive Stars and its Dependence on the Neutron Capture Cross Sections*, The Astrophysical Journal **710** 1557.

Podsiadlowski, P., Z. Han, A. E. Lynas-Gray and D. Brown (2008), "Hot Subdwarfs in Binaries as the Source of the Far-UV Excess in Elliptical Galaxies", *Hot Subdwarf Stars and Related Objects*, ed. by U. Heber, C. S. Jeffery and R. Napiwotzki, vol. 392, Astronomical Society of the Pacific Conference Series 15.

Podsiadlowski, P., P. C. Joss and J. J. L. Hsu (1992), *Presupernova Evolution in Massive Interacting Binaries*, The Astrophysical Journal **391** 246.

Podsiadlowski, P., N. Langer, A. J. T. Poelarends et al. (2004), *The Effects of Binary Evolution on the Dynamics of Core Collapse and Neutron Star Kicks*, The Astrophysical Journal **612** 1044.

Podsiadlowski, P., S. Rappaport and Z. Han (2003), *On the formation and evolution of black hole binaries*, Monthly Notices of the Royal Astronomical Society **341** 385.

Podsiadlowski, P., K. Nomoto, K. Maeda et al. (2002), *Formation of the Black Hole in Nova Scorpii*, The Astrophysical Journal **567** 491.

Podsiadlowski, P. (1992), *The Progenitor of SN 1987A*, Publications of the Astronomical Society of the Pacific **104** 717.

Poeckert, R. (1981), *A spectroscopic study of the binary Be star phi Per.*, Publications of the Astronomical Society of the Pacific **93** 297.

Pols, O. R. (1994), *Case A evolution of massive close binaries: formation of contact systems and possible reversal of the supernova order*, Astronomy & Astrophysics **290** 119.

– (2007), "Mass and Angular Momentum Loss in Massive Binary Evolution", *Massive Stars in Interactive Binaries*, ed. by N. St.-Louis and A. F. J. Moffat, vol. 367, Astronomical Society of the Pacific Conference Series 387.

Pols, O. R., J. Cote, L. B. F. M. Waters and J. Heise (1991), *The formation of Be stars through close binary evolution.*, Astronomy & Astrophysics **241** 419.

Pols, O. R. and M. Marinus (1994), *Monte-Carlo simulations of binary stellar evolution in young open clusters*, Astronomy & Astrophysics **288** 475.

Popham, R. and R. Narayan (1991), *Does Accretion Cease When a Star Approaches Breakup?*, The Astrophysical Journal **370** 604.

Portegies Zwart, S. F. (1995), *The formation of Be stars in close binary systems. The importance of kicks and angular-momentum loss*, Astronomy & Astrophysics **296** 691.

Portegies Zwart, S. F. and F. Verbunt (1996), *Population synthesis of high-mass binaries.*, Astronomy & Astrophysics **309** 179.

Porter, J. M. and T. Rivinius (2003), *Classical Be Stars*, Publications of the Astronomical Society of the Pacific **115** 1153.

Prša, A., A. Kochoska, K. E. Conroy et al. (2022), *TESS Eclipsing Binary Stars. I. Short-cadence Observations of 4584 Eclipsing Binaries in Sectors 1-26*, The Astrophysical Journal Supplement Series **258** 16.

Pustylnik, I. (1998), *The Early History of Resolving the Algol Paradox*, Astronomical and Astrophysical Transactions **15** 357.

Raguzova, N. V. (2001), *Population synthesis of Be/white dwarf binaries in the Galaxy*, Astronomy & Astrophysics **367** 848.

Raguzova, N. V. and V. M. Lipunov (1998), *High-eccentric X-ray binaries: evolution, wind rose effect, accretor-propeller luminosity gap*, Astronomy & Astrophysics **340** 85.

– (1999), *The evolutionary evidence for Be/black hole binaries*, Astronomy & Astrophysics **349** 505.

Rahman, N., H.-T. Janka, G. Stockinger and S. E. Woosley (2022), *Pulsational pair-instability supernovae: gravitational collapse, black hole formation, and beyond*, Monthly Notices of the Royal Astronomical Society **512** 4503.

Ramachandran, V., L. M. Oskinova, W.-R. Hamann et al. (2022), *Phase-resolved spectroscopic analysis of the eclipsing black hole X-ray binary M33 X-7: System properties, accretion, and evolution*, Astronomy & Astrophysics **667** A77.

Renzo, M. and Y. Götberg (2021), *Evolution of Accretor Stars in Massive Binaries: Broader Implications from Modeling ζ Ophiuchi*, The Astrophysical Journal **923** 277.

Renzo, M., E. Zapartas, S. E. de Mink et al. (2019), *Massive runaway and walkaway stars. A study of the kinematical imprints of the physical processes governing the evolution and explosion of their binary progenitors*, Astronomy & Astrophysics **624** A66.

Renzo, M., E. Zapartas, S. Justham et al. (2023), *Rejuvenated Accretors Have Less Bound Envelopes: Impact of Roche Lobe Overflow on Subsequent Common Envelope Events*, The Astrophysical Journal Letters **942** L32.

Repetto, S., M. B. Davies and S. Sigurdsson (2012), *Investigating stellar-mass black hole kicks*, Monthly Notices of the Royal Astronomical Society **425** 2799.

Repetto, S. and G. Nelemans (2015), *Constraining the formation of black holes in short-period black hole low-mass X-ray binaries*, Monthly Notices of the Royal Astronomical Society **453** 3341.

Riess, A. G., A. V. Filippenko, P. Challis et al. (1998), *Observational Evidence from Supernovae for an Accelerating Universe and a Cosmological Constant*, The Astronomical Journal **116** 1009.

Riley, J., P. Agrawal, J. W. Barrett et al. (2022), *Rapid Stellar and Binary Population Synthesis with COMPAS*, The Astrophysical Journal Supplement Series **258** 34.

Ritter, A. (1883a), *Untersuchungen über die Constitution gasförmiger Weltkörper. 16. Abtheilung*, Annalen der Physik **256** 137.

– (1883b), *Untersuchungen über die Constitution gasförmiger Weltkörper. 17. Abtheilung*, Annalen der Physik **256** 897.

– (1883c), *Untersuchungen über die Constitution gasförmiger Weltkörper. 18. Abtheilung*, Annalen der Physik **256** 910.

– (1898), *On the constitution of gaseous celestial bodies*, Astrophysical Journal, vol. 8, p. 293 **8** 293.

Rivinius, T., R. Klement, S. D. Chojnowski et al. (2022), *MWC656: A Be+BH or a Be+sdO?*, arXiv e-prints arXiv:2208.12315.

Rivinius, T., A. C. Carciofi and C. Martayan (2013), *Classical Be stars. Rapidly rotating B stars with viscous Keplerian decretion disks*, The Astronomy and Astrophysics Review **21** 69.

Romero-Shaw, I., R. Hirai, A. Bahramian et al. (2023), *Rapid population synthesis of black hole high-mass X-ray binaries: implications for binary stellar evolution*, Monthly Notices of the Royal Astronomical Society **524** 245.

Rubele, S., L. Girardi, L. Kerber et al. (2015), *The VMC survey - XIV. First results on the look-back time star formation rate tomography of the Small Magellanic Cloud*, Monthly Notices of the Royal Astronomical Society **449** 639.

Rubele, S., G. Pastorelli, L. Girardi et al. (2018), *The VMC survey - XXXI: The spatially resolved star formation history of the main body of the Small Magellanic Cloud*, Monthly Notices of the Royal Astronomical Society **478** 5017.

Russell, H. N. (1914a), *Relations Between the Spectra and Other Characteristics of the Stars*, Popular Astronomy **22** 275.

– (1914b), *Relations Between the Spectra and Other Characteristics of the Stars*, Popular Astronomy **22** 331.

– (1914c), *Relations Between the Spectra and other Characteristics of the Stars. I. Historical*, Nature **93** 227.

– (1914d), *Relations Between the Spectra and other Characteristics of the Stars. II. Brightness and Spectral Class*, Nature **93** 252.

– (1914e), *Relations Between the Spectra and other Characteristics of the Stars. III.*, Nature **93** 281.

Rutherford, E. (1907), *Some Cosmical Aspects of Radioactivity*, Journal of the Royal Astronomical Society of Canada **1** 145.

Saha, M. N. (1921), *On a Physical Theory of Stellar Spectra*, Proceedings of the Royal Society of London Series A **99** 135.

Salpeter, E. E. (1955), *The Luminosity Function and Stellar Evolution.*, The Astrophysical Journal **121** 161.

Sampson, R. A. (1895), *Sun, rotation and mechanical state of the*, Monthly Notices of the Royal Astronomical Society **55** 280.

Sana, H., A. de Koter, S. E. de Mink et al. (2013), *The VLT-FLAMES Tarantula Survey. VIII. Multiplicity properties of the O-type star population*, Astronomy & Astrophysics **550** A107.

Sana, H., S. E. de Mink, A. de Koter et al. (2012), *Binary Interaction Dominates the Evolution of Massive Stars*, Science **337** 444.

Sana, H. and C. J. Evans (2011), "The multiplicity of massive stars", *Active OB Stars: Structure, Evolution, Mass Loss, and Critical Limits*, ed. by C. Neiner, G. Wade, G. Meynet and G. Peters, vol. 272 474.

Sandage, A. R. and M. Schwarzschild (1952), *Inhomogeneous Stellar Models. II. Models with Exhausted Cores in Gravitational Contraction.*, The Astrophysical Journal **116** 463.

Sander, A. A. C. and J. S. Vink (2020), *On the nature of massive helium star winds and Wolf-Rayet-type mass-loss*, Monthly Notices of the Royal Astronomical Society **499** 873.

Sanyal, D., L. Grassitelli, N. Langer and J. M. Bestenlehner (2015), *Massive main-sequence stars evolving at the Eddington limit*, Astronomy & Astrophysics **580** A20.

Sanyal, D., N. Langer, D. Szécsi et al. (2017), *Metallicity dependence of envelope inflation in massive stars*, Astronomy & Astrophysics **597** A71.

Sarna, M. J. (1993), *The evolutionary status of beta Per.*, Monthly Notices of the Royal Astronomical Society **262** 534.

Savonije, G. J. and R. J. Takens (1976), *Evolution of helium stars: a self-consistent determination of the boundary of a helium burning convective core.*, Astronomy & Astrophysics **47** 231.

Scalo, J. M. (1986), *The Stellar Initial Mass Function*, Fundamentals of Cosmic Physics **11** 1.

Schmidt, B. P., N. B. Suntzeff, M. M. Phillips et al. (1998), *The High-Z Supernova Search: Measuring Cosmic Deceleration and Global Curvature of the Universe Using Type IA Supernovae*, The Astrophysical Journal **507** 46.

Schneider, F. R. N., R. G. Izzard, N. Langer and S. E. de Mink (2015), *Evolution of Mass Functions of Coeval Stars through Wind Mass Loss and Binary Interactions*, The Astrophysical Journal **805** 20.

Schneider, F. R. N., P. Podsiadlowski and E. Laplace (2024), *Pre-supernova evolution and final fate of stellar mergers and accretors of binary mass transfer*, Astronomy & Astrophysics **686** A45.

Schneider, F. R. N., P. Podsiadlowski and B. Müller (2021), *Pre-supernova evolution, compact-object masses, and explosion properties of stripped binary stars*, Astronomy & Astrophysics **645** A5.

Schneider, F. R. N., S. T. Ohlmann, P. Podsiadlowski et al. (2019), *Stellar mergers as the origin of magnetic massive stars*, Nature **574** 211.

Schootemeijer, A., Y. Götberg, S. E. de Mink et al. (2018), *Clues about the scarcity of stripped-envelope stars from the evolutionary state of the sdO+Be binary system φ Persei*, Astronomy & Astrophysics **615** A30.

Schootemeijer, A. and N. Langer (2018), *Wolf-Rayet stars in the Small Magellanic Cloud as testbed for massive star evolution*, Astronomy & Astrophysics **611** A75.

Schootemeijer, A., N. Langer, N. J. Grin and C. Wang (2019), *Constraining mixing in massive stars in the Small Magellanic Cloud*, Astronomy & Astrophysics **625** A132.

Schootemeijer, A., N. Langer, D. Lennon et al. (2021), *A dearth of young and bright massive stars in the Small Magellanic Cloud*, Astronomy & Astrophysics **646** A106.

Schootemeijer, A., D. J. Lennon, M. Garcia et al. (2022), *A census of OBe stars in nearby metal-poor dwarf galaxies reveals a high fraction of extreme rotators*, Astronomy & Astrophysics **667** A100.

Schootemeijer, A., T. Shenar, N. Langer et al. (2024), *An absence of binary companions to Wolf-Rayet stars in the Small Magellanic Cloud: implications for mass loss and black hole masses at low metallicity*, arXiv e-prints arXiv:2406.01420.

Schreier, E., R. Levinson, H. Gursky et al. (1972), *Evidence for the Binary Nature of Centaurus X-3 from UHURU X-Ray Observations.*, The Astrophysical Journal Letters **172** L79.

Schürmann, C. and N. Langer (2024), *Exploring the boundary between stable mass transfer and L_2 overflow in close binary evolution*, Astronomy & Astrophysics **691** A174.

Schürmann, C., N. Langer, J. A. Kramer et al. (2024), *Analytic approximations for massive close post-mass transfer binary systems*, Astronomy & Astrophysics **690** A282.

Schürmann, C., N. Langer, X. Xu and C. Wang (2022), *The spins of stripped B stars support magnetic internal angular momentum transport*, Astronomy & Astrophysics **667** A122.

Schürmann, C., X.-T. Xu, N. Langer et al. (2025), *Populations of evolved massive binary stars in the Small Magellanic Cloud II: Predictions from rapid binary evolution*, arXiv e-prints arXiv:2503.23878.

Schuster, A. (1902), *The Solar Atmosphere*, The Astrophysical Journal **16** 320.

– (1905), *Radiation Through a Foggy Atmosphere*, The Astrophysical Journal **21** 1.

Schwarzschild, K. (1900), *Über die Photographische Vergleichung der Helligkeit Verschiedenfarbiger Sterne*, Sitzungsberichte der Kaiserlichen Akademie der Wissenschaften in Wien, Mathematisch-Naturwissenschaftliche Klasse, Abteilung IIa **109** 1127.

Schwarzschild, K. (1906), *Über das Gleichgewicht der Sonnenatmosphäre*, Nachrichten von der Gesellschaft der Wissenschaften zu Göttingen, Mathematisch-Physikalische Klasse **1906** 41.

Schwarzschild, M., I. Rabinowitz and R. Härm (1953), *Inhomogeneous Stellar Models. III. Models with Partially Degenerate Isothermal Cores.*, The Astrophysical Journal **118** 326.

Schwarzschild, M. (1946), *On the Helium Content of the Sun.*, The Astrophysical Journal **104** 203.

– (1958), *Structure and evolution of the stars.* Princeton University Press.

Secchi, A. (1866), *Schreiben des Herrn Prof. Secchi, Directors der Sternwarte des Collegio Romano, an den Herausgeber*, Astronomische Nachrichten **68** 63.

Sen, K., N. Langer, P. Marchant et al. (2021), *Detailed models of interacting short-period massive binary stars*, arXiv e-prints arXiv:2111.03329.

Sen, K., N. Langer, P. Marchant et al. (2022), *Detailed models of interacting short-period massive binary stars*, Astronomy & Astrophysics **659** A98.

Sen, K., N. Langer, D. Pauli et al. (2023), *Reverse Algols and hydrogen-rich Wolf-Rayet stars from very massive binaries*, Astronomy & Astrophysics **672** A198.

Shao, Y. and X.-D. Li (2014), *On the Formation of Be Stars through Binary Interaction*, The Astrophysical Journal **796** 37.

– (2016), *Nonconservative Mass Transfer in Massive Binaries and the Formation of Wolf-Rayet+O Binaries*, The Astrophysical Journal **833** 108.

– (2019), *Population Synthesis of Black Hole Binaries with Normal-star Companions. I. Detached Systems*, The Astrophysical Journal **885** 151.

– (2020), *Population Synthesis of Black Hole X-Ray Binaries*, The Astrophysical Journal **898** 143.

– (2021), *Population Synthesis of Galactic Be-star Binaries with a Helium-star Companion*, The Astrophysical Journal **908** 67.

Shapiro, S. L. and S. A. Teukolsky (1983), *Black holes, white dwarfs and neutron stars. The physics of compact objects*, Wiley-VCH.

Shaviv, G. and S. Starrfield (1988), *Accretion onto Main-Sequence Stars. I. The Transient Phase*, The Astrophysical Journal **335** 383.

Shenar, T., J. Bodensteiner, M. Abdul-Masih et al. (2020a), *The "hidden" companion in LB-1 unveiled by spectral disentangling*, Astronomy & Astrophysics **639** L6.

Shenar, T., A. Gilkis, J. S. Vink et al. (2020b), *Why binary interaction does not necessarily dominate the formation of Wolf-Rayet stars at low metallicity*, Astronomy & Astrophysics **634** A79.

Shenar, T., R. Hainich, H. Todt et al. (2016), *Wolf-Rayet stars in the Small Magellanic Cloud. II. Analysis of the binaries*, Astronomy & Astrophysics **591** A22.

Shenar, T., R. Hainich, H. Todt et al. (2018), *The shortest-period Wolf-Rayet binary in the Small Magellanic Cloud: Part of a high-order multiple system. Spectral and orbital analysis of SMC AB 6*, Astronomy & Astrophysics **616** A103.

Shenar, T., D. P. Sablowski, R. Hainich et al. (2019), *The Wolf-Rayet binaries of the nitrogen sequence in the Large Magellanic Cloud. Spectroscopy, orbital analysis, formation, and evolution*, Astronomy & Astrophysics **627** A151.

Shenar, T., H. Sana, L. Mahy et al. (2022), *An X-ray-quiet black hole born with a negligible kick in a massive binary within the Large Magellanic Cloud*, Nature Astronomy **6** 1085.

Siess, L. (2006), *Evolution of massive AGB stars. I. Carbon burning phase*, Astronomy & Astrophysics **448** 717.

Siess, L. and M. Arnould (2008), *Production of ^{26}Al by super-AGB stars*, Astronomy & Astrophysics **489** 395.

Siess, L., E. Dufour and M. Forestini (2000), *An internet server for pre-main sequence tracks of low- and intermediate-mass stars*, Astronomy & Astrophysics **358** 593.

Siess, L., R. G. Izzard, P. J. Davis and R. Deschamps (2013), *BINSTAR: a new binary stellar evolution code. Tidal interactions*, Astronomy & Astrophysics **550** A100.

Slettebak, A. (1954), *The Spectra and Rotational Velocities of the Bright Stars of Draper Types B8-A2.*, The Astrophysical Journal **119** 146.

Soberman, G. E., E. S. Phinney and E. P. J. van den Heuvel (1997), *Stability criteria for mass transfer in binary stellar evolution.*, Astronomy & Astrophysics **327** 620.

Spruit, H. C. (2002), *Dynamo action by differential rotation in a stably stratified stellar interior*, Astronomy & Astrophysics **381** 923.

Stanway, E. R. and J. J. Eldridge (2018), *Re-evaluating old stellar populations*, Monthly Notices of the Royal Astronomical Society **479** 75.

Steinacker, A. and J. C. B. Papaloizou (2002), *Three-dimensional Magnetohydrodynamic Simulations of an Accretion Disk with Star-Disk Boundary Layer*, The Astrophysical Journal **571** 413.

Stevenson, S., A. Vigna-Gómez, I. Mandel et al. (2017), *Formation of the first three gravitational-wave observations through isolated binary evolution*, Nature Communications **8** 14906.

Struve, O. (1931), *On the Origin of Bright Lines in Spectra of Stars of Class B*, The Astrophysical Journal **73** 94.

Suijs, M. P. L., N. Langer, A.-J. Poelarends et al. (2008), *White dwarf spins from low-mass stellar evolution models*, Astronomy & Astrophysics **481** L87.

Sukhbold, T., S. E. Woosley and A. Heger (2018), *A High-resolution Study of Presupernova Core Structure*, The Astrophysical Journal **860** 93.

Tauris, T. M. and M. Bailes (1996), *The origin of millisecond pulsar velocities.*, Astronomy & Astrophysics **315** 432.

Tauris, T. M., M. Kramer, P. C. C. Freire et al. (2017), *Formation of Double Neutron Star Systems*, The Astrophysical Journal **846** 170.

Tauris, T. M., N. Langer and M. Kramer (2012), *Formation of millisecond pulsars with CO white dwarf companions - II. Accretion, spin-up, true ages and comparison to MSPs with He white dwarf companions*, Monthly Notices of the Royal Astronomical Society **425** 1601.

Tauris, T. M. and R. J. Takens (1998), *Runaway velocities of stellar components originating from disrupted binaries via asymmetric supernova explosions*, Astronomy & Astrophysics **330** 1047.

Tauris, T. M. and E. P. J. van den Heuvel (2006), "Formation and evolution of compact stellar X-ray sources", *Compact stellar X-ray sources*, vol. 39 623.

Tauris, T. M., N. Langer and P. Podsiadlowski (2015), *Ultra-stripped supernovae: progenitors and fate*, Monthly Notices of the Royal Astronomical Society **451** 2123.

Tauris, T. M. and G. J. Savonije (1999), *Formation of millisecond pulsars. I. Evolution of low-mass X-ray binaries with P_{orb} > 2 days*, Astronomy & Astrophysics **350** 928.

Tauris, T. M. and E. P. J. van den Heuvel (2023), *Physics of Binary Star Evolution. From Stars to X-ray Binaries and Gravitational Wave Sources*, Princeton University Press.

Terman, J. L., R. E. Taam and C. O. Savage (1998), *A population synthesis study of high-mass X-ray binaries*, Monthly Notices of the Royal Astronomical Society **293** 113.

Thielemann, F.-K., A. Arcones, R. Käppeli et al. (2011), *What are the astrophysical sites for the r-process and the production of heavy elements?*, Progress in Particle and Nuclear Physics **66** 346.

Thomson, W. (1854), *On the mechanical energies of the solar system*, The London, Edinburgh, and Dublin Philosophical Magazine and Journal of Science **8** 409.

– (1862), *On the Age of the Sun's Heat*, Macmillan's Magazine **5** 388.

Thorne, K. S. and A. N. Żytkow (1975), *Red giants and supergiants with degenerate neutron cores.*, The Astrophysical Journal Letters **199** L19.

– (1977), *Stars with degenerate neutron cores. I. Structure of equilibrium models.*, The Astrophysical Journal **212** 832.

Tolman, R. C. (1939), *Static Solutions of Einstein's Field Equations for Spheres of Fluid*, Physical Review **55** 364.

Toonen, S., G. Nelemans and S. Portegies Zwart (2012), *Supernova Type Ia progenitors from merging double white dwarfs. Using a new population synthesis model*, Astronomy & Astrophysics **546** A70.

Townsend, L. J., M. J. Coe, R. H. D. Corbet and A. B. Hill (2011), *On the orbital parameters of Be/X-ray binaries in the Small Magellanic Cloud*, Monthly Notices of the Royal Astronomical Society **416** 1556.

Townsend, R. H. D., S. P. Owocki and I. D. Howarth (2004), *Be-star rotation: how close to critical?*, Monthly Notices of the Royal Astronomical Society **350** 189.

Trundle, C., P. L. Dufton, I. Hunter et al. (2007), *The VLT-FLAMES survey of massive stars: evolution of surface N abundances and effective temperature scales in the Galaxy and Magellanic Clouds*, Astronomy and Astrophysics, Volume 471, Issue 2, August IV 2007, pp.625-643.

Tutukov, A. V. and L. R. Yungel'Son (1993), *Formation of neutron stars in binary systems*, Astronomy Reports **37** 411.

Ulrich, R. K. and H. L. Burger (1976), *The accreting component of mass-exchange binaries.*, The Astrophysical Journal **206** 509.

Unsöld, A. and B. Baschek (2002), *Der neue Kosmos. Einführung in die Astronomie und Astrophysik*.

Van Bever, J. and D. Vanbeveren (2000), *Hard X-rays emitted by starbursts as predicted by population synthesis models including a realistic fraction of interacting binaries*, Astronomy & Astrophysics **358** 462.

van Bever, J. and D. Vanbeveren (1997), *The number of B-type binary mass gainers in general, binary Be stars in particular, predicted by close binary evolution.*, Astronomy & Astrophysics **322** 116.

van der Meer, A., L. Kaper, M. H. van Kerkwijk et al. (2007), *Determination of the mass of the neutron star in SMC X-1, LMC X-4, and Cen X-3 with VLT/UVES*, Astronomy & Astrophysics **473** 523.

van Kerkwijk, M. H., P. A. Charles, T. R. Geballe et al. (1992), *Infrared helium emission lines from Cygnus X-3 suggesting a Wolf-Rayet star companion*, Nature **355** 703.

van Rensbergen, W., J. P. De Greve, C. De Loore and N. Mennekens (2008), *Spin-up and hot spots can drive mass out of a binary*, Astronomy & Astrophysics **487** 1129.

van Rensbergen, W., C. De Loore and K. Jansen (2006), *Evolution of interacting binaries with a B type primary at birth*, Astronomy & Astrophysics **446** 1071.

Van Rossum, G. and F. L. Drake (2009), *Python 3 Reference Manual*, Scotts Valley, CA: CreateSpace, ISBN: 1441412697.

Van Rossum, G. and F. L. Drake Jr (1995), *Python reference manual*, Centrum voor Wiskunde en Informatica Amsterdam.

van Son, L. A. C., S. E. de Mink, T. Callister et al. (2022), *The Redshift Evolution of the Binary Black Hole Merger Rate: A Weighty Matter*, The Astrophysical Journal **931** 17.

Vanbeveren, D., E. De Donder, J. Van Bever et al. (1998), *The WR and O-type star population predicted by massive star evolutionary synthesis*, New Astronomy **3** 443.

Vanbeveren, D. and C. De Loore (1994), *The evolution of the mass gainer in massive close binaries.*, Astronomy & Astrophysics **290** 129.

Vanbeveren, D., J. van Bever and E. De Donder (1997), *The effect of binary evolution on the theoretically predicted distribution of WR and O-type stars in starburst regions and in abruptly-terminated star formation regions.*, Astronomy & Astrophysics **317** 487.

Venn, K. A. (1999), *A-Type Supergiant Abundances in the Small Magellanic Cloud: Probes of Evolution*, The Astrophysical Journal **518** 405.

Vigna-Gómez, A., C. J. Neijssel, S. Stevenson et al. (2018), *On the formation history of Galactic double neutron stars*, Monthly Notices of the Royal Astronomical Society **481** 4009.

Vinciguerra, S., C. J. Neijssel, A. Vigna-Gómez et al. (2020), *Be X-ray binaries in the SMC as indicators of mass-transfer efficiency*, Monthly Notices of the Royal Astronomical Society **498** 4705.

Vink, J. S. (2022), *Theory and Diagnostics of Hot Star Mass Loss*, Annual Review of Astronomy and Astrophysics **60** 203.

Virtanen, P., R. Gommers, T. E. Oliphant et al. (2020), *SciPy 1.0: Fundamental Algorithms for Scientific Computing in Python*, Nature Methods **17** 261.

Vogel, H. C. (1890), *Spectrographische Beobachtungen an Algol*, Astronomische Nachrichten **123** 289.

von Zeipel, H. (1924), *The radiative equilibrium of a rotating system of gaseous masses*, Monthly Notices of the Royal Astronomical Society **84** 665.

Wang, C. (2022), *The impact of binary interaction on the main-sequence morphology of young star clusters*, PhD thesis: Rheinische Friedrich-Wilhelms-Universität Bonn, URL: `https://hdl.handle.net/20.500.11811/9662`.

Wang, C., B. Hastings, A. Schootemeijer et al. (2023), *The initial spin distribution of B-type stars revealed by the split main sequences of young star clusters*, Astronomy & Astrophysics **670** A43.

Wang, C., N. Langer, A. Schootemeijer et al. (2020), *Effects of Close Binary Evolution on the Main-sequence Morphology of Young Star Clusters*, The Astrophysical Journal Letters **888** L12.

Wang, C., N. Langer, A. Schootemeijer et al. (2022), *Stellar mergers as the origin of the blue main-sequence band in young star clusters*, Nature Astronomy **6** 480.

Wang, L., D. R. Gies, G. J. Peters et al. (2021), *The Detection and Characterization of Be+sdO Binaries from HST/STIS FUV Spectroscopy*, The Astronomical Journal **161** 248.

Waters, L. B. F. M., O. R. Pols, S. J. Hogeveen et al. (1989), *The formation and detectability of Be + white dwarf systems.*, Astronomy & Astrophysics **220** L1.

Webbink, R. F. (1984), *Double white dwarfs as progenitors of R Coronae Borealis stars and type I supernovae.*, The Astrophysical Journal **277** 355.

– (1985), "Stellar evolution and binaries", *Interacting Binary Stars*, ed. by J. E. Pringle and R. A. Wade 39.

Webster, B. L. and P. Murdin (1972), *Cygnus X-1 — a Spectroscopic Binary with a Heavy Companion?*, Nature **235** 37.

Weizsäcker, C. F. v. (1937), *Über Elementumwandlungen im Innern der Sterne. I*, Physikalische Zeitschrift **38** 176.
– (1938), *Über Elementumwandlungen im Inneren der Sterne. II*, Physikalische Zeitschrift **39** 633.
Wellstein, S., N. Langer and H. Braun (2001), *Formation of contact in massive close binaries*, Astronomy & Astrophysics **369** 939.
Willems, B., M. Henninger, T. Levin et al. (2005), *Understanding Compact Object Formation and Natal Kicks. I. Calculation Methods and the Case of GRO J1655-40*, The Astrophysical Journal **625** 324.
Wolf, C. J. E. and G. Rayet (1867), *Spectroscopie stellaire*, Academie des Sciences Paris Comptes Rendus **65** 292.
Woosley, S. E. (2019), *The Evolution of Massive Helium Stars, Including Mass Loss*, The Astrophysical Journal **878** 49.
Xu, X. (2024), *Comprehensive population synthesis predictions for massive binary stars in the Small Magellanic Cloud*, PhD thesis: Rheinische Friedrich-Wilhelms-Universität Bonn, URL: https://hdl.handle.net/20.500.11811/11282.
Yoon, S.-C., N. Langer and C. Norman (2006), *Single star progenitors of long gamma-ray bursts. I. Model grids and redshift dependent GRB rate*, Astronomy & Astrophysics **460** 199.
Yoon, S.-C., S. E. Woosley and N. Langer (2010), *Type Ib/c Supernovae in Binary Systems. I. Evolution and Properties of the Progenitor Stars*, The Astrophysical Journal **725** 940.
Zahn, J.-P. (1977), *Tidal friction in close binary systems.*, Astronomy & Astrophysics **57** 383.
Zhang, F., X.-D. Li and Z.-R. Wang (2004), *Where Are the Be/Black Hole Binaries?*, The Astrophysical Journal **603** 663.
Zhao, Z.-Q., Z.-W. Li, L. Xiao et al. (2024), *The radius variations of accreting main-sequence stars and mass transfer instability*, Monthly Notices of the Royal Astronomical Society **531** L45.
Zhu, C.-H., G.-L. Lü, X.-Z. Lu and J. He (2023), *Formation and Destiny of White Dwarf and Be Star Binaries*, Research in Astronomy and Astrophysics **23** 025021.
Zorec, J., Y. Frémat, A. Domiciano de Souza et al. (2016), *Critical study of the distribution of rotational velocities of Be stars. I. Deconvolution methods, effects due to gravity darkening, macroturbulence, and binarity*, Astronomy & Astrophysics **595** A132.
Zuo, Z.-Y., X.-D. Li and Q.-S. Gu (2014), *Population synthesis on high-mass X-ray binaries: prospects and constraints from the universal X-ray luminosity function*, Monthly Notices of the Royal Astronomical Society **437** 1187.

Further resources

Data analysis and visualisation

- Python (Van Rossum and Drake Jr, 1995; Van Rossum and Drake, 2009)
- NumPy (Harris et al., 2020)
- Matplotlib (Hunter, 2007)
- SciPy (Virtanen et al., 2020)

Writing, spelling, libraries

- Overleaf, https://www.overleaf.com

- Brock, I. (2024), *University of Bonn thesis, v11.0*, https://www.pi.uni-bonn.de/brock/en/thesis-guide
- DeepL Write, https://www.deepl.com/write
- SAO/NASA Astrophysics Data System (ADS), https://ui.adsabs.harvard.edu/
- Google Scholar, https://scholar.google.de/

APPENDIX A

Appendix to Chapter 2

Here we reproduce the puplication Langer et al. (2020).

A&A 638, A39 (2020)
https://doi.org/10.1051/0004-6361/201937375
© ESO 2020

Astronomy & Astrophysics

Properties of OB star−black hole systems derived from detailed binary evolution models

N. Langer[1,2], C. Schürmann[1,2], K. Stoll[1], P. Marchant[3,4], D. J. Lennon[5,6], L. Mahy[3], S. E. de Mink[7,8], M. Quast[1], W. Riedel[1], H. Sana[3], P. Schneider[1], A. Schootemeijer[1], C. Wang[1], L. A. Almeida[9,10], J. M. Bestenlehner[11], J. Bodensteiner[3], N. Castro[12], S. Clark[13], P. A. Crowther[11], P. Dufton[14], C. J. Evans[15], L. Fossati[16], G. Gräfener[1], L. Grassitelli[1], N. Grin[1], B. Hastings[1], A. Herrero[6,17], A. de Koter[8,3], A. Menon[8], L. Patrick[6,17], J. Puls[18], M. Renzo[19,8], A. A. C. Sander[20], F. R. N. Schneider[21,22], K. Sen[1,2], T. Shenar[3], S. Simón-Díaz[6,17], T. M. Tauris[23,24], F. Tramper[25], J. S. Vink[20], and X.-T. Xu[1]

(Affiliations can be found after the references)

Received 20 December 2019 / Accepted 9 April 2020

ABSTRACT

Context. The recent gravitational wave measurements have demonstrated the existence of stellar mass black hole binaries. It is essential for our understanding of massive star evolution to identify the contribution of binary evolution to the formation of double black holes.

Aims. A promising way to progress is investigating the progenitors of double black hole systems and comparing predictions with local massive star samples, such as the population in 30 Doradus in the Large Magellanic Cloud (LMC).

Methods. With this purpose in mind, we analysed a large grid of detailed binary evolution models at LMC metallicity with initial primary masses between 10 and 40 $M_\odot$, and identified the model systems that potentially evolve into a binary consisting of a black hole and a massive main-sequence star. We then derived the observable properties of such systems, as well as peculiarities of the OB star component.

Results. We find that ∼3% of the LMC late-O and early-B stars in binaries are expected to possess a black hole companion when stars with a final helium core mass above 6.6 $M_\odot$ are assumed to form black holes. While the vast majority of them may be X-ray quiet, our models suggest that these black holes may be identified in spectroscopic binaries, either by large amplitude radial velocity variations ($\gtrsim$50 km s^{-1}) and simultaneous nitrogen surface enrichment, or through a moderate radial velocity ($\gtrsim$10 km s^{-1}) and simultaneous rapid rotation of the OB star. The predicted mass ratios are such that main-sequence companions can be excluded in most cases. A comparison to the observed OB+WR binaries in the LMC, Be and X-ray binaries, and known massive black hole binaries supports our conclusion.

Conclusions. We expect spectroscopic observations to be able to test key assumptions in our models, with important implications for massive star evolution in general and for the formation of double black hole mergers in particular.

Key words. stars: evolution – stars: massive – binaries: close – stars: black holes – stars: early-type – stars: rotation

1. Introduction

Massive stars play a central role in astrophysics. They dominate the evolution of star-forming galaxies by providing chemical enrichment, ionising radiation, and mechanical feedback (e.g. Mac Low & Klessen 2004; Hopkins et al. 2014; Crowther et al. 2016). They also produce spectacular and energetic transients, ordinary and superluminous supernovae, and long-duration gamma-ray bursts (Smartt 2009; Fruchter et al. 2006; Quimby et al. 2011), which signify the birth of neutron stars (NSs) and black holes (BHs) (Heger et al. 2003; Metzger et al. 2017).

Massive stars are born predominantly as members of binary and multiple systems (Sana et al. 2012, 2014; Kobulnicky et al. 2014; Moe & Di Stefano 2017). As a consequence, most of them are expected to undergo strong binary interaction, which drastically alters their evolution (Podsiadlowski et al. 1992; Van Bever & Vanbeveren 2000; O'Shaughnessy et al. 2008; de Mink et al. 2013). On the one hand, the induced complexity is one reason that many aspects of massive star evolution are yet not well understood (Langer 2012; Crowther 2019). On the other hand, the observations of binary systems provide excellent and unique ways to determine the physical properties of massive stars (Hilditch et al. 2005; Torres et al. 2010; Pavlovski et al. 2018; Mahy et al. 2020) and to constrain their evolution (Ritchie et al. 2012; Clark et al. 2014; Abdul-Masih et al. 2019).

Gravitational wave astronomy has just opened a new window towards understanding massive star evolution. Since the first detection of cosmic gravitational waves on September 14, 2015 (Abbott et al. 2016), reports about the discovery of such events have become routine (Abbott et al. 2019), with a current rate of about one per week. Most of these sources correspond to merging stellar mass BHs with high likelihood[1]. It is essential to explore which fraction of these gravitational wave sources reflects the end product of massive close binary evolution, compared to products of dynamical (Kulkarni et al. 1993; Sigurdsson & Hernquist 1993; Antonini et al. 2016; Samsing & D'Orazio 2018; Fragione et al. 2019; Di Carlo et al. 2019) and primordial (Nishikawa et al. 2019) formation paths.

Two different evolutionary scenarios for forming compact double BH binaries have been proposed. The first scenario involves chemically homogeneous evolution (Maeder 1987; Langer 1992; Yoon & Langer 2005), which may lead to the avoidance of mass transfer in very massive close binaries (de Mink et al. 2009) and allows compact main-sequence binaries to directly

[1] cf. `https://gracedb.ligo.org/latest/`

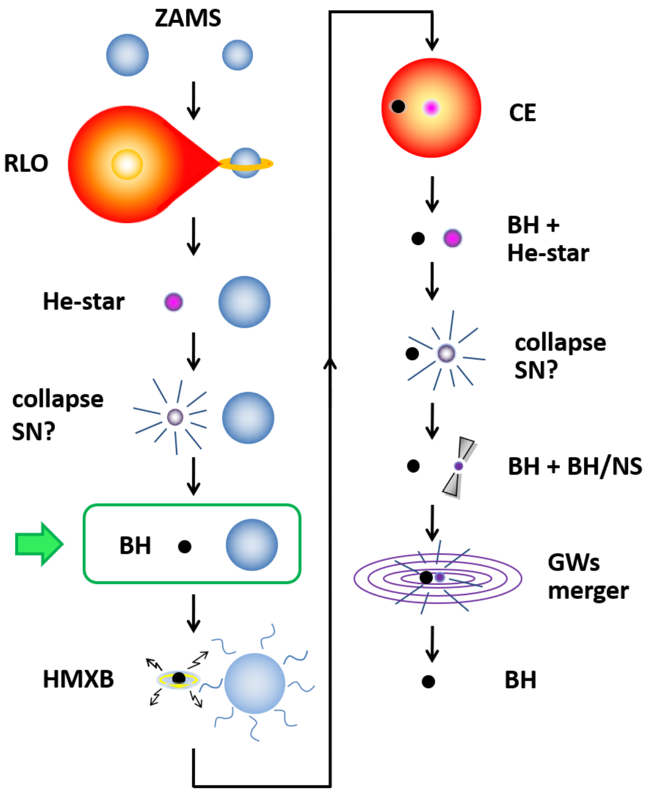

Fig. 1. Schematic evolution of close binary systems from the zero-age main sequence (ZAMS) to the formation of compact double BH or BH-NS systems. The evolution involves mass transfer through Roche-lobe overflow (RLO), the formation of a He-star (could be a Wolf-Rayet star, if sufficiently massive), and a common envelope phase (CE). The core collapse events leading to BHs may or may not launch a supernova explosion (SN). Light green highlights the OB+BH stage, which is the focus of this paper. Adapted from Kruckow et al. (2018).

evolve into compact BH binaries (Mandel & de Mink 2016). This scenario has been comprehensively explored through detailed binary evolution models (Marchant et al. 2016), showing that it leads to double BH mergers only at low metallicity ($Z \lesssim Z_{\odot}/10$), and is restricted to rather massive BHs ($\gtrsim 30\ M_{\odot}$; see also de Mink & Mandel 2016).

The second proposed path towards the formation of compact double BH binaries is more complex and involves mass transfer through Roche-lobe overflow and common-envelope evolution (Belczynski et al. 2016; Giacobbo et al. 2018; Kruckow et al. 2018). At the same time, this path predicts a wide range of parameters for the produced double compact binaries. It resembles those paths suggested for the formation of merging double NSs (e.g., Bisnovatyi-Kogan & Komberg 1974; Flannery & van den Heuvel 1975; Tauris et al. 2017), double white dwarfs (WDs; Iben & Tutukov 1984; Webbink 1984), and WD-NS binaries (Toonen et al. 2018). Although this type of scenario has not been verified through detailed binary evolution models, there is little doubt that the majority of objects in the observed populations of close double WDs (Breedt et al. 2017; Napiwotzki et al. 2020) and double NSs (Tauris et al. 2017; Stovall et al. 2018; Andrews & Zezas 2019) have been evolving accordingly. Consequently, we may expect that close double BHs also form in a similar way.

Figure 1 gives an example for the schematic formation path of double compact binaries (Kruckow et al. 2018). It involves several stages for which current theoretical predictions are very uncertain, most notably those of Roche-lobe overflow, common-envelope evolution, and BH formation. Evidently, it is desirable to obtain observational tests for as many as possible of the various involved evolutionary stages. To do this, it is important to realise that in many of the steps that are shown in Fig. 1, a large fraction of the binary systems may either merge or break up, such that the birth rate of double compact systems at the end of the path is several orders of magnitude lower than that of the double main-sequence binaries at the beginning of the path. Observational tests may therefore be easier for the earlier stages, where we expect many more observational counter parts.

Here, the OB+BH stage, where a BH orbits an O or early B-type star, has a prominent role in theory and observations. From the theoretical perspective, it is the last long-lived stage that can be reached from the double main-sequence stage with detailed stellar evolution calculation. Whereas the preceding Roche-lobe overflow phase also bears large uncertainties, it can be modelled by solving the differential equations of stellar structure and evolution, rather than having to rely on simple recipes for the structure of the two stars. At the same time, only about half of all main-sequence binaries are expected to merge during the first Roche-lobe overflow phase, such that the number of OB+BH binaries is expected to be significant.

In this paper, we describe the properties of OB+BH binaries as obtained from a large grid of detailed binary evolution models. In Sect. 2 we explain the method we used to obtain our results. Our Sect. 3 focuses on the derived distributions of the properties of the OB+BH binaries, while Sect. 4 discusses the key uncertainties that enter our calculations. We compare our results with earlier work in Sect. 5 and provide a comparison with observations in Sect. 6. In Sect. 7 we discuss observational strategies for finding OB+BH binaries, and in Sect. 8 we consider their future evolution. We summarise our conclusions in Sect. 9.

2. Method

Our results are based on a dense grid of detailed massive binary evolution models (Marchant 2016). These models were computed with the stellar evolution code Modules for Experiments in Stellar Astrophysics (MESA, Version No. 8845) with a physics implementation as described by Paxton et al. (2015). All necessary files to reproduce our MESA simulations are available online[2].

In particular, differential rotation and magnetic angular momentum transport are included as in Heger et al. (2000, 2005), with physics parameters set as in Brott et al. (2011). Mass and angular momentum transfer are computed according to Langer et al. (2003) and Petrovic et al. (2005), and the description of tidal interaction follows Detmers et al. (2008). Convection is modelled according to the standard mixing length theory (Böhm-Vitense 1958), with a mixing length parameter of $\alpha_{\rm MLT} = 1.5$.

Semiconvection is treated as in Langer (1991), that is, using $\alpha_{\rm SC} = 0.01$. We note that recent evidence may favour higher values of this parameter, which could lead to a nuclear timescale post-main-sequence expansion to the red supergiant stage of massive low-metallicity stars in a limited mass range (Schootemeijer et al. 2019; Higgins & Vink 2020; Klencki et al. 2020). The consequences of this for massive binary evolution will need to be explored (cf. Wang et al. 2020). It could lead to the prediction of a significant sub-population of Roche-lobe-filling X-ray bright B- and A-type supergiant BH binaries (Quast et al. 2019; Klencki et al. 2020), which, especially at low

[2] https://doi.org/10.5281/zenodo.3698636

metallicity, appears not to be observed. Clearly, more work is needed to clarify the situation.

Thermohaline mixing is performed as in Cantiello & Langer (2010), and convective core overshooting is applied with a step-function extending the cores by 0.335 pressure scale heights (Brott et al. 2011). However, overshooting is only applied to layers that are chemically homogeneous. This implies that mean molecular weight gradients are fully taken into account in the rejuvenation process of mass-gaining main-sequence stars (cf. Braun & Langer 1995). The models are computed with the same initial chemical composition as those of Brott et al. (2011), that is, taking the non-solar abundance ratios in the LMC into account. Differently from Brott et al. (2011), here custom-made OPAL opacities (Iglesias & Rogers 1996) in line with the adopted initial abundances were produced and included in the calculations.

The masses of the primary stars range from 10 to 39.8 $M_{\odot}$ in steps of $\log(M_1/M_{\odot}) = 0.050$. For each primary mass, systems with different initial mass ratios $q_i = M_2/M_1$ ranging from 0.25 to 0.975 in intervals of 0.025 were computed, and for each mass ratio, there were models with orbital periods from 1.41 to 3160 d in steps of $\log(P_i/d) = 0.025$. The grid consisted of a total of 48240 detailed binary evolution models. Binaries with initial periods below ~5 d (for a primary mass of 10 $M_{\odot}$) and 25 d (for a primary mass of 39.8 $M_{\odot}$) undergo mass transfer while both stars fuse hydrogen in their cores (Case A systems), while most longer-period binaries undergo mass transfer immediately after the primary leaves the main sequence (Case B systems). For higher primary masses, envelope inflation due to the Eddington limit (Sanyal et al. 2015) would prevent stable Case B mass transfer from occurring (cf. Sect. 4). Figure 2 gives an overview of the evolutionary end points obtained for models with an initial primary mass of ~25.12 $M_{\odot}$, with examples for other primary masses provided in Appendix B.

Our models were computed assuming tidal synchronisation at zero age, which avoids introducing the initial rotation rate of both stars as additional parameters. While this is not physically warranted, it is justified because moderate rotation does not affect the evolution of the individual stars very much (Brott et al. 2011; Choi et al. 2016), and the fastest rotators may be binary evolution products (de Mink et al. 2013; Wang et al. 2020). Moreover, the initially closer binary models (typically those of Case A) quickly evolve into tidal locking (de Mink et al. 2009), independent of the initial stellar spins. Moreover, the spins of the components of all post-interaction binaries, in particular those of the OB+BH binaries analysed here, are determined through the interaction process, where the mass donor fills its Roche-volume in synchronised rotation in Case B systems as well, and the mass gainer is spun up by the accretion process.

The evolution of our models was stopped when mass overflow at the outer Lagrangian point L2 occurred (purple color in Fig. 2) in contact binaries (black hatching in Fig. 2), which were otherwise modelled as in Marchant (2016). We also stopped the evolution when inverse mass transfer occurred from a post-main-sequence component (yellow in Fig. 2), or when a system exceeded the upper mass-loss rate limit (green in Fig. 2). Any of these condition was assumed to lead to a merger. Here, the upper mass-loss rate limit was set by the condition that the energy required to remove the emitted fraction of the transferred matter exceeds the radiated energy of both stars. Models surpassing the weaker condition that the momentum required to remove the non-accreted mass exceeds their photon momentum were assumed to survive as binaries. The systems were evolved at least until central helium depletion of the mass gainer, while those with helium core masses lower than 13 $M_{\odot}$ were followed until core carbon depletion.

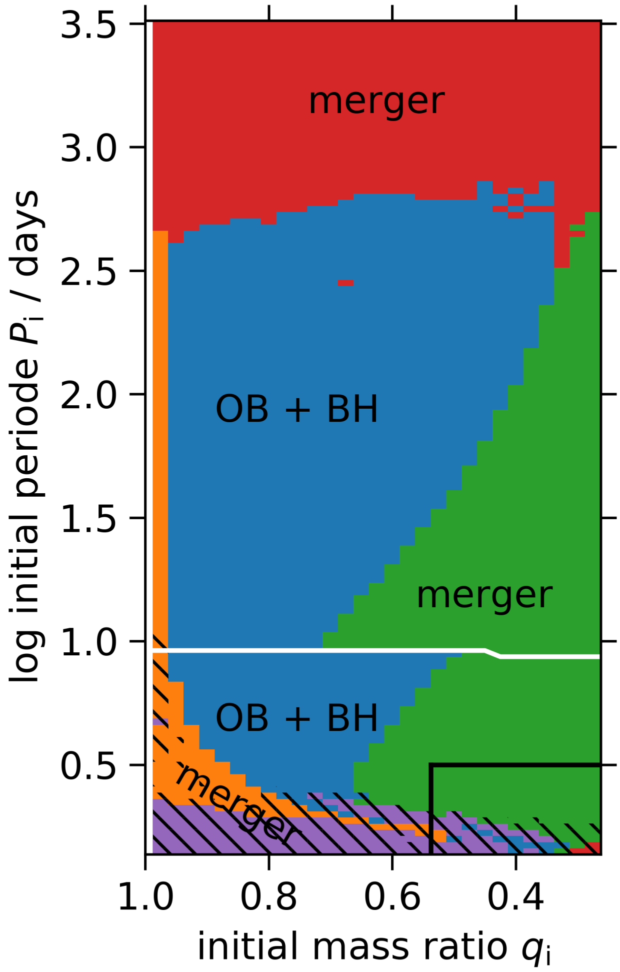

Fig. 2. Outcome of the 4020 binary evolution models with an initial primary mass of $\log M/M_{\odot} = 1.4$ (~25.12 $M_{\odot}$) as function of their initial orbital period P_i and mass ratio q_i. Each of the 30 × 134 pixels in this plot represents one detailed binary evolution model. The dark blue systems evolve to the OB+BH stage. Systems that evolve into a contact configuration are marked by black hatching. Purple indicates systems that evolve into mass overflow at the outer Lagrangian point L2, and systems that evolve into inverse mass transfer occurring from a post-main-sequence component are marked in yellow; we assume that the binaries merge in both situations. We also assume those systems to merge that exceed the upper mass-loss rate limit (see main text), marked in green. The systems with the longest initial orbital periods, marked in red, impart a classical common-envelope evolution; for simplicity, we assume that all of them merge as well. Systems below the nearly horizontal white line undergo the first mass transfer while both stars are core hydrogen burning (Case A), while the primaries in initially wider systems start mass transfer after core hydrogen exhaustion (Case B). The area framed by the black line in the lower right corner marks the part of the parameter space that is disregarded in our results (see Sect. 2). Equivalent plots for four more initial primary masses are provided in the appendix.

In the systems with the longest initial orbital periods, the mass transfer rate grows on near-dynamical timescales to very high values, with a classical common-envelope evolution to follow (red in Fig. 2). In some systems, in particular those with the longest initial periods and the most massive secondary stars, a merger as consequence of the common-envelope evolution may be avoided. Here, we assumed that these systems also merge, such that the numbers and frequencies of OB+BH systems that we obtain below must be considered as lower limits. The systems that survive a common envelope evolution would likely contribute to the shortest period OB+BH binaries. As such, they would likely evolve into an OB star-BH merger later on, and not contribute to the production of double compact binaries. More details about the binary evolution grid can be found in Marchant (2016).

An inspection of the detailed results showed that some of the contact systems were erroneous. In these cases, the primary continued to expand after contact was reached, but no mass transfer was computed. This situation is unphysical. An example case is the model with the initial parameters ($\log M_{1,\rm i}, q_{\rm i}, \log P_{\rm orb,i}$) = (1.4, 0.4, 0.2). In Fig. 2, this concerns the ten blue pixels inside the frame in the lower right corner. The error caused these systems to survive until and including the OB+BH stage. The error did not occur for initial mass ratios above 0.5. In a recalculation of several of the erroneous systems with MESA Version No. 12115, the unphysical situation did not occur. In these calculations, the systems merged while both stars underwent core hydrogen burning. In order to avoid any feature of the erroneous models in our results for OB+BH binaries, we manually deselected binary models for which simultaneously $q_{\rm i} < 0.55$ and $\log P_{\rm orb,i} < 0.5$, such that none of the non-erroneous systems in this part of the parameter space contributes to the OB+BH binary population. These systems remain to be considered during their pre-interaction evolution.

To account for OB+BH systems, we assessed the helium core masses of our models. We considered the pre-collapse single star models of Sukhbold et al. (2018), who evaluated the explodability of their models based on their so-called compactness parameter (O'Connor & Ott 2011; Ugliano et al. 2012). Near an initial mass of 20 $M_\odot$, this parameter shows a sudden increase, with most stellar models below this mass providing supernovae and NSs, and most models above this mass expected to form BHs. This mass threshold has been essentially confirmed by Ertl et al. (2016) and Müller et al. (2016) based on different criteria, and it corresponds to a final helium core mass of 6.6 $M_\odot$ and a final CO-core mass of 5 $M_\odot$ (Sukhbold et al. 2018). Sukhbold et al. (2018) also reported that the threshold depended only weakly on metallicity. Whereas these three papers all predict a non-monotonous behaviour as a function of the initial mass, with the possibility of some successful supernovae occurring above 20 $M_\odot$, we neglected this possibility for simplicity and assumed BHs to form in models with a helium core mass above 6.6 $M_\odot$ at the time of core carbon exhaustion.

While our adopted BH formation criterion is based on single stars, it has been argued that in stripped stars, the helium core does not grow in mass during helium burning, such that the ^{12}C-abundance remains higher, which ultimately leads to a higher likelihood for NS production than in corresponding single stars (Brown et al. 2001). On the other hand, recent pre-collapse models that evolved from helium stars (Woosley 2019) show a similar jump of the compactness parameter as quoted above. The onset of this jump is shifted to higher helium core masses by about 0.5 $M_\odot$, while the peak is shifted by $\sim$2 $M_\odot$. The helium star models also predict an island of low compactness in the He-core mass range 10–12 $M_\odot$ that is absent or much reduced in the models that are clothed with a H-rich envelope. With our BH formation criterion as mentioned above, we may therefore overpredict relatively low-mass BHs. We discuss the corresponding uncertainty in Sect. 4.

We further assumed that the mass of the BH is the same as the mass of the He-core of its progenitor, and that the BHs form without a momentum kick. The validity of these assumptions depends on the amount of neutrino energy injection into the fallback material after core bounce (Batta et al. 2017). In the direct collapse scenario, the BH forms very quickly, and a strong kick and mass ejection from the helium star may be avoided. However, in particular near the NS-BH formation boundary, both assumptions may be violated to some extent. This introduces some additional uncertainty for our model predictions in the lower part of the BH mass range (cf. Sect. 4)

Because our binary evolution grid has a high density, it is well suited for constructing synthetic stellar populations. In order to do so, sets of random initial binary parameters were defined under the condition that they obeyed chosen initial distribution functions. This was done here by requiring that the primary masses follow the Salpeter (1955) initial mass function and that the initial mass ratios and orbital periods follow the distributions obtained by Sana et al. (2013, see also Almeida et al. 2017) for the massive stars observed in the VLT FLAMES Tarantula survey (Evans et al. 2011). The adopted initial mass function should serve to constrain the lower limits on the number of systems (cf. adopting the shallower value for the 30 Doradus region from Schneider et al. 2018).

Models may be selected at a predefined age to construct synthetic star clusters (cf. Wang et al. 2020), or, as done here, a constant star formation rate may be considered. We then considered a given binary model an OB+BH system when it fulfilled our BH formation criterion for the initially more massive star, and when the initially less massive star still underwent core hydrogen burning ($X_{\rm c} \geq 0.01$). We then considered its statistical weight in accordance with the above-mentioned distribution functions, and its lifetime as OB+BH binary. With this taken into account, its properties were evaluated at the time of BH formation.

3. Results

Because we focus on the properties of OB+BH binaries in this paper, in the following we discuss only systems that avoid to merge before they form the first compact object. To do this, it is useful to consider the Case A systems separately from the Case B systems. Not only are the predictions from both classes of binaries quite distinct from each other (see below), but the physics that is involved in the mass transfer process is different as well.

To a large extent, tidal effects can be neglected in the wider Case B systems, while they play an important role in Case A systems. In the latter, tidal coupling slows down or prevents the spin-up of the mass gainer during mass transfer, while direct-impact accretion also reduces the specific angular momentum of the accreted matter (Langer 2012). Consequently, the mass transfer efficiency, that is, the ratio of the mass accreted by the mass gainer over the amount of transferred mass, can be high in Case A systems. We find accretion efficiencies of up to nearly one, with an average of about 30% for all Case A binaries, and the highest values are achieved for the most massive systems and highest initial mass ratios (i.e. $q \simeq 1$). In contrast, the mass transfer is rather inefficient in most of our Case B systems because the mass gainer is quickly spun up to critical rotation, such that any further accretion remains very limited. The overall accretion efficiency remains at a level of 10% or less.

3.1. OB star masses, BH masses, and mass ratios

As found in previous binary evolution calculations (e.g. Yoon et al. 2010), the mass donors of our model binaries are stripped of nearly their entire hydrogen envelope as a consequence of

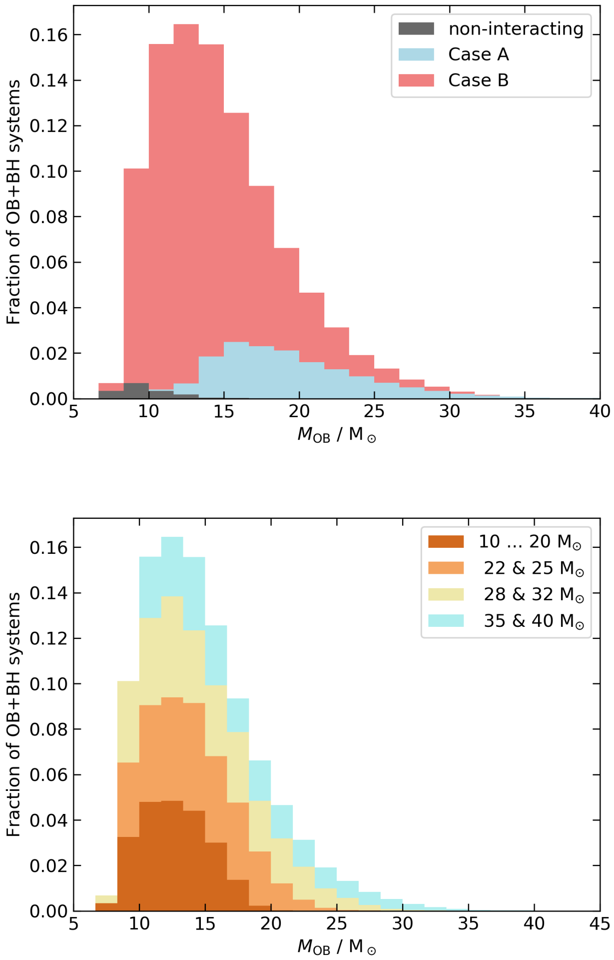

Fig. 3. *Top*: distribution of the OB star masses of systems in our binary evolution model grid that reach the OB+BH stage, assuming constant star formation, weighted with the initial mass function and the initial binary parameter distribution functions, and with their lifetime as OB+BH binary. The red and blue areas represent Case B and Case A systems. Black indicates the small number of non-interacting systems in our binary grid. The results are stacked, such that the upper envelope corresponds to the total number of systems. The ordinate values are normalised such that the value for each bin gives its relative contribution to the total number of systems. *Bottom*: same distribution as in the top plot, but different initial masses of the BH progenitors are distinguished (see legend).

Roche-lobe overflow. Whereas small amounts of hydrogen may remain in the lower-mass primaries (Gilkis et al. 2019), it is reasonable to consider them as helium stars after the mass transfer phase. Whereas the initial helium star mass emerging from Case B binaries is very similar to the initial helium core mass (i.e. at core helium ignition) of single stars, we emphasise that because larger amounts of mass are transferd during the MS stage, Case A binaries produce helium stars with significantly lower mass (cf. Fig. 14 of Wellstein et al. 2001), an effect that is mostly not accounted for in simplified binary evolution models.

Figure 3 evaluates the distribution of the masses of the OB stars in our OB+BH models at the time of the formation of the first compact object. In addition to the Case A and B systems, it distinguishes for completeness the systems in our grid that never interact. The results shown in Fig. 3 are weighted by the initial mass and binary parameter distribution functions (see Sect. 2), and by the duration of the OB+BH phase of the individual binary models. Figure 3 thus predicts the measured distribution of the OB star masses in idealised and unbiased observations of OB+BH binaries.

The distribution of the masses of the OB stars in our OB+BH binaries shown in Fig. 3 peaks near 14 $M_\odot$. Towards lower OB masses, the chance increases that the final helium core mass of the mass donor falls below our threshold mass for BH formation. Whereas for the initial masses of the donor star, there is a cut-off near 18 $M_\odot$ below which no BHs are produced, the distribution of the masses of their companions leads to a spread in the lower mass threshold of the secondaries, that is, the OB stars in BH+OB systems, which leads to the lowest masses of the BH companions: about 8 $M_\odot$. The drop in the number of systems for OB star masses above 14 $M_\odot$ is mainly produced by the initial mass function and by the shorter lifetime of more massive OB stars. Because our model grid is limited to initial primary masses below 40 $M_\odot$, we may be missing stars in the distribution shown in Fig. 3 above ~20 $M_\odot$. However, their contribution is expected to be small, and it is very uncertain because the corresponding stars show envelope inflation (cf. Sect. 4).

The upper panel of Fig. 3 shows that the majority of OB+BH systems is produced via Case B evolution, as expected from Fig. 2 when the areas covered by Case A and Case B in the q_i−P_i-plane are compared (but our initial distributions are not exactly flat in log P_i and q_i). The peak in the OB mass distribution of the Case A models is shifted to higher masses (~16 $M_\odot$) than in the Case B distribution because the accretion efficiency in Case A is higher. For the same reason, the most massive OB stars in the OB+BH systems produced by our grid, with masses of up to 47 $M_\odot$, evolved following Case A (cf. Sect. 7). The Case B binaries produce only OB star companions to BHs with masses below ~34 $M_\odot$, notably because the most massive Case B systems with mass ratios above ~0.9 lead to mergers before the BH is formed.

The bottom panel of Fig. 3 provides some insight into the mass dependence of the production of OB+BH binaries (see also the bottom panel of Fig. 4) by comparing the contributions from binary systems with four different initial primary mass ranges. Systems with successively more massive primaries produce more massive OB stars in OB+BH binaries. Moreover, the range of OB star masses in OB+BH binaries originating from systems with more massive primaries is larger. This reflects our criterion for mergers in Case B systems (Sect. 2), which implies that it is easier for more massive binaries to drive the excess mass that the spun-up mass gainer can no longer accrete out of the system.

Figure 4 shows the resulting distribution of mass ratios of our OB+BH binary models, produced with the same assumptions as Fig. 3. Remarkably, the distribution drops sharply for BH/OB star mass ratios below 0.5. The main reason is that the BH is produced by the initially more massive star in the binary. This means that binaries with a low initial mass ratio (e.g. $M_{2,i}/M_{1,i} \simeq 1/3$; cf. Fig. 2) easily produce BHs as massive as their companion or more massive, such that their BH/OB mass ratios is one or higher. Because the accretion efficiency in our models is mostly quite low, binaries starting with a mass ratio near one, on the other hand, obtain BH/OB mass ratios higher than 0.3 because more than one-third of the primaries' initial mass ends up in the BH. Because the corresponding fraction is larger in more massive primaries, we find that more massive primaries lead to higher BH/OB mass ratios, where those with initial primary masses below 20 $M_\odot$ produce only OB+BH binaries with $M_{BH}/M_{OB} < 1$ (Fig. 4, bottom panel).

The distribution of the BH masses produced in our binaries shows a broad peak near 10 $M_\odot$ (Fig. 5), with a sharp lower limit of 6.6 $M_\odot$ as introduced by our assumptions on BH formation

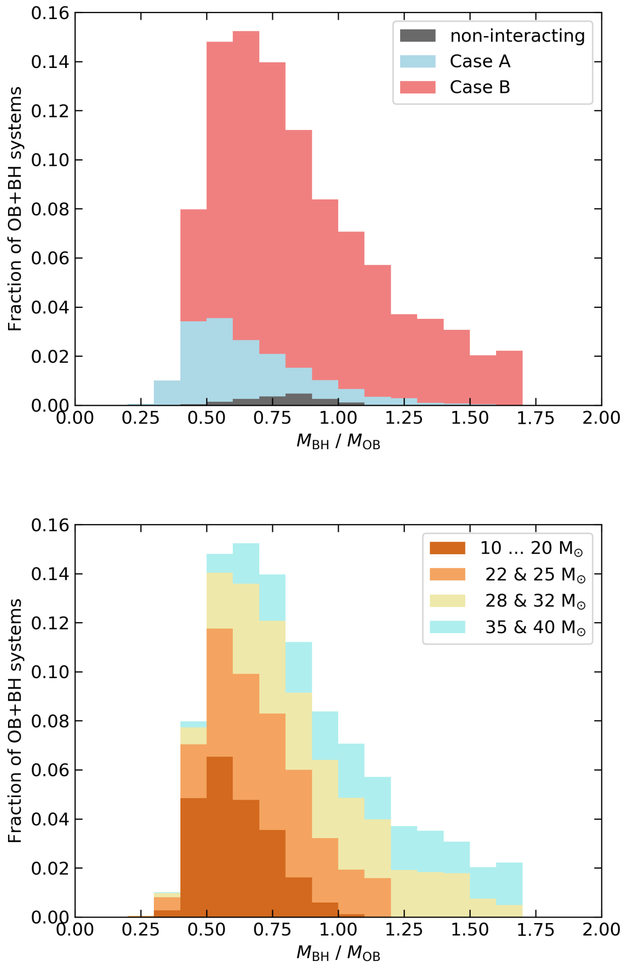

Fig. 4. *Top*: as Fig. 3, here showing the distribution of the BH/OB star mass ratios in our predicted OB+BH binaries. *Bottom*: same distribution as in the top plot, but distinguishing between different initial masses of the BH progenitors (see legend).

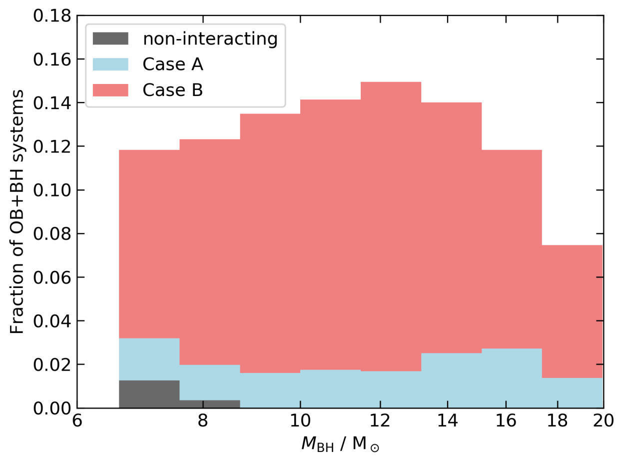

Fig. 5. As Fig. 3, here showing the distribution of the BH masses at the time of BH formation in our predicted OB+BH binaries.

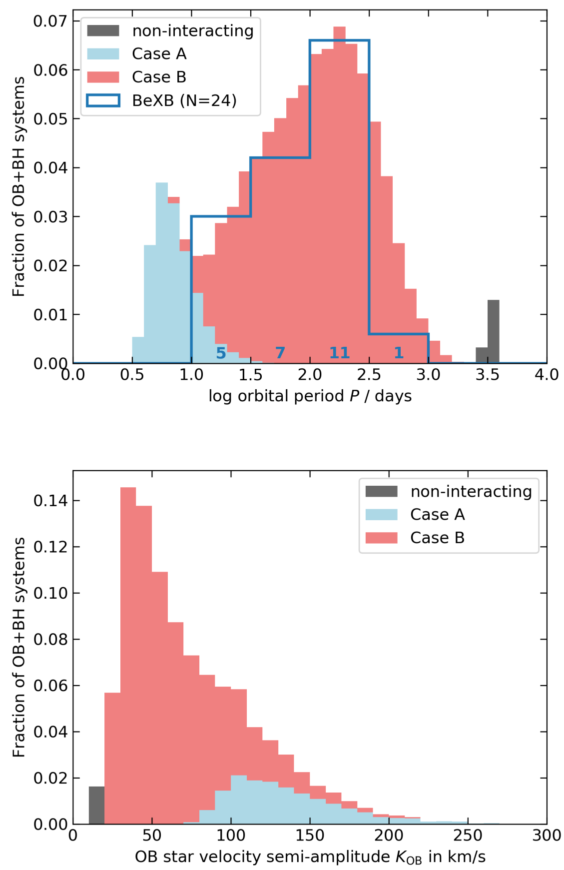

Fig. 6. As Fig. 3, here showing the distribution of the orbital periods at the time of BH formation (*top*), and of the orbital velocity amplitudes (*bottom*) of our OB+BH binaries. The blue line in the top plot shows the distribution of the orbital periods of the Galactic Be/X-ray binaries (Walter et al. 2015).

(Sect. 2). While the drop in the initial mass function towards higher masses leads to a decrease in the number of BHs for increasing BH mass, this effect is less drastic than for the OB star mass (Fig. 3). This can be understood by considering the systems with the most massive primaries in our grid, which form the most massive BHs. These systems produce OB+BH binaries with a broad range of OB star masses (blue part in the bottom panel of Fig. 3), such that their contribution to Fig. 5 will benefit from a broad range of durations of the OB+BH phase. The masses of the produced BHs in our grid are limited to about 22 $M_\odot$, in agreement with earlier predictions (Belczynski et al. 2010). This is due to the heavy wind mass loss of the BH progenitors during their phase as Wolf-Rayet stars and may therefore be strongly dependent on metallicity.

3.2. Orbital periods and velocities

The top panel of Fig. 6 shows the predicted distribution of orbital periods of the OB-BH binaries found in our model grid. We find that non-interacting binaries may produce OB+BH binaries with orbital periods in excess of about 3 yr. In Fig. 6 we can show only the non-interacting binaries with the shortest periods because of the upper initial period bound of our binary grid. Many more such binaries might form, but even small BH formation kicks could break them up, the easier the longer the period. Because these systems would also be the hardest to observe, we focus here on OB+BH binaries, which emerge after mass transfer through Roche-lobe overflow.

As seen in Fig. 6, the distribution of these post-interaction OB+BH binaries shows two distinct peaks that we can attribute to the two different modes of mass transfer. As expected, the Case A systems are found at shorter periods and remain below ~30 d, while the Case B systems are spread between about

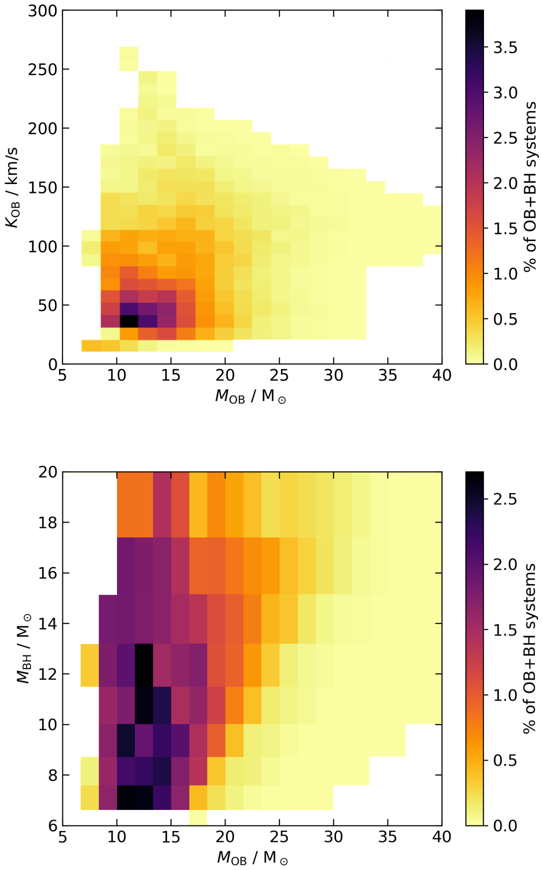

Fig. 7. Predicted number distribution of OB+BH systems in the parameter space OB star mass–orbital velocity (*top panel*) and OB star mass–BH mass (*bottom panel*). The expected numbers in each pixel are colour-coded and normalised such that the sum over all pixels is 100%.

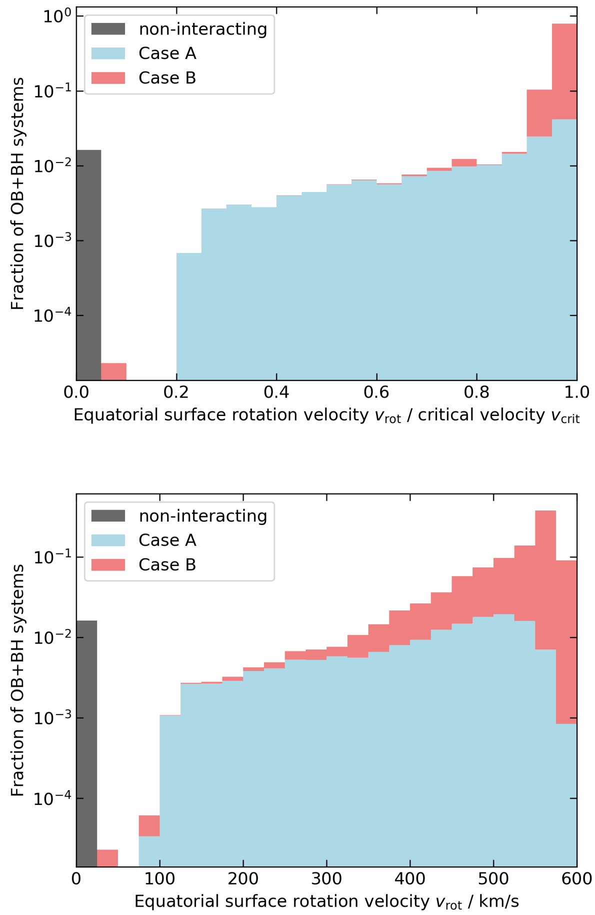

Fig. 8. Distribution of the ratio of the equatorial surface rotation velocity to critical rotation velocity for the OB stars in OB+BH binaries at the moment of BH formation, as predicted by our population synthesis model (*top panel*). *Bottom panel*: corresponding distribution of the absolute equatorial surface rotation velocities of the OB stars as obtained in the indicated mass bins. In both plots, the small peak near zero rotation is due to the widest, non-interacting binaries; it is non-physical and should be disregarded.

10 d and 1000 d, with a pronounced maximum near 150 d. The observed orbital period distribution of 24 Galactic Be/X-ray binaries is overplotted in Fig. 6. We discuss the striking similarity with the period distribution of our OB+BH models in Sect. 6.

Through Kepler's laws, we can convert the period distribution into a distribution of orbital velocities of the OB star components in OB+BH systems, which we show in the bottom panel of Fig. 6. As expected, the orbital velocities are highest in Case A binaries and lowest in the Case B systems. These values are all so high that they can easily be measured spectroscopically (cf. Sect. 7).

Figure 7 illustrates the 2D distributions of the component masses and the orbital velocity. In accordance with Fig. 3, we see that the OB masses are strongly concentrated in the mass range 8 $M_\odot$–25 $M_\odot$. The top panel shows that the OB+BH binaries are most abundant in a small area in the plane of the orbital velocity versus OB mass, that is, near $M_{OB} \simeq 13\,M_\odot$ and $K_{OB} \simeq 50\,\mathrm{km\,s^{-1}}$. More than half of all systems are expected to have OB masses below 17 $M_\odot$ with orbital velocities of $K_{OB} < 70\,\mathrm{km\,s^{-1}}$. At the same time, the bottom plot of Fig. 7 shows that the expected BH companions to $\simeq 13\,M_\odot$ B stars have a rather flat distribution between 7 $M_\odot$ and 20 $M_\odot$ (see also Fig. 5).

3.3. OB star rotation and surface abundances

As pointed out in Sect. 2, our detailed binary stellar evolution models accurately keep track of the angular momentum budget of both stars. They consider internal angular momentum transfer through differential rotation, angular momentum loss by winds, angular momentum gain by accretion, and spin-orbit angular momentum exchange through tides.

Figure 8 shows that most of the OB components in our OB+BH binary models are rapid rotators. At the time of BH formation, as many as half of them rotate very close to critical rotation. In particular, a high fraction of those systems that originate from Case B mass transfer, where tidal breaking is unimportant, rotate very close to critical. The Case A systems have a much broader distribution in Fig. 8. The minimum value of $\upsilon_{rot}/\upsilon_{crit} = 0.2$ corresponds to the widest systems where tidal breaking still works, that is, where the synchronisation timescale becomes comparable to the nuclear timescale of the OB star.

The absolute values of the rotational velocities shown in the bottom panel of Fig. 8 reveal a broader distribution. This is mostly an effect of the mass and time dependence of the critical rotational velocity. However, even the Case A binaries stretch out to high rotation velocities, such that on average, their rotation rate is much higher than that of an average O star (i.e. $\sim$150 km s^{-1}, Ramirez-Agudelo et al. 2013).

We point out that Fig. 8 depicts the rotation of the OB stars when the BH forms. In the time span between the end of the mass-transfer-induced spin-up process and the BH formation,

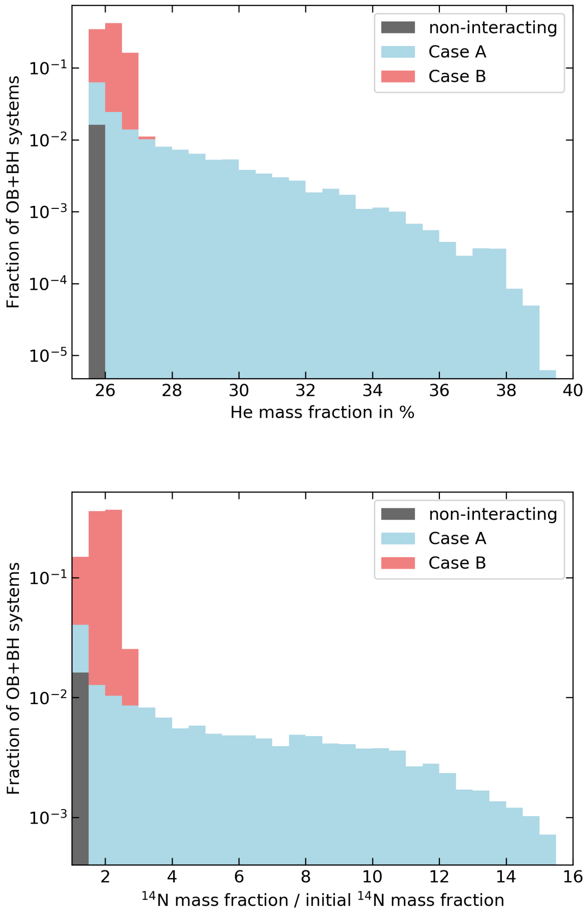

Fig. 9. Result of our population synthesis calculations for the probability distribution of the surface helium (*top*) and nitrogen (*bottom*) surface abundances of the OB stars in OB+BH binaries.

which corresponds to the core helium-burning time of the BH progenitor in most cases, the OB star spin may have changed. The same is true for the lifetime of the OB star with a BH companion. Here, in particular the O stars are expected to lose some angular momentum through their (non-magnetic) wind (Langer 1998; Renzo et al. 2017). On the other hand, single B stars are expected to spin up as a consequence of their core hydrogen-burning evolution (Ekstrom et al. 2008; Brott et al. 2011; Hastings et al. 2020). This explains that the B stars in our OB+BH binaries (i.e. the OB components with a mass below $\sim 15\,M_{\odot}$), which are brought to critical rotation due to accretion, remain at critical rotation for their remaining hydrogen-burning lifetimes.

A second signature of accretion in the OB component of OB+BH binaries may be the presence of hydrogen-burning products at the surface of the OB star. We note that in our models, rotationally induced mixing, semiconvection, and thermohaline mixing are included in detail. We find that the main enrichment effect is produced by the accretion of processed matter from the companion, and the subsequent dilution through thermohaline mixing. Despite the fast rotation of the OB components, rotational mixing plays no major role. The reason is that in contrast to rapidly rotating single-star models, the spun-up mass gainers did not have an extreme rotation before the onset of mass transfer. During that stage, they could establish a steep H/He gradient in their interior, which provides an impenetrable barrier to rotational mixing after accretion and spin-up have occurred.

To quantify the obtained enrichment, we show the distribution of the surface helium and nitrogen abundances of our OB stars with BHs in Fig. 9. The OB stars in Case B binaries remain essentially unenriched. The reason for this is that our Case B mass gainers accrete only small amounts of mass (about 10% of their initial mass). Furthermore, this accretion occurs early during the mass transfer process because the accretion efficiency drops after the stars are spun up. Therefore, only material from the outer envelope of the donor star is accreted, which is generally not enriched in hydrogen-burning products. We expect the near-critically rotating OB stars in our Case B systems to be Be stars. Because Be stars are often not or only weakly enriched in nitrogen (Lennon et al. 2005; Dunstall et al. 2011), in contrast to predictions from rotating single-star models, the population of Be stars may be dominated by binary-interaction products.

In Case A binaries, on the other hand, much more mass is accreted, also matter from the deeper layers of the mass donor, which have been part of the convective core in the earlier stages of hydrogen burning. The surface helium mass fraction increases to $\sim$35%. This is accompanied by a strong nitrogen enhancement by up to a factor of 12.

4. Key uncertainties

4.1. Envelope inflation

The highest considered initial primary mass in the LMC binary evolution model grid of Marchant (2016) is $39.8\,M_{\odot}$. In a sense, this mass limit is an experimental result because it was found that for the next higher initial primary mass to be considered ($44.7\,M_{\odot}$), the MESA code was unable to compute through the mass transfer evolution of most systems. This is expected because single-star models computed with very similar physics assumptions (Brott et al. 2011) predict that such stars with LMC metallicity expand so strongly that they become red supergiants during core hydrogen burning. From an analysis of the internal structure of these models, Sanyal et al. (2015, 2017) found that this drastic expansion is a consequence of the corresponding models reaching the Eddington limit in their outer envelopes, when all opacity sources (i.e. not only electron scattering) are considered in the Eddington limit.

This so-called envelope inflation can be easily prevented from occuring in stellar models. The corresponding envelope layers are convective, and an enhancement of the convective energy transport efficiency leads to a deflation of the envelope (Fig. B.1 of Sanyal et al. 2015). However, there is no reason to doubt the energy transport efficiency of the classical mixing length theory (Böhm-Vitense 1958) in this context. On the contrary, by the low densities in the inflated envelope, it is evident that vertically moving convective eddies radiate away their heat surplus faster than they move, implying a low energy transport efficiency as computed by the standard mixing length theory (Gräfener et al. 2012), which is also verified by corresponding 3D hydrodynamic model calculations (Jiang et al. 2015). The inflation effect has been connected with observations of so-called luminous blue variables (Gräfener et al. 2012; Sanyal et al. 2015; Grassitelli et al. 2020), which are hydrogen-rich stars; however, inflation is also predicted to occur in hydrogen-free stars (Ishii et al. 1999; Petrovic et al. 2006; Gräfener et al. 2012; Grassitelli et al. 2016).

Hydrogen-rich massive stars generally increase their luminosity and expand during their evolution. As a consequence, stars above a threshold mass reach the Eddington limit earlier in their evolution the higher their mass (cf. Fig. 5 of

Sanyal et al. 2017). For the metallicity of the LMC, inflation occurs in stellar models above $\sim 40\,M_\odot$ during late stages of hydrogen burning, and it occurs already at the zero-age main sequence for masses above $\sim 100\,M_\odot$. The implication for binary evolution above $\sim 40\,M_\odot$ is that all models evolve into Case A mass transfer, that is, Case B no longer occurs. Furthermore, the mass donors above $\sim 40\,M_\odot$ have an inflated envelope at the onset of Roche-lobe overflow beyond a limiting initial orbital period that is shorter for higher donor mass. For hydrogen-free stars with the metallicity of the LMC, inflation occurs above a threshold mass of about $24\,M_\odot$ (Ishii et al. 1999; Köhler et al. 2015; Ro 2019).

The inflated envelope of massive star models is fully convective (Sanyal et al. 2015). Furthermore, any mass loss increases the luminosity-to-mass ratio, thus increasing the Eddington factor. It is therefore not surprising that Quast et al. (2019) found the mass-radius exponent in such models to be negative (unless steep H/He-gradients are present in the outermost envelope). Quast et al. (2019) showed that correspondingly, mass transfer through Roche-lobe overflow is unstable, like in the case of red supergiant donors. In the absence of more detailed predictions, we therefore assume that mass transfer with an inflated mass donor leads to a common-envelope evolution, and successively to the merging of both stars, in most cases.

In the mass-period diagram (Fig. 10), we have drawn the line beyond which a hydrogen-rich donor star (assuming here a hydrogen mass fraction of $X = 0.4$) would exceed its Eddington limit. To construct this line, we used the positions of single-star models in the HR diagram in which inflation has increased the stellar radius by a factor of two, which coincides roughly (Fig. 22 of Sanyal et al. 2015) with the hot edge of the LBV instability strip (Smith et al. 2004). For a given luminosity on this line, we obtained a corresponding stellar mass from the mass-luminosity relation of Gräfener et al. (2011) for a hydrogen mass fraction of $X = 0.4$, and used the corresponding radius to obtain a binary orbital period for which stars on this line would fill their Roche-lobe radius for a mass ratio of 0.7. Considering that the orbital period change during Case A mass transfer is small (Qin et al. 2019), we would not expect to find WR+OB post-mass transfer binaries with H-rich WR stars above this line if binaries with significantly inflated donor stars would merge. For hydrogen-free Wolf-Rayet stars, the Eddingtion limit translates into a simple mass limit, which is also included in Fig. 10.

In Fig. 10 we plot the masses and orbital periods of the WN-type binaries in the LMC (Shenar et al. 2019). We note a group of five massive H-rich short-period WN+O binaries, for which it is unclear whether they did undergo mass transfer (cf. Shenar et al. 2019). In any case, they are indeed found below the Eddington limit, and are thus not in contradiction to having had mass transfer. The two very massive long-period binaries in Fig. 10, on the other hand, are clearly pre-interaction systems. Even though for lower hydrogen abundances, the line for the H-rich Eddington limit is expected to extend to lower masses, the two systems with WN masses just above $30\,M_\odot$ ($\log M_{\rm WN} \gtrsim 1.5$) show a hydrogen mass fraction of ~ 0.2 in the WN star, for which they would still not violate the Eddington limit. Furthermore, all hydrogen-free WN stars are located below the corresponding horizontal line. We conclude that the properties of the LMC WN binaries are in agreement with the assumption that inflated donors lead to mergers.

Because H-free Wolf-Rayet stars may be very close to collapsing into a BH, we add the massive BH binaries to Fig. 10 for which the BH mass is well constrained. We do not include the low- and intermediate-mass BH binaries here (cf. Casares & Jonker 2014); their progenitor evolution is not well understood (Wang et al. 2016). Figure 10 shows that the massive BH binaries occupy a similar parameter space as the hydrogen-free WN stars. Figure 10 cannot resolve whether binaries with initial primary masses above $40\,M_\odot$ contribute to the massive BH-binary population. However, the properties of M 33 X-7 argue for such a contribution because in this binary the BH companion is an O star of $\sim 70\,M_\odot$. This does not imply a conflict with the Eddington limit, because the orbital period of M 33 X-7 is short, which implies a progenitor evolution through Case A mass transfer (Valsecchi et al. 2010; Qin et al. 2019).

Nevertheless, Fig. 10 suggests that the contribution of stars above $40\,M_\odot$ to the population of massive BH-binaries is mostly constrained to orbital periods below ~ 10 d. Therefore, we can consider the predictions for the number of OB+BH binaries from our Case A binary evolution models as a lower limit, and the corresponding OB star mass distribution for Case A (Fig. 3) to stretch out to higher OB masses. Our predictions for longer period OB+BH binaries, which are mostly due to Case B evolution, might not be affected much by this uncertainty.

4.2. Mass transfer efficiency

Observations of massive post-mass transfer binaries suggest that the mass transfer efficiency, that is, the ratio of the amount of mass accreted by the mass gainer to the amount of mass lost by the mass donor through Roche-lobe overflow, is not the same in different binaries. Whereas some can be better understood with a high mass-transfer efficiency, others require highly non-conservative mass transfer (e.g. Wellstein & Langer 1999; Langer et al. 2003). Petrovic et al. (2005) argued for lower efficiency in systems with more extreme mass ratios, and de Mink et al. (2007) derived evidence for a lower efficiency in wider binary systems.

Our mass transfer model (cf. Sect. 2), which assumes that the mass transfer efficiency drops when the mass gainer is spinning rapidly, does in principle account for these variations. However, it requires that sufficient mass is removed from the binary to prevent the mass gainer from exceeding critical rotation. We applied the condition that the photon energy emitted by the stars in a binary is higher than the gravitational energy needed to remove the excess material. Otherwise, we stopped the model and assumed the binary to merge. Figure 2 shows the dividing line between surviving and merging for our models with an initial primary mass of $25.12\,M_\odot$. The predicted number of OB+BH binaries is roughly proportional to the area of surviving binaries in this figure.

This condition for distinguishing stable mass transfer from mergers is rudimentary and will eventually need to be replaced by a physical model. Correspondingly uncertain is the number of predicted OB+BH binaries. However, Wang et al. (2020) have shown that the distribution of the sizable Be population of NGC 330 (Milone et al. 2018) in the colour-magnitude diagram is well reproduced by detailed binary evolution models. In order to explain their number, however, the condition for stable mass transfer would have to be relaxed such that merging is prevented in more systems. A corresponding measure would increase the predicted number of OB+BH binaries, such that, again, our current numbers could be considered as a lower limit.

4.3. Black hole formation

As discussed in Sect. 2, our BH formation model is very simple. By applying the single-star helium core mass limit according to simple criteria based on 1D pre-collapse models, and by

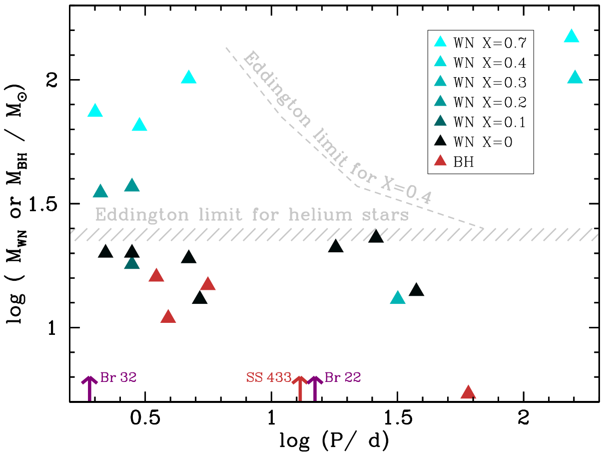

Fig. 10. Masses and orbital periods of LMC WN binaries with an O or early-B star companion (Shenar et al. 2019). The orbital periods of the two LMC WC binaries Brey 22 (right) and Brey 32 (left; Boisvert et al. 2008) and of SS 433 (Hillwig & Gies 2008) are indicated by arrows. We also plot the masses and orbital periods of the well-characterised BHs with an O or early-B companion, which are in order of increasing orbital period M 33 X-7 (Orosz et al. 2007), LMC X-1 (Orosz et al. 2011), Cyg X-1 (Orosz et al. 2011), and MCW 656 (Casares et al. 2014). Above $\sim 24\,M_\odot$ (or a corresponding luminosity of $\log L/L_\odot = 5.8$; Gräfener et al. 2011), no H-free Wolf-Rayet stars are known in the LMC, potentially because this corresponds to their Eddington limit (see text).

neglecting small mass ranges above this limit that may lead to NSs rather than BHs, we may overpredict the number of OB+BH systems. However, the anticipated BH mass distribution is rather flat (Fig. 5), such that this overprediction is likely rather small. Our assumption that the BH mass equals the final helium core mass is perhaps not very critical because it does not affect the predicted number of OB+BH systems.

The neglect of a BH birth kick may again lead to an overprediction of OB+BH binaries. However, because BHs have higher masses than NSs, birth kicks with similar momenta as those given to NSs upon their formation would still leave most of the OB+BH binaries intact. While Janka (2013) suggested that NS and BH kick velocities can be comparable in BHs that are produced by asymmetric fallback, Chan et al. (2018) found only modest BH kicks in their simulations. By considering the galactic distribution of low-mass BH binaries, Repetto & Nelemans (2015) reported that two out of seven systems were consistent with a relatively high BH formation kick. This result was confirmed by Repetto et al. (2017), who found, on the other hand, that the galactic scale hight of the low-mass BH binaries is smaller than that of the low-mass NS binaries. Mirabel (2017) provided evidence that the BHs of $\sim 10\,M_\odot$ and $\sim 15\,M_\odot$ in the high-mass BH binaries GRS 1915+105 and Cygnus X-1 formed with essentially no kick. Furthermore, the systems that may correspond most closely to our predicted OB+BH distribution, the galactic Be+BH binary MCW 656 (Casares & Jonker 2014) and the potential B+BH binary LB1 (Liu et al. 2019; see our discussion of this in Sect. 6), appear to have low eccentricities. We consider the systematics of BH kicks to be still open and return to a discussion of their effect on OB+BH systems in Sect. 5.

5. Comparison with earlier work

The computation of large and dense grids of binary evolution models has so far been performed mostly using so-called rapid binary evolution codes (e.g. Hurley et al. 2002; Voss & Tauris 2003; Izzard et al. 2004; Vanbeveren et al. 2012; de Mink et al. 2013; Lipunov & Pruzhinskaya 2014; Stevenson et al. 2017; Kruckow et al. 2018). On the one hand, such calculations can comprehensively cover the initial binary parameter space, and they allow an efficient exploration of uncertain physics ingredients. On the other hand, stars are spatially resolved by only two grid points, and binary interaction products are often described by interpolating in single star models. Therefore, many genuine binary evolution effects are difficult to include, which is true for the uncertainties discussed in Sect. 4.

The computation of dense grids of detailed binary evolution models has become feasible during the past two decades (Nelson & Eggleton 2001; de Mink et al. 2007; Eldridge et al. 2008; Eldridge & Stanway 2016; Marchant 2016; Marchant et al. 2017; see also Van Bever & Vanbeveren 1997). Whereas the computational effort is much larger, detailed calculations are preferable over rapid binary evolution calculations whenever feasible. Detailed binary model grids have been used to explore various stages and effects of binary evolution, including the production of runaway stars (Eldridge et al. 2011), double BH mergers (Eldridge & Stanway 2016; Marchant 2016), long-duration gamma-ray bursts (Chrimes et al. 2020), ultraluminous X-ray sources (Marchant et al. 2017), and galaxy spectra (Stanway & Eldridge 2019). However, a detailed prediction of the OB+BH binary population has not yet been performed.

Many rapid binary evolution calculations exist. Here, papers predicting OB+BH populations often aim at reproducing the observed X-ray binary populations (e.g. Dalton & Sarazin 1995; Tauris & van den Heuvel 2006; Van Bever & Vanbeveren 2000; Andrews et al. 2018). For example, based on the apparent lack of B+BH binaries in the population of Galactic X-ray binaries, Belczynski & Ziolkowski (2009) predicted a very small number of such systems based on rapid binary evolution models. Since the discovery of the massive BH mergers through gravitational waves, many predictions for the expected number of double compact mergers have been computed based on rapid binary evolution models (e.g. Chruslinska et al. 2018; Kruckow et al. 2018; Vigna-Gomez et al. 2018; Spera et al. 2019). However, whereas the binary evolution considered in these papers includes the OB+compact object stage, their predictions are focused on the double compact mergers.

In the past few years, based on an analytic considerations, Mashian & Loeb (2017), Breivik et al. (2017), Yamaguchi et al. (2018), Yalinewich et al. (2018), and Masuda & Hotokezaka (2019) developed predictions for the BH-binary population in the Galaxy. Much of this work concentrated on low-mass MS+BH binaries, in view of the currently known 17 low-mass BH X-ray binaries (McClintock & Remillard 2006; Arur & Maccarone 2018). Shenar et al. (2019) have recently simulated the Galactic BH-binary population through rapid binary evolution models, with detailed predictions for OB+BH binaries. Because they are largely consistent with the outcome of the quoted earlier papers, we compare our results with theirs.

As shown in Sect. 6, our results imply that the LMC should currently contain about 120 OB+BH binaries. A ten times higher star formation rate in the Milky Way (Diehl et al. 2006; Robitaille & Whitney 2010) would lead to 1200 Galactic OB+BH binaries. Here we neglect the metallicity difference between the two systems, which for stars below $40\,M_\odot$ is not expected to cause a great differences (e.g. Brott et al. 2011) at the level of the accuracy of our consideration. Shao & Li exploited the advantage of rapid binary calculations by producing four population models for Galactic MS+BH binaries that differ in the assumptions made for the BH kick distribution (see also

Renzo et al. 2019). The authors reported that essentially no low-mass BH-binaries are produced when efficient BH kicks are assumed. Based on the observed number of low-mass BH X-ray binaries, Shao & Li discarded the possibility of efficient BH kicks. For the other cases, they predict between 4000 and 12 000 Galactic OB+BH binaries. This number exceeds our estimate for the number of Galactic OB+BH binaries by a factor of 3 to 10.

We find three potential reasons for this. First, Shao & Li adopted a very low accretion efficiency. As in our detailed models, they assumed that the spin-up of the mass gainer limits the mass accretion. However, in our models, we verified whether the energy in the radiation field of both stars is sufficient to remove the excess material from the binary system and assumed that the binary merges when this is not the case. No such verification was applied by Shao & Li, with the consequence that binaries with initial mass ratios as low as 0.17 undergo stable mass transfer. A comparison with our Fig. 2 shows that this might easily lead to a factor of two more OB+BH binaries. Furthermore, Shao & Li assumed that BH can form from stripped progenitors with masses above $5\,M_{\odot}$ (we adopted a limit of $6.8\,M_{\odot}$; see Sect. 2), and did not discard progenitors with initial primary masses above $40\,M_{\odot}$ because envelope inflation (see Sect. 4) is not considered in their models. While both effects lead to more OB+BH binaries, they may not be as important as the first one.

The distribution of the properties of the OB+BH binaries found by Shao & Li is similar to those predicted by our models. The OB stars show a peak in their mass distribution near $10\,M_{\odot}$, and the BH masses fall in the range 5−15 $M_{\odot}$ with a peak near $8\,M_{\odot}$. The orbital periods span from 1 to 1000 days, with a peak near ∼100 days, and is similar to that found by Shao & Li (2014) for Be+BH binaries. The peak produced by our Case A systems (Fig. 6) is not reproduced by the rapid binary evolution models by design.

6. Comparison with observations

The global Hα-derived star formation rate of the LMC is about $\sim 0.2\,M_{\odot}\,\mathrm{yr}^{-1}$ (Harris & Zaritsky 2009). About a quarter of this is associated with the Tarantula region, for which the number of O stars is approximately 570 (Doran et al. 2013; Crowther 2019). We therefore expect about 2000 O stars to be present in the LMC. About 370 of them have been observed in the spectroscopic VLT Flames Tarantula survey (Evans et al. 2011). Adopting a 3% probability for a BH companion, as suggested by our results (cf. Sect. 7), we expect about 60 O+BH binaries currently in the LMC. About 10 of them may have been picked up by the Tarantula Massive Binary Monitoring survey (Almeida et al. 2017).

At the same time, we also predict about 1.5% of the B stars above $\sim 10\,M_{\odot}$ to have a BH companion, most of which would likely be Be stars. As they live about twice as long as O stars, and accounting for a Salpeter mass function, we expect about 60 B+BH binaries amongst the ∼4000 B stars above $10\,M_{\odot}$ expected in the LMC. This means that our models predict more than 100 OB+BH systems in the LMC, while we know only LMC X-1. The implication is either that our model predictions are off by some two orders of magnitude, or that the majority of OB+BH binaries are X-ray quiet.

One way to decide which of these two answers is correct is to consider the Wolf-Rayet binaries in the LMC. Shenar et al. (2019) have provided the properties of 31 known or suspected WN-type LMC binaries. Of these, an orbital period is known for 16, which we show in Fig. 10. Of these 16 WN binaries, 7 are hydrogen rich (with hydrogen mass fractions in the range 0.7−0.2), very massive, and likely still undergoing core hydrogen burning. The other 9 are very hot, and most of them are hydrogen free, such that they are likely undergoing core helium burning. Because this implies a short remaining lifetime, they are likely close to core collapse. If we were to take their measured mass-loss rates and adopt an average remaining Wolf-Rayet lifetime of 250 000 yr, most of them would be at the end of their lives well above $10\,M_{\odot}$. We can therefore assume here that these 9 OB+WN binaries will form OB+BH systems. After the Wolf-Rayet stars forms a BH, the OB stars will on average still live for a long time. A remaining OB star lifetime of 1 or 2 Myr leads to the expectation of 18−36 OB+BH binaries currently in the LMC, which is rather close to our model prediction. About 16% of the 154 Wolf-Rayet stars in the LMC are of type WC or WO (Breysacher et al. 1999; Bartzakos et al. 2001; Neugent et al. 2018). Their properties are less well known; however, at least 3 of the 24 WC stars are binaries (the two with well-determined orbital period are included in Fig. 10). Including the WC binaries will increase the expected number of OB+BH binaries (Sander et al. 2019).

The properties of the observed WR+OB binaries show that the OB star masses in the mentioned nine binaries (13−44 $M_{\odot}$) are well within the range predicted by our models (Fig. 3). However, the average observed OB mass of the nine WR+OB binaries is $\sim 26\,M_{\odot}$, while the average OB mass of our OB+BH models is about $15\,M_{\odot}$ (Fig. 3). Of the nine considered LMC systems, only one has a B dwarf component (Brey 23). Of the other potential WR-binaries listed by Shenar et al. (2019), one has a B dwarf companion but no measured orbital period, and three apparently have rather faint B supergiant companions (which is difficult to understand in evolutionary terms). We note that our models predict that the B stars in such binaries might be rotating rapidly, and that it is unclear whether a Be disc can be present next to a WR star with a powerful wind. Potentially, the spectral appearance of B stars in this situation may be unusual. Furthermore, O dwarfs are perhaps easier to identify as WR star companions than the fainter B dwarfs, such that more of the latter might still be discovered. Another aspect to consider is that a considerable fraction of the He-star companions of B dwarfs might not have a WR-type spectral appearance. Their luminosity-to-mass ratio might simply be too low to yield a sufficient mass loss for an emission-line spectrum (Sander et al. 2020; Shenar et al. 2020), eliminating them from being found in WR surveys.

Concerning the orbital periods, a comparison of Fig. 6 with Fig. 10 shows that five of the nine considered WN+OB binaries are found in the period range predicted by our Case A binary models, whereas the other four fall into the Case B regime. Notably, the gap in the observed periods (7−15 d) coincides with the minimum in the predicted period distribution produced between the Case A and Case B peaks in the top panel of Fig. 6. On the other hand, our Case B models predict a broad distribution of orbital periods with a peak near 100 d, whereas the longest measured period is 38 d (Brey 53). Again, this could mean two things. Either our models largely overpredict long-period OB+WN binaries (with core helium-burning WN stars), or many long-period systems have not yet been identified. In this respect, we note that Shenar et al. (2019) listed nine more binaries in which the WR star is likely undergoing core helium burning but for which no period has been determined. Because longer periods are harder to measure, there might be a bias against finding long-period systems.

This idea is fostered by considering the Be/X-ray binaries. This may be meaningful because their evolutionary stage is directly comparable to the OB+BH stage, only that the primary star collapsed into an NS, rather than a BH. Because of the larger mass loss and the expected larger kick during NS formation, in particular the longest period OB+NS systems may break up at this stage, whereas comparable OB+BH systems might survive. However, otherwise, we would expect their properties to be quite similar to those of OB+BH systems. The orbital period distribution of the Galactic Be/X-ray binaries is quite flat and stretches between 10 d and 500 d (Reig 2011; Knigge et al. 2011; Walter et al. 2015). We overplot in Fig. 6 the observed orbital period distribution of 24 Galactic Be/X-ray binaries following (Walter et al. 2015). Figure 6 shows that the orbital period distribution of the Be/X-ray binaries matches the prediction of our Case B OB+BH binaries very closely. Because the pre-collapse binary evolution does not know whether an NS or BH will be produced by the mass donor, the observed Be/X-ray binary period distribution argues for the existence of long-period OB+BH binaries, as predicted by our models.

The location of the four massive BHs binaries in the mass-orbital period plot in comparison to the OB+WR binaries in Fig. 10 shows that three of them coincide well with the short-period helium-burning WR binaries within the Case A range of our models (see also Qin et al. 2019). Only the Be-BH binary MCW 656 has a rather long orbital period of 60 d. Our conjecture of the existence of many more long-period OB+BH binaries agrees with the anticipation of Casares et al. (2014), who considered MCW 656 as only the tip of the iceberg. The reason is that MCW 656, in contrast to the short-period OB+BH systems, is X-ray silent, which is likely because the wind material falling onto the BH does not form an accretion disc, but an advection-dominated inflow (Shakura & Sunyaev 1973; Karpov & Lipunov 2001; Narayan & McClintock 2008; Quast & Langer, in prep.). We note that the recently detected B star−BH binary system LB-1 (Liu et al. 2019) might also fall into this class. While it was first proposed that the BH in this system is very massive, it has subsequently been shown that its mass is consistent with being quite ordinary (Abdul-Masih et al. 2020; El-Badry & Quataert 2020; Simon-Diaz et al. 2020), if it is a BH at all (Irrgang et al. 2020). Remarkably, the long-period OB+BH binaries have the highest probability of producing a double-compact binary that may merge within one Hubble time.

7. OB+BH binary detection strategies

We showed above that our binary evolution models predict that about 100 OB+BH binaries remain to be discovered in the LMC. Scaling this with the respective star formation rates would lead to about 500 to several thousand OB+BH binaries in the MW. Simplified binary population synthesis models predict similar numbers and show that the order of magnitude of the expected number of OB+BH binaries is only weakly dependent on the major uncertainties in the models (Yamaguchi et al. 2018; Yalinewich et al. 2018; Shao & Li 2019). At the same time, as discussed in Sect. 6, the observations of Wolf-Rayet binaries and of Be/X-ray binaries lend strong support to these numbers. Finding these OB+BH binaries, and measuring their properties, would provide invaluable boundary conditions for the evolution and explosions of massive stars.

One possibility is to monitor the sky position of OB stars and determine the presence of dark companions from detecting periodic astrometric variations. It has been demonstrated recently that the *Gaia* satellite offers excellent prospects for identifying OB+BH binaries in this way (Breedt et al. 2017; Mashian & Loeb 2017; Yalinewich et al. 2018; Yamaguchi et al. 2018; Andrews et al. 2019). Furthermore, a BH companion induces a photometric variability to an OB star in several ways (Zucker et al. 2007; Masuda & Hotokezaka 2019). In the closest OB+BH binaries, the OB star will be deformed, which leads to ellipsoidal variability. In wide binaries seen edge-on, gravitational lensing of the BH can lead to significant signals (Appendix A). Additionally, relativistic beaming due to the orbital motion affects the light curve of OB+BH binaries. Masuda & Hotokezaka (2019) found that the TESS satellite may help to identify OB+BH binaries, in particular short-period ones. Finally, OB+BH binaries can be identified spectroscopically through the periodic radial velocity shift of the OB component in so-called SB1 systems, in which only one star contributes to the optical signal. Spectacular examples are provided by the discovery of the first known Be-BH binary (Casares et al. 2014), the potentially similar B[e]-BH binary candidate found by Khokhlov et al. (2018), and the recently found potential B-BH binary LB-1 (Liu et al. 2019; see Sect. 6). Existing surveys include the TMBM survey in the LMC (Almeida et al. 2017) and the Galactic LAMOST survey (Yi et al. 2019).

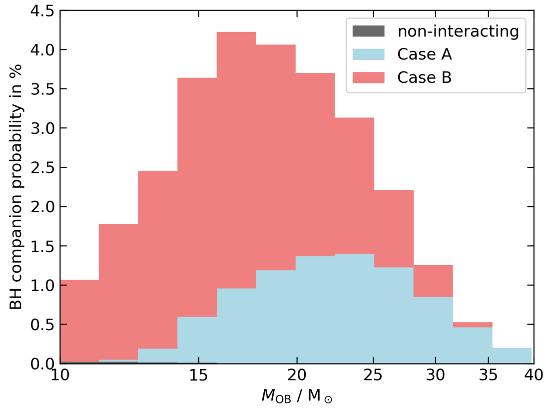

Fig. 11. Probability of OB stars of a given mass to have a BH companion as a function of the mass of the OB star, according to our population synthesis model. The initial mass function, initial binary parameter distributions, and the lifetimes of the OB+BH systems have been considered. A initial binary fraction of 100% has been assumed.

Regardless of how the BHs in binary systems affect the signal we observe from the companion star, the BH per se will remain unobservable. This means that the conclusion of having a BH in a given binary will always remain indirect, and somewhat tentative because physics can never deliver proofs. This is the more so because the technique with which BH detections are generally associated, namely X-ray observations, clearly appears to fail for the vast majority of OB+BH binaries (cf. Sect. 6). For this reason, it will be beneficial if, firstly, OB+BH binaries are detected in more than one way, and secondly, if the properties of the OB component are measured spectroscopically, to see whether its surface abundances and its rotation rate fall within expectations, for example.

In our grid of binary evolution models, we produce (potential) OB+BH binaries, but the model systems spend most of their time as OB+OB binaries. In order to evaluate the probability that a randomly picked OB star has a BH companion, we divided the number of systems in the mass bin of our OB star by the corresponding number of OB binaries with any type of companion. The result is plotted in Fig. 11. Here, OB single stars are neglected. Considering them reduces the probabilities obtained in Fig. 11 by the assumed binary fraction.

Figure 11 resembles the overall OB star mass distribution derived in Fig. 3. However, its ordinate values represent actual BH companion probabilities. Therefore, we find that the fraction

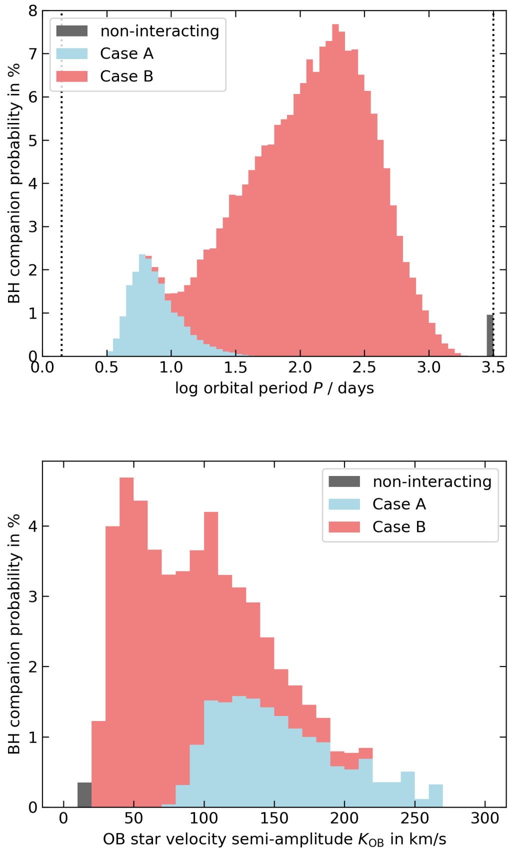

Fig. 12. Prediction of our population synthesis model for the probability of OB stars to have a BH companion as a function of the observed orbital period (*top*) and of the observed radial velocity semi-amplitude (*bottom*), respectively.

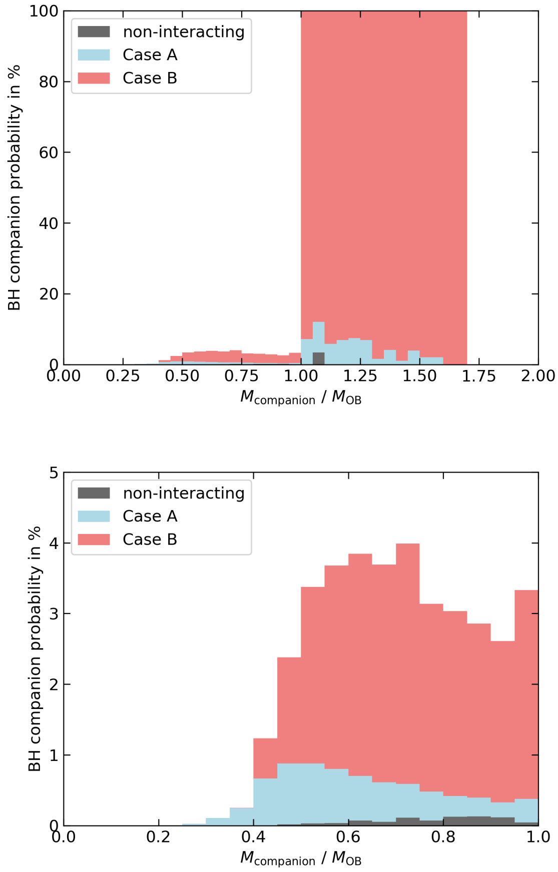

Fig. 13. Prediction of our population synthesis model for the probability of a randomly picked OB binary to have a BH companion as a function of the mass ratio (*top*). Here, a mass ratio above one means that the BH has a higher mass than the OB star; if such an OB binary is picked, its probability of having a BH companion is one. *Bottom panel*: zoom of the part with a mass ratio lower than one.

of OB stars with BH companions is highest in the OB star mass range 14−22 $M_\odot$, with the probability of an accompanying BH of about 4%. For B stars near 10 $M_\odot$, the BH companion probability is still about 1%. For more massive OB stars, we expect BH companions in at least 1% of the stars up to about 32 $M_\odot$, where an additional contribution from binaries with initial primary masses above 40 $M_\odot$ is possible (see Sect. 4).

In the upper panel of Fig. 12, we show the probability of a randomly picked OB binary to have a BH companion as a function of its orbital period. For example, when our chosen binary has an orbital period of 10 d, then its probability to be accompanied by a BH is about 1.5%. For a period of 180 d, on the other hand, it is almost 8%. Figure 12 shows that the expected orbital periods in OB+BH binaries are somewhat ordered according to their initial orbital periods. The Case A systems have the shortest initial periods (cf. Fig. 2), and they produce the shortest period OB+BH binaries in our results. On the opposite side, the initial period range of the Case B binaries is mapped into a quite similar period range as the OB+BH binaries.

The lower panel of Fig. 12 shows the corresponding distribution of orbital velocities. Again, the ordinate value in this plot reflects the probability of a randomly picked OB binary to contain a BH, this time as a function of its orbital velocity. The Case A systems, which have initial orbital periods as short as 1.4 d, provide the fastest moving OB stars, while the Case B binaries form many OB+BH systems with orbital velocities of just a few tens of km s^{-1}.

Figure 13 gives the probability of a randomly picked OB binary to be accompanied by a BH as a function of the mass ratio $q = M_{companion}/M_{OB}$. For $q > 1$, this probability is one. In this case, the companion must be a BH and cannot be an ordinary star because otherwise, the ordinary companion star would be the more luminous star of the two, and it would have been picked as the primary OB star.

The lowest mass ratios are dominated by Case A systems, which is a consequence of the rather high accretion efficiency in them: the OB stars in such binaries gained a substantial amount of mass. Combined with Fig. 12, this means that the OB+BH binaries with the lowest mass ratios have short orbital periods.

Finally, Fig. 13 shows that the highest mass ratios produced by our model binaries is about $q = 1.7$. Binaries with such high mass ratios originate from OB+OB binaries with initially massive primaries and an extreme mass ratio, for instance, 40 $M_\odot$ + 13 $M_\odot$, in which the secondary accretes little material. The OB stars in such systems are therefore expected to be be early-B or late-O stars.

Above, we have discussed the BH companion probabilities of randomly picked OB stars, and found them to be of the order of a few percent. When we consider observing campaigns that search for OB+BH binaries, an efficiency of a few percent is rather low. However, the OB stars in OB+BH binaries have had a turbulent life, and signs of this may still be visible. In particular, all OB stars in our OB+BH model binaries have accreted some amount of matter from their companion. Because the accretion efficiency in our models drops after the mass gainer has reached critical rotation, and because a mass increase by about 10% is required to achieve this (Packet 1981; Petrovic et al. 2005), this is roughly the minimum mass increase of our OB mass gainers.

From the properties of the OB stars in OB+BH binaries as described in Sect. 3, most OB stars with a BH companion are expected to stand out amongst the ordinary OB stars. In Case A systems, the OB star rotation is expected to be relatively fast, but because only the projected rotation velocity can be easily measured, this is not an unambiguous selection criterion. However, in our models, the BH companion induces a radial velocity variation of 200 km s^{-1} or more ($K \gtrsim 100$ km s^{-1}; Fig. 8), which should be easily seen even though the observed value will again be lower because of projection (by 21% on average). In addition, our models predict a significant surface enrichment with products of hydrogen burning in the vast majority of all cases, the strongest signature being a clear nitrogen enrichment.

In Case B binaries, surface enrichment of the OB components is predicted to be low. However, their rotation velocity is expected to exceed 300 km s^{-1}, with values close to critical rotation in those with masses below $\sim 20\,M_{\odot}$. Even in Case B, the expected radial velocity variations of the OB stars exceed 40 km s^{-1}, with an average well above 100 km s^{-1}.

We note that the mass ratios of our OB+BH binaries are also rather favourable. This means that when we assume that an MS companion would still be detected as such for mass ratios above 0.5, then such a companion could be excluded in potential observations of almost all of our OB+BH model binaries. Based on the clues accumulated above, a corresponding search for BHs in SB1 spectroscopic binaries might thus be promising.

Finally, we wish to emphasise that additional possibilities of identifying potential OB+BH binaries exist when the population of young star clusters is considered. In particular, many of the OB stars in our OB+BH model binaries that evolved through Case A mass transfer have gained a substantial amount of mass. The mass increase may cause the stars to appear above the cluster turn-off, and the convective core mass increase will rejuvenate them such that they appear younger than most other cluster stars (Van Bever & Vanbeveren 1997; Schneider et al. 2014; Wang et al. 2020).

8. Further evolution and connection to double-compact mergers

As shown in Fig. 1, the OB+BH stage on which we focus here is the last evolutionary stage of massive binaries that can be reached so far with detailed calculations from the zero age main sequence. Therefore, predictions for later stages become increasingly uncertain and are not derived from our models. Nevertheless, it is interesting to speculate about the future evolution of the OB+BH.

First of all, because of the rather long orbital periods of our OB+BH systems (Fig. 6), in almost all of our model binaries the OB star would fill its Roche-volume only after core hydrogen exhaustion (Case B). We would therefore expect a mass transfer from the OB star to the BH on a thermal timescale, with a mass transfer rate of $\dot{M} \simeq LR/(GM)$. Because this stage is very short ($\sim 10^4$ yr), we would expect to observe only very few systems in this stage, SS 433 perhaps being one of them (Hillwig & Gies 2008). It depends on the mass ejection rate from the mass-transferring binary whether a common envelope evolution is initiated or avoided at this stage. For shorter periods and rather low-mass donors, it can perhaps be avoided, as estimated by King et al. (2000) for SS 433, which has an orbital period of 13.1 d and for which a mass ejection rate of about $10^{-4}\,M_{\odot}\,\mathrm{yr}^{-1}$ has been determined. For the bulk of our systems, the stellar radius will be far larger and the luminosity will far higher, and the mass transfer rate would typically be $10^{-2}\,M_{\odot}\,\mathrm{yr}^{-1}$, such that common-envelope evolution appears more likely. With the assumptions for the common-envelope evolution as in Kruckow et al. (2016), except for possibly the widest systems, we would expect a merging of the two stars.

In any case, the accretion of matter of BHs inside a stellar envelope and the common-envelope evolution of a BH and a non-degenerate star, cannot yet be predicted with certainty. Therefore it remains an open question whether there is a critical orbital period in our predicted OB+BH period distribution (Fig. 6) beyond which the systems survive the common-envelope evolution as a binary, and what its value would be. The fact that the peak of the period distribution corresponds to a rather high value (~200 d) leaves room for the speculation that a significant fraction of the OB+BH binaries will lead to tight double BH systems.

9. Conclusions

We have provided predictions for the properties of the OB+BH binary population in the LMC. These predictions are based on almost 50 000 detailed binary evolution models. These models include internal differential rotation, mass and angular momentum transfer due to Roche-lobe overflow, and no inhibition of envelope inflation due to the Eddington limit. Only models that undergo stable mass transfer were considered, implying that common-envelope evolution may add more OB+BH binaries to our synthetic population. Our results are subject to substantial uncertainties, which we discussed in detail in Sect. 4. However, they represent the last long-lived stage of massive binaries on their way to double-compact binaries that can be modelled in detail without interruption starting from the double main-sequence stage, which allows the prediction of their properties with a rather limited number of assumptions (Sect. 2). This includes the initially closest binaries that undergo mass transfer during hydrogen burning (Case A), which can be treated only rudimentary in rapid binary evolution calculations.

We compared our predictions with the number and properties of the observed OB+WR binaries in the LMC, which may be the direct progenitors of OB+BH binaries. We find good agreement with the mass distribution and with the orbital period distribution up to ~40 d. However, there is a lack of observed long-period (~100 d) OB+WR binaries and of B+WR binaries compared to our predictions. While the corresponding observational biases are not well understood, the similarity of the observed Be/X-ray binary period distribution to that predicted for the OB+BH binaries argues for the so far undetected presence of long-period unevolved binary companions in a significant fraction of the WR star population.

We derived the distribution of masses, mass ratios, and orbital periods of the expected OB+BH binary population, and showed that OB stars with BH companions may be identified through their radial velocity variations, their rotation rate, or their surface abundances. Our results imply that an average O or early-B star in the LMC has a BH companion with a probability of a few percent, which argues for about 120 OB+BH binaries currently in the LMC. With a star formation rate higher by about five to ten times, the Milky Way may thus harbour about 1000 of such system. Altogether, only four such binaries have been found so far, one of them in M 33.

The vast majority of the predicted OB+BH binaries are expected to be X-ray quiet. The reason is that because of their rather long expected orbital periods (Fig. 12), wind material may be accreted in an advection-dominated flow rather than through an accretion disc. This picture is confirmed by the Be-BH binary MCW 656, which has an orbital period of 60 d. In any case, we have shown that the expected orbital velocities are sufficiently high for identifying OB+BH binaries spectroscopically (Fig. 12), which is easier here than in their OB+WR progenitors, that the mass ratios are such that main-sequence companions can easily be excluded, and that rapid rotation and/or chemical surface enrichment may help to identify candidate systems.

We find the accumulated evidence for a so far undetected large population of OB+BH binaries significant. Its discovery would greatly help to reduce the uncertainty in massive binary evolutionary models, and pave the way for understanding the contribution of close binary evolution to the BH merger events observed through their gravitational wave emission.

Acknowledgements. A.A.C.S. and J.S.V. are supported by STFC funding under grant number ST/R000565/1. T.M.T. acknowledges an AIAS–COFUND Senior Fellowship funded by the European Union's Horizon 2020 Research and Innovation Programme (grant agreement no 754513) and Aarhus University Research Foundation. J.B. acknowledges support from the FWO Odysseus program under project G0F8H6N. A.H. and S.S.D. acknowledge funding by the Spanish Government Ministerio de Ciencia e Innovacion through grants PGC-2018-0913741-B-C22 and SEV 2015-0548, and from the Canarian Agency for Research, Innovation and Information Society (ACIISI), of the Canary Islands Government, and the European Regional Development Fund (ERDF), under grant with reference ProID2017010115.

References

Abbott, B. P., Abbott, R., Abbott, T. D., et al. 2016, Phys. Rev. Lett., 116, 061102
Abbott, B. P., Abbott, R., Abbott, T. D., et al. 2019, Phys. Rev. X, 9, 031040
Abdul-Masih, M., Sana, H., Sundqvist, J., et al. 2019, ApJ, 880, 115
Abdul-Masih, M., Banyard, G., Bodensteiner, J., et al. 2020, Nature, 580, 11
Almeida, L. A., Sana, H., Taylor, W., et al. 2017, A&A, 598, A84
Andrews, J. J., & Zezas, A. 2019, MNRAS, 486, 3213
Andrews, J. J., Zezas, A., & Fragos, T. 2018, ApJS, 237, 1
Andrews, J. J., Breivik, K., & Chatterjee, S. 2019, ApJ, 886, 68
Antonini, F., Chatterjee, S., Rodriguez, C. L., et al. 2016, ApJ, 816, 65
Arur, K., & Maccarone, T. J. 2018, MNRAS, 474, 69
Batta, A., Ramirez-Ruiz, E., & Fryer, C. 2017, ApJ, 846, L15
Belczynski, K., & Ziolkowski, J. 2009, ApJ, 707, 870
Belczynski, K., Bulik, T., Fryer, C., et al. 2010, ApJ, 714, 1217
Belczynski, K., Holz, D. E., Bulik, T., & O'Shaughnessy, R. 2016, Nature, 534, 512
Bisnovatyi-Kogan, G. S., & Komberg, B. V. 1974, Astron. Zh., 51, 373
Böhm-Vitense, E. 1958, ZA, 46, 108
Boisvert, P., Marchenko, S. V., St-Louis, N., & Moffat, A. F. J. 2008, ApJ, 683, 449
Bartzakos, P., Moffat, A. F. J., & Niemela, V. S. 2001, MNRAS, 324, 18
Braun, H., & Langer, N. 1995, A&A, 297, 483
Breedt, E., Steeghs, D., Marsh, T. R., et al. 2017, MNRAS, 468, 2910
Breivik, K., Chatterjee, S., & Larson, S. L. 2017, ApJ, 850, L13
Breysacher, J., Azzopardi, M., & Testor, G. 1999, A&AS, 137, 117
Brott, I., de Mink, S. E., Cantiello, M., et al. 2011, A&A, 530, A115
Brown, G. E., Heger, A., Langer, N., Lee, C.-H., & Bethe, H. A. 2001, New Astron., 6, 457
Cantiello, M., & Langer, N. 2010, A&A, 521, A9
Casares, J., & Jonker, P. G. 2014, Space Sci. Rev., 183, 223
Casares, J., Negueruela, I., Ribo, M., et al. 2014, Nature, 505, 378
Chan, C., Müller, B., & Heger, A. 2018, ApJ, 852, L19
Choi, J., Dotter, A., Conroy, C., et al. 2016, ApJ, 823, 102
Chrimes, A. A., Stanway, E. R., & Eldridge, J. J. 2020, MNRAS, 491, 3479
Chruslinska, M., Belczynski, K., Klencki, J., & Benacquista, M. 2018, MNRAS, 474, 2937
Clark, J. S., Ritchie, B. W., Najarro, F., et al. 2014, A&A, 565, A90
Crowther, P. A. 2019, Galaxies, 7, 88
Crowther, P. A., Caballero-Nieves, S. M., Bostroem, K. A., et al. 2016, MNRAS, 458, 624
Dalton, W. W., & Sarazin, C. L. 1995, ApJ, 440, 280
de Mink, S. E., & Mandel, I. 2016, MNRAS, 460, 3545
de Mink, S. E., Pols, O. R., & Hilditch, R. W. 2007, A&A, 467, 1181
de Mink, S. E., Cantiello, M., Langer, N., et al. 2009, A&A, 497, 243
de Mink, S. E., Langer, N., Izzard, R. G., et al. 2013, ApJ, 764, 166
Detmers, R. G., Langer, N., Podsiadlowski, P., & Izzard, R. G. 2008, A&A, 484, 831
Di Carlo, U. N., Giacobbo, N., Mapelli, M., et al. 2019, MNRAS, 487, 2947
Diehl, R., Halloin, H., Kretschmer, K., et al. 2006, Nature, 439, 45
Doran, E. I., Crowther, P. A., de Koter, A., et al. 2013, A&A, 558, A134
D'Orazio, D. J., & di Stefano, R. 2020, MNRAS, 491, 1506
Dunstall, P. R., Brott, I., & Dufton, P. L. 2011, A&A, 536, A65
Ekstrom, S., Meynet, G., Maeder, A., & Barblan, F. 2008, A&A, 478, 467
El-Badry, K., & Quataert, E. 2020, MNRAS, 493, L22
Eldridge, J. J., & Stanway, E. R. 2016, MNRAS, 462, 3302
Eldridge, J. J., Izzard, R. G., & Tout, C. A. 2008, MNRAS, 384, 1109
Eldridge, J. J., Langer, N., & Tout, C. A. 2011, MNRAS, 414, 3501
Ertl, T., Janka, H.-T., Woosley, S. E., Sukhbold, T., & Ugliano, M. 2016, ApJ, 813, 23
Evans, C. J., Taylor, W. D., Hénault-Brunet, V., et al. 2011, A&A, 530, A108
Flannery, B. P., & van den Heuvel, E. P. J. 1975, A&A, 39, 61
Fragione, G., Grishin, E., Leigh, N. W. C., et al. 2019, MNRAS, 488, 47
Fruchter, A. S., Levan, A. J., Strolger, L., et al. 2006, Nature, 441, 463
Giacobbo, N., Mapelli, M., & Spera, M. 2018, MNRAS, 474, 2959
Gilkis, A., Vink, J. S., Eldridge, J. J., & Tout, C. A. 2019, MNRAS, 486, 4451
Gräfener, G., Vink, J. S., de Koter, A., & Langer, N. 2011, A&A, 535, A56
Gräfener, G., Owocki, S. P., & Vink, J. S. 2012, A&A, 538, A40
Grassitelli, L., Chené, A.-N., Sanyal, D., et al. 2016, A&A, 590, A12
Grassitelli, L., Langer, N., Gräfener, G., et al. 2020, A&A, submitted
Harris, J., & Zaritsky, D. 2009, AJ, 138, 1243
Hastings, B., Wang, C., & Langer, N. 2020, A&A, 633, A165
Heger, A., Langer, N., & Woosley, S. E. 2000, ApJ, 528, 368
Heger, A., Fryer, C. L., Woosley, S. E., et al. 2003, ApJ, 591, 288
Heger, A., Woosley, S. E., & Spruit, H. C. 2005, ApJ, 626, 350
Higgins, E. R., & Vink, J. S. 2020, A&A, 635, A175
Hilditch, R. W., Howarth, I. D., & Harries, T. J. 2005, MNRAS, 357, 304
Hillwig, T. C., & Gies, D. R. 2008, ApJ, 676, L37
Hopkins, P. F., Keres, D., Onorbe, J., et al. 2014, MNRAS, 445, 581
Hurley, J. R., Tout, C. A., & Pols, O. R. 2002, MNRAS, 329, 897
Iben, I., Jr., & Tutukov, A. V. 1984, ApJS, 54, 335
Iglesias, C. A., & Rogers, F. J. 1996, ApJ, 464, 943
Irrgang, A., Geier, S., Kreuzer, S., et al. 2020, A&A, 633, L5
Ishii, M., Ueno, M., & Kato, M. 1999, PASJ, 51, 417
Izzard, R. G., Ramirez-Ruiz, E., & Tout, C. A. 2004, MNRAS, 348, 1215
Janka, H.-T. 2013, MNRAS, 434, 1355
Jiang, Y.-F., Cantiello, M., & Bildsten, L. 2015, ApJ, 813, 74
Karpov, S. V., & Lipunov, V. M. 2001, Astron. Lett., 27, 645
Khokhlov, S. A., Miroshnichenko, A. S., Zharikov, S. V., et al. 2018, ApJ, 856, 158
King, A. R., Taam, R. E., & Begelman, M. C. 2000, ApJ, 530, L25
Klencki, J., Nelemans, G., Istrate, A., & Pols, O. R. 2020, A&A, in press https://doi.org/10.1051/0004-6361/202037694
Knigge, C., Coe, M. J., & Podsiadlowski, P. 2011, Nature, 479, 372
Kobulnicky, H. A., Kiminki, D. C., Lundquist, M., et al. 2014, ApJS, 213, 34
Köhler, K., Langer, N., de Koter, A., et al. 2015, A&A, 573, A71
Kruckow, M. U., Tauris, T. M., Langer, N., et al. 2016, A&A, 596, A58
Kruckow, M. U., Tauris, T. M., Langer, N., Kramer, M., & Izzard, R. G. 2018, MNRAS, 481, 1908
Kulkarni, S. R., Hut, P., & McMillan, S. 1993, Nature, 364, 421
Langer, N. 1991, A&A, 252, 669
Langer, N. 1992, A&A, 265, L17
Langer, N. 1998, A&A, 329, 551
Langer, N. 2012, ARA&A, 50, 107
Langer, N., Wellstein, S., & Petrovic, J. 2003, IAU Symp., 212, 275
Lennon, D. J., Lee, J.-K., Dufton, P. L., & Ryans, R. S. I. 2005, A&A, 438, 265
Lipunov, V. M., & Pruzhinskaya, M. V. 2014, MNRAS, 440, 1193
Liu, J., Zhang, H., Howard, A. W., et al. 2019, Nature, 575, 618
Mac Low, M.-M., & Klessen, R. 2004, Rev. Mod. Phys., 76, 125
Maeder, A. 1987, A&A, 178, 159
Mahy, L., Sana, H., Abdul-Masih, M., et al. 2020, A&A, 634, A118
Mandel, I., & de Mink, S. E. 2016, MNRAS, 458, 2634
Marchant, P. 2016, PhD Thesis, Bonn University, Germany
Marchant, P., Langer, N., Podsiadlowski, P., Tauris, T., & Moriya, T. 2016, A&A, 588, A50
Marchant, P., Langer, N., Podsiadlowski, P., et al. 2017, A&A, 604, A55
Mashian, N., & Loeb, A. 2017, MNRAS, 470, 2611
Masuda, K., & Hotokezaka, K. 2019, ApJ, 883, 169

McClintock, J. E., & Remillard, R. A. 2006, in Compact Stellar X-ray Sources, eds. W. H. G. Lewin, & M. van der Klis (Cambridge, UK: Cambridge University Press), Camb. Astrophys. Ser., 39, 157
Milone, A. P., Marino, A. F., Di Criscienzo, M., et al. 2018, MNRAS, 477, 2640
Mirabel, I. F. 2017, IAU Symp., 324, 303
Metzger, B. D., Berger, E., & Margalit, B. 2017, ApJ, 841, 14
Moe, M., & Di Stefano, R. 2017, ApJS, 230, 15
Müller, B., Heger, A., Liptai, D., & Cameron, J. B. 2016, MNRAS, 460, 742
Napiwotzki, R., Karl, C. A., Lisker, T., et al. 2020, A&A, in press, https://doi.org/10.1051/0004-6361/201629648
Narayan, R., & McClintock, J. E. 2008, New Astron. Rev., 51, 733
Nelson, C. A., & Eggleton, P. P. 2001, ApJ, 552, 664
Neugent, K. F., Massey, P., & Morrell, N. 2018, ApJ, 863, 181
Nishikawa, H., Kovetz, E. D., Kamionkowski, M., & Silk, J. 2019, Phys. Rev. D, 99, d3533
O'Connor, E., & Ott, C. D. 2011, ApJ, 730, 70
Orosz, J. A., McClintock, J. E., Narayan, R., et al. 2007, Nature, 449, 872
Orosz, J. A., McClintock, J. E., Aufdenberg, J. P., et al. 2011, ApJ, 742, 84
O'Shaughnessy, R., Kim, C., Kalogera, V., & Belczynski, K. 2008, ApJ, 672, 479
Packet, W. 1981, A&A, 102, 17
Pavlovski, K., Southworth, J., & Tamajo, E. 2018, MNRAS, 481, 3129
Paxton, B., Marchant, P., Schwab, J., et al. 2015, ApJS, 220, 15
Petrovic, J., Langer, N., & van der Hucht, K. A. 2005, A&A, 435, 1013
Petrovic, J., Pols, O., & Langer, N. 2006, A&A, 450, 219
Podsiadlowski, P., Joss, P. C., & Hsu, J. J. L. 1992, ApJ, 391, 246
Qin, Y., Marchant, P., Fragos, T., Meynet, G., & Kalogera, V. 2019, ApJ, 870, L18
Quast, M., Langer, N., & Tauris, T. M. 2019, A&A, 628, A19
Quimby, R. M., Kulkarni, S. R., Kasliwal, M. M., et al. 2011, Nature, 474, 487
Ramirez-Agudelo, O. H., Simon-Diaz, S., Sana, H., et al. 2013, A&A, 560, A29
Reig, P. 2011, Ap&SS, 332, 1
Renzo, M., Ott, C. D., Shore, S. N., & de Mink, S. E. 2017, A&A, 603, A118
Renzo, M., Zapartas, E., de Mink, S. E., et al. 2019, A&A, 624, A66
Repetto, S., & Nelemans, G. 2015, MNRAS, 453, 3341
Repetto, S., Igoshev, A. P., & Nelemans, G. 2017, MNRAS, 467, 298
Ritchie, B. W., Stroud, V. E., Evans, C. J., et al. 2012, A&A, 537, A29
Ro, S. 2019, ApJ, 873, 76
Robitaille, T. P., & Whitney, B. A. 2010, ApJ, 710, L11
Salpeter, E. E. 1955, ApJ, 121, 161
Samsing, J., & D'Orazio, D. J. 2018, MNRAS, 481, 5445
Sana, H., de Mink, S. E., de Koter, A., et al. 2012, Science, 337, 444
Sana, H., de Koter, A., de Mink, S. E., et al. 2013, A&A, 550, A107
Sana, H., Le Bouquin, J.-B., Lacour, S., et al. 2014, ApJS, 215, 15
Sander, A. A. C., Hamann, W.-R., Todt, H., et al. 2019, A&A, 621, A92
Sander, A. A. C., Vink, J. S., & Hamann, W.-R. 2020, MNRAS, 491, 4406
Sanyal, D., Grassitelli, L., Langer, N., et al. 2015, A&A, 580, A20
Sanyal, D., Langer, N., Szécsi, D., et al. 2017, A&A, 597, A71
Schneider, F. R. N., Izzard, R. G., de Mink, S. E., et al. 2014, ApJ, 780, 117
Schneider, F. R. N., Sana, H., Evans, C. J., et al. 2018, Science, 359, 69
Schootemeijer, A., Langer, N., Grin, N. J., & Wang, C. 2019, A&A, 625, A132
Shakura, N. I., & Sunyaev, R. A. 1973, A&A, 24, 337
Shao, Y., & Li, X.-D. 2014, ApJ, 796, 37
Shao, Y., & Li, X.-D. 2019, ApJ, 885, 151
Shenar, T., Sablowski, D. P., Hainich, R., et al. 2019, A&A, 627, A151
Shenar, T., Gilkis, A., Vink, J. S., Sana, H., & Sander, A. A. C. 2020, A&A, 634, A79
Sigurdsson, S., & Hernquist, L. 1993, Nature, 364, 423
Simon-Diaz, S., Maiz Apellaniz, J., Lennon, D. J., et al. 2020, A&A, 634, L7
Smith, N., Vink, J. S., & de Koter, A. 2004, ApJ, 615, 475
Smartt, S. J. 2009, ARA&A, 47, 63
Spera, M., Mapelli, M., Giacobbo, N., et al. 2019, MNRAS, 485, 889
Stanway, E. R., & Eldridge, J. J. 2019, A&A, 621, A105
Stevenson, S., Vigna-Gomez, A., Mandel, I., et al. 2017, NatCo, 8, 14906
Stovall, K., Freire, P. C. C., Chatterjee, S., et al. 2018, ApJ, 854, L22
Sukhbold, T., Woosley, S. E., & Heger, A. 2018, ApJ, 860, 22
Tauris, T. M., & van den Heuvel, E. P. J. 2006, in Formation and Evolution of Compact Stellar X-ray Sources, eds. W. H. G. Lewin, & M. van der Klis (Cambridge: Cambridge Univ. Press), 623
Tauris, T. M., Kramer, M., Freire, P. C. C., et al. 2017, ApJ, 846, 170
Toonen, S., Perets, H. B., Igoshev, A., et al. 2018, A&A, 619, A53
Torres, G., Andersen, J., & Giménez, A. 2010, A&ARv, 18, 67
Ugliano, M., Janka, H.-T., Marek, A., & Arcones, A. 2012, ApJ, 757, 69
Valsecchi, F., Glebbeek, E., Farr, W. M., et al. 2010, Nature, 468, 77
Van Bever, J., & Vanbeveren, D. 1997, A&A, 322, 116
Van Bever, J., & Vanbeveren, D. 2000, A&A, 358, 462
Vanbeveren, D., Mennekens, N., & De Greve, J. P. 2012, A&A, 543, A4
Vigna-Gomez, A., Neijssel, C. J., Stevenson, S., et al. 2018, MNRAS, 481, 4009
Voss, R., & Tauris, T. M. 2003, MNRAS, 342, 1169
Walter, R., Lutovinov, A. A., Bozzo, E., & Tsygankov, S. S. 2015, A&ARv, 23, 2
Wang, C., Jia, K., & Li, X.-D. 2016, MNRAS, 457, 1015
Wang, C., Langer, N., Schootemeijer, A., et al. 2020, ApJ, 888, L12
Webbink, R. F. 1984, ApJ, 277, 355
Wellstein, S., & Langer, N. 1999, A&A, 350, 148
Wellstein, S., Langer, N., & Braun, H. 2001, A&A, 369, 939
Woosley, S. E. 2019, ApJ, 878, 49
Yalinewich, A., Beniamini, P., Hotokezaka, K., & Zhu, W. 2018, MNRAS, 481, 930
Yamaguchi, M. S., Kawanaka, N., Bulik, T., & Piran, T. 2018, ApJ, 861, 21
Yi, T., Sun, M., & Gu, W.-M. 2019, ApJ, 886, 97
Yoon, S.-C., & Langer, N. 2005, A&A, 443, 643
Yoon, S.-C., Woosley, S. E., & Langer, N. 2010, ApJ, 725, 940
Zucker, S., Mazeh, T., & Alexander, T. 2007, ApJ, 670, 1326

[1] Argelander-Institut für Astronomie, Universität Bonn, Auf dem Hügel 71, 53121 Bonn, Germany
e-mail: nlanger@astro.uni-bonn.de
[2] Max-Planck-Institut für Radioastronomie, Auf dem Hügel 69, 53121 Bonn, Germany
[3] Institute of Astrophysics, KU Leuven, Celestijnenlaan 200D, 3001 Leuven, Belgium
[4] Center for Interdisciplinary Exploration and Research in Astrophysics (CIERA) and Department of Physics and Astronomy, Northwestern University, 2145 Sheridan Road, Evanston, IL 60208, USA
[5] Instituto de Astrofisica de Canarias, 38200 La Laguna, Tenerife, Spain
[6] Departamento de Astrofisica, Universidad de La Laguna, 38205 La Laguna, Tenerife, Spain
[7] Center for Astrophysics, Harvard-Smithsonian, 60 Garden Street, Cambridge, MA 02138, USA
[8] Anton Pannenkoek Institute for Astronomy, University of Amsterdam, 1090 GE Amsterdam, The Netherlands
[9] Departamento de Física, Universidade do Estado do Rio Grande do Norte, Mossoró, RN, Brazil
[10] Departamento de Física, Universidade Federal do Rio Grande do Norte, UFRN, CP 1641, Natal, RN 59072-970, Brazil
[11] Department of Physics and Astronomy, Hicks Building, Hounsfield Road, University of Sheffield, Sheffield S3 7RH, UK
[12] AIP Potsdam, An der Sternwarte 16, 14482 Potsdam, Germany
[13] School of Physical Sciences, The Open University, Walton Hall, Milton Keynes MK7 6AA, UK
[14] Astrophysics Research Centre, School of Mathematics and Physics, Queen's University Belfast, Belfast BT7 1NN, UK
[15] UK Astronomy Technology Centre, Royal Observatory Edinburgh, Blackford Hill, Edinburgh, EH9 3HJ, UK
[16] Space Research Institute, Austrian Academy of Sciences, Schmiedlstrasse 6, 8042 Graz, Austria
[17] Universidad de La Laguna, Dpto. Astrofisica, 38206 La Laguna, Tenerife, Spain
[18] LMU Munich, Universitätssternwarte, Scheinerstrasse 1, 81679 München, Germany
[19] Center for Computational Astrophysics, Flatiron Institute, New York, NY 10010, USA
[20] Armagh Observatory, College Hill, Armagh BT61 9DG, UK
[21] Zentrum für Astronomie der Universität Heidelberg, Astronomisches Rechen-Institut, Mönchhofstr. 12-14, 69120 Heidelberg, Germany
[22] Heidelberger Institut für Theoretische Studien, Schloss-Wolfsbrunnenweg 35, 69118 Heidelberg, Germany
[23] Aarhus Institute of Advanced Studies (AIAS), Aarhus University, Hoegh-Guldbergs Gade 6B, 8000 Aarhus C, Denmark
[24] Department of Physics and Astronomy, Aarhus University, Ny Munkegade 120, 8000 Aarhus C, Denmark
[25] IAASARS, National Observatory of Athens, Vas. Pavlou and I. Metaxa, Penteli 15236, Greece

Appendix A: Self-lensing of OB+BH binaries

The presence of a BH can potentially be verified by gravitational-lensing magnification. When the OB star is sufficiently well aligned behind the sightline form observer to BH, the BH can cause a magnification on the stellar flux (Masuda & Hotokezaka 2019; D'Orazio & di Stefano 2020). This lensing magnification would be detected as a symmetric peak in the light curve of the OB star once per orbit. The maximum magnification is obtained when star, BH, and observer are perfectly aligned, and for a star of radius R_* with uniform surface brightness, its value is $\mu_{\rm max} = \rho^{-1}\sqrt{4+\rho^2}$, where $\rho = R_{\rm OB}/R_{\rm E}$ is the ratio of stellar radius and Einstein radius. Because the distance of the binary system is much larger than the orbital radius a of the binary, the Einstein radius for a BH of mass $M_{\rm BH}$ is

$$R_{\rm E} \approx \sqrt{\frac{4GM_{\rm BH}}{c^2}\,a} \approx 7.7\times10^{9}\,{\rm cm}\left(\frac{M_{\rm BH}}{10\,M_\odot}\right)^{1/2}\left(\frac{a}{10^{13}\,{\rm cm}}\right)^{1/2}.$$

Therefore, the dimensionless stellar radius ρ becomes

$$\rho \approx 65\left(\frac{R_{\rm OB}}{5\times10^{11}\,{\rm cm}}\right)\left(\frac{M_{\rm BH}}{10\,M_\odot}\right)^{-1/2}\left(\frac{a}{10^{13}\,{\rm cm}}\right)^{-1/2},$$

and is thus $\gg$1. We can therefore expand the maximum magnification to yield a maximum brightening of the star by

$$|\Delta m|_{\rm max} = 1.086\,\ln\mu_{\rm max} \approx \frac{2.17}{\rho^2}$$
$$\approx 5.2\times10^{-4}\left(\frac{R_{\rm OB}}{5\times10^{11}\,{\rm cm}}\right)^{-2}\left(\frac{M_{\rm BH}}{10\,M_\odot}\right)\left(\frac{a}{10^{13}\,{\rm cm}}\right). \quad \text{(A.1)}$$

Thus, the maximum brightness increase of the star is about one milli-magnitude for the fiducial parameters, and scales linearly with the orbital radius and BH mass. The magnification decreases with the misalignment of star, BH, and observer, such that it drops to about half the value given in Eq. (A.1) when the star is misaligned by approximately its own radius. Requiring that the star passes behind the BH with a misalignment not larger than its own radius places a constraint on the inclination angle i of the orbital plane of the binary, $\sin(i) \lesssim R_*/a$, or

$$i \lesssim 2.85\,{\rm deg}\left(\frac{R_{\rm OB}}{5\times10^{11}\,{\rm cm}}\right)\left(\frac{a}{10^{13}\,{\rm cm}}\right)^{-1}.$$

This means that the orbital plane needs to be well aligned with the sightline to the binary system in order to yield a brightening higher than $\sim 0.5|\Delta m|_{\rm max}$.

The prospects for observing lensing magnification in such binary systems depends sensitively on the photometric accuracy with which the light curve can be recorded. The lensing nature of the magnification peaks can be further verified by spectroscopic studies: because the OB star is predicted to rotate rapidly, the shape of spectral lines will change during the magnification event because stellar surface regions with approaching and receding (rotational) velocity will be magnified consecutively. We therefore expect to see a characteristic time variability of spectral shapes during the magnification event. Verifying a lensing event places a strong constraint on the object causing the lensing: it has to be smaller than the Einstein radius.

Appendix B: Outcome of the binary models for four additional primary masses

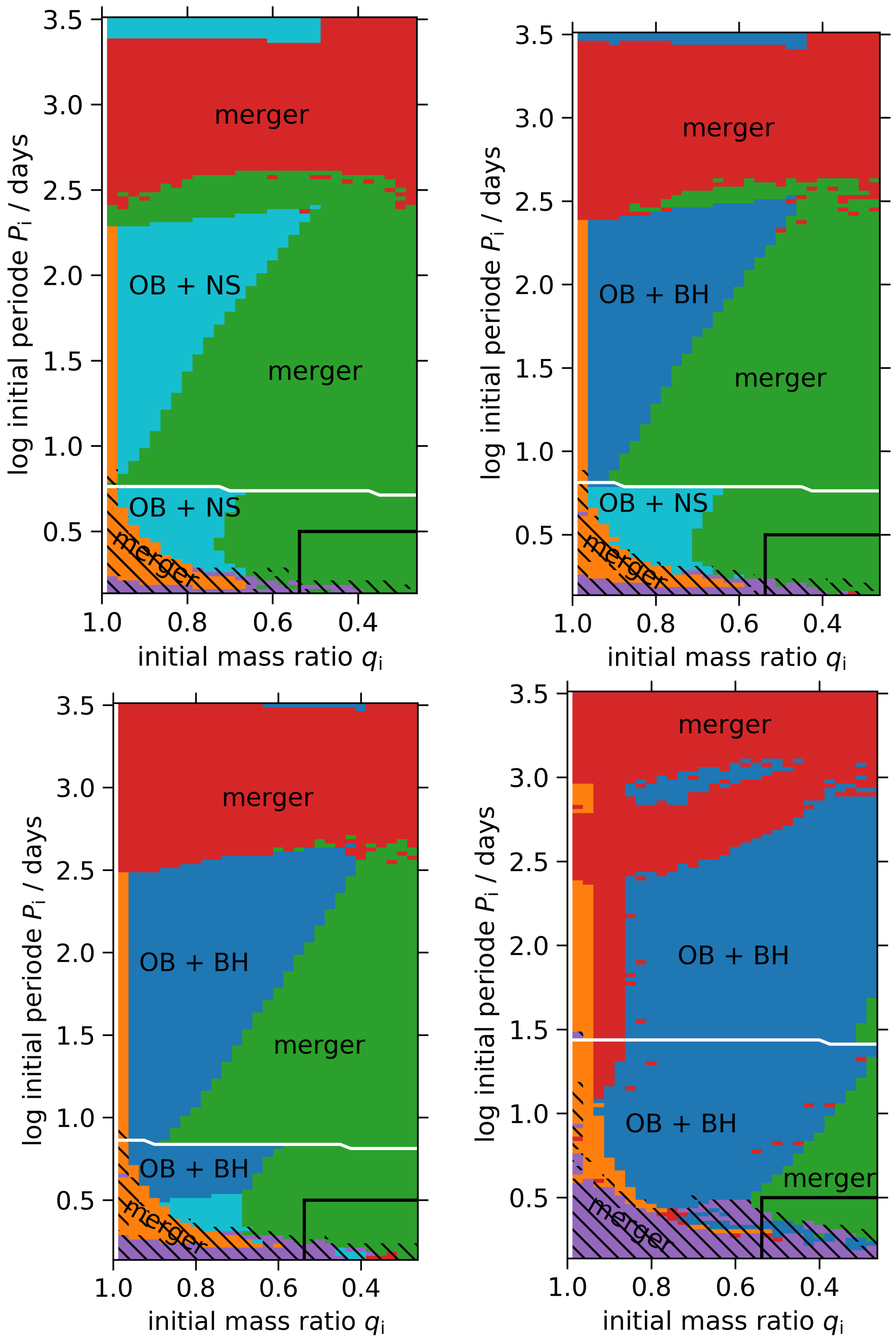

Fig. B.1. As Fig. 2, but for initial primary masses of 15.85 $M_\odot$ (*top left*), 17.78 $M_\odot$ (*top right*), 19.95 $M_\odot$ (*bottom left*), and 39.81 $M_\odot$ (*bottom right*). The colour-coding indicates fates as in Fig. 2 (purple: L2-overflow, yellow: inverse mass transfer, green: mass-loss limit violation, and red: common-envelope evolution; all assumed to lead to a merger). Black hatching marks contact evolution, and the dark blue systems evolve to the OB+BH stage. Here, light blue marks systems where the mass donor is assumed to form a NS rather than a BH. The white line separates Case A and Case B evolution, and the area framed by the black line in the lower right corner marks the part of the parameter space that is disregarded in our results (see Sect. 2).

APPENDIX B

Appendix to Chapter 3

Here we reproduce the puplication Schürmann et al. (2022).

A&A 667, A122 (2022)
https://doi.org/10.1051/0004-6361/202244153
© C. Schürmann et al. 2022

Astronomy & Astrophysics

The spins of stripped B stars support magnetic internal angular momentum transport

C. Schürmann[1,2], N. Langer[2,1], X. Xu[1,2], and C. Wang[2,3]

[1] Max-Planck-Institut für Radioastronomie, Auf dem Hügel 69, 53121 Bonn, Germany
[2] Argelander-Institut für Astronomie, Universität Bonn, Auf dem Hügel 71, 53121 Bonn, Germany
e-mail: chr-schuermann@uni-bonn.de
[3] Max-Planck-Institut für Astrophysik, Karl-Schwarzschild-Str. 1, 85748 Garching, Germany

Received 31 May 2022 / Accepted 3 August 2022

ABSTRACT

In order to predict the spins of stellar remnants we need to understand the evolution of the internal rotation of stars, and to identify at which stage the rotation of the contracting cores of evolved stars decouples from their expanding envelopes. The donor stars of mass transferring binaries lose almost their entire envelope and may thus offer a direct view on their core rotation. After the mass transfer event they contract and fade rapidly, although they are well observable when caught in the short-lived B-star phase. The B-type primary of the galactic binary system LB-1, which was originally suggested to contain a massive black hole, is nicely explained as a stripped star accompanied by a fainter Be star. The narrow absorption lines in the primary's spectrum signify extremely slow rotation, atypical of B-type main-sequence stars. Here we investigate the evolution of mass donors in generic grids of detailed binary evolution models, where both stars include differential rotation, internal angular momentum transport, and spin-orbit coupling. Whereas the mass gainers are typically spun-up during the mass transfer, we find that the spins of the stripped donor models depend sensitively on the employed mechanism for internal angular momentum transport. Purely hydrodynamic transport cannot explain the observed slow rotation, while models including magnetic angular momentum transport are able to reproduce the observed rotation of LB-1 and similar stars, independent of the initial rotation rate. In such models the spin of the white dwarfs that emerge at the end of the evolution is independent of the mass stripping. We find evidence that the mass transfer in LB-1 was moderately non-conservative.

Key words. stars: evolution – stars: rotation – stars: magnetic field – stars: emission-line, Be – binaries: close – subdwarfs

1. Introduction

It is well known that upper main-sequence stars are often rapid rotators. For a long time stellar rotation was considered a second-order effect, but it turned out, most notably in O- and B-type stars, that it can strongly affect their evolution. While it may be at the core of observed phenomena such as gamma-ray bursts or luminous blue variables, numerical simulations still struggle to yield a convincing overall picture (Maeder & Meynet 2000; Langer 2012, and references therein).

Rotation may be faster in stars with companions (de Mink et al. 2013). In a binary system, the two stars can interchange material and thus angular momentum. Furthermore, tidal forces, which grow with the stars' Roche-lobe filling-factors (Zahn 1977), act on both of them. The internal rotational structure does not need to be uniform, but it may depend on the radial coordinate (Spiegel & Zahn 1992; Zahn 1992). Such a differential rotation is counteracted by turbulent viscosity (Heger et al. 2000) and magnetic fields (Spruit 2002), forcing a star close to rigid rotation (Maeder & Meynet 2004). Unfortunately these processes are hidden under the stellar surface. A direct look at the stellar core would be illuminating. In this context, stripped stars are of great interest as they provide the desired opportunity to look deep inside the stellar structure.

Recently, Liu et al. (2019) proposed that the galactic B-type binary LB-1 contains a 70 $M_\odot$ black hole (BH). They found an antiphase radial velocity variation of the thin absorption lines and the Hα emission lines in the composite spectrum. This, together with a typical mass for the early B-type star is the basis for the mass estimate, as the Hα emission was assumed to originate from the vicinity of the BH. This observation caused great interest in the community since such a massive BH was not expected to be able to form in a high metallicity environment (e.g. Heger & Woosley 2002; Kruckow et al. 2018; Belczynski 2020). Irrgang et al. (2020) examined the stellar absorption lines and found the B-type star to be a stripped helium star leading to a smaller BH mass or even just a neutron star. In contrast, Simón-Díaz et al. (2020) classified it as a slightly evolved main-sequence star with solar surface helium abundance. Both studies found an enrichment in CNO processed material. However a systematic mismatch between the observed line profiles and fits remained.

El-Badry & Quataert (2020) and Abdul-Masih et al. (2020) state that the movement of the Hα emission line may not be real, but an effect of combining a stationary Hα line with a varying Hα absorption yielding an apparent movement of the combined line in antiphase with the absorption feature. According to El-Badry & Quataert (2020) the unseen companion is a stellar mass BH and the Hα emission is caused by a circumbinary disc. However, the observations of Liu et al. (2020) out-ruled such a disc in the system.

A convincing overall picture was achieved by Shenar et al. (2020), who analysed the system by spectral disentangling. The authors were able to identify two stellar components, one narrow-lined helium-enriched star and one rapidly rotating star, whose absorption lines are very broad and difficult to spot. This

Open Access article, published by EDP Sciences, under the terms of the Creative Commons Attribution License (https://creativecommons.org/licenses/by/4.0), which permits unrestricted use, distribution, and reproduction in any medium, provided the original work is properly cited.
This article is published in open access under the Subscribe-to-Open model. Open access funding provided by Max Planck Society.

second star is also the source of the Hα emission as it is identified as a Be star. The helium-rich star was found to be CNO-enriched, suggesting that it was the mass donor in a Roche-lobe overflow (RLO), in which the emission line star received mass and angular momentum, transforming it into a Be star (Waters et al. 1989; Wang et al. 2020; Langer et al. 2020a). As the stripped B-type star (Bstr) has a temperature and surface gravity of a slightly evolved main-sequence star, it seems likely that the RLO happened quite recently and that the stripped star is contracting towards a φ Per-like OB subdwarf (sdOB) in orbit with a Be star. Lennon et al. (2021) tested this model and the original one (B+BH, Liu et al. 2019) with a Hubble UV-visual-IR spectrum and found that neither could reproduce all the observed properties.

The LB-1 system is apparently not the only one of its kind. Bodensteiner et al. (2020b) re-analysed the apparent (B+BH)+Be-system HR 6819 first examined by Rivinius et al. (2020) and found it to consist of a stripped B star and a Be star. El-Badry & Quataert (2021) came to the same result. Eldridge et al. (2020), Bodensteiner et al. (2020b), and El-Badry & Quataert (2021) provide numerical evolutionary models for LB-1 and HR 6819. According to El-Badry & Burdge (2022), NGC 1850 BH1 found by Saracino et al. (2022) is also a Bstr+Be system.

For this study, we adopt the Be+Bstr model for LB-1. We employ this model to examine the aforementioned processes influencing stellar rotation since the low mass of their envelope is very sensitive to core-envelope-coupling. As LB-1 (and HR 6819) is likely in a short-lived phase, a post-RLO contraction, the coupling could not have reached an equilibrium yet, which makes it a valuable target. Thus, the objectives of this study are first to identify a numerical model describing the stripped star of LB-1 and if possible the system as a whole, and second to use the predicted and observed rotational velocity to draw conclusions about the angular momentum transport mechanisms in the stellar interior.

In Sect. 2 of this paper we summarise the observed properties of LB-1 and place this kind of system into the context of binary stellar evolution. In Sect. 3 we present our numerical method, and in Sect. 4 present its results, the progenitor model of LB-1, and its rotational evolution. Finally, in Sect. 5, we discuss similar systems, earlier work, and the orbital evolution. We draw our conclusions in Sect. 6.

2. Empirical properties of Be stars with stripped companions

We summarise in Table 1 the empirical properties of the LB-1 system and the atmospheric properties of the stripped star according to the two studies discussing the Be+Bstr scenario. For our following analysis we adopt a surface temperature of 12 500 K and a surface gravity of 3.0. It is also clear that the stripped star's surface is enriched with helium and CNO-products. Shenar et al. (2020) and Lennon et al. (2021) report $Y \approx 0.45$, while Hawcroft & Shenar (priv. comm.) find $Y \approx 0.55$. Two studies (Irrgang et al. 2020; Simón-Díaz et al. 2020) assuming the B+BH model prefer $Y \approx 0.65$ and $Y \approx 0.29$ (i.e. solar), respectively. The scatter in the proposed helium abundances is quite large. We give a higher weight to the Be+Bstr models and use an interval of $Y \in [0.4, 0.6]$ for our study. For the relative abundance of nitrogen and carbon we adopt $2.0 < [\mathrm{N/C}] < 2.5$. Furthermore we assume a projected equatorial rotational velocity of the stripped star of $7 \pm 2\,\mathrm{km\,s^{-1}}$.

Table 1. Orbital and atmospheric properties of the stripped star in LB-1 according to Shenar et al. (2020) and Lennon et al. (2021) in the Be+Bstr scenario.

	Shenar et al. (2020)	Lennon et al. (2021)
$P_{\mathrm{orb}}/\mathrm{d}$	78.7999 ± 0.0097	–
q	4.7 ± 0.4	–
$M_{\mathrm{tot}} \sin^3 i/M_\odot$	2.16 ± 0.05	–
$T_{\mathrm{eff}}/\mathrm{K}$	$12\,700 \pm 2000$	$12\,500 \pm 100$
$\log g/\mathrm{cm\,s^{-2}}$	3.0 ± 0.2	3.0 ± 0.2
$v_{\mathrm{rot}} \sin i/\mathrm{km\,s^{-1}}$	7 ± 2	7
$n_{\mathrm{He}}/n_{\mathrm{H}}$	0.21 [(a)]	0.2
$\log(L/M/L_\odot/M_\odot)$	2.81 ± 0.34	2.80 ± 0.21
Y_{surface}	0.46 [(a)]	0.44 ± 0.12
[N/C]	>0 [(b)]	2.25 ± 0.21 [(c)]

Notes. The last three lines were calculated by us. [(a)]Hawcroft & Shenar (priv. comm.) find $n_{\mathrm{He}}/n_{\mathrm{H}} = 0.31 \pm 0.05 \Leftrightarrow Y = 0.55 \pm 0.04$. [(b)]Hawcroft & Shenar (priv. comm.) find $[\mathrm{N/C}] = 2.24 \pm 0.38$. [(c)]Estimated from their Table 3.

A similar synopsis could be made for HR 6819 (Rivinius et al. 2020; Bodensteiner et al. 2020b; El-Badry & Quataert 2021), but unfortunately only an upper limit for the rotation of the stripped star is known ($v_{\mathrm{rot}} \sin i < 20\,\mathrm{km\,s^{-1}}$, El-Badry & Quataert 2021), which is not precise enough for the analysis presented below. For NGC 1850 BH1 these measurements are not published.

LB-1, HR 6819, and NGC 1850 BH1 may be the first members of a new family of B-type stars, and Be stars in particular. To date, only a small fraction of Be stars are known to have a companion (Langer et al. 2020a) even though binary interaction is a proposed formation channel (e.g. Pols et al. 1991; Wang et al. 2020). On the other hand, all known companions are post-interaction objects and no Be star with a main-sequence companion is know, although these stars should be easily detectable and a large number of B+B binaries are known (Bodensteiner et al. 2020a).

Most known Be star companions, besides neutron stars, are sdOB stars, of which Wang et al. (2018) list 16 detections and candidates. The most prominent member of this family is φ Per (e.g. Poeckert 1981; Gies et al. 1998; Schootemeijer et al. 2018). It is believed that these stars are the stripped cores of the mass donors that spun up the Be stars to high rotation. Be+Bstr systems such as LB-1 and HR 6819 may evolve into Be+sdOB systems (Shenar et al. 2020) as the donor star crosses the main sequence during its evolution from Roche-lobe filling to sdOB star. It is also possible, but less likely because the timescale is about ten times shorter (El-Badry & Quataert 2021), that LB-1 and HR 6819 are in the evolutionary stage after core helium exhaustion of the sdOB star, when it expands again due to shell helium burning to become a helium giant. Recently, El-Badry et al. (2022) proposed that HD 15124 is a Be star with a Roche-lobe filling companion, which will evolve first to a LB-1 like system and then to a sdOB+Be-system.

Although predicted by abundance (about 70%, Raguzova 2001), a white dwarf (WD) companion is proposed for only six Be stars (Kennea et al. 2021). Moving up the mass ladder, many Be stars with neutron stars are known as Be/X-ray binaries. Even one BH accompanying a Be star is observed (Casares et al. 2014). LB-1 and HR 6819 are likely the progenitors of the presumed Be+WD systems, as their stripped stars appear to have a mass of less than $1.5\,M_\odot$ (Shenar et al. 2020; Lennon et al. 2021; Bodensteiner et al. 2020b).

3. Method

The basis of our analysis is a large grid of detailed binary evolution models with the Small Magellanic Cloud (SMC) metallicity calculated by Wang et al. (2022), using MESA version 8845 (Paxton et al. 2011, 2013, 2015). Their initial zero age main sequence (ZAMS) equatorial velocity is set to 0.55 times the critical velocity, corresponding to the high velocity peak of the bimodal distribution of Dufton et al. (2013). The other initial binary properties were randomly drawn from empirical distributions (Monte Carlo method). Initial primary masses range from $3\,M_\odot$ to $100\,M_\odot$, mass ratios range from 1 to 0.1, and the initial orbital periods lie between initial contact and 3000 d.

We set the stellar physical parameters as follows. The overshooting is assumed to be mass dependent (Castro et al. 2014; Martinet et al. 2021). For $M < 1.25\,M_\odot$ we use $\alpha_{\rm ov} = 0$, for $1.25\,M_\odot < M < 1.7\,M_\odot$ we set $\alpha_{\rm ov} = 0.05$, and above $1.7\,M_\odot$ we follow Schootemeijer et al. (2019) by increasing $\alpha_{\rm ov}$ linearly from 0.1 at $1.7\,M_\odot$ to 0.3 at $20\,M_\odot$. Semiconvection is set to $\alpha_{\rm sc} = 10$, as suggested by Schootemeijer et al. (2019). In the case of mass transfer by stable RLO, we assume that the accretor gains mass until it reaches critical rotation (Petrovic et al. 2005a; Paxton et al. 2015). Then the transferred material is expelled with the accretor's orbital angular momentum. This leads to an accretion efficiency of less than 5% in systems where for the accretor (Langer et al. 2020b) tidal forces do not play a role (in general in RLOs after the donor has left the main sequence). Whether the mass transfer is stable and all the material that cannot be accreted is ejected successfully or the binary undergoes a common envelope phase and merges is decided by an energy criterion. If the combined luminosity of the two stars is large enough to unbind excess material from the system, we assume the RLO avoids a common envelope (Marchant 2018; Langer et al. 2020b).

If no external factors such as stellar wind, accretion, and tides act on the model, its total spin angular momentum is conserved. MESA treats rotation by assigning an angular velocity to each mass shell of the stellar model (Paxton et al. 2013). The angular velocity ω of each shell can change by two means according to

$$\frac{\partial\omega}{\partial t} = -\frac{\omega}{i}\frac{\partial i}{\partial t} + \frac{1}{i}\frac{\partial}{\partial m}\left((4\pi r^2\rho)^2 i\nu\frac{\partial\omega}{\partial m}\right). \tag{1}$$

The first term is the change in specific moment of inertia i. The second, the change in specific angular momentum of a shell, is described by a diffusion ansatz (Heger et al. 2000) parametrised by a viscosity ν, which serves as an effective description of all the physical processes involved in the coupling between the shells. The most important process is convection, which is assumed to impose rigid body rotation (Heger et al. 2000). Semiconvection and thermohaline mixing are also included, as well as atomic viscosity. Rotation itself induces a set of instabilities leading to angular momentum transport: the dynamical shear instability, the Solberg-Høiland instability, the secular shear instability, the Eddington-Sweet circulations, and the Goldstein-Schubert-Fricke instability (Heger et al. 2000). An important contribution to the viscosity is assumed to be due to magnetic fields in the form of the Spruit–Tayler mechanism (Spruit 2002; Heger et al. 2005). This magnetic viscosity depends on the −4th power of the Brunt–Väisälä frequency, which means that gradients in entropy or mean molecular weight reduce the magnetic viscosity.

We use our grid of SMC models to infer possible initial masses, initial mass ratios, and initial orbital periods of LB-1, as described in Sect. 4.1. However, the grid is not dense enough to contain a model that closely matches the inferred properties. Therefore, we ran additional models with our favoured regime of the initial binary properties. For these we chose solar metallicity since LB-1 is a Milky Way binary. We found the differences between the SMC and Milky Way stripped stellar models to be small. In order to characterise the impact of the initial rotation, and of the magnetic angular momentum transport, we calculated solar metallicity models without magnetic angular momentum transport, and models rotating at 0.2 times their critical rotation velocity at ZAMS. Additionally, we calculated a single-star model of the primary using our fiducial physics.

4. Results

In this section we present our findings based on the set of SMC binary models and on the recalculated models at Milky Way metallicity. First we identify possible progenitor models of LB-1 in Sect. 4.1, and continue a brief review of evolutionary stages with similar surface properties (Sect. 4.2). We then turn to the evolution of rotation and the transport of angular momentum in our solar metallicity model in Sect. 4.3. We discuss models with different initial rotations and without the Spruit–Tayler dynamo (Sect. 4.3.2), and we compare our binary result to that of a single star (Sect. 4.3.3). To round off we discuss predictions about systems similar to LB-1 (Sect. 4.4).

4.1. Progenitor models for LB-1

In order to identify the models in our model grid which most closely resemble LB-1 in the Be+Bstr scenario, we search for a contracting stripped stellar model in a binary system that underwent RLO without merging, with a mass donor with a temperature of about 12 500 K and a surface gravity of about 3.0 and which has not yet depleted central helium burning. The last criterion means that it is contracting towards the sdOB phase.

The typical evolution of such a system has been described in previous works, for example by Pols et al. (1991). We use our fiducial model, which we discuss in detail in Sect. 4.3.1, as an illustration (Fig. 1). Both stellar models start as main-sequence models, until the primary ends core hydrogen burning, ignites hydrogen shell-burning, and starts to expand rapidly. The evolution through the Hertzsprung-gap is halted by the finite size of its Roche lobe (Case B RLO, Kippenhahn & Weigert 1967). The model starts to lose its hydrogen-rich envelope, and the helium-enriched layers are exposed at its surface. The RLO ends before the helium core is completely revealed. The mass transfer phase ends with the ignition of the helium core-burning. After the end of RLO we obtain a stellar model, whose surface is helium- and nitrogen-enriched ($Y = 0.59$ and [N/C] = 2.47), but still contains hydrogen. The envelope contracts, which results in an increase in the model's surface temperature and the surface gravity. The shell source eventually turns off as the envelope is not heavy enough to supply the necessary pressure. This reduces the model's luminosity by almost one order of magnitude. The model settles down slightly to the right of the ZAMS of pure helium stars, where it can be identified as a sdOB star, and continues burning helium in its core. After central helium depletion it expands again, becoming a helium giant. A second RLO can occur, which increases the surface helium abundance further. Otherwise after RLO the surface helium abundance does

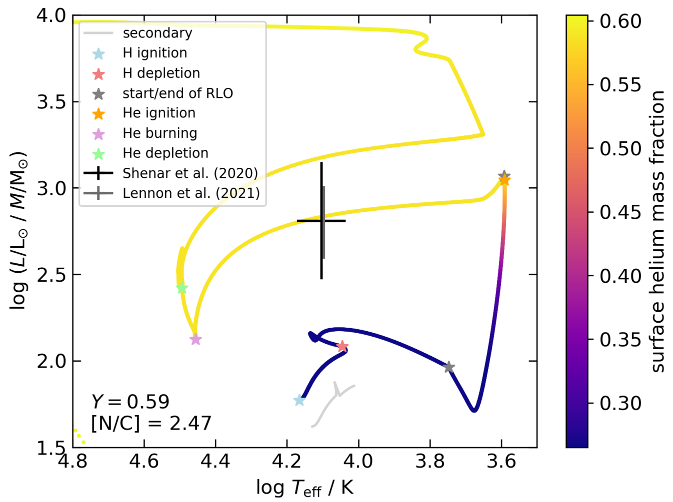

Fig. 1. Spectroscopic Hertzsprung-Russell diagram of a possible LB-1 progenitor. The helium abundance of the donor is indicated by colour. The mass gainer, which does not leave the main sequence as the binary model ends when the primary becomes a WD, is shown in grey. The ZAMS parameters are $M_1 = 4.0\,M_{\odot}$, $M_2 = 3.5\,M_{\odot}$, and $P_{\rm orb} = 16$ d. After the RLO the parameters were $M_1 = 0.7\,M_{\odot}$, $M_2 = 3.5\,M_{\odot}$, and $P_{\rm orb} = 223$ d. The surface abundances of the donor after RLO are shown in the lower left corner. The star symbols indicate Roche-lobe decoupling, helium ignition, middle of helium burning phase (sdOB observationally), and central helium depletion. The observations of Shenar et al. (2020) and Lennon et al. (2021) are shown in black and grey.

not change, as no process is present to dredge up material from the interior onto the surface. The model ends its life as a WD.

Our simulations also contain systems that undergo Case A RLO (RLO while the donor is burning hydrogen in its core, Kippenhahn & Weigert 1967). These systems are not considered in our analysis as their post-RLO orbits are too narrow ($\lesssim$10 d) to be of relevance for LB-1. We are aware that other studies consider Case A and discuss this aspect in Sect. 5.3.

We find that the state of the model at the end of a Case B RLO is very well defined. The initial mass determines the mass of the helium core and this fixes the luminosity of the hydrogen shell source, which is the dominant source of luminosity at the end of RLO and during the early phase of contraction. This causes the luminosity-to-mass ratio L/M to remain nearly constant for a wide range of surface temperatures, making it an ideal diagnostic tool as it can be determined from spectroscopic observations via $T_{\rm eff}$ and $\log g$. The tight correlation between initial mass, helium core mass, and luminosity of the mass donor immediately after RLO is shown in Fig. 2a, where we plot these quantities of all our models that survive Case B mass transfer. We only show models with initial masses up to 6.5 $M_{\odot}$ as higher masses turn out to be too bright to describe LB-1.

The mass of the stripped star model after RLO is not as strictly correlated to the initial mass as its helium core mass. This can be seen in Fig. 2b, where we show L/M instead of the luminosity L of the stripped model. The higher the mass after RLO, the lower the L/M, and the higher the (envelope) mass, the lower the surface helium abundance. The reason is that when the model loses more mass during RLO, the deeper layers and thus more helium-rich material is exposed.

As in the Bstr+Be-scenario of LB-1 the mass donor has a temperature of about 12 500 K, Fig. 2c shows the relation between the initial mass and the luminosity of the donor for the time when the models reached that temperature while contracting towards the sdOB phase. It demonstrates that the luminosity of the stripped star models decreased during this early phase of contraction and that this decrease depends on the surface helium abundance. We point out again that this abundance is a tracer of the mass of the envelope. As in horizontal branch stars, a more massive envelope causes the model to have a lower effective temperature than a model with a less massive envelope for the same conditions in the core. As we select the stellar models by surface temperature, we catch the stars with a more massive envelope at a later phase of contraction where the hydrogen shell is dimmer.

Therefore, if one evaluates the L/M of a stripped stellar model at a specified temperature (here 12 500 K), there are two effects adding scatter to its relation with the initial donor mass (Fig. 2d). Most of the models still lie on one sequence, but a notable fraction deviates towards a lower L/M. We also indicate the L/M value of LB-1 derived by Shenar et al. (2020) and Lennon et al. (2021). It intersects with the dominant sequence of the simulations just below an initial mass of 3 $M_{\odot}$, our lower mass limit. However, a notable fraction of our models lies within the error range allowing for initial primary masses of more than 5 $M_{\odot}$.

In Fig. 2d we flag all models that show a helium surface abundance within our adopted range. It yields a sequence of models parallel to the main feature that intersects with the most probable observed L/M value at an initial mass of around 4 $M_{\odot}$. These stripped models also have masses of about 1 $M_{\odot}$, in agreement with the mass estimates of Shenar et al. (2020) and Lennon et al. (2021). We therefore consider the most likely initial primary mass to be about 4 $M_{\odot}$. The initial secondary mass is therefore below this value. This is in agreement with the mass estimate of the Be star in the analysis of Lennon et al. (2021), who report $3.4^{+3.5}_{-1.8}$ $M_{\odot}$, and Shenar et al. (2020), who find a spectroscopic mass of 5 $M_{\odot}$, where both studies imply slightly different accretion efficiencies on the secondary. In any case, we found no strong dependencies of the accretor masses on the properties of the stripped models. We return to the accretion efficiency in Sect. 5.3, where we also discuss the implications for the orbital evolution of the system.

4.2. *Post-core-He-burning expansion phase and pre-WD phase*

So far we have focused on the contraction phase of the donor star immediately after the end of the RLO. However there are two other evolutionary stages during which the donor star may be observationally picked up in the B star regime. These are the expansion phase following core helium depletion, and the transition from the helium giant branch towards the WD phase, which may or may not be separated by a second RLO phase during helium shell-burning (Case BB, Savonije & Takens 1976; De Greve & De Loore 1976). In these two evolutionary stages, the stripped star's luminosity in our fiducial model (Fig. 1) exceeds the value it has during the contraction phase after the first RLO stage by about a factor of 2 and 10, respectively. On the other hand, the lifetime in the B star regime is shorter in these two stages, by factors of 3 and 160 compared to the post-RLO contraction phase. In a population study, certainly the first two of the considered stages should be taken into account, while the pre-WD evolutionary stage is less likely to be observed as it is very short. In this paper we focus on the first stage, since it has the largest observing probability (see also El-Badry & Quataert 2021) and, as we discuss below, for a given effective temperature in the B-type regime the rotational velocities in the

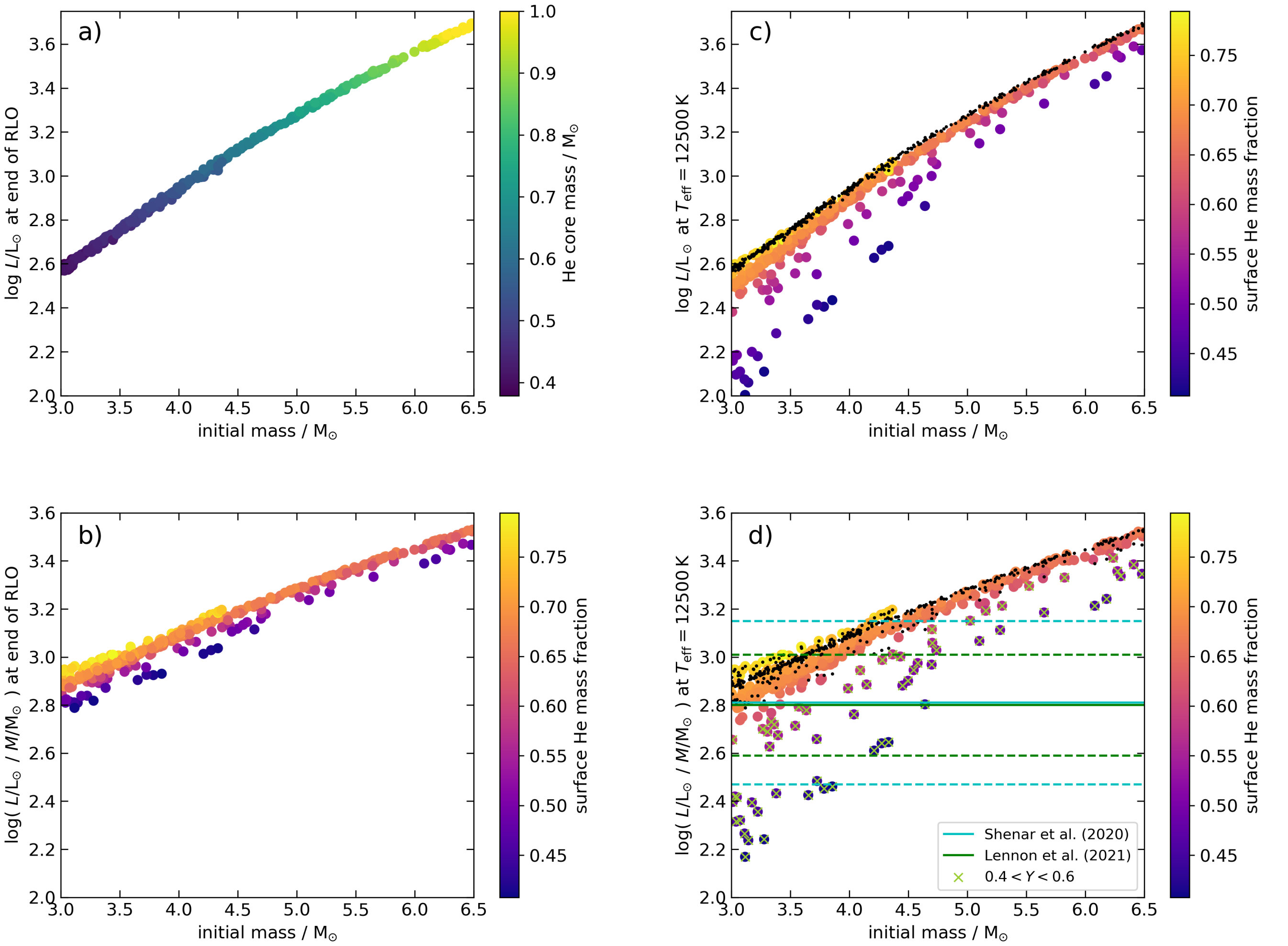

Fig. 2. Relation between the initial mass of our models and their luminosity or luminosity-to-mass ratio at selected evolutionary phases. (*a*) Luminosity and helium core mass of the mass donor immediately after the end of RLO as a function of the initial mass. All shown models underwent a Case B mass transfer. (*b*) Luminosity-to-mass ratio and surface helium mass fraction immediately after end of RLO as well as the initial masses of the models above. (*c*) Luminosity and surface helium mass fraction when the donor star surface temperature is 12 500 K during the contraction after RLO Case B as a function of initial mass. The black dots represent the state immediately after RLO (*panel a*). A few models have such a massive envelope that they never reach 12 500 K, and are not included. (*d*) Luminosity-to-mass ratio and surface helium mass fraction when the surface temperature is 12 500 K depending in the initial mass. The black dots represent the state at RLO end (*panel b*). The blue and green lines (almost superimposed) indicate the L/M from Shenar et al. (2020) and Lennon et al. (2021) with errors shown as dashed lines. Models with a surface helium abundance within the adopted range ([0.4, 0.6]) are indicated by green crosses.

first two crossings of the B-type regime are quite similar (see Sect. 4.3.1).

During the transition from the helium giant branch or a second (Case BB) mass transfer stage towards the WD phase, the stellar models are typically more than one order of magnitude more luminous than in the contraction phase after the first RLO. This means that if LB-1 was on such a path, its donor ZAMS masses would need to be much lower than 4 $M_\odot$, which in in disagreement with the empirical L/M ratio. We therefore consider it unlikely that LB-1 is in that stage.

4.3. Spin evolution

4.3.1. Our fiducial model

Since our model grid analysed in Sect. 4.1 was not dense enough for our purpose, we computed an additional model suitable for the analysis of LB-1 according to the findings above. Its initial parameters are ZAMS masses of 4 $M_\odot$ and 3.5 $M_\odot$, an initial orbital period of 16 d, and an initial equatorial rotational velocity of 0.6 times the critical velocity. The evolution of the mass donor in the Hertzprung–Russell diagram is shown in Fig. 1. The model's primary star matches the observed values of $T_{\rm eff}$, L/M, surface helium, and [N/C] as well as the mass ratio determined by Shenar et al. (2020). The final orbital period of 223 d is longer than the observed one. The final orbital period is not relevant for the stripped star's properties, and is discussed in Sect. 5.3.

The evolution from Roche-lobe decoupling to the subdwarf stage of this model takes several million years, with a strongly decelerating rate of change of temperature and luminosity. This means that the more a stripped star has contracted, the more likely it is to be observed. The subdwarf phase lasts about 20 million years. Therefore, it is not surprising that we know of almost two dozen systems with subdwarfs (Wang et al. 2018, 2021; Chojnowski et al. 2018), but only three (LB-1, HR 6819, and possibly NGC 1850 BH1) with stripped stars near the main sequence and none to the right of the main sequence.

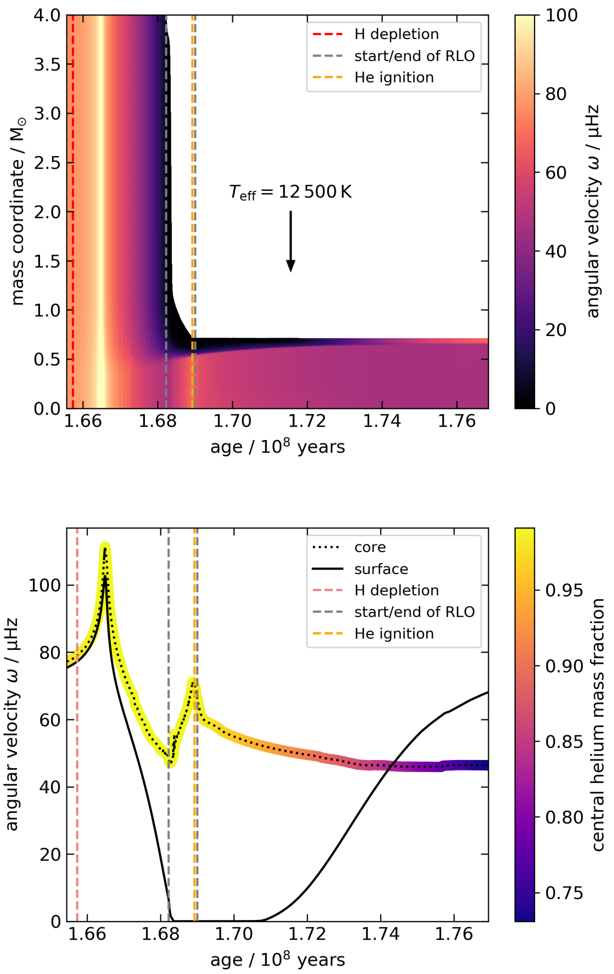

Fig. 3. Evolution of the rotation frequency of the mass donor of our fiducial model. *Top*: Kippenhahn-type diagram the model, showing the internal evolution of its rotational frequency (see colour bar at right) after TAMS. The arrow marks the time when $T_{\rm eff} = 12\,500$ K. *Bottom*: angular velocity of the model near its centre, colour-coded by the central helium mass fraction, and at the surface. The vertical dashed lines in both panels indicate certain evolutionary steps.

The evolution of the internal rotation of our fiducial mass donor is depicted in Fig. 3 (top). Until the end of core hydrogen burning, the model rotates close to a rigid body. At terminal age main sequence (TAMS), at an age of about 1.665×10^8 years, core and envelope have an angular velocity of roughly 100 μHz. Thereafter the envelope expands, the core contracts, and eventually their rotation rates grow apart. This can be seen in Fig. 3 (bottom) where we show the rotation frequency of the innermost mass shell and the surface of the model. The difference between the core and surface rotation rates increases with time indicating that the rotational coupling weakens. The surface slows down to a velocity of about 10^{-2} km s^{-1} due to tides and its growing moment of inertia and adjusts to the binary orbital frequency of about 0.2 nHz. On the other hand, the core halves its rotation rate due to the combined effect of the Spruit–Tayler dynamo, which decelerates the core, and contraction of the helium core, which accelerates it.

The rotation of core and envelope are decoupled at an age of 1.68×10^8 years; at this age the core is not slowing down, but rather is increasing due to contraction, its rotation rate uninhibited by the slowly rotating envelope. This time coincides with the age when the model fills its Roche lobe. The core rotation rate reaches a maximum at an age of about 1.69×10^8 years, which is when the RLO ends and helium core-burning is ignited. The end of the RLO and helium ignition take place nearly at the same time since helium ignition terminates the core contraction, and thus the envelope expands due to the mirror principle (Kippenhahn & Weigert 1967). Only a small fraction of the envelope remains at this time, which is still rotating at the same frequency as the orbit. What follows is the contraction of the envelope, speeding up its rotation. The rotation of the core does not change much more thereafter. Its mass grows as long as the hydrogen shell-burning is active, and thus low angular momentum material is incorporated into the core.

We have thus shown that during core hydrogen burning the star rotates close to a rigid body and that after central hydrogen exhaustion, the rotation rates of core and envelope decouple. This can be explained by the magnetic torque of the Spruit–Tayler dynamo. During hydrogen core-burning, the gradients of entropy and mean molecular weight are small enough to result in a high magnetic viscosity, which maintains core and envelope at the same rotation rate. This is not true any more after central hydrogen exhaustion, when the hydrogen shell-burning enlarges these gradients. This can be seen in Fig. 4, where we show the internal profiles of the effective viscosity and its contributions. A clear drop is visible at mass coordinates of ~$0.52\,M_\odot$ (top) and ~$0.61\,M_\odot$ (bottom). This drop in the magnetic viscosity makes the angular momentum transport between core and envelope so inefficient that they develop different rotation rates. Convection only plays a role in the helium-burning core and in the outer envelope during early contraction (orange lines in Fig. 4). The helium burning core and the radiative zone above, which together form the helium core, are strongly coupled as predicted by Maeder & Meynet (2014).

At an age of ~1.74×10^8 years the envelope starts to move more quickly than the core, leading to a positive angular velocity gradient in the early sdOB phase. This occurs due to the rapid contraction of the envelope after the end of RLO, from a convective expanded state to a radiative and more compact structure (Heger & Langer 1998). This feature demonstrates that core and envelope evolve independently, meaning that the evolution of the rotation rate of the envelope is not driven by the core, but rather by its own contraction. The $\partial\omega/\partial m$ term in Eq. (1) would not lead to a deviation from uniform rotation, which was nearly archived at an age of ~1.74×10^8 years. During the helium core- and shell-burning phases the core and envelope continue to rotate at different angular velocities. The rotation rates do not adjust since no angular momentum exchange between core and envelope takes place (i.e. they remain rotationally decoupled).

Figure 5 shows the evolution of the surface rotational velocity of our fiducial model from the end of RLO until the end of the contraction towards the sdOB state. In this phase the model's radius decreases, while the mass and angular momentum remain constant. As the star shrinks, the surface temperature, gravity, and rotational velocity increase. While the evolution of temperature and gravity can be simply explained by the change in radius assuming constant luminosity, the rotational evolution cannot, as indicated by the red lines arising from the main curve every one million years in Fig. 5. They reflect the evolution of the rotational velocity under the assumption that the specific angular momentum at the stellar surface is conserved, that is

$$v_{\rm rot} = R_0 v_{\rm rot,0} \sqrt{\frac{4\pi\sigma T_{\rm eff}^4}{L}}, \qquad (2)$$

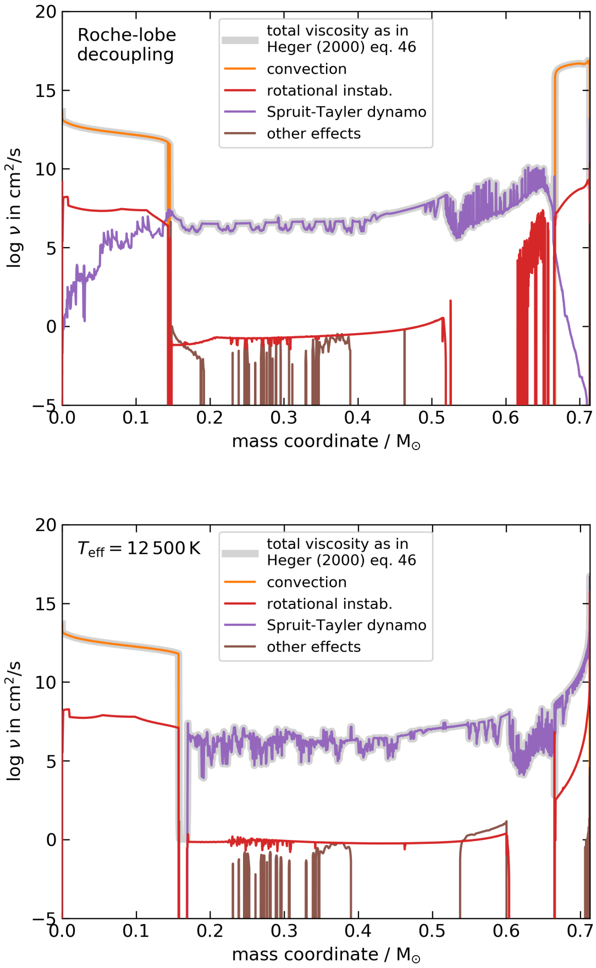

Fig. 4. Contributions to the viscosity ν for the angular momentum transport as a function of mass coordinate in our fiducial model, at the time of Roche-lobe decoupling (*top*) and when the effective temperature reached 12 500 K (*bottom*).

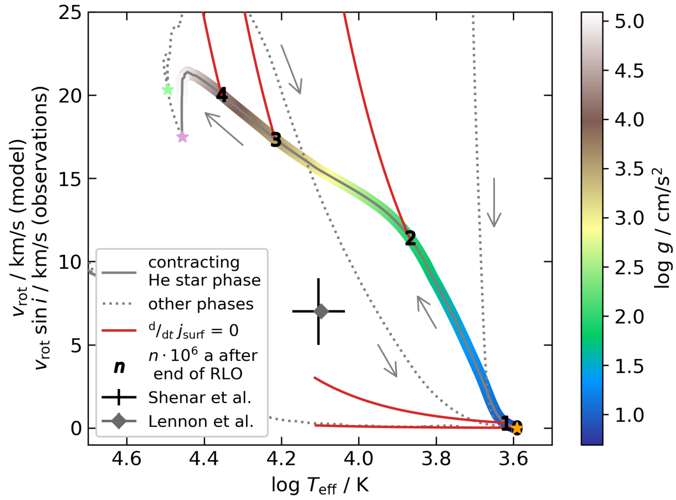

Fig. 5. Surface rotational velocity and surface gravity (colour-coded) as a function of the effective temperature of the stripped component of our fiducial binary model. The coloured part of the curve indicates the contraction phase from RLO decoupling towards the sdOB phase. The dashed black lines show the evolution before and after that phase, with arrows indicating the direction of evolution. The time elapsed after the RLO is indicated in Ma by the numbers on the curve. The two observational data points (black and grey) are from Shenar et al. (2020) and Lennon et al. (2021, the errors are smaller than symbol size). The measured rotational velocity includes a factor of sin i. The red lines indicate the rotational evolution if the specific angular momentum of the stellar surface was conserved. The star symbols indicate the evolutionary stages, as in Fig. 1.

where R_0 and $v_{\rm rot,0}$ are the radius and the rotational velocity at that point where the red lines start (i.e. every million years).

The first two red lines follow lower rotational velocities than the model curve, which implies that the surface layers in the MESA model gain angular momentum, which happens because the tidal forces do not keep the surface in co-rotation any more. Because they behave as $(R/a)^6$ (Zahn 1977), a small decrease in the radius can render the tides inefficient. Hence, the convective angular momentum transport forces the envelope back to rigid rotation (see Fig. 3). Thereafter the contraction of the envelope leads to a reduction of the surface angular momentum. This can be seen by the red lines lying above the evolutionary curve. The physical reason is that the envelope rotates almost as a rigid body (see Fig. 3) and that its angular momentum is conserved. As the radius of the core envelope boundary, and therefore the moment of inertia of the base of the envelope, barely change after helium ignition (Kippenhahn et al. 2013), the contraction induced rigid acceleration of the envelope increases the specific angular momentum of the base of the envelope. This angular momentum can only come from the top of the envelope, and thus the surface's specific angular momentum decreases (see also Heger & Langer 1998).

Figure 5 also shows the measurement of Shenar et al. (2020) and Lennon et al. (2021) for the stripped star in LB-1. While both numbers lie below the model curve, they include a factor of sin i. With an inclination of approximately 30° (sin $i \approx 0.5$), which is close to the inclination value inferred by Shenar et al. (2020), our model consistently fits the observed properties of LB-1 in the Be+Bstr-scenario. Lennon et al. (2021) argue for sin $i \approx 0.8$, but (as they note) their spectroscopic mass estimate assumes spherical symmetry.

4.3.2. Alternative models

To study the influence of the initial stellar spin, we computed another model for which we kept all parameters as in our fiducial model, except for the initial rotation velocity, which we fix here at 0.2 times the critical rotation at ZAMS. We then computed two additional models identical to the fiducial one and its slower spinning counterpart, but neglecting magnetic angular momentum transport. The figures corresponding to the three alternative models (Figs. A.1–A.3) can be found in the Appendix.

Setting the initial rotational velocity to 20% of the critical velocity reduces the angular velocities in the whole the star during central hydrogen burning (Fig. A.1). After RLO, the core spins notably more quickly than before, with a rotation rate nearly identical to that of the fiducial model at that time (Fig. 3, bottom). The reason is that core and envelope decouple earlier than in the fiducial model, namely between TAMS and Roche-lobe filling. Hence, the core transfers less angular momentum to the envelope. The envelope rotation evolves similarly to the original model (Figs. 5 and A.1 lower left panel). The rotation of the envelope is controlled by the same tidal forces, which set the surface velocity to the same synchronised value in both cases. Therefore, the surface rotation during the contraction phase afterwards also occurs as in the fiducial model.

Turning off the magnetic angular momentum transport has strong effects on the rotational evolution, independently of the initial spin. This is visible in Figs. A.2 and A.3, which show that core and envelope already decouple during the central hydrogen burning phase. This leads to a core spinning much faster than the envelope as the former contracts and the latter expands on a timescale shorter than the timescale of any present angular momentum transport process. At the end of RLO the envelope is rotating extremely slowly, as in the original model, but is soon spun up by the core, even though magnetic coupling is absent. The angular velocity gradient is large enough to transport angular momentum from the core to the envelope even if only the hydrodynamic rotational instabilities contribute to the viscosity. However, unlike in the magnetic case, a strong angular velocity gradient between core and envelope remains. Comparing Fig. 3 (bottom) and Fig. A.2 (bottom right) reveals the impact of the magnetic coupling; before the onset of helium burning the core's angular velocity grows at a much larger rate than in the fiducial model. Figure A.2 (lower left panel) shows that the non-magnetic simulation with an initial rotation of 0.6 times the critical rotation is not in agreement with LB-1.

The model without the dynamo and with an initial rotation rate of 0.2 times the critical rotation (Fig. A.3 bottom left), however, is in agreement with LB-1. During the contraction phase the model's rotational velocity is about $10\,\mathrm{km\,s^{-1}}$, which fits with LB-1. When the model has ended its contraction and reached the sdOB phase, the rotational velocity is about $50\,\mathrm{km\,s^{-1}}$. This value is caused by the fast rotation of the core as the strong angular velocity gradient between core and envelope together with the hydrodynamical angular momentum transport mechanisms increase the rotation of the envelope notably (Fig. A.3 bottom right), and in contradiction with the empirical rotational velocities of sdOB stars like φ Per discussed in Sect. 5.1. All the observed sdOB stars show rotational velocities below $50\,\mathrm{km\,s^{-1}}$ (Sect. 5.1), except one (QY Gem). This means that only stellar models with the Spruit–Tayler dynamo can reproduce the observed rotational velocities after a RLO. The initial rotation rate does not play a role.

4.3.3. Comparison to single-star models

Because of its relatively low mass, the stripped star of LB-1 will end up as a WD. The same is true if the stripped star's progenitor is a single star. Here, we investigate whether the binary interaction has an influence on the WD spin. Figure 6 (top) displays $J(m)/m^{5/3}$, which is the integrated angular momentum $J(m) = \int_0^m j(m)\,\mathrm{d}m$ at mass coordinate m, divided by $m^{5/3}$, such that homogeneous and rigidly rotating regions would result in a horizontal line in the plot (Suijs et al. 2008). We plot this quantity at ZAMS, TAMS, helium ignition, in the middle of helium burning when the luminosity has its lowest value, and at helium depletion, for both the $4\,M_\odot$ star in the binary discussed in Sect. 4.3.1 and as a single-star model. The lines from different evolutionary stages trace the flow of angular momentum through the mass shells since $J(m)$ and therefore $J(m)/m^{5/3}$ remain constant in a given mass shell if no angular momentum is transported through this shell.

At ZAMS, TAMS, and helium ignition there is no significant difference in the angular momentum distribution between the single-star and binary model (except that the missing envelope in the star of the binary model results in a lower mass and that the Roche lobe filling star holds barely any angular momentum in its outermost layers). For the first two evolutionary stages this is not surprising as the binary model behaves like a single-star model

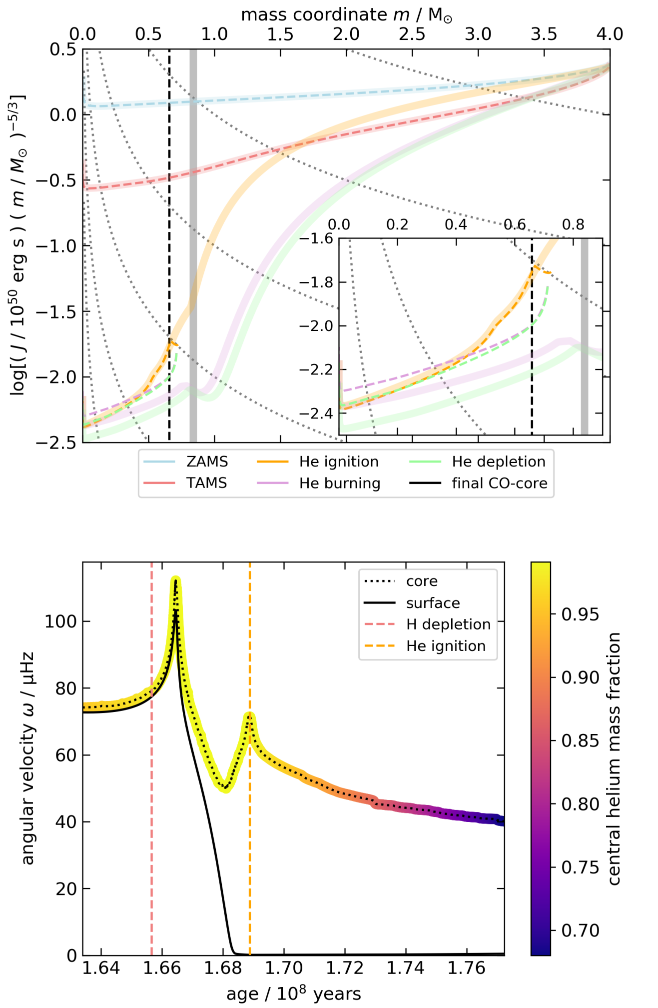

Fig. 6. Rotational properties of the single-star model. *Top*: angular momentum $J(m)$ within the mass coordinate m divided by $m^{5/3}$ as a function of m at different evolutionary stages for the primary star of the binary model examined in Sect. 4.3.1 (dashed) and its primary star as a single star (thick lines). The vertical black lines indicate the last calculated mass of the CO-core of the models. The thin dotted lines represent constant values of the angular momentum J: (*from top to bottom*) $\log J/10^{50}\,\mathrm{erg\,s} = \{1, 0, -1, -2, -3, -4\}$. *Bottom*: evolution of the angular velocity of the single-star model near the centre (coloured by the central helium mass fraction) and at the surface. The vertical lines indicate hydrogen depletion and helium ignition.

if it remains much smaller than its Roche lobe. Flat curves indicate rotation close to a rigid body. The curve is slightly steeper at TAMS than at ZAMS since angular momentum flows from the core into the envelope (Suijs et al. 2008). During the transition from TAMS to helium ignition the core rotation decouples from that of the envelope. Figure 6 (bottom) shows that this happens at the same time in the single-star model as in our fiducial binary model (Fig. 3). The evolution of the core's angular velocities in the two models is nearly identical during the shown times. Likewise the angular momentum distribution at helium ignition of the binary model and in the core of the single-star model are almost indistinguishable. This indicates that at this stage it does not matter whether the rotation of the envelope is braked by tidal forces or by the expansion induced by the variation of the moment of inertia. The strong gradient in the angular momentum profile shows that the models are rotating differentially and that in the case of the single-star model angular momentum was transferred from the core to the envelope.

Slight differences in the angular momentum distribution between the single-star and binary model appear during helium burning. In the model of the stripped star some angular momentum is lost due to tides when the star still fills a notable fraction of its Roche lobe. This can be seen in Fig. 6 (top), where the orange dashed line (helium ignition) extends to larger angular momenta than the purple line (middle of helium core-burning) and the green line (central helium depletion). Thereafter the angular momentum of the stripped star model is conserved and only subtle changes of the internal angular momentum distribution occur (the ends of the green and purple dashed lines overlap). In the single-star model, hydrogen shell-burning increases the core's mass and angular momentum, but decreases its specific angular momentum as the added envelope material contains little angular momentum. This is indicated by the green line, which lies below the purple line, which in turn lies below the orange line. When material is added to the core, it adapts to the core's rotation, as shown in Fig. 6 (top). The bumps in the thick green and plum line around $m = 0.8\,M_\odot$, which indicate the angular velocity gradient between core and envelope, move to a higher mass coordinate. This happens because below the burning shell no chemical gradient weakens the magnetic torques.

To estimate the spin angular momentum of the emerging WD, we use the spin of the CO-core at helium depletion as no significant changes in the core specific angular momentum are expected in later phases (Suijs et al. 2008). The binary model was terminated during the contraction phase following central helium exhaustion, and the evolution of the single-star model ended during the thermally pulsing asymptotic giant-branch phase. We use the CO-core masses of the last calculated model of the simulations to estimate the expected WD masses, which differ due to hydrogen shell-burning in the single-star case, as $0.66\,M_\odot$ for the binary model and $0.84\,M_\odot$ for the single star. The integrated angular momenta at this mass coordinate at the time of central helium depletion is equal to 5.03×10^{47} erg s for the binary model and to 5.82×10^{47} erg s for the single-star case. The corresponding mean specific core angular momenta are $3.82 \times 10^{14}\,\mathrm{cm^2\,s^{-1}}$ (binary) and $3.47 \times 10^{14}\,\mathrm{cm^2\,s^{-1}}$ (single). Thus, we find no significant imprint of the binary evolution on the resulting WD spin. This is not surprising as we have already shown that cores evolve nearly identically until helium ignition in the two models (Fig. 6). After that the rotation of the core of the binary model is decoupled from the envelope and the changes in the core's mass and angular momentum of the single-star model are small.

4.4. Rotation, orbital period, and helium abundance after RLO

Here we consider the predicted properties of stripped star models at given effective temperatures during their contraction, using the set of stellar models discussed in Sect. 4.1. Figure 7 shows the orbital period and donor surface helium abundances after RLO together with the rotational velocity of the donor. While the orbital period and surface abundances remain constant during the contraction phase, the rotational velocity increases (see Sect. 4.3.1). Figure 7 depicts the equatorial rotational velocity of our models at the time when their effective temperature has reached 12 500 K.

The relation between orbital period and rotation follows a narrow U-shape for two reasons. For short orbital periods tidal forces keep the donor in co-rotation, and longer periods imply smaller rotation velocities. For wide binaries, the donor radius at Roche lobe decoupling is large. Hence the star must contract further to reach the adopted surface temperature, which leads to larger rotational velocities.

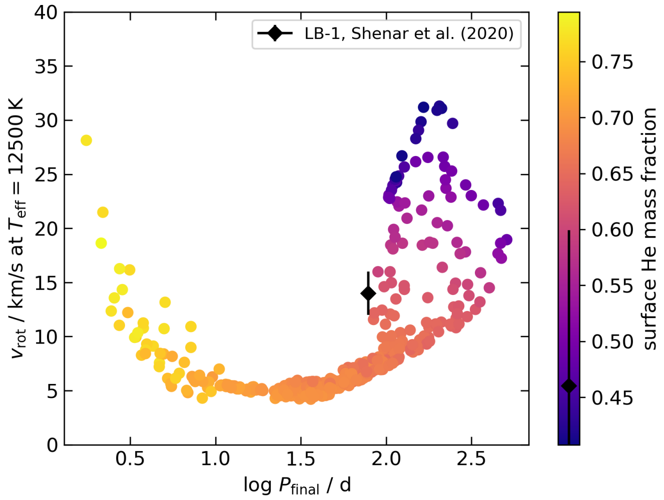

Fig. 7. Orbital period vs donor rotational velocity, and surface helium abundance (colour-coded) of our donor star models contracting after RLO when reaching an effective temperature of 12 500 K. The corresponding quantities derived for LB-1, assuming an inclination of $i = 30°$, are shown by the black dot (Shenar et al. 2020).

For periods above ~100 d, the distribution in Fig. 7 widens in two ways. At a given period, the models show a wide range of rotation rates, and a wide range of surface helium abundances, such that the faster rotators show a smaller helium abundance. We show in Sect. 5.3 that this behaviour can be attributed to the onset of convection in the donor during RLO.

For Fig. 7 we adopted a fixed primary effective temperature of 12 500 K. As we show in Sect. 4.3.1, the surface angular momentum is not conserved during contraction. Therefore, the product $v_{\rm rot} T_{\rm eff}^{-2}$ is not constant (cf. Eq. (2) for constant luminosity), and the distributions for different values of the donor surface temperature do not follow in a straightforward way from Fig. 7. We provide plots for the different temperatures in Fig. B.1.

As mentioned above, our models predict a longer orbital period than that observed in LB-1, which may be related to the low mass transfer efficiency of our models (see Sect. 5.3). Higher mass transfer efficiencies would shift the models to smaller orbital periods (Soberman et al. 1997). The helium abundance is in broad agreement with LB-1, as the observations are uncertain. However, we expect that the shape of the distribution of points in Fig. 7, and the connection to the helium abundance, remains qualitatively similar for different mass transfer prescriptions because the physical effects leading to it (tides and contraction) are still in place. Therefore, observing a large population of contracting post-RLO stars and comparing them with Figs. 7 and B.1 would yield strong constraints on the mass transfer efficiency and orbital evolution during RLO.

5. Discussion

In this section we compare LB-1 with the similar system HR 6819, and with sdOB stars like φ Per (Sect. 5.1) and relate our results to earlier work on angular momentum transport in stars (Sect. 5.2). Then we discuss the implications of our results for the orbital evolution of binaries in Sect. 5.3.

Table 2. Orbital and atmospheric properties of the stripped star in HR 6819 according to Bodensteiner et al. (2020b) and El-Badry & Quataert (2021).

	Bodensteiner et al. (2020b)	El-Badry & Quataert (2021)
$P_{\rm orb}$/d	40.335 ± 0.007	40.3 ± 0.3
q	15 ± 3	14 ± 6
$T_{\rm eff}$/K	13 000 ± 1000	16 000 ± 1000
$\log g$/cm s^{-2}	2.8 ± 0.2	2.75 ± 0.35
$\upsilon_{\rm rot} \sin i$/km s^{-1}	<25	<20
$\log(L/M)$	3.41 ± 0.23	3.46 ± 0.37
$Y_{\rm surface}$	~solar	0.54 ± 0.11
[N/C]	>0	1.6 ± 0.4

5.1. Similar systems and φ Per stars

The system HR 6819 (Table 2) is resembles to LB-1 in several respects. Similarly to LB-1, it was first suggested that HR 6819 contains a BH since Rivinius et al. (2020) identified it as consisting of a close B3 III+BH binary with a Be-star orbiting it. Bodensteiner et al. (2020b) and El-Badry & Quataert (2021) pointed out that it may actually be composed of a Be star and a stripped star. Both studies performed an atmospheric analysis of the stripped star and received consistent results. The stripped component of HR 6819 is slightly hotter and has a stronger surface gravity than that of LB-1. Bodensteiner et al. (2020b) derive $\upsilon_{\rm rot} \sin i < 25\,{\rm km\,s^{-1}}$, and El-Badry & Quataert (2021) $\upsilon_{\rm rot} \sin i < 20\,{\rm km\,s^{-1}}$. Both upper limits, imply a high probability for very slow rotation, atypical of B stars, but expected for stripped star (see Fig. B.1). The Roche-lobe filling component of HD 15124 rotates critically as expected (El-Badry et al. 2022). For NGC 1850 BH1 (El-Badry & Burdge 2022) no rotation rates have been measured so far.

As the stripped stars of LB-1 and HR 6819 contract further, they will become sdOB stars in a φ Persei-like binary (i.e. a sdOB+Be-system). While this configuration is expected to be common for Be-stars (El-Badry & Quataert 2021; Wang et al. 2021), it is hard to identify as the Be-star outshines the subdwarf, and so far fewer than 20 such systems are known (16 confirmed plus 3 candidates) and have been spectroscopically analysed (Wang et al. 2018, 2021; Chojnowski et al. 2018). We compiled the effective temperature, gravity, and rotation (if available) of the subdwarfs as well as the orbital period of the systems in Table 3. For two sdOB stars, the projected rotational velocity is known, but for 12 we know only an upper limit. We show them in Fig. 8 together with the calculated values from our binary models discussed in Sect. 4.1. In this diagram we show the stripped star models at the time of smallest radius during core helium burning (see Fig. 2). This relatively long-lasting phase is close to the helium main sequence.

Figure 8 shows that the helium-rich models follow a rather narrow correlation, with the hotter models rotating faster. Models with a lower surface helium abundance deviate from this pattern as their larger envelopes make them larger, and thus the surface temperature is cooler. The values of the observed sdOB stars fall well within the predicted range. However, they do not follow the trend drawn by the models. Since for most of the stars only an upper limit of the projected rotation velocity is known, a more detailed comparison is difficult.

Three stars are remarkable in Fig. 8: φ Per, QY Gem, and FY CMa. φ Per shows a significantly slower projected rotation than expected. While the inclination of the system could be small, it could also imply that its stripped star is past core helium exhaustion (see Fig. 5). Disregarding rotation, Schootemeijer et al. (2018) found that a helium shell-burning model agrees with φ Per. However, Fig. 5 implies that a rotation velocity below $10\,{\rm km\,s^{-1}}$ is only achieved during the fast final contraction towards the WD stage. QY Gem and FY CMa have a relatively high rotation velocity, which is not explained by our models. Their sdOB star could be spun up by accretion from the Be star's disc, as proposed by Wang et al. (2021).

5.2. Angular momentum transport in stellar models

In the course of stellar evolution, the core of a star contracts, while the envelope, separated from the core by a jump in chemical composition, expands. This happens already during the main-sequence evolution (Hastings et al. 2020), and much more so after core hydrogen exhaustion, after which the hydrogen burning shell source strongly adds to the entropy jump between core and envelope. In rotating stars, one may therefore expect the core rotation frequency to increase with time, while the envelope does the opposite.

During the last decades, observational evidence has accumulated showing that this is not the case, or at least to a much lower degree than expected from local angular momentum conservation. The specific angular momentum in upper main-sequence stars is typically 10^{17}–$10^{18}\,{\rm cm^2\,s^{-1}}$, while it is three to four orders of magnitude smaller in WDs (Suijs et al. 2008) and young neutron stars (Heger et al. 2005). This shows that angular momentum is drained from the stellar cores, and transported into the stellar envelopes during their evolution. In red giant stars this process has been traced as a function of the evolutionary stage through the analyses of their oscillations (Mosser et al. 2012; Deheuvels et al. 2014; Gehan et al. 2018). The physical mechanism responsible for this angular momentum transport is still debated, with magnetic torques and internal waves being the strongest candidates (Aerts et al. 2019). Since the latter still have to be explored systematically in stellar evolution calculations, we focus here on models employing magnetic torques.

Several groups have studied the angular momentum transport imposed by the magnetic torques as proposed by Spruit (2002). Maeder & Meynet (2004) demonstrated that its inclusion in single-star calculations leads to near solid body rotation during the main-sequence evolution. In contrast, in models that include only hydrodynamic angular momentum transport (Heger et al. 2000), the core and envelope rotate nearly rigidly, but each with its individual rotation frequency, and the difference amplifies during the main-sequence evolution. Here the non-magnetic transport mechanisms are not able to overcome the gradient of entropy and mean molecular weight that separates core and envelope. After central hydrogen exhaustion the difference in rotational frequency grows to several orders of magnitude. Our models with and without the magnetic transport follow these patterns.

Heger et al. (2005) showed that the magnetic torques proposed by Spruit (2002) remove angular momentum from the core of main-sequence models compared to non-magnetic models (see also Yoon et al. 2006). Most of this happens between core hydrogen depletion and helium ignition. As we observe in our models, Heger et al. (2005) noted that the helium burning core rotates nearly rigidly. Similarly, Suijs et al. (2008) demonstrated that calculations incorporating magnetic torques lead to WD spins close to the observed values, while WD models resulting from non-magnetic models are rotating orders of magnitude too rapidly. Our binary and single-star model behave in a comparable manner.

Table 3. Properties of the sdOB stars in known and candidate Be+sdOB systems as well as HR 6819.

HD number	Name	$T_{\rm eff}$/kK	$\log g$/cm s^{-2}	$\upsilon_{\rm rot} \sin i$/km s^{-1}	Orbital period/d	Reference
10516	φ Per	53 ± 3	4.2 ± 0.1	<10	127	Gies et al. (1998)
29441	V1150 Tau	40.0 ± 2.5	–[a]	<15	–	Wang et al. (2021)
41335	HR 2142	>43 ± 5	>4.75	<30	80.9	Peters et al. (2016)
43544	HR 2249	38.2 ± 2.5	–[a]	<15	–	Wang et al. (2021)
51354	QY Gem	43.5 ± 2.5	–[a]	102 ± 4	–	Wang et al. (2021)
55606	MWC 522	40.9 ± 2.5	–[a]	<24	93.8[b]	Wang et al. (2021)
58978	FY CMa	45 ± 5	4.3 ± 0.6	41 ± 5	37.3	Peters et al. (2008)
60855	V378 Pup	42.0 ± 2.5	–[a]	<27	346	Wang et al. (2021)
113120	LS Mus	45.0 ± 2.5	–[a]	<36	–	Wang et al. (2021)
137387	κ Aps	40.0 ± 2.5	–[a]	<17	84	Wang et al. (2021)
152478	V846 Ara	42.0 ± 2.5	–[a]	<15	–	Wang et al. (2021)
157042	ι Ara	33.8 ± 2.5	–[a]	<36	–	Wang et al. (2021)
157832	V750 Ara	–	–	–	–	Wang et al. (2018)
191610	28 Cyg	–	–	–	–	Wang et al. (2018)
194335	V2119 Cyg	43.5 ± 2.5	–[a]	<15	60.3	Wang et al. (2021)
200120	59 Cyg	52.1 ± 4.8	5.0 ± 1.0	<40	28.2	Peters et al. (2013)
200310	60 Cyg	42 ± 4	>4.75	–	147	Wang et al. (2017)

Notes. [a]4.75 was assumed by Wang et al. (2021). [b]Chojnowski et al. (2018).

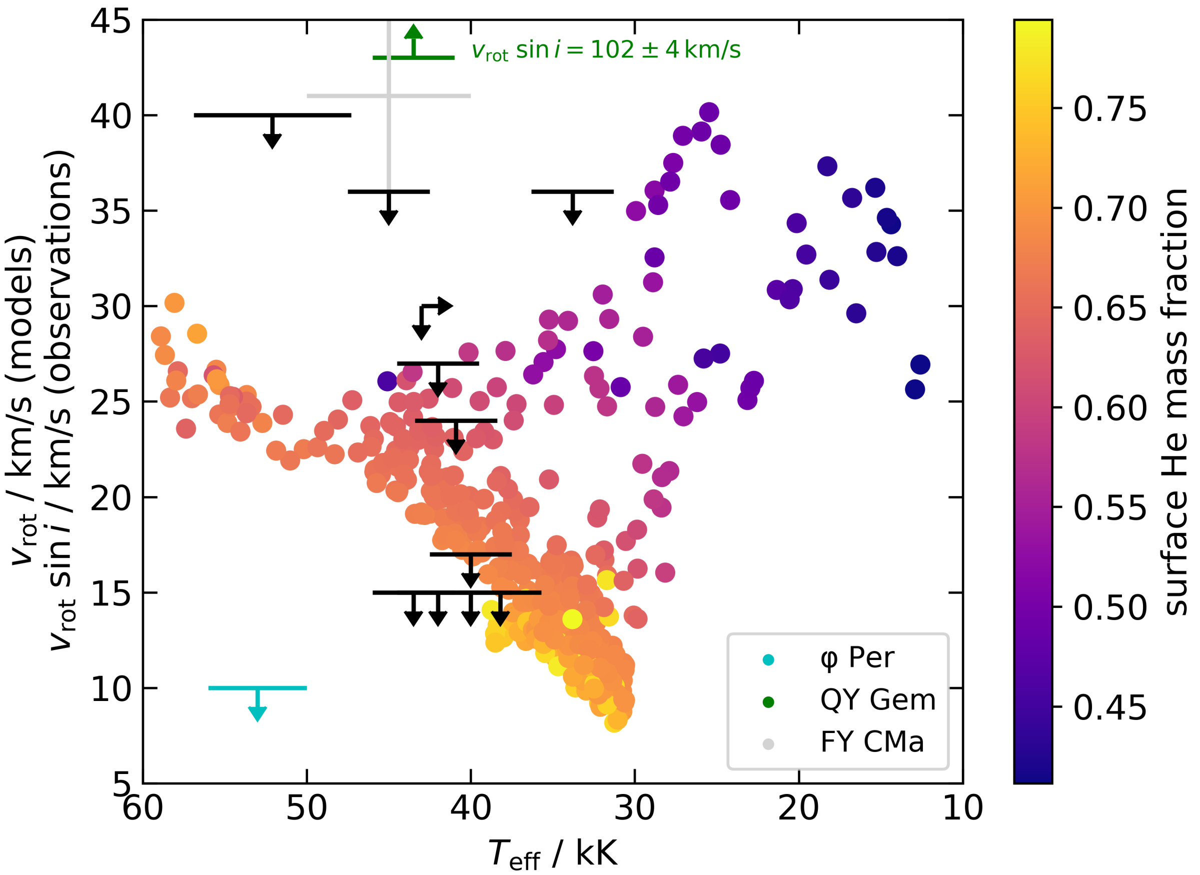

Fig. 8. Effective temperature, rotational velocity, and surface helium abundance of our stripped core helium burning models at time of minimum radius (only systems with an initial donor mass below 10 $M_\odot$ are shown). The values measured for the sdOB stars in the known sdOB+Be stars (references in Table 3) are also shown. The rotational velocity of QY Gem (102 ± 4 km s^{-1}, green) lies beyond the figure's limit.

The first binary calculations with magnetic transport were performed by Petrovic et al. (2005b). They noted that the extraction of angular momentum from the cores renders the formation of long-duration gamma-ray bursts through this channel unlikely. As in single stars, magnetic torques during the main-sequence and early hydrogen shell-burning evolution are able to remove angular momentum from the stellar cores. Additionally, the authors find that the mass donors have an extremely slow rotation after RLO. Cantiello et al. (2007) calculated, as we do, a Case B binary including magnetic transport, but for higher masses. Nevertheless, they found the donors to rotate slowly after RLO (see their Table 1). Both works are in agreement with our models.

Yoon et al. (2010) computed binary evolution models of type Ib/c supernova progenitors with and without magnetic angular momentum transport. Their magnetic models show that the cores lose, as in our models, large amounts of angular momentum during RLO. In Case A models tides play a role; instead, in Case AB (mass transfer subsequent to Case A after central hydrogen depletion, Kippenhahn & Weigert 1967) and B mass transfer, magnetic transport is responsible for this angular momentum loss. This becomes evident through their non-magnetic model, where the core's angular momentum barely changes during Case AB RLO. More recently, Marchant & Moriya (2020) showed that magnetic angular momentum transport has an impact on the upper black hole mass-gap between 45 $M_{\odot}$ and 120 $M_{\odot}$.

As for massive stars, magnetic transport due to the Spruit–Tayler dynamo has been extensively tested in low mass models at various stages, on the main sequence and for the Sun (Eggenberger et al. 2005, 2019), on the subgiant and red-giant branches (Maeder & Meynet 2014), and for WDs (Suijs et al. 2008; Neunteufel et al. 2017). For more evolved stars the results become more complex. Cantiello et al. (2014) demonstrated that the original Spruit–Tayler dynamo alone is not able to reproduce the observed angular momentum loss of the core of red giants and helium core-burning low mass stars. Other studies (Ceillier et al. 2013; Belkacem et al. 2015; Wheeler et al. 2015; Spada et al. 2016; Eggenberger et al. 2017; Ouazzani et al. 2019) enforce the conclusion that additional angular momentum transport may be required. Fuller et al. (2019) have reanalysed the formulation of the Spruit–Tayler dynamo and proposed a revision, which, as they demonstrate in stellar evolution calculations, allows the observed core angular momentum evolution in red giants to be reproduced.

While some authors debate the functionality of the Spruit–Tayler dynamo on theoretical grounds (Braithwaite 2006; Zahn et al. 2007) or question its existence based on observations (e.g. Denissenkov et al. 2010), angular momentum transport by magnetic torques from toroidal B-fields are undisputed. Takahashi & Langer (2021) presented magneto-rotational stellar evolution calculations in which the internal magnetic field evolution is described by two time-dependent differential equations, which are solved along with the stellar structure equations. Their models obtain angular momentum transport by magnetic torques on the Alfvén timescale, which was shown to be able to reproduce the red giant observations. Overall, while the description of angular momentum transport by magnetic fields in 1D stellar evolution models is still improving, this mechanism is a strong candidate to provide a realistic description of the evolution of the internal rotation of evolved stars.

5.3. Orbital evolution and mass transfer efficiency

In Sects. 4.1 and 4.3.1 we presented our fiducial binary evolution model, which reproduces the observed properties of the stripped star in LB-1. However the final orbital period we found did not agree with the observed value. In Fig. 9 we show the orbital period, helium abundance, and luminosity-to-mass ratios for all the models discussed in Sect. 4.1, at a time when the mass donor after RLO has reached $T_{\rm eff}$ = 12 500 K. We find no model in our set with all three observed properties of the stripped star fitting to LB-1, although some come close to it.

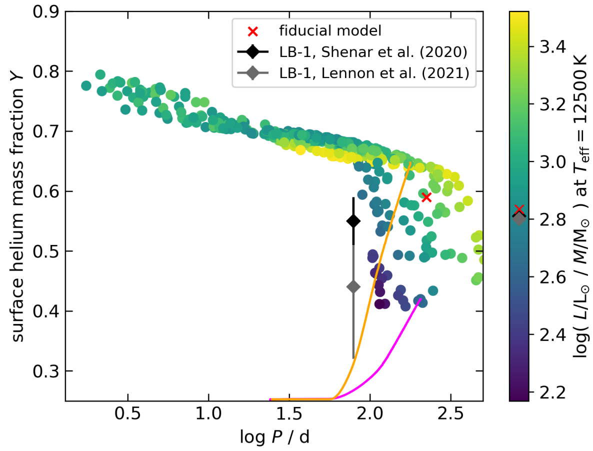

Fig. 9. Period, surface helium abundance, and luminosity-to-mass ratio during the contraction phase after RLO, when the stripped star has obtained an effective temperature of 12 500 K (close to that derived for LB-1). The black and grey symbols indicate the values for LB-1, as derived by Shenar et al. (2020) and Lennon et al. (2021, almost superimposed in the colour bar). The fiducial model is shown in red. The orange curve (initially 4.27 $M_{\odot}$ + 4.07 $M_{\odot}$ at $P_{\rm orb}$ = 24.2 d) shows the surface helium evolution of a mass donor, which does not develop convection in its outer layers during RLO. In the magenta curve (initially 5.86 $M_{\odot}$ + 4.20 $M_{\odot}$ at $P_{\rm orb}$ = 25.4 d) convection sets in.

In Fig. 9 we can identify two groups, one group above Y = 0.6 with a tight correlation between orbital period and helium abundance, and a more scattered group at periods above 80 d. The reason for this scatter is the development of convection in the mass donors' outer layers during RLO. Donors in close orbits have small Roche lobes, and therefore they cannot expand enough to become cool enough to develop a notable envelope convection zone, while in wide orbit binaries a convective envelope can develop that mixes hydrogen into the regions that were helium-enriched during the main-sequence evolution. After the mass transfer, these regions are exposed at the surface, resulting in a lower surface helium abundance compared to models for which convection does not occur.

This can be seen from the two curves indicated in Fig. 9. They show the evolution of the surface helium abundance during the RLO for two selected models. As the donor loses mass, the orbit widens and at some point helium-enriched layers appear at the surface. In the orange curve in Fig. 9 the convection zone never extends into the layers, which were helium-enriched during hydrogen burning, and thus the helium abundance grows quickly as deeper regions are uncovered. In the magenta curve convection sets in in the outer layers before the helium-rich layers are exposed. The convective region grows and eventually its lower boundary reaches the helium-enriched region, and thus hydrogen-rich material is mixed into that region. If this region is exposed later, its helium abundance does not reach values as high as in the case without convection. Thus, the magenta curve is not as steep as the orange one, and models with convection do not reach final helium values as high as those without convection, and the correlation between the orbital period and helium abundance disappears.

In Fig. 9 we also plot the measurements of Shenar et al. (2020) and Lennon et al. (2021). Both lie slightly below the low period interval covered by the scattered group. The value of Shenar et al. (2020) fits well to the helium abundance and the luminosity-to-mass ratio of the fiducial model, but it does not reproduce the orbital period. The helium abundance measured by Lennon et al. (2021) deviates more from the model, but has an uncertaintly that is quite large. In Fig. 9 their data point lies closest to models with luminosity-to-mass ratios certainly below their measurement. If all the models were shifted by about 0.5 dex to the left, the fiducial model's orbital period would be consistent with the observations and the two observations surrounded by models with luminosity-to-mass ratios in agreement with them.

We attribute the mismatch in orbital period to the uncertain mass and angular momentum loss of the binary during the RLO. Our fiducial model for example increases its orbital period from an initial value of 16 d to 223 d, while the orbital period of LB-1 is 79 d (Table 1). A prescription including either a similar mass loss from the binary which carries more angular momentum per mass unit or a lower mass loss from the binary systems would lead to models with shorter periods and in better agreement to the observations. Schootemeijer et al. (2018) and Pols (2007) for φ Per, as well as Shao & Li (2014) for Be star binaries, report a preference for non-conservative mass transfer with higher mass transfer efficiencies than those in our highly non-conservative models (<5% mass transfer efficiency). Similarly, Shao & Li (2021) performed a population synthesis analysis of LB-1 assuming different mass transfer models and found a strong preference for non-conservative mass transfer. We decided against searching for a model with matching orbital period, as both the accretion efficiency and the specific angular momentum of the expelled matter are unknown. The large uncertainty of the mass measurement of the Be star (Shenar et al. 2020; Lennon et al. 2021) would not allow the degeneracy impeding a sound result to be lifted.

Bodensteiner et al. (2020b) and El-Badry & Quataert (2021) provide MESA models for HR 6819. Bodensteiner et al. (2020b) restrict themselves to an initial mass ratio of 1/3, and find that initially very close systems, which evolve through Case A mass transfer, can reproduce the observations. In our simulations, Case A systems show orbital periods that are too short to be relevant for LB-1 and HR 6819. However, the helium abundance in the stripped star model ($Y = 0.87$) of Bodensteiner et al. (2020b) does not match the observations of El-Badry & Quataert (2021, $Y = 0.54 \pm 0.11$, Table 2). El-Badry & Quataert (2021) provide a set of calculations with varying mass transfer efficiency, some of which lead to solutions comparable with LB-1 and HR 6819. However, in their analysis, and in that of Eldridge et al. (2020), the helium abundance is not considered. We demonstrated that this quantity is very constraining, as it strongly correlated with the post-RLO orbital period and with the rotational velocity in most of the model parameter space. Our results imply that it may be feasible to compare binary models with varying mass transfer efficiencies to measurements of period and surface helium abundance for LB-1, HR 6819, and the known sdOB+Be systems in order to constrain the physical mechanisms driving mass transfer.

6. Conclusions

In this study our aim was to constrain the angular momentum transport mechanisms in the stellar interior by modelling the mass donor of the binary system LB-1, composed of a stripped B-type star and a Be star. To this end, we analysed a large grid of MESA binary evolution models to investigate the rotational evolution of the mass donors after mass transfer, and to identify models corresponding to the evolutionary phase of LB-1 and similar binaries in the stripped star scenario. We focused on the luminosity-to-mass ratio of the stripped star which is observationally well determined. We found that in Case B models (mass transfer after donor core hydrogen exhaustion) this parameter is uniquely determined by the donor's initial mass at the moment of Roche-lobe detachment. However, the ensuing drop in the luminosity-to-mass ratio also depends on the mass of the remaining envelope, which is indicated by the final surface helium abundance, which is set in turn by the initial orbital period. Based on the observed luminosity-to-mass ratio and surface helium abundance, we obtained an initial mass for the stripped star in LB-1 of about 4 $M_{\odot}$.

We examined the internal rotation, and the evolution of the surface rotation rate of our donor star models. To do so we calculated MESA models including magnetic angular momentum transport by the Spruit–Tayler dynamo, which removes angular momentum from the stellar core during and after central hydrogen exhaustion and yields low surface rotational velocities in the stripped mass donor after RLO. The braking, which is caused by tidal forces, leads to about the same core angular momentum and final WD spin as obtained in single-star models where the core rotation is braked by the expanded envelope and the mass growth of the core. In the binary case the envelope accelerates again while the star contracts towards sdOB phase. Our results agree qualitatively with observations, suggesting that angular momentum is removed from the stellar cores by magnetic angular momentum transport through the Spruit–Tayler dynamo until well into the hydrogen shell-burning stage, based on asteroseismic results and spin rates of WDs and neutron stars.

We considered models with and without angular momentum transport by magnetic torques, and models with different initial rotation rates. When comparing the rotation velocity of our models during the contraction phase to the observed value for LB-1 (Shenar et al. 2020; Lennon et al. 2021), we found that it can be reproduced only by our magnetic models, independent of the initial rotation. Our models predict a relation between the orbital period, temperature, and equatorial rotation of contracting post-RLO stars, which may be used to determine the mass transfer efficiency during RLO. A comparison to a larger sample of observed sdOB+Be-systems, where often only upper limits for the rotational velocities of the stripped star are known, shows a broad agreement with our models.

Furthermore, we find evidence that our employed mass transfer scheme underestimates the mass transfer efficiency during RLO, such that our models can only marginally reproduce the observed orbital period of LB-1 and similar systems. This suggests, in line with previous studies, that the Be stars in the considered systems have accreted notable amounts of material. A population synthesis study should be able to determine the accretion efficiency of the RLO and the specific angular momentum the expelled matter carries. The surface helium abundance of stripped stars, together with their orbital periods, offers a new tool to tightly constrain the accretion efficiency in mass transferring binaries.

Acknowledgements. We would like to thank Tomer Shenar and Julia Bodensteiner for discussing the observational aspects with us as well as Pablo Marchant for sharing his MESA framework with us.

References

Abdul-Masih, M., Banyard, G., Bodensteiner, J., et al. 2020, Nature, 580, E11
Aerts, C., Mathis, S., & Rogers, T. M. 2019, ARA&A, 57, 35
Belczynski, K. 2020, ApJ, 905, L15
Belkacem, K., Marques, J. P., Goupil, M. J., et al. 2015, A&A, 579, A31
Bodensteiner, J., Shenar, T., & Sana, H. 2020a, A&A, 641, A42
Bodensteiner, J., Shenar, T., Mahy, L., et al. 2020b, A&A, 641, A43

Braithwaite, J. 2006, A&A, 449, 451
Cantiello, M., Yoon, S. C., Langer, N., & Livio, M. 2007, A&A, 465, L29
Cantiello, M., Mankovich, C., Bildsten, L., Christensen-Dalsgaard, J., & Paxton, B. 2014, ApJ, 788, 93
Casares, J., Negueruela, I., Ribó, M., et al. 2014, Nature, 505, 378
Castro, N., Fossati, L., Langer, N., et al. 2014, A&A, 570, L13
Ceillier, T., Eggenberger, P., García, R. A., & Mathis, S. 2013, A&A, 555, A54
Chojnowski, S. D., Labadie-Bartz, J., Rivinius, T., et al. 2018, ApJ, 865, 76
De Greve, J. P., & De Loore, C. 1976, Ap&SS, 43, 35
de Mink, S. E., Langer, N., Izzard, R. G., Sana, H., & de Koter, A. 2013, ApJ, 764, 166
Deheuvels, S., Doğan, G., Goupil, M. J., et al. 2014, A&A, 564, A27
Denissenkov, P. A., Pinsonneault, M., Terndrup, D. M., & Newsham, G. 2010, ApJ, 716, 1269
Dufton, P. L., Langer, N., Dunstall, P. R., et al. 2013, A&A, 550, A109
Eggenberger, P., Maeder, A., & Meynet, G. 2005, A&A, 440, L9
Eggenberger, P., Lagarde, N., Miglio, A., et al. 2017, A&A, 599, A18
Eggenberger, P., Buldgen, G., & Salmon, S. J. A. J. 2019, A&A, 626, L1
El-Badry, K., & Burdge, K. B. 2022, MNRAS, 511, 24
El-Badry, K., & Quataert, E. 2020, MNRAS, 493, L22
El-Badry, K., & Quataert, E. 2021, MNRAS, 502, 3436
El-Badry, K., Conroy, C., Quataert, E., et al. 2022, MNRAS, 516, 3602
Eldridge, J. J., Stanway, E. R., Breivik, K., et al. 2020, MNRAS, 495, 2786
Fuller, J., Piro, A. L., & Jermyn, A. S. 2019, MNRAS, 485, 3661
Gehan, C., Mosser, B., Michel, E., Samadi, R., & Kallinger, T. 2018, A&A, 616, A24
Gies, D. R., Bagnuolo, W. G., Jr., Ferrara, E. C., et al. 1998, ApJ, 493, 440
Hastings, B., Wang, C., & Langer, N. 2020, A&A, 633, A165
Heger, A., & Langer, N. 1998, A&A, 334, 210
Heger, A., & Woosley, S. E. 2002, ApJ, 567, 532
Heger, A., Langer, N., & Woosley, S. E. 2000, ApJ, 528, 368
Heger, A., Woosley, S. E., & Spruit, H. C. 2005, ApJ, 626, 350
Irrgang, A., Geier, S., Kreuzer, S., Pelisoli, I., & Heber, U. 2020, A&A, 633, L5
Kennea, J. A., Coe, M. J., Evans, P. A., et al. 2021, MNRAS, 508, 781
Kippenhahn, R., & Weigert, A. 1967, ZAp, 65, 251
Kippenhahn, R., Weigert, A., & Weiss, A. 2013, Stellar Structure and Evolution (Berlin, Heidelberg: Springer-Verlag)
Kruckow, M. U., Tauris, T. M., Langer, N., Kramer, M., & Izzard, R. G. 2018, MNRAS, 481, 1908
Langer, N. 2012, ARA&A, 50, 107
Langer, N., Baade, D., Bodensteiner, J., et al. 2020a, A&A, 633, A40
Langer, N., Schürmann, C., Stoll, K., et al. 2020b, A&A, 638, A39
Lennon, D. J., Maíz Apellániz, J., Irrgang, A., et al. 2021, A&A, 649, A167
Liu, J., Zhang, H., Howard, A. W., et al. 2019, Nature, 575, 618
Liu, J., Zheng, Z., Soria, R., et al. 2020, ApJ, 900, 42
Maeder, A., & Meynet, G. 2000, ARA&A, 38, 143
Maeder, A., & Meynet, G. 2004, A&A, 422, 225
Maeder, A., & Meynet, G. 2014, ApJ, 793, 123
Marchant, P. 2018, Ph.D. Thesis, Rheinische Friedrich-Wilhelms-Universität Bonn, Germany
Marchant, P., & Moriya, T. J. 2020, A&A, 640, L18
Martinet, S., Meynet, G., Ekström, S., et al. 2021, A&A, 648, A126
Mosser, B., Goupil, M. J., Belkacem, K., et al. 2012, A&A, 548, A10
Neunteufel, P., Yoon, S. C., & Langer, N. 2017, A&A, 602, A55
Ouazzani, R. M., Marques, J. P., Goupil, M. J., et al. 2019, A&A, 626, A121
Paxton, B., Bildsten, L., Dotter, A., et al. 2011, ApJS, 192, 3
Paxton, B., Cantiello, M., Arras, P., et al. 2013, ApJS, 208, 4
Paxton, B., Marchant, P., Schwab, J., et al. 2015, ApJS, 220, 15
Peters, G. J., Gies, D. R., Grundstrom, E. D., & McSwain, M. V. 2008, ApJ, 686, 1280
Peters, G. J., Pewett, T. D., Gies, D. R., Touhami, Y. N., & Grundstrom, E. D. 2013, ApJ, 765, 2
Peters, G. J., Wang, L., Gies, D. R., & Grundstrom, E. D. 2016, ApJ, 828, 47
Petrovic, J., Langer, N., & van der Hucht, K. A. 2005a, A&A, 435, 1013
Petrovic, J., Langer, N., Yoon, S. C., & Heger, A. 2005b, A&A, 435, 247
Poeckert, R. 1981, PASP, 93, 297
Pols, O. R. 2007, in Massive Stars in Interactive Binaries, eds. N. St.-Louis, & A. F. J. Moffat, ASP Conf. Ser., 367, 387
Pols, O. R., Cote, J., Waters, L. B. F. M., & Heise, J. 1991, A&A, 241, 419
Raguzova, N. V. 2001, A&A, 367, 848
Rivinius, T., Baade, D., Hadrava, P., Heida, M., & Klement, R. 2020, A&A, 637, L3
Saracino, S., Kamann, S., Guarcello, M. G., et al. 2022, MNRAS, 511, 2914
Savonije, G. J., & Takens, R. J. 1976, A&A, 47, 231
Schootemeijer, A., Götberg, Y., de Mink, S. E., Gies, D., & Zapartas, E. 2018, A&A, 615, A30
Schootemeijer, A., Langer, N., Grin, N. J., & Wang, C. 2019, A&A, 625, A132
Shao, Y., & Li, X.-D. 2014, ApJ, 796, 37
Shao, Y., & Li, X.-D. 2021, ApJ, 908, 67
Shenar, T., Bodensteiner, J., Abdul-Masih, M., et al. 2020, A&A, 639, L6
Simón-Díaz, S., Maíz Apellániz, J., Lennon, D. J., et al. 2020, A&A, 634, L7
Soberman, G. E., Phinney, E. S., & van den Heuvel, E. P. J. 1997, A&A, 327, 620
Spada, F., Gellert, M., Arlt, R., & Deheuvels, S. 2016, A&A, 589, A23
Spiegel, E. A., & Zahn, J. P. 1992, A&A, 265, 106
Spruit, H. C. 2002, A&A, 381, 923
Suijs, M. P. L., Langer, N., Poelarends, A. J., et al. 2008, A&A, 481, L87
Takahashi, K., & Langer, N. 2021, A&A, 646, A19
Wang, C., Langer, N., Schootemeijer, A., et al. 2020, ApJ, 888, L12
Wang, C., Langer, N., Schootemeijer, A., et al. 2022, Nat. Astron., 6, 480
Wang, L., Gies, D. R., & Peters, G. J. 2017, ApJ, 843, 60
Wang, L., Gies, D. R., & Peters, G. J. 2018, ApJ, 853, 156
Wang, L., Gies, D. R., Peters, G. J., et al. 2021, AJ, 161, 248
Waters, L. B. F. M., Pols, O. R., Hogeveen, S. J., Cote, J., & van den Heuvel, E. P. J. 1989, A&A, 220, L1
Wheeler, J. C., Kagan, D., & Chatzopoulos, E. 2015, ApJ, 799, 85
Yoon, S. C., Langer, N., & Norman, C. 2006, A&A, 460, 199
Yoon, S. C., Woosley, S. E., & Langer, N. 2010, ApJ, 725, 940
Zahn, J. P. 1977, A&A, 500, 121
Zahn, J. P. 1992, A&A, 265, 115
Zahn, J. P., Brun, A. S., & Mathis, S. 2007, A&A, 474, 145

Appendix A: Variations in initial rotation and dynamo

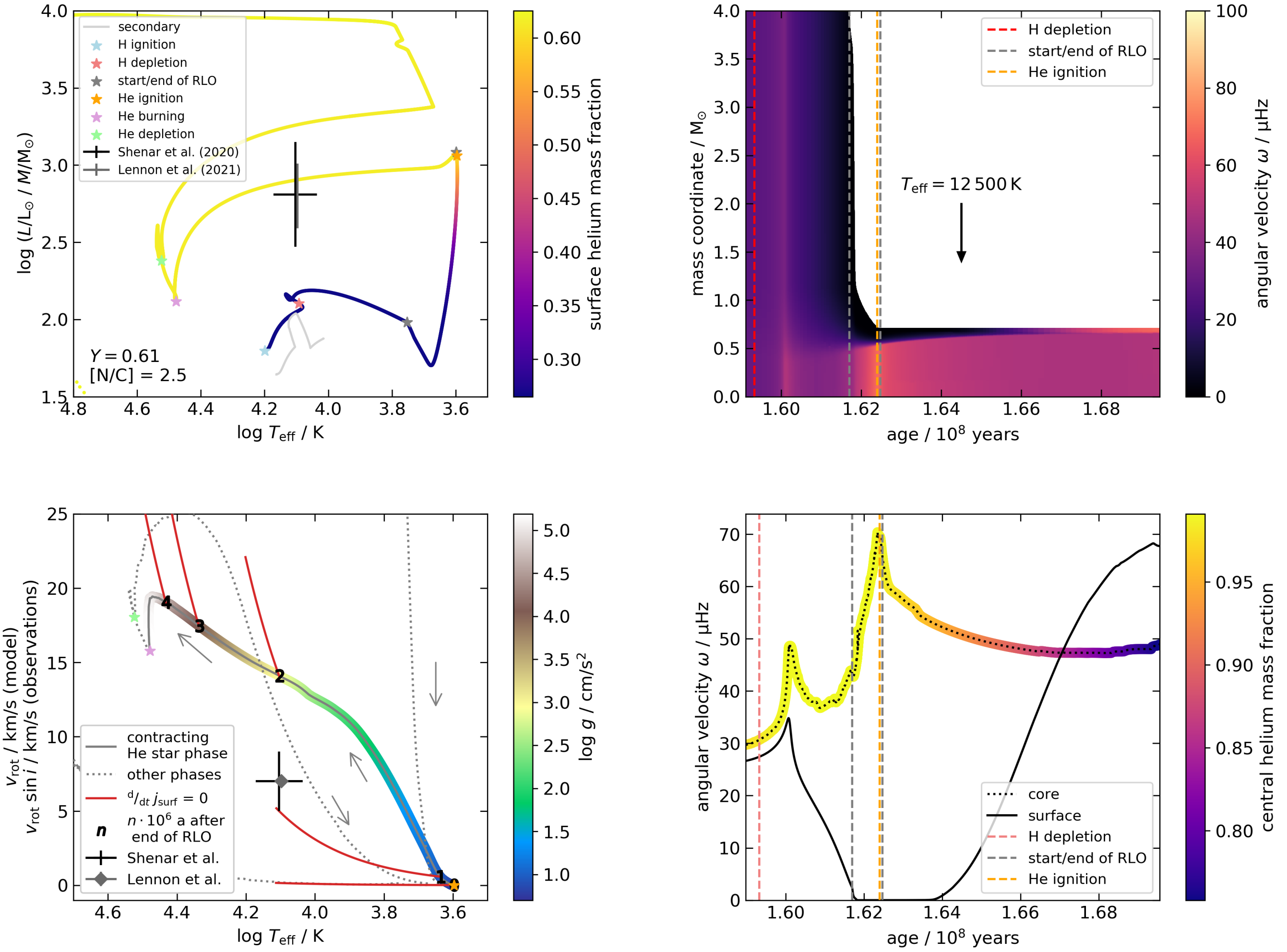

Fig. A.1. Same as Figs. 1, 3, and 5, but with an initial rotation of 20% of the critical rotation.

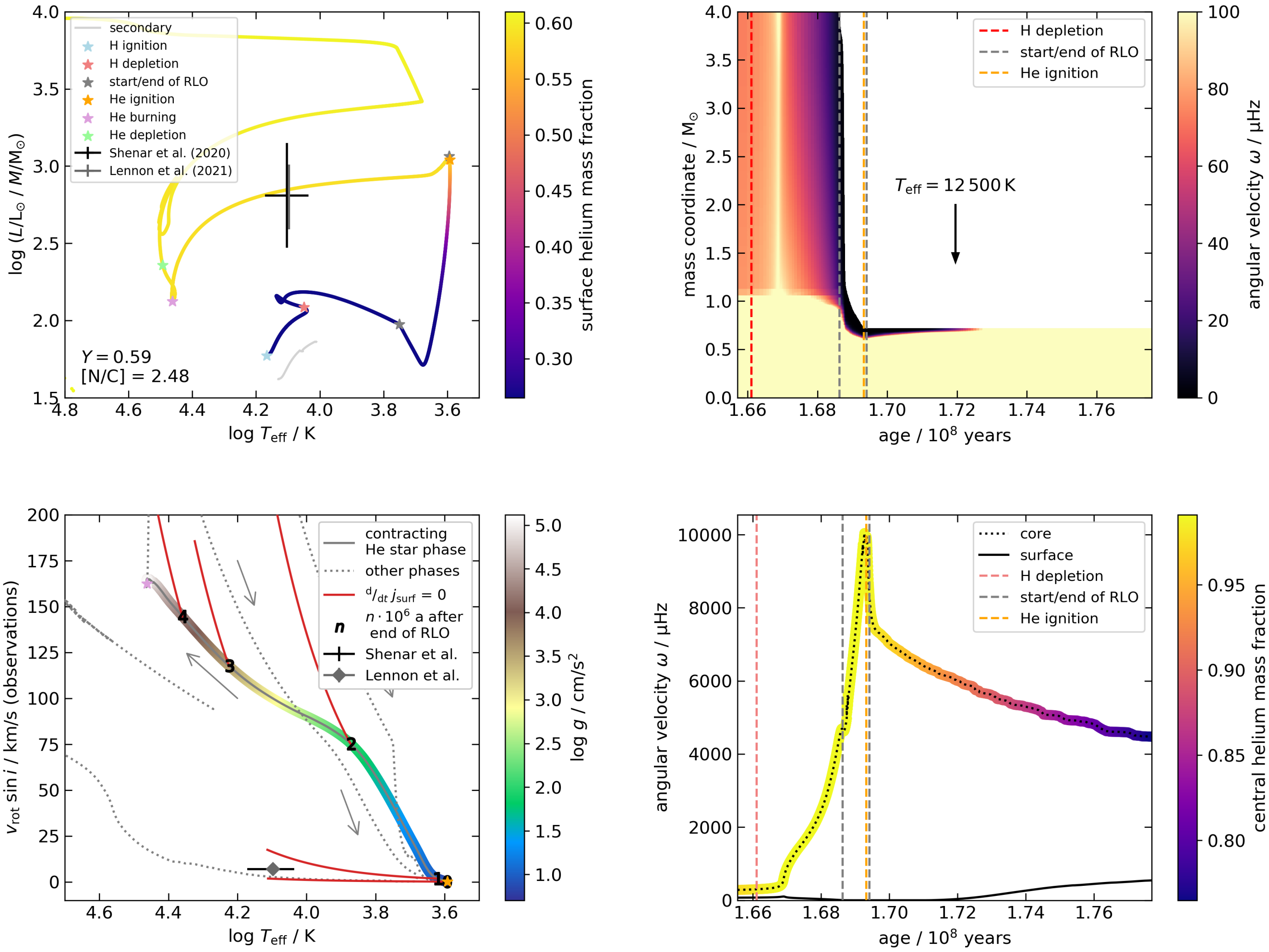

Fig. A.2. Same as Figs. 1, 3, and 5, but without the Spruit–Tayler dynamo. The top right panel only depicts angular velocities up to 100 μHz.

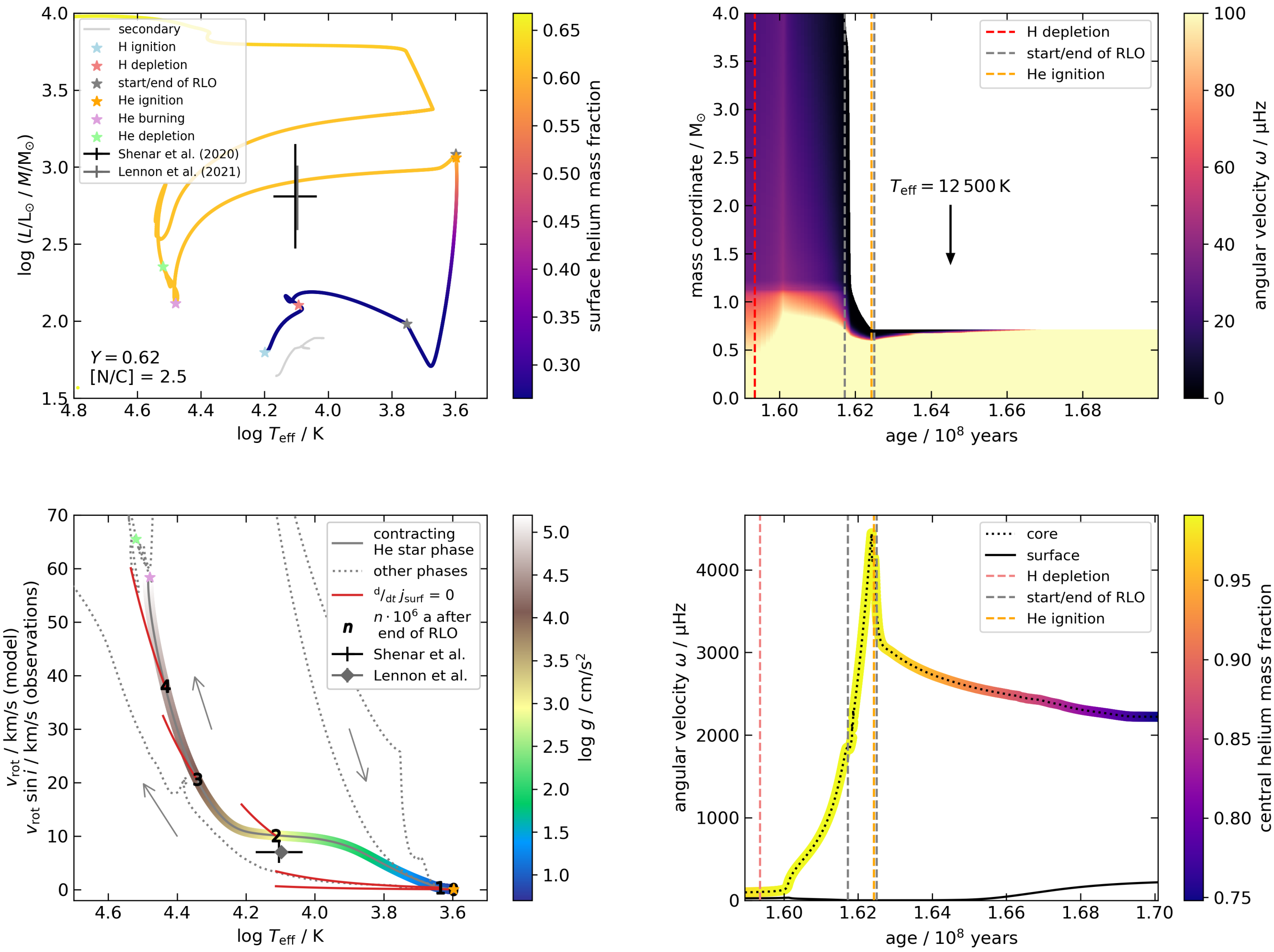

Fig. A.3. Same as Figs. 1, 3, and 5, but with an initial rotation of 20% of the critical rotation and without the Spruit–Tayler dynamo. The top right panel only depicts angular velocities up to 100 μHz.

Appendix B: Predictions for orbital period, rotational velocity, and surface helium abundance of donor star models contracting after RLO

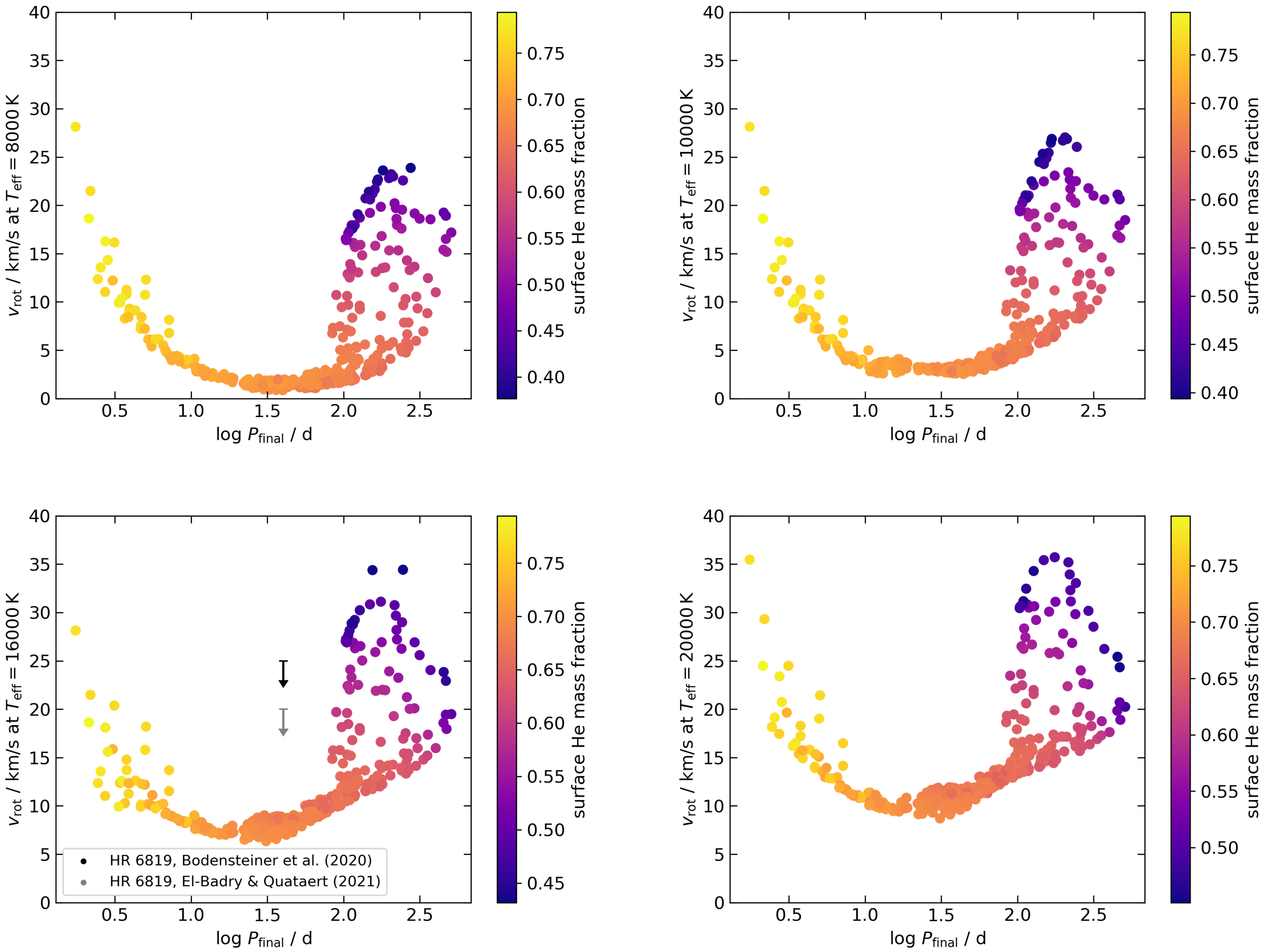

Fig. B.1. Same as Fig. 7, but with an effective temperature of 8 000 K (*top left*), 10 000 K (*top right*), 16 000 K (*bottom left*), and 20 000 K (*bottom right*). The bottom left panel shows the measurements of Bodensteiner et al. (2020b) and El-Badry & Quataert (2021) for HR 6819.

APPENDIX C

Appendix to Chapter 4

C.1 Fits as a function of main-sequence lifetime

For the application of our results, it may be more practical to use the ratio of the time t_{RLO} when the RLO begins to the main-sequence lifetime t_{MS} of the donor as the independent quantity instead of the initial orbital period. We show that in Fig. C.1. The ratio of the post-Case AB mass to the post-Case B mass increases and the core hydrogen burning lifetime decreases with $t_{\mathrm{RLO}}/t_{\mathrm{MS}}$. In this representation the two quantities become mass dependent again. For the mass after Case AB, we find a rational function of the form

$$\frac{M_{\mathrm{AB}}}{M_{\mathrm{B}}} = a + \frac{b}{\log M_{\mathrm{ini}}} + \frac{c t_{\mathrm{RLO}}}{t_{\mathrm{MS}}} + \frac{d t_{\mathrm{RLO}}}{t_{\mathrm{MS}} \log M_{\mathrm{ini}}} \tag{C.1}$$

well fitting. We find $(a, b, c, d) = (2.76 \pm 0.03, -3.75 \pm 0.05, -1.60 \pm 0.04, 3.47 \pm 0.05)$ for the LMC and $(a, b, c, d) = (2.03 \pm 0.07, -2.50 \pm 0.10, -0.86 \pm 0.08, 2.21 \pm 0.11)$ for the SMC. The root mean square relative deviations are 2% and 4%, and the maximum relative deviations are 12% and 21%.

For the increase in core hydrogen burning lifetime, we find a power law of the form

$$\frac{t'_{\mathrm{MS}}}{t_{\mathrm{MS}}} = 1 + a \cdot M_{\mathrm{ini}}^{-b} \cdot \left(1 - \frac{t_{\mathrm{RLO}}}{t_{\mathrm{MS}}}\right)^{c} \tag{C.2}$$

well fitting. We find $(a, b, c) = (116.8 \pm 1.7, 1.618 \pm 0.004, 1.465 \pm 0.003)$ for the LMC and $(a, b, c) = (80.5 \pm 4.7, 1.438 \pm 0.016, 1.649 \pm 0.012)$ for the SMC. The root mean square relative deviations are 0.3% and 0.9%, and the maximum relative deviations are 4% and 6%.

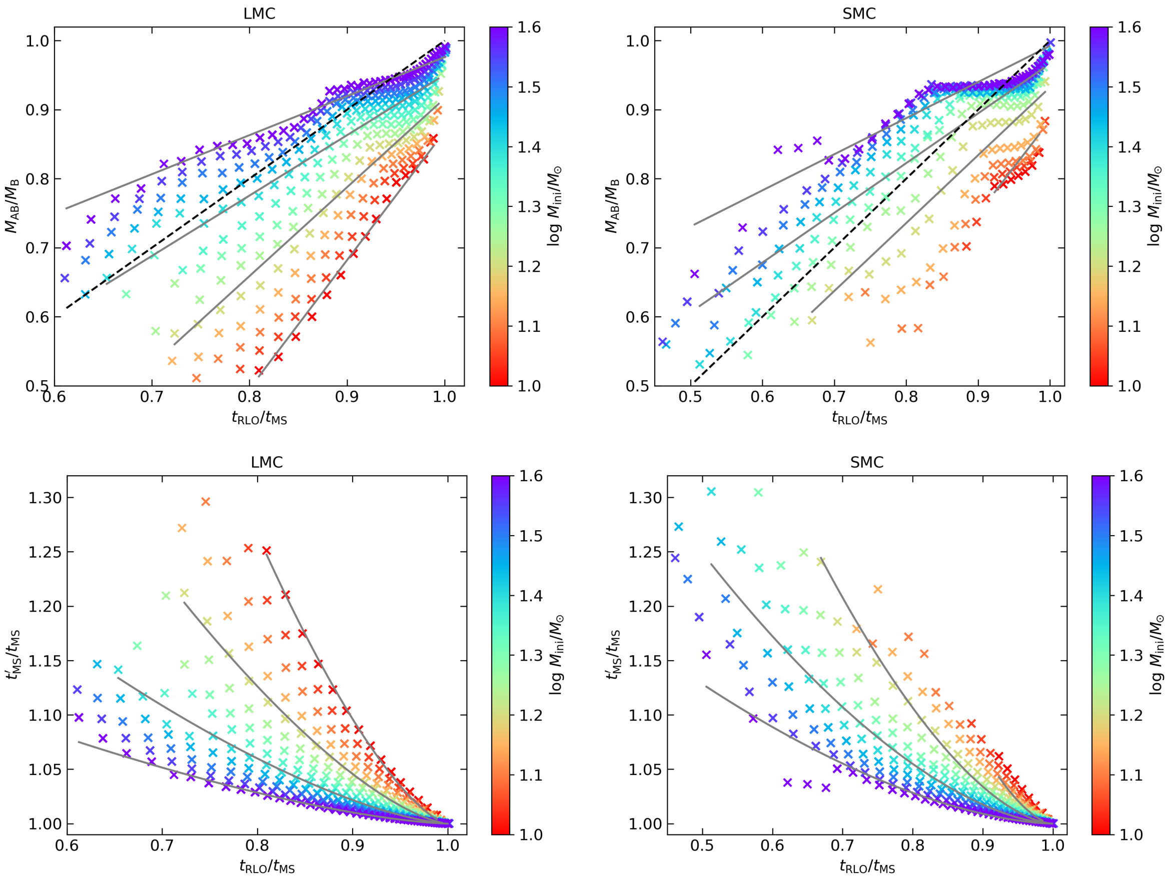

Figure C.1: Same as Fig. 4.1 (top, also top here) and 4.3 (top, here bottom), but as a function of the fraction in donor hydrogen burning lifetime when the RLO begins. Grey lines indicate our best fit to the data and the black dashed line shows the approach of Romero-Shaw et al. (2023), i.e. $M_{\rm AB} = M_{\rm B} t_{\rm RLO}/t_{\rm MS}$. The panels on the left show LMC models, and on the right SMC show models.

APPENDIX D

Appendix to Chapter 5

Here, we provide the HRDs of accreting single-star models for different initial masses (Fig. D.1 and D.2), boundaries for contact avoidance for different angular momentum budgets (Fig. D.3 to D.5), and more analyses of WR stars (Fig. D.6).

D.1 Hertzsprung-Russell diagrams of accreting stellar models

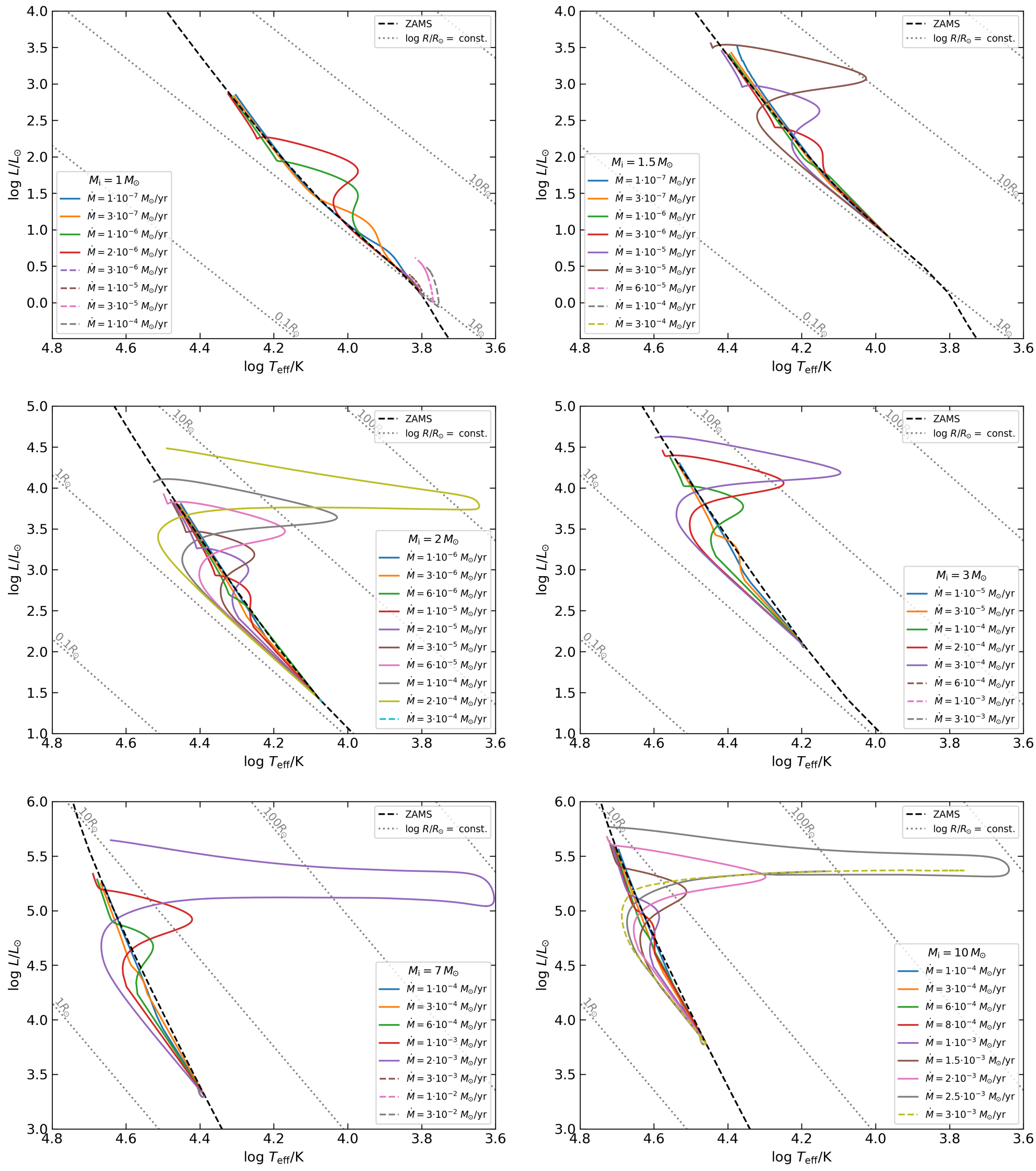

Figure D.1: HRDs of our $1M_{\odot}$, $1.5M_{\odot}$, $2M_{\odot}$, $3M_{\odot}$, $7M_{\odot}$, and $10M_{\odot}$ models for different accretion rates (indicated by colour) together with the final mass of the models.

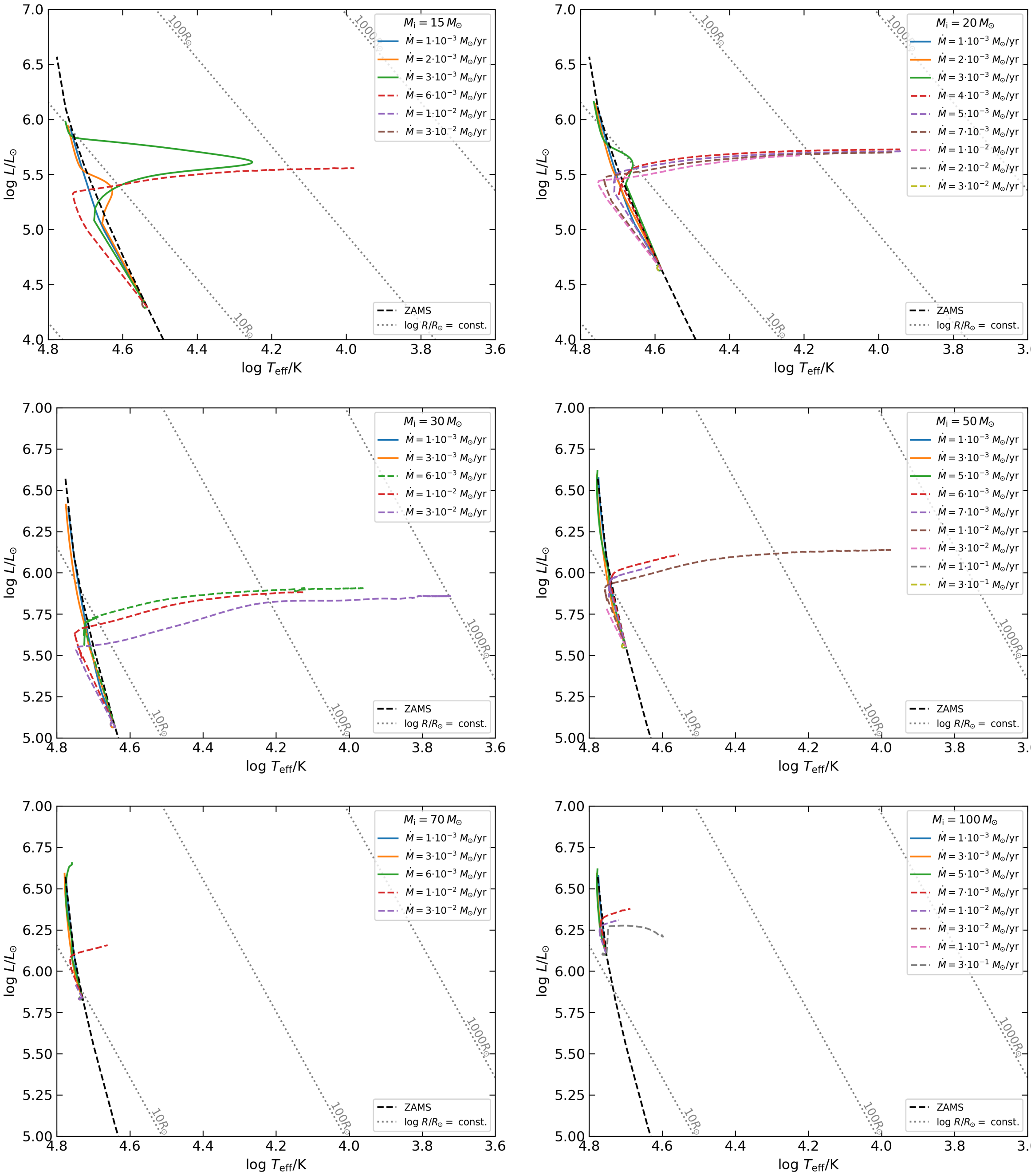

Figure D.2: HRDs of our $15M_\odot$, $20M_\odot$, $30M_\odot$, $50M_\odot$, $70M_\odot$, and $100M_\odot$ models for different accretion rates (indicated by colour) together with the final mass of the models.

D.2 Boundaries of contact/L$_2$-overflow avoidance regions

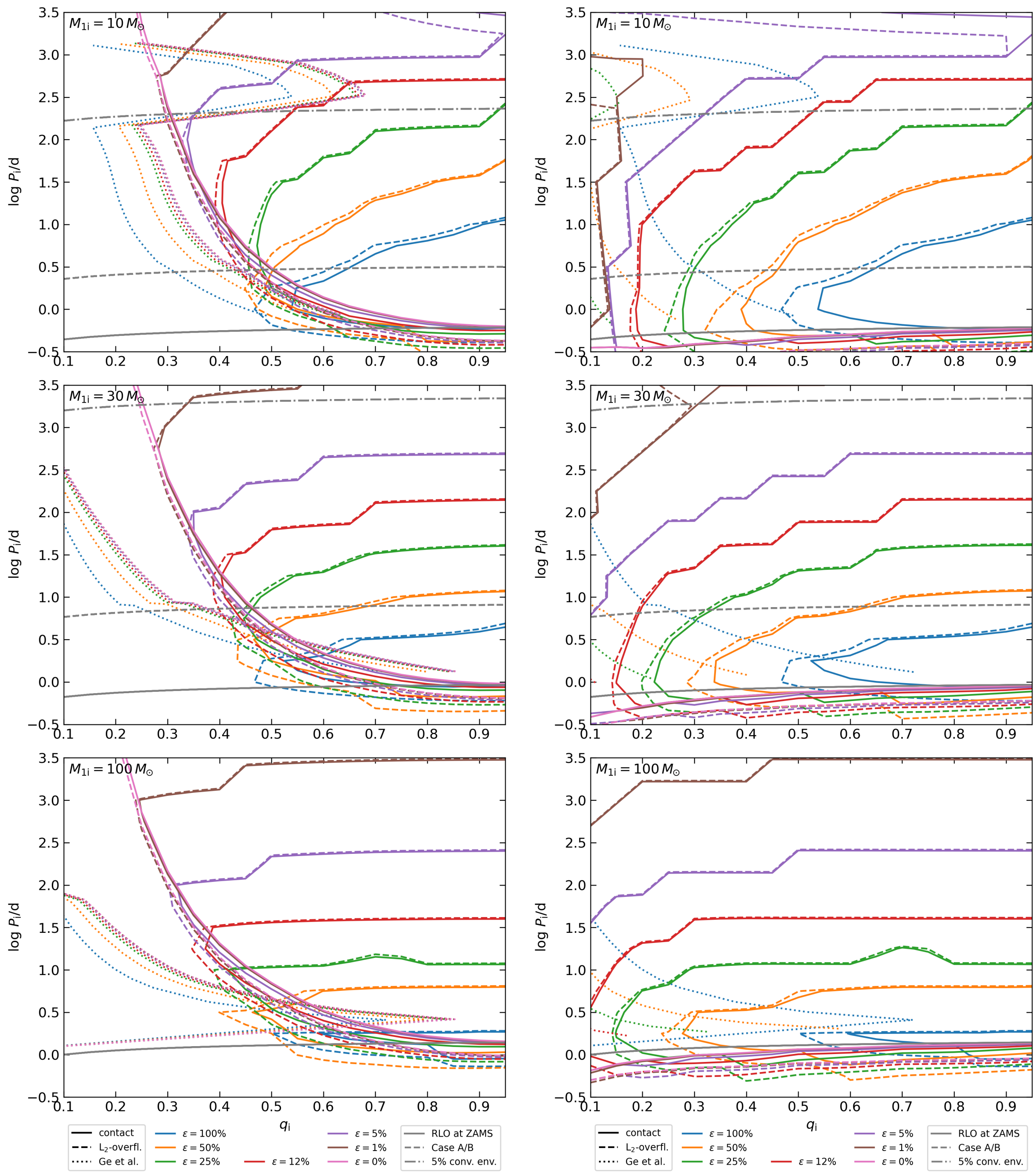

Figure D.3: Same as Fig. 5.8, but the ejected material carries double the donor's specific orbital angular momentum (i.e. $\alpha = \eta = 0$, $\beta = -\varepsilon$, $B = 2$) or no angular momentum ($A = B = H = 0$, right).

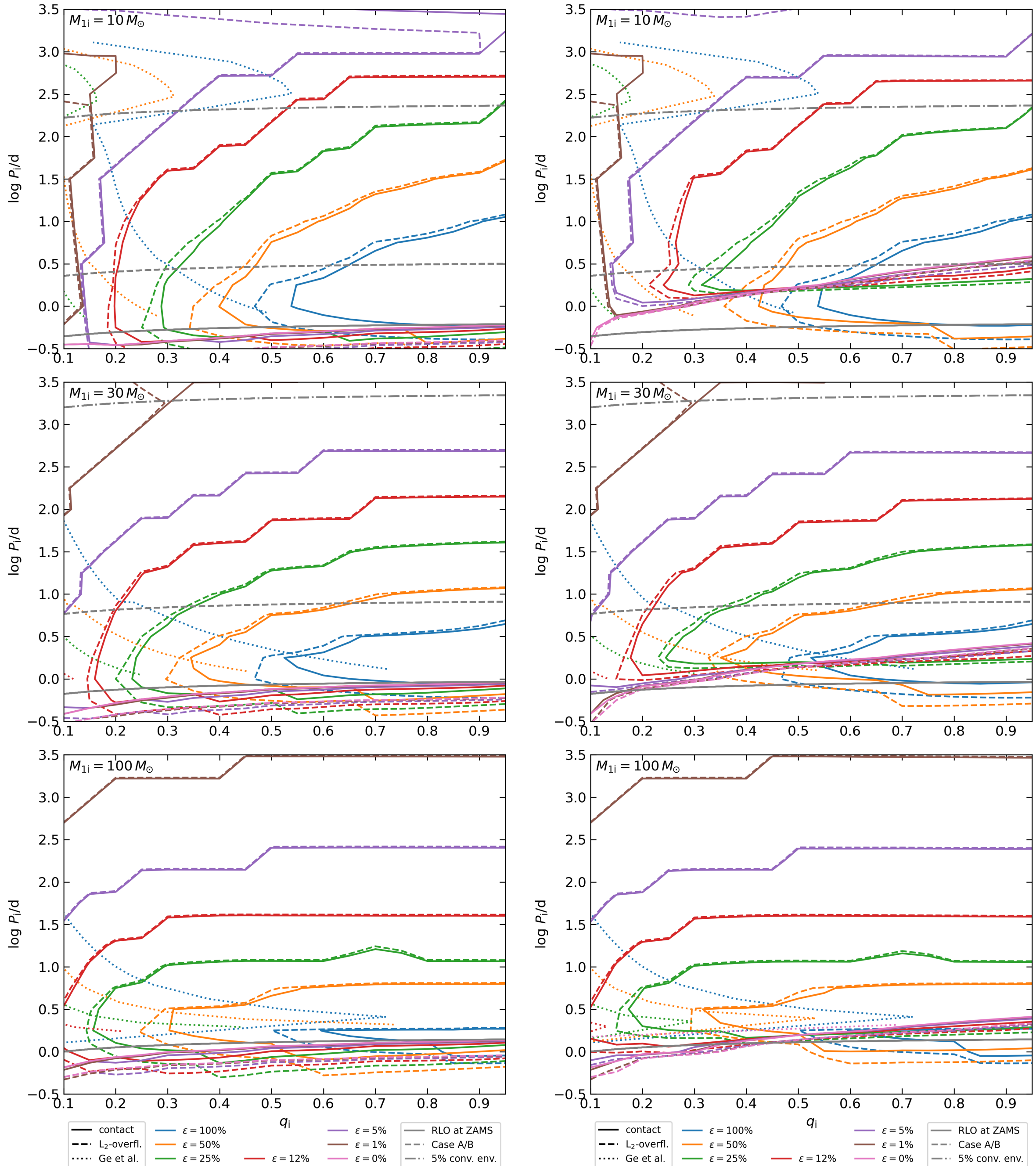

Figure D.4: Same as Fig. 5.8, but the ejected material carries single (i.e. $A = 1$, left) or double (i.e. $A = 2$, right) the donor's specific orbital angular momentum ($\beta = \eta = 0$, $\alpha = -\varepsilon$).

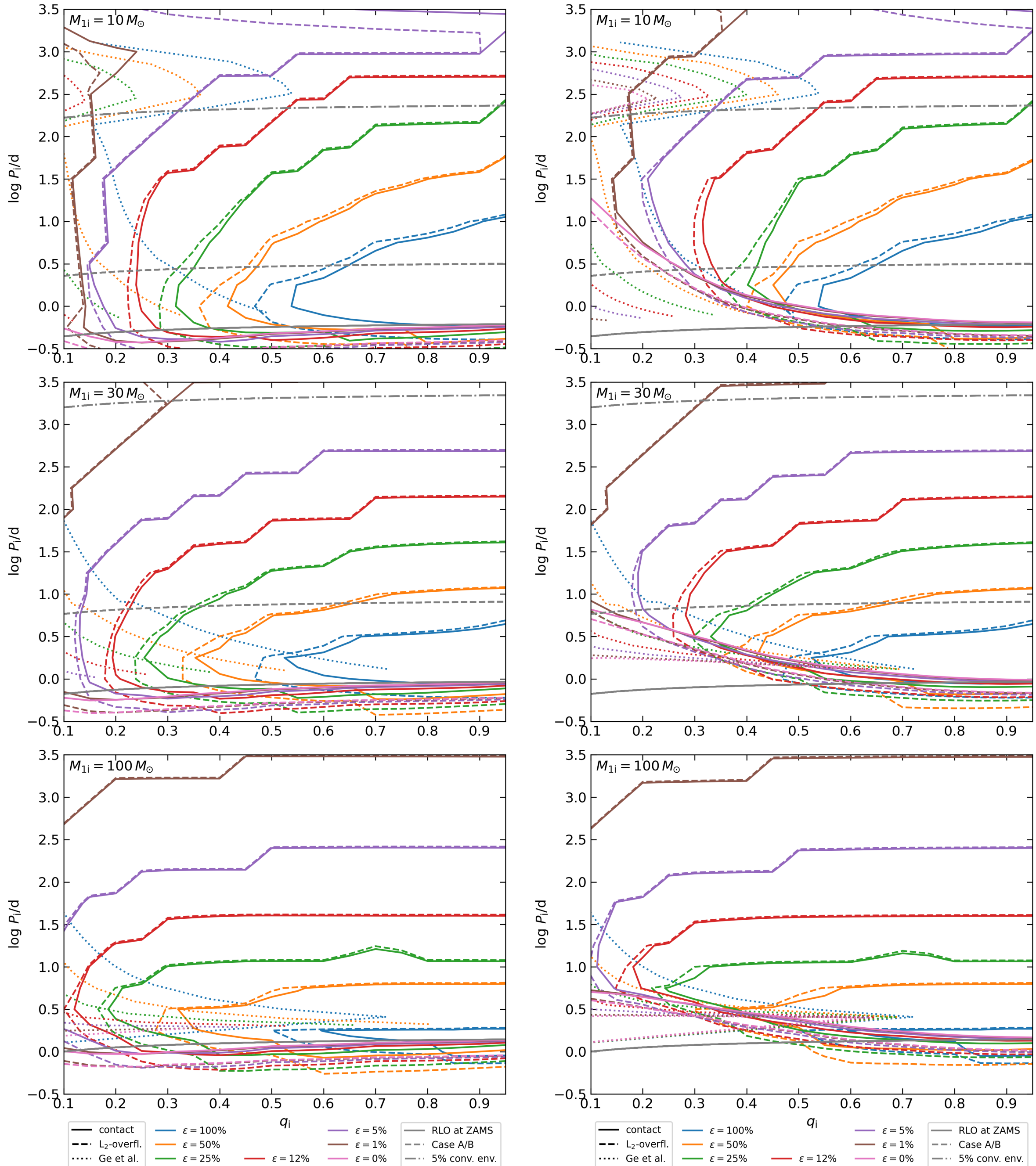

Figure D.5: Same as Fig. 5.8, but the ejected material carries single (i.e. $H = 1$, left) or double (i.e. $H = 2$, right) the system's specific orbital angular momentum ($\alpha = \beta = 0$, $\eta = -\varepsilon$).

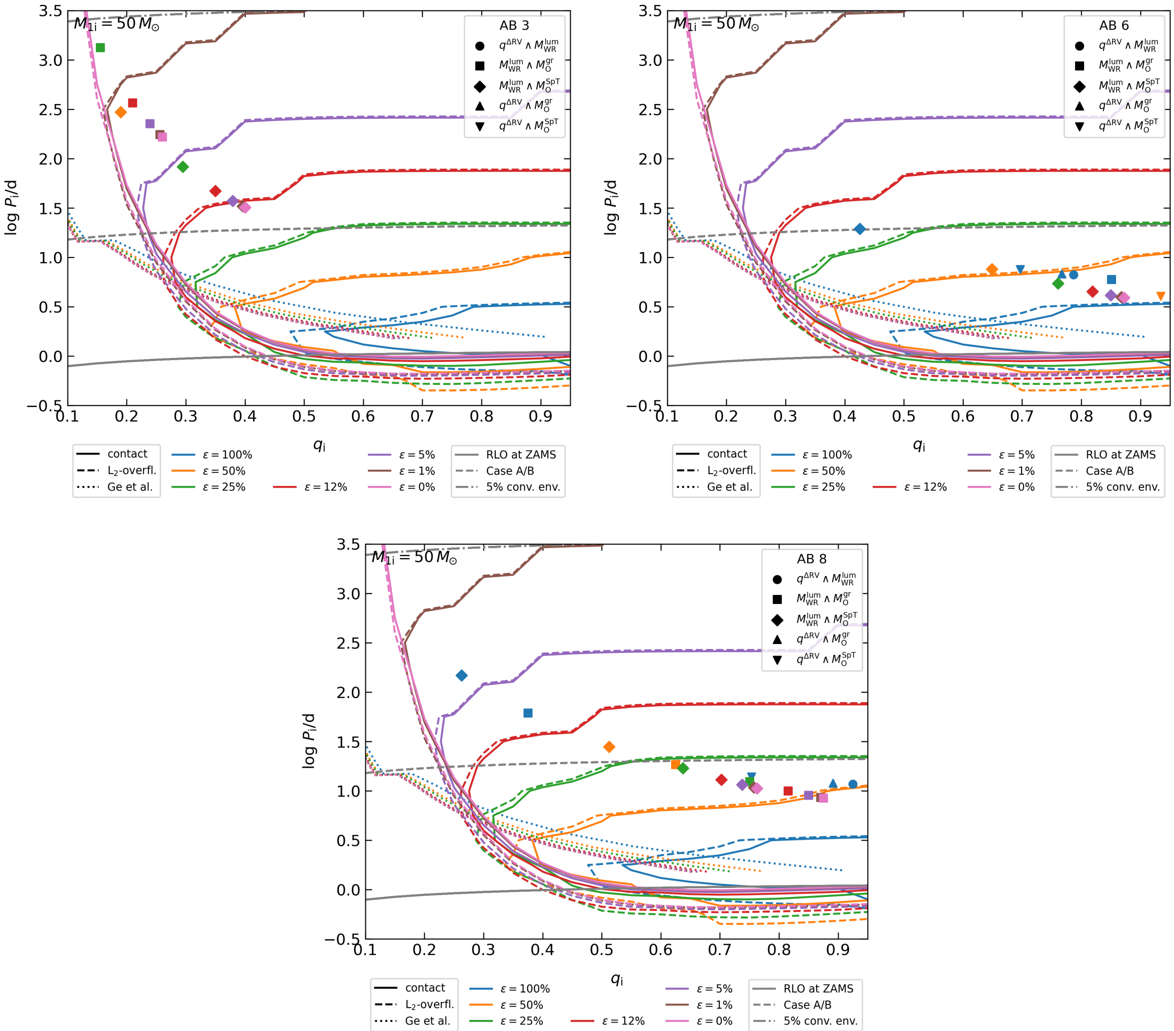

Figure D.6: Same as Fig. 5.9, but for AB 3 (left), AB 6 (right), and AB 8 (bottom). We assumed a WR progenitor mass of $50M_\odot$, which is a typical number (see Table 5.3), and since the area of the contact avoiding region varies not so strongly with mass.

APPENDIX E

Appendix to Chapter 6

On the following pages, we provide diagrams about the evolution of binary systems until one components ends its live for the merger of the system (such as Fig. 6.3) for different masses ($8M_{\odot}$, $9M_{\odot}$, $12M_{\odot}$, $15M_{\odot}$, $20M_{\odot}$, $25M_{\odot}$, $30M_{\odot}$, $40M_{\odot}$, $50M_{\odot}$, $70M_{\odot}$, and $100M_{\odot}$) and predicted numbers of OBe and normal OB stars for different initial distributions in Fig. E.12.

E.1 More q–log P diagrams

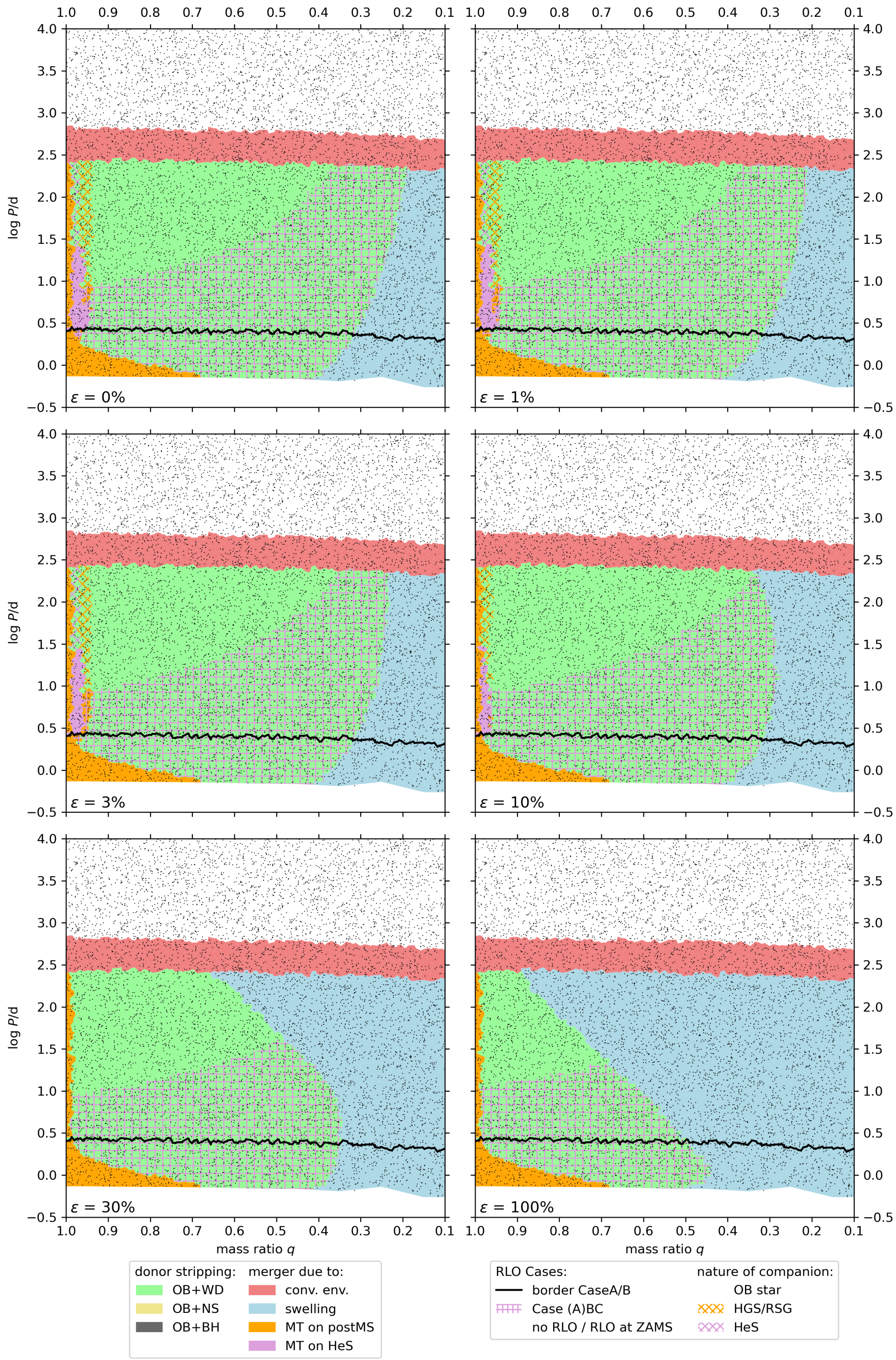

Figure E.1: Same as 6.3, but for a primary mass of $8M_{\odot}$.

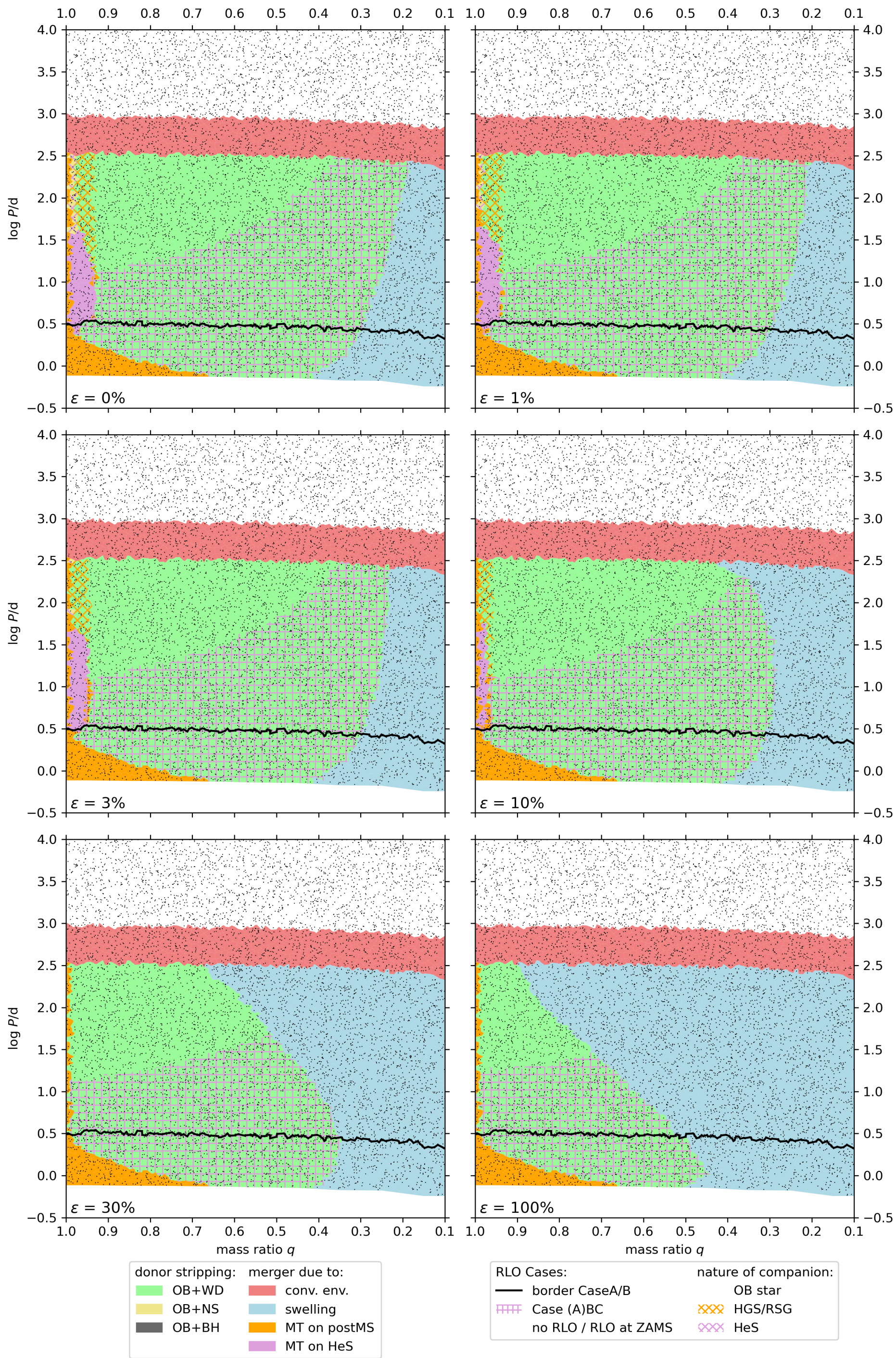

Figure E.2: Same as 6.3, but for a primary mass of $9M_{\odot}$.

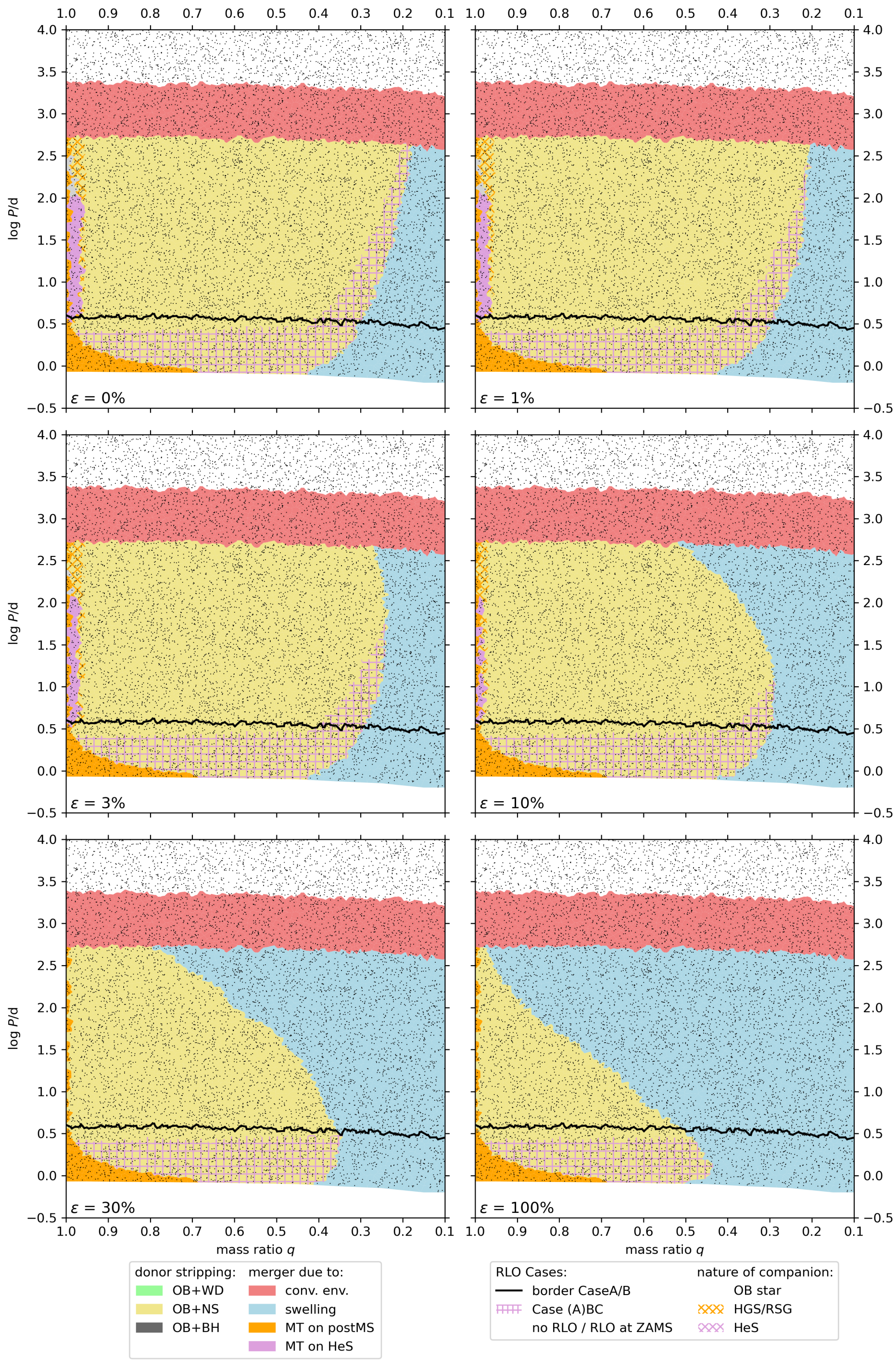

Figure E.3: Same as 6.3, but for a primary mass of $12M_{\odot}$.

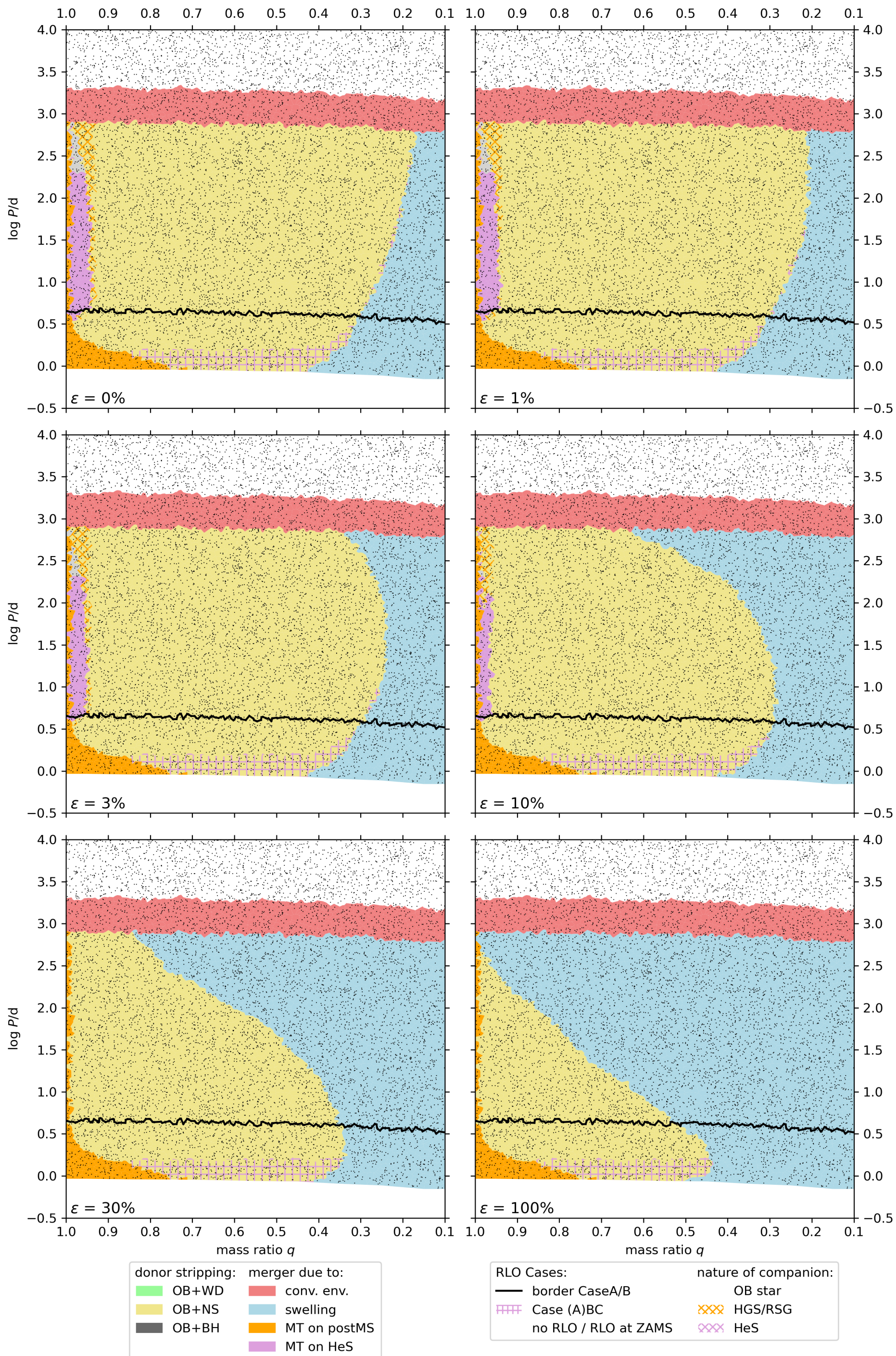

Figure E.4: Same as 6.3, but for a primary mass of $15M_{\odot}$.

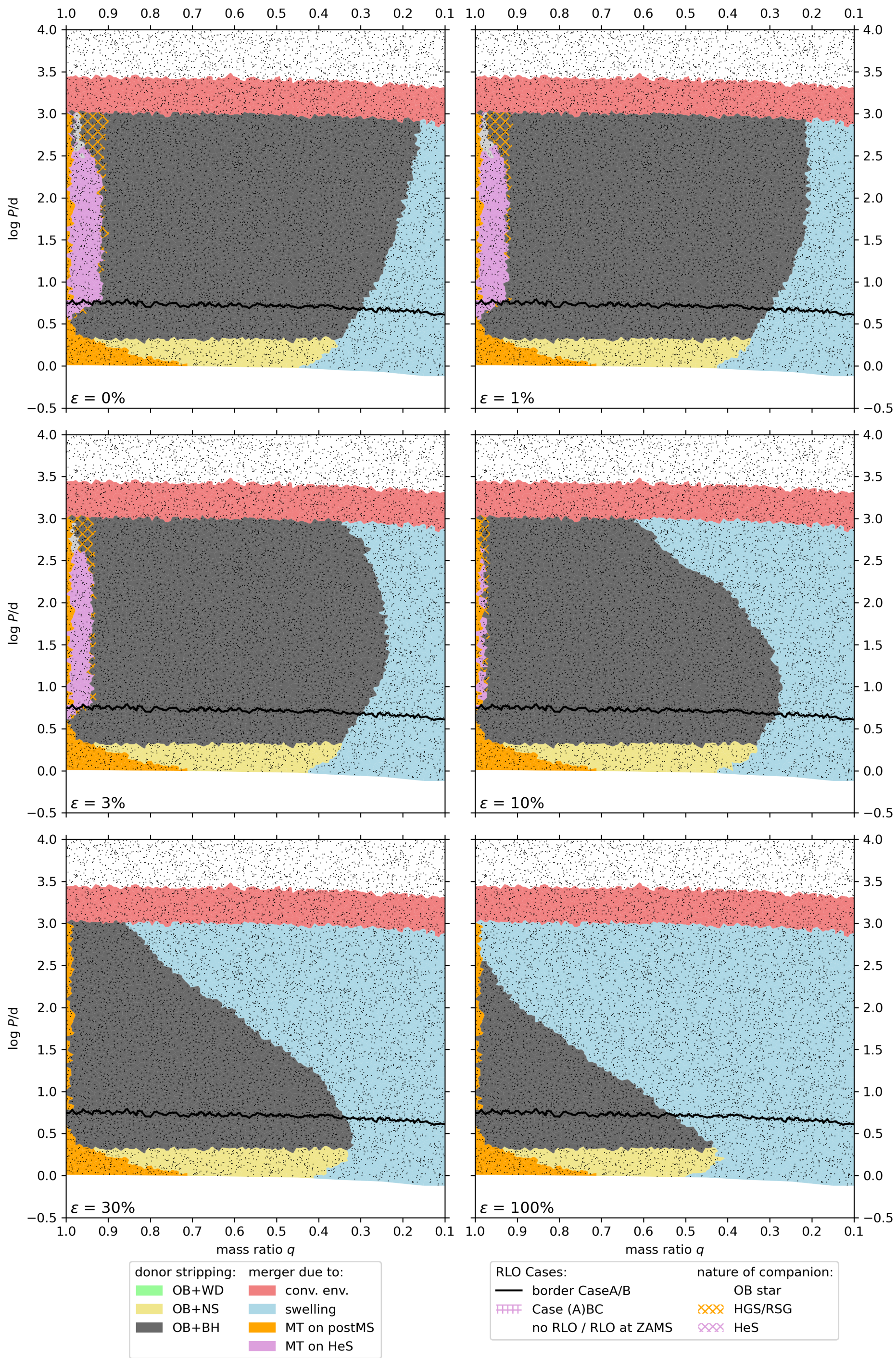

Figure E.5: Same as 6.3, but for a primary mass of $20M_{\odot}$.

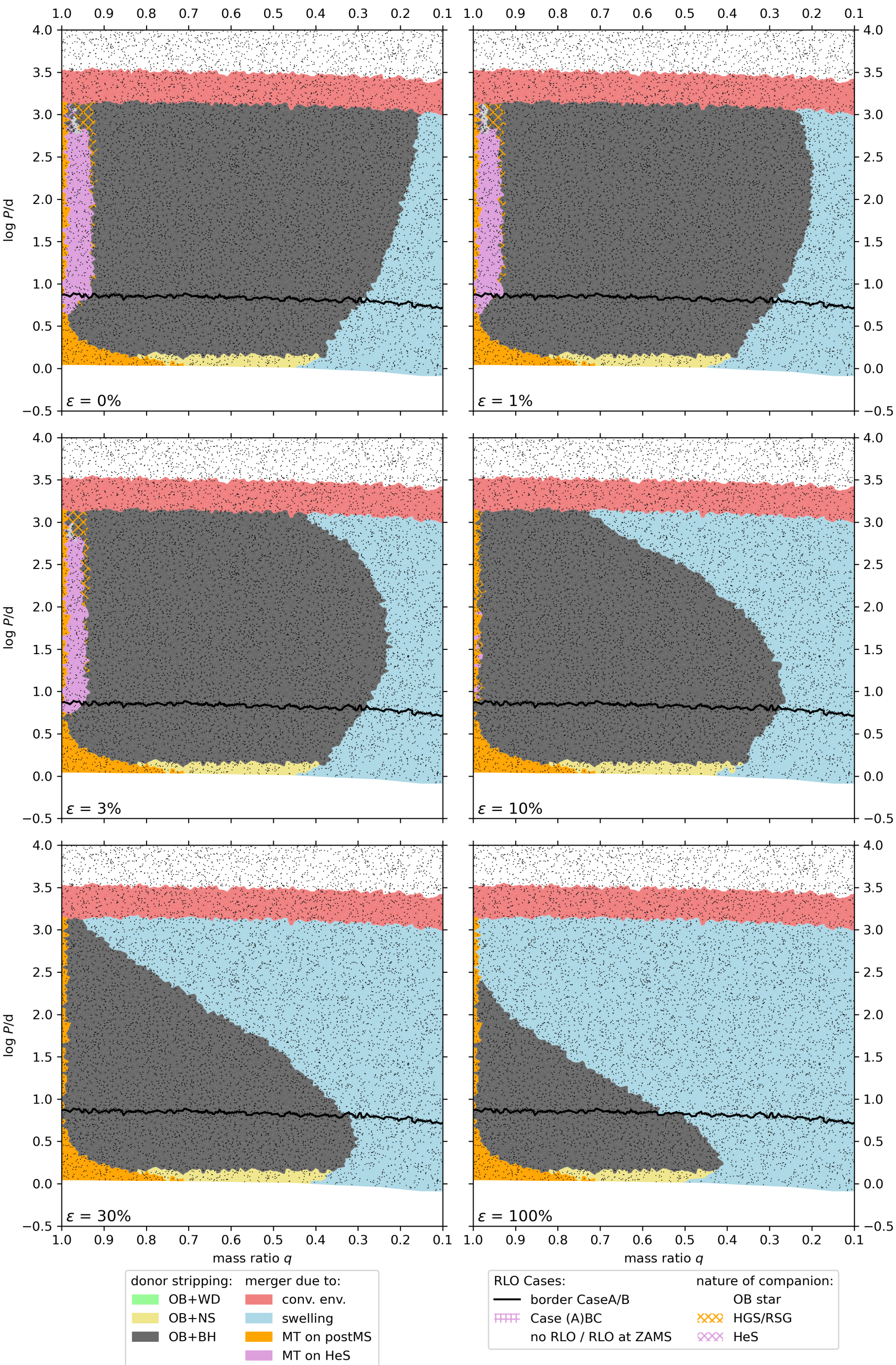

Figure E.6: Same as 6.3, but for a primary mass of $25M_{\odot}$.

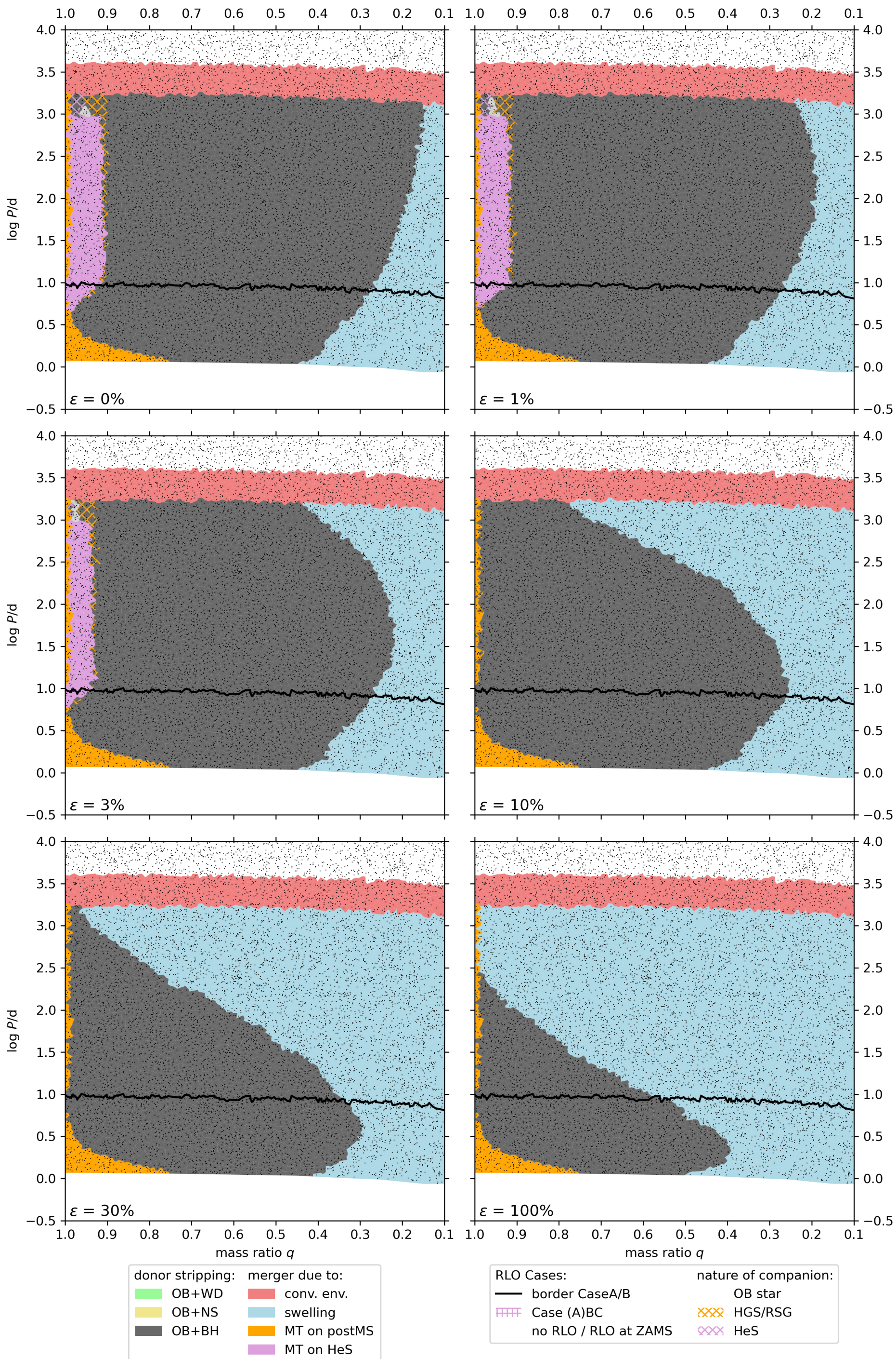

Figure E.7: Same as 6.3, but for a primary mass of $30M_{\odot}$.

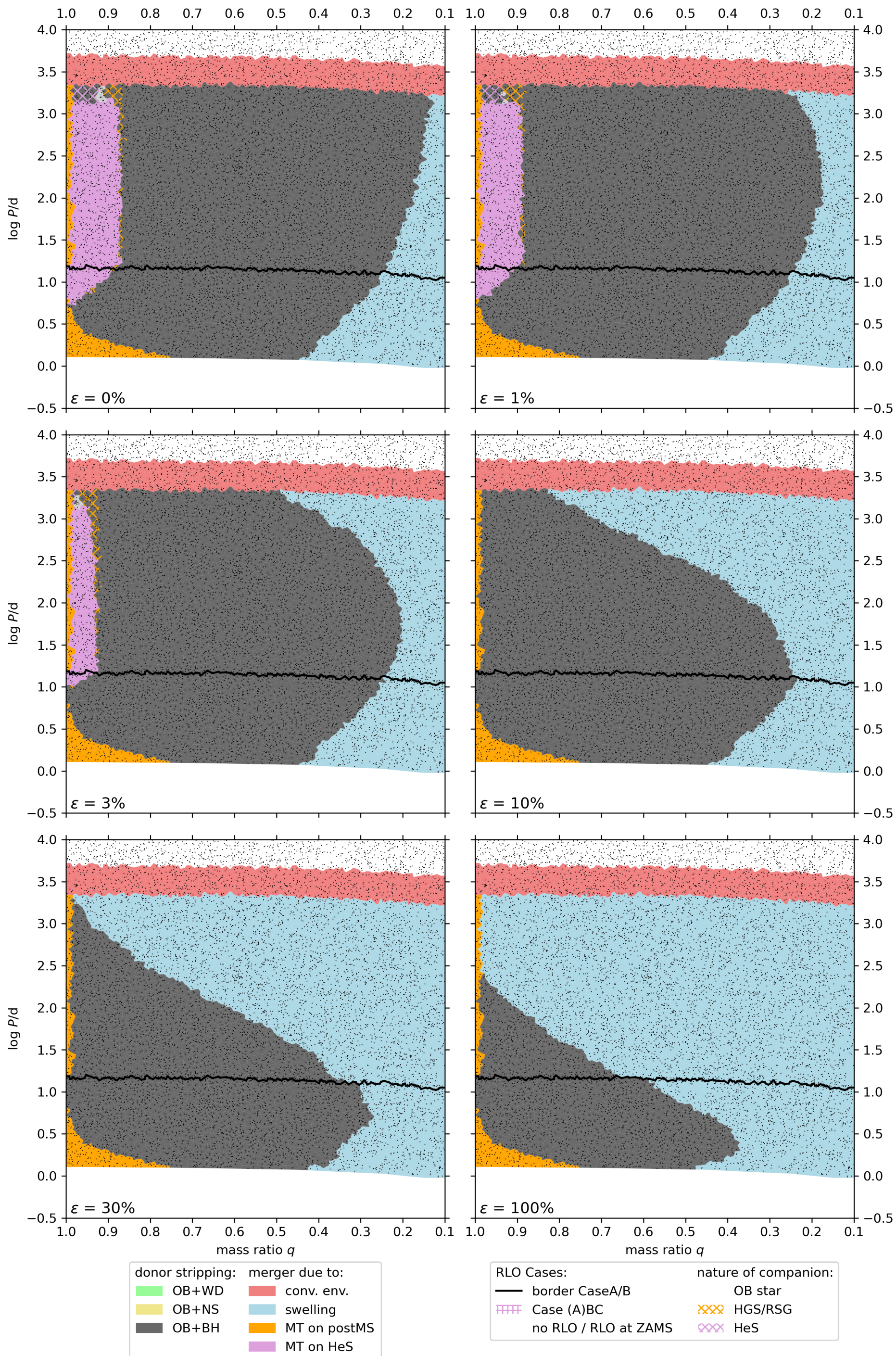

Figure E.8: Same as 6.3, but for a primary mass of $40M_{\odot}$.

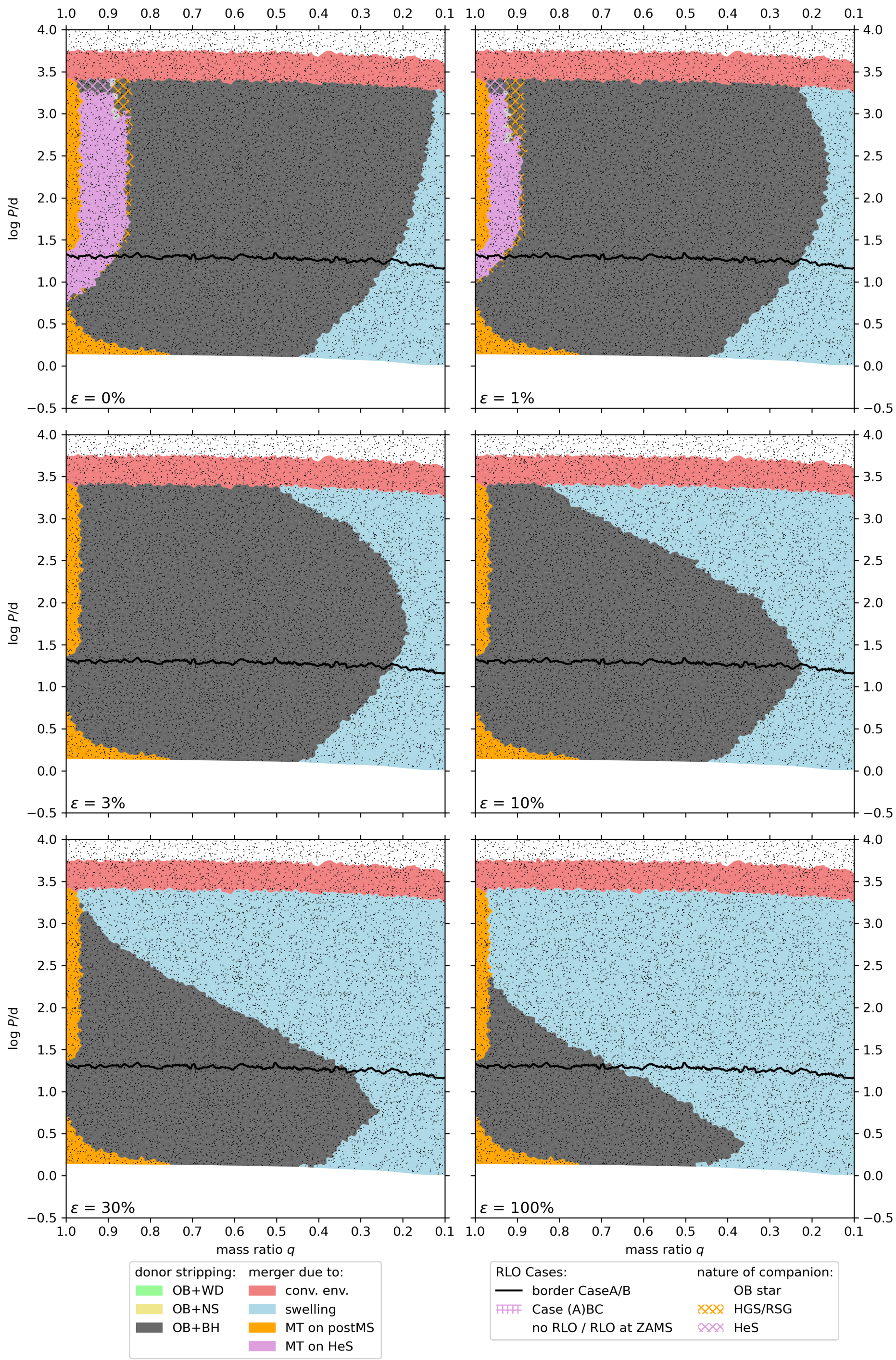

Figure E.9: Same as 6.3, but for a primary mass of $50 M_{\odot}$.

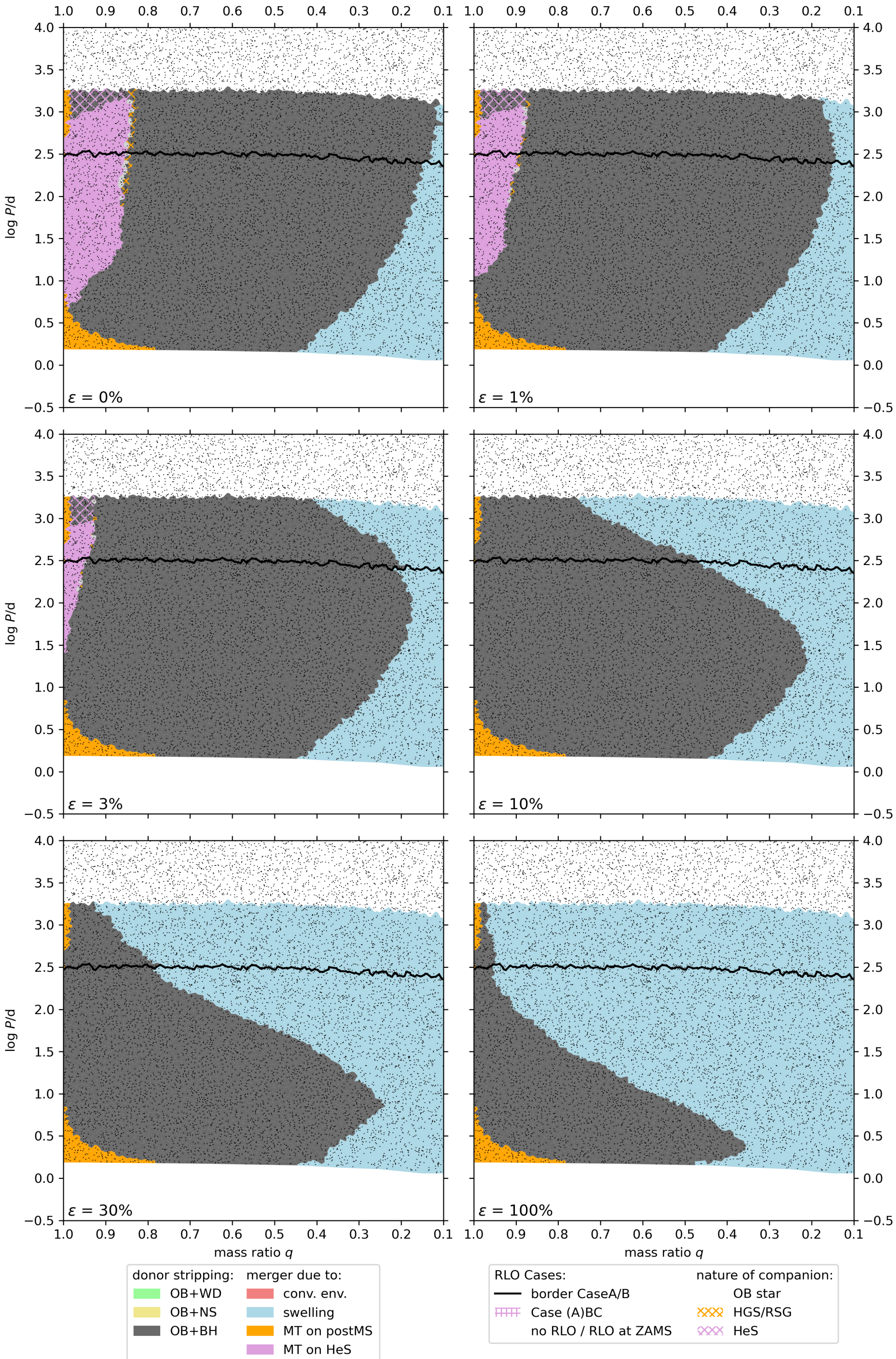

Figure E.10: Same as 6.3, but for a primary mass of $70M_{\odot}$.

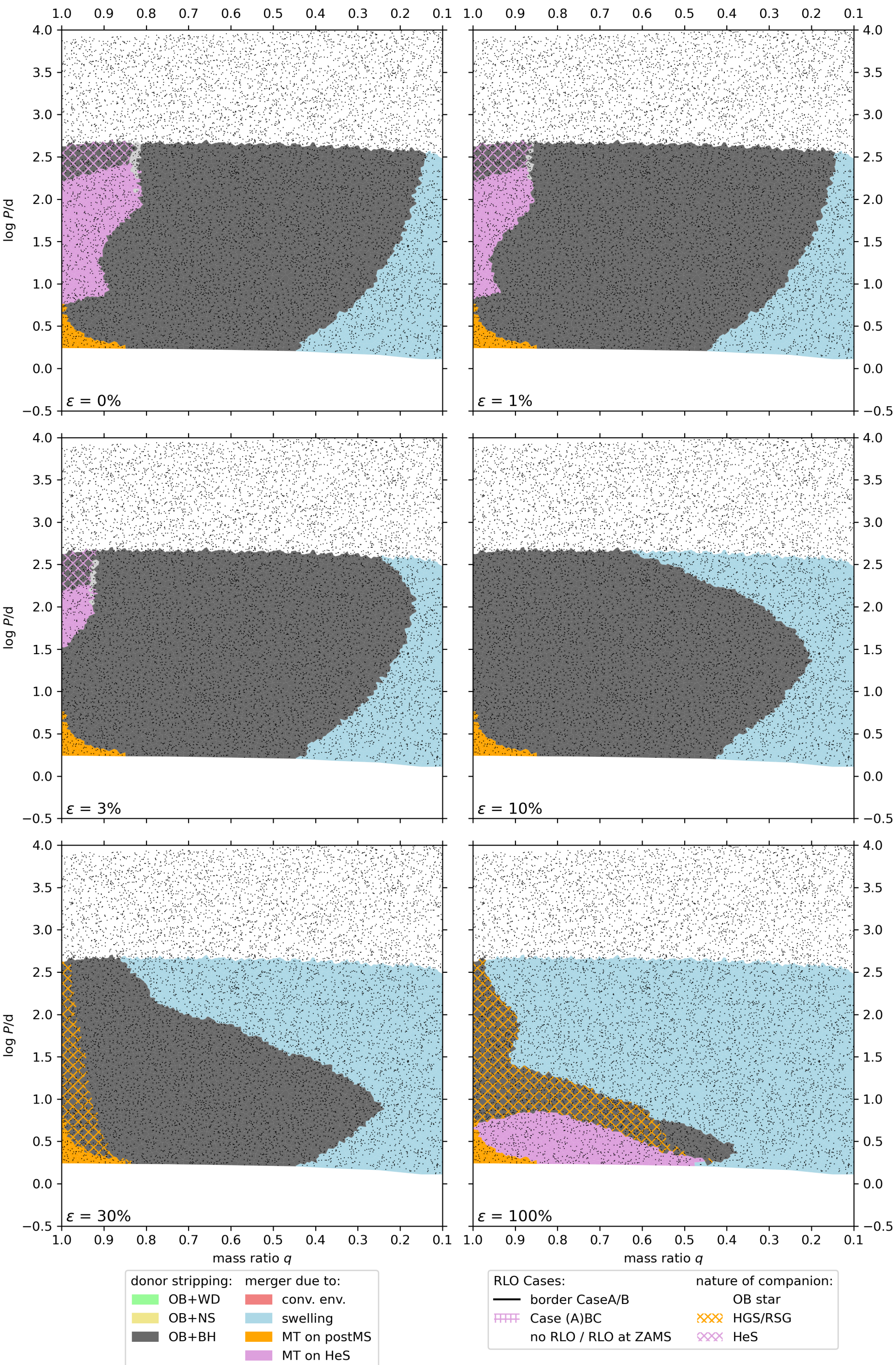

Figure E.11: Same as 6.3, but for a primary mass of $100M_{\odot}$.

E.2 More predicted numbers for different initial binary distributions

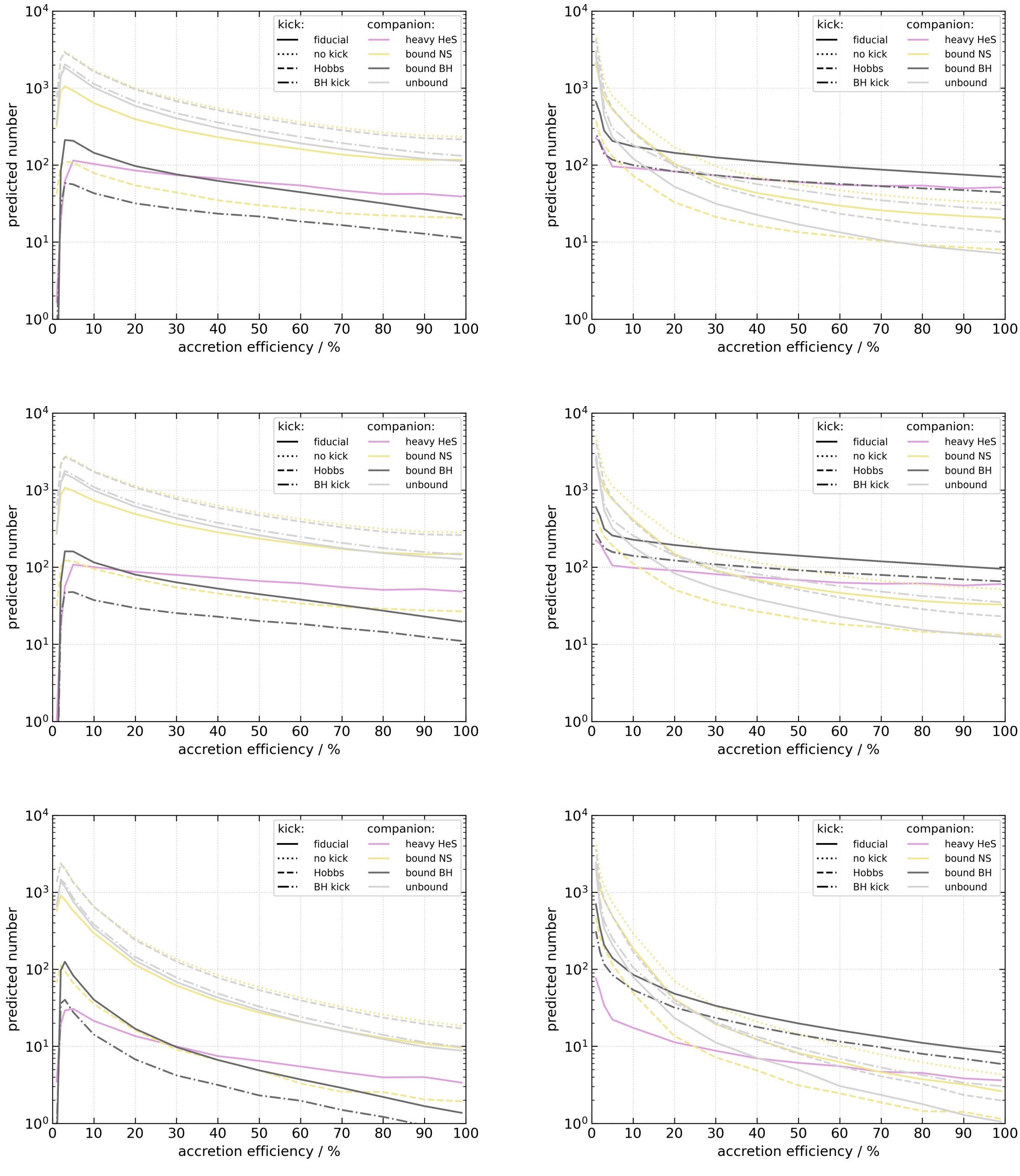

Figure E.12: Predicted number of OBe (left) and normal OB star (right) companions (colour) and different kick scenarios (line style) as a function of accretion efficiency for initially flat binary distributions (top), Sana et al. (2012, middle), and Dunstall et al. (2015, bottom).

Acknowledgements

"It's done!"

— Frodo in *The Lord of the Rings: The Return of the King* by Peter Jackson

Hier nun, am Ende dieser Arbeit möchte ich allen jenen danken, die mich auf dieser Reise unterstützt haben. Am allermeisten hat dies mein Doktorvater Norbert Langer. Nur durch sein immenses Wissen über die Sterne, seine unstillbare Neugier und seine wissenschaftliche Gründlichkeit ist diese Arbeit zu dem geworden, was sie ist. Von ihm habe ich unglaublich viel gelernt!

Viel Hilfe, gute Ideen, konstruktive Kritik und kluge Fragen kamen nicht nur von Norbert selbst, sondern auch aus seiner Arbeitsgruppe in Bonn. Das waren und sind Thomas Tauris (der Betreuer meiner Masterarbeit, ohne den ich vielleicht in einem ganz anderen Themengebiet gelandet wäre), Matthias (von dem ich ComBinE übernommen habe), Martin (Nebulium), Chen, Abel, Nathan, Jonathan, Götz, Patrick, David, Daniel, Koushik, Ben, Xiao-Tian, Harim, Andrea und Caroline. Dazu kommen einige Astros, die ich auf Konferenzen und Treffen kennen und schätzen gelernt habe, und zwar Julia, Tomer, Pablo, Lee, Soetkin, Eva, Lieke, Tinne, John, Dori, Fabian, Sergio, Hughes, Alex, Danny und Selma.

Die Arbeit der Bonner Gruppe und auch meine eigene wäre nicht möglich gewesen ohne die großartige Unterstützung der Mitarbeiter am AIfA und am MPIfR. Hier danke ich besonders Elisabeth, Sabine, Kira, Andreas und Ole.

Wenn man eine so große Aufgabe bewältigen will, darf man den Spaß an der Arbeit (also an der Physik) nicht verlieren – oder sollte ihn zumindest schnell wieder finden! Dabei hat mir besonders die Physikshow der Uni Bonn geholfen, wofür ich mich bei Herbi Dreiner, Michael Kortmann und allen Student:innen der Physikshow, die in den letzten zehn Jahren dabei waren, bedanken möchte: Katha, Julia, Jana, Jana, Timo, Anne, Laura, Finn, Alexandra, Sarah, Johann, Lennart, David, Niklas, Laurita, Till, Krissi, Steffi, Lara und Jeremy sowie Timo und Sacha. Ohne den regelmäßigen Quatsch mit euch wäre ich durchgedreht!

Genauso durchgedreht wäre ich ohne die Feierabendbiere im MIUB. Prost, Felix, Timon, Sebastian, Tobias, Matthias, Julian, Armin und Andreas!

Das alles ist nur möglich gewesen, weil ich eine tolle Familie habe, die mich all die Jahre begleitet und unterstützt hat. Ohne meine Eltern, meine Patentante und meinen Bruder wäre ich nie so weit gekommen.

Die letzten Wochen waren der anstrengendste Teil dieser Arbeit. Ohne Svenja hätte ich das nicht geschafft.